Study of the physical mechanisms involved in the femtosecond laser optical breakdown of dielectric materials

Alexandros Mouskeftaras

Thèse présentée pour obtenir le grade de

DOCTEUR DE L'ECOLE POLYTECHNIQUE

Spécialité: Physique

par

ALEXANDROS MOUSKEFTARAS

Sujet de la thèse :

Study of the physical mechanisms involved in the femtosecond laser optical breakdown of dielectric materials

Soutenue le 11 Février 2013 devant le jury composé de :

Dr.	Marc	SENTIS	Président
Prof.	Bärbel	RETHFELD	Rapporteur
Dr.	Razvan	STOIAN	Rapporteur
Prof.	Manuel	JOFFRE	Examinateur
Dr.	Stéphane	GUIZARD	Directeur de thèse

Thèse préparée au Laboratoire des Solides Irradiées

Remerciements

D'abord, je souhaite exprimer ma gratitude aux personnes qui ont permis la réalisation de ce travail de thèse. Cette dernière a été realisée au *laboratoire des solides irradiés* (LSI) de l'Ecole Polytechnique d'Octobre 2009 au Janvier 2013. Je tiens à remercier Martine SOYER en tant que directrice du laboratoire pour m'avoir accueilli au sein de cela.

Ensuite, je souhaite remercier Prof. Bärbel RETHFELD et Dr. Razvan STOIAN pour avoir accepté de se charger de la lourde tache de rapporter cette thèse ainsi que pour leurs remarques qui ont permis d'améliorer la qualité de ce manuscrit. Je remercie également Dr. Marc SENTIS et Prof. Manuel JOFFRE d'avoir accepté de faire partie de mon jury. Je suis très reconnaissant à l'ensemble des membres du jury pour leur flexibilité et leur bonne volonté, notamment quand il a fallu changer de salle en pleine séance des questions.

Je remercie très profondement mon directeur de thèse Dr. Stéphane GUIZARD pour m'avoir guidé tout au long de cette aventure scientifique. J'ai eu la chance de travailler avec un scientifique d'une qualité exceptionnelle. J'ai encore plus de chance d'avoir établi une très belle amitié avec Stéphane qui perdurera, je suis sûr, dans le temps.

Durant ma thèse, j'ai eu la chance également de travailler avec Dr. Sergei KLIMENTOV qui m'a accompagné lors de nombreuses expériences d'interferometrie fréquentielle et de spectroscopie de pohtoélectrons. J'ai particulièrement apprecié nos discussions scientifiques et son goût pour la science. Je n'oublie pas Dr. Nikita FEDOROV, qui a partagé ses compétences en tant qu'expérimentateur d'exception lors de ma première année de thèse.

Ce travail doit beaucoup aux personnes qui se sont occupé du bon fonctionnement de la chaîne *Laser Ultra-Court Accordable* (LUCA), au comissariat à energie atomique (CEA) du centre Saclay. Je souhaite remercier notamment Olivier GOBERT, Michel PERDRIX, Fabien LEPETIT et Delphine JOURDAIN.

Je souhaite également remercier Dr. Ghita GEOFFROY, directrice adjointe au *Centre Lasers Intenses et Applications* (CELIA) de Bordeaux, pour sa collaboration lors des expériences de spectroscopie de photoelectrons.

Enfin, je souhaite remercier l'ensemble des personnes qui m'ont permis d'arriver

jusqu'à là. Je pense notamment à Olivier (le Rouennais) et Olivier (le Breton) qui m'ont beaucoup soutenu lors de ma première année en France et aussi par la suite, pendant toutes mes années universitaires, Keven qui a toujours été un ami dont j'étais fier et Debajyoti de partager une belle amitié. Je suis très reconnaissant à Yorgo pour avoir été ami et père adoptif.

Abstract

We have carried out detailed time resolved experimental studies of the mechanism of electron excitation-relaxation, when an ultrashort (60 fs -1 ps) laser (ultraviolet (400 nm for this thesis) (UV) and infrared (800 nm for this thesis) (IR)) pulse interacts with a wide band gap dielectric material. The studies cover a range of different dielectric materials and the investigated regimes span from non-destructive ionization of the material at the low power end ($\sim$ TW/cm^2) to ablative domain at a higher laser power ($\sim$ 10 TW/cm^2). This gives fundamental insight into the understanding of the laser damaging process taking place under our irradiation conditions. The usage of time-resolved spectral interferometry technique allows to directly measure the electron density of the irradiated material under different excitation conditions and hence leads to quantification of the process. The measurements, carried out at the optical breakdown threshold utilizing different pulse durations, raise questions regarding the usage of critical excitation density as a universal ablation criterion. A new criterion related to the exchanged energy is proposed. Additionally, the use of an experimental setup implementing a double pump pulse allows the identification of different excitation mechanisms taking place at time scales of the order of the pulse duration used. Electronic avalanche is observed in some materials (SiO_2, NaCl) while this is not the case for others (Al_2O_3, NaCl). These differences are discussed in detail. Next, we measure the energy spectrum of excited electrons with a complementary technique: the photoemission spectroscopy. These results allow us on one hand to show a crossed effect between the two pump pulses and on the other hand to measure electron relaxation characteristic times, as a function of their kinetic energy. Finally, a morphological study of craters resulting from ablation in the case of a single pulse has been carried out for different irradiation parameters: number of shots, energy and pulse duration. This work has been extended to the case of double pulse damage, with the relative delay being the studied parameter.

Contents

List of Figures

Acronyms

UV ultraviolet (400 nm for this thesis) 1

IR infrared (800 nm for this thesis) 1

MPI multiphoton ionization 29

TI tunnelling ionization 29

AI avalanche ionization 62

FDI frequency domain interferometry 63

CB conduction band 10

VB valence band 8

STE self-trapped exciton 10

EM electromagnetic 79

VUV vacuum ultraviolet 119

DTH damage threshold 8

SDTH single pulse damage threshold; UV or IR pulse alone 8

CDTH combined pulse damage threshold: IR fluence for a UV-IR sequence . . . 9

LIPSS laser induced periodic surface structures 142

Introduction

It all started somewhere in 1960 with the first and successful laser emission from a ruby crystal by Theodore Maiman. Shortly after (1961), the second harmonic generation from this rubidium laser has been observed in quartz [28] Soon (in 1967) this spatially confined energy source (continuous wave), provided a directional emission, found its applications in the industry with the first laser cut event on stainless steel, using a 300 W, CO_2 laser. Later and with further confinement of the energy in time (pulsed-laser), a wider range of applications was made possible while the spatial and temporal coherence of this source offered a new powerful tool for diagnostics. The laser-matter interaction field was making its debuts. Further development of the laser sources, involving new wavelengths and higher peak power helped materialize previously predicted theoretical considerations based on nonlinear interaction research.

By the end of the 80s, it was assumed that everything was known about mode-locked femtosecond lasers. Then, starting in 1990 and using Ti:Sapphire lasers, 160 fs [45] and 60 fs [90] pulses have been successfully produced. This along with the chirped pulse amplification (CPA,[93]) technique combined together, made possible the delivery of mJ laser pulses, with pulse durations below 100 fs. Optimal temporal resolution and energy localization had been achieved providing both the tool for extreme stimulation and subsequent response study of the materials.

Over the years, a large variety of applications for ultrashort pulses ($\sim$ fs $-$ ps) have made their appearance exploiting different aspects of this irradiation. Sub-micron machining has been reported as early as 1995 by Pronko [70] on a silver film, where a nano-hole with a depth of 52 nm has been produced. However, although early investigations focused on metals, ablation is possible in transparent dielectric materials as well, in bulk or on the surface. The longitudinal confinement, a consequence of using fs or ps laser pulses, has been studied in sapphire by S. Guizard et al. [39]. In parallel, the lateral confinement of a gaussian laser pulse along with the precise energy threshold in this time scale revealed sub-micron features. These involve 15 nm holes in fused silica [47] (see figure 1) and the laser drilling of nano-channels in thick glass ($\sim$ 400 nm in diameter and $\sim$ 43 μm deep) [8]. The latter may be of great interest for nano-photonics and/or nano-

fluidics. Finally, ultrashort laser pulse machining may be used for processing fine structures in a variety of materials [64]. These applications involve fabrication of medical implants (stent), cap of a fuel injection nozzle and other.

The spatial and temporal confinement present in the interaction of ultrashort laser pulse with matter makes it an excellent candidate for precision and quality machining applications. Moreover, any type of material (ceramics, tooth, explosives, diamond, polymers, eye etc.) may be machined theoretically with this process. Since the nature of the interaction involves electron excitation, the ablation threshold is extremely sensitive on the material properties and thus selective ablation is made possible [43]. Furthermore, the quality of the ablated surface seems to considerably improve with short pulses [17].

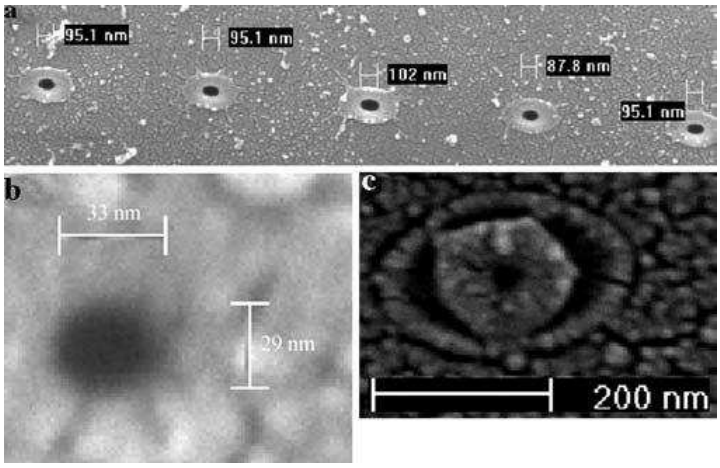

Figure 1: a SEM of a row of holes in Corning 0211 glass. b, c Examples of nanometer-scale holes. The hole in c is 15 nm in diameter. Figure from [47].

Often, femtosecond ablation has been attributed an athermal characteristic, responsible for the fine quality surface of the ablated spots. However, microwelding has been achieved using femtosecond laser pulses [96] thus questioning the latter property. Furthermore, thermal effects are present on the morphology of the irradiated surface [6], but of less importance than for longer pulses (ns).

A very common problem at moderate intensities, often encountered by groups working on laser sources development and maintenance is the optical strength of the materials and the evolution of the latter as a function of the laser pulse spatial profile (hot spots) and most importantly with extrinsic properties of the material (defects resulting from polishing process, contamination from residual gases etc.). The strong absorption of these defects may have as a result their subsequent growth in size and thus the decrease of the optical strength of the material [63, 10]. The laser beam on its turn, will be diffracted and higher intensities may be reached at

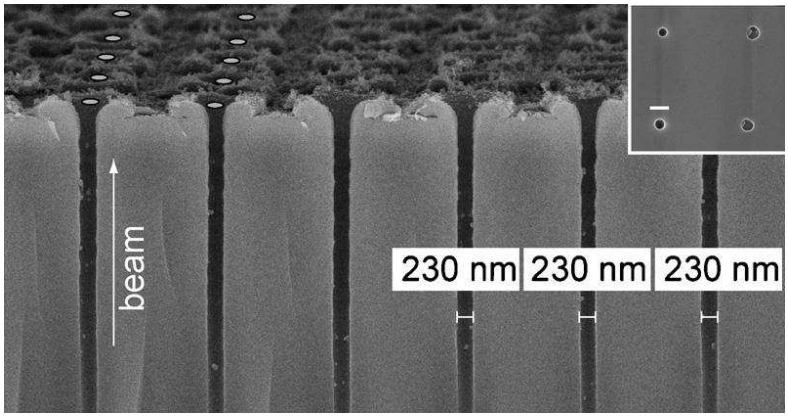

Figure 2: Profile of an array of channels drilled with identical 0.70 μJ energy per pulse and beam position such that channel length is 10 μm and diameter 230 nm. The pitch is 1.6 μm. White circles indicate channel positions. Inset shows post-processed surface for an additional sample closer to threshold with pitch 800 nm. Scale bar is 200 nm. Figure from [8].

later stages menacing the optical components that are met. The study of these interactions has great impact on fiber optics.

At lower intensities, ultrashort pulses may be used for surface structuring. Such examples involve micro-structures observed on gold film [51] and ripples [42] present in almost any material. These patterns may be exploited to enhance absorption of metals [100] or to give hydrophobic properties to silicon [4]. Periodic structured may be used as well for colouring 3 or marking of precious stones. Moreover, femtosecond laser processing may be used for inscribing 3D photonic functions in the bulk of the material. Localized refractive index changes can be exploited for fabrication of light-guiding structures [56] and modulated photo-induced structures can be used for polarization related applications as they present birefringent properties [16, 59].

Of course, the development of such sources did not come without the appearance of new problems asking for solution. At high intensity regimes (close and above ionization threshold), a rather challenging situation, involving laser-matter interaction, arises. The propagation of ultrashort laser pulses in transparent materials (silica windows) may have as a consequence the damage of the entrance surface by stimulated brillouin scattering and the damage at the rear of the window due to self-focusing and subsequent filamentation of the beam. Filamentation, from a general point of view, is detrimental to beam quality [7] and source of damages [20]. Avoiding such issues is necessary in applications with high energy lasers propagating in transparent media (i. e. megajoule project, ns pulses, $\sim$ 1.2 TW, at 355 nm).

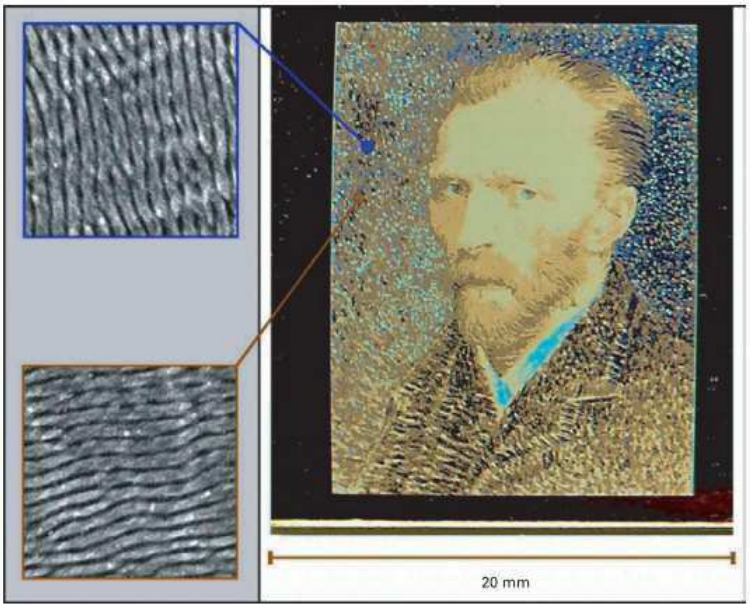

Figure 3: Colouring resulting from laser micro-inscription on stainless steel, performed at Laboratoire Hubert Curien (LaHC).

In parallel with the development of these applications came the need for extended control over the different processes that are involved. Growing demands in the applications field ask for a better understanding of the ultrashort pulses interaction with matter, from a fundamental point of view and this is where this thesis comes into play. The physical mechanisms of this interaction being only partially known, there is need for an extensive study of the elementary mechanisms that are being involved: How is the energy being deposited on the solid ? What is its evolution at later times ? These are the main questions that this thesis aims to answer.

Our investigation has focused on wide-bandgap, dielectric solids with different intrinsic properties (i.e. $\alpha - SiO_2$, Al_2O_3 etc.) and more precisely on the experimental study of the transient aspects of the interaction. We have taken on the subject from different angles thanks to the wide variety of equipment made available from "Laboratoire des Solides Irradies" (LSI) and collaborations present in the group. We have mainly worked on a time-resolved experimental setup using the frequency domain interferometry technique supplied by femtosecond laser pulses to directly study the nonlinear excitation and relaxation mechanisms, taking part at different stages, in the above mentioned crystals. The obtained results will be presented on chapter 2. An additional experimental technique, the photoemission

spectroscopy, complementary to the first one, has been employed also and these results can be found on chapter 3.

Finally, one of our objectives has been to study the laser-induced nano-patterns on the dielectric surface as a function of different parameters: pulse duration, number of shots and pulse delay in a double-pulse scheme. Our aim has been to understand the formation mechanism responsible for these structures. The SEM micrographs acquired and a discussion over the subject will be the object of chapter 4. For now, we invite the reader to take a look to the theoretical background of the studied processes in solids for the sake of familiarization with the topic (see chapter 1).

Chapter 1

Theoretical description of the short pulsed laser-dielectric interaction

In this first part of the manuscript, we will try to give a detailed picture of the laser light interaction with matter from a fundamental point of view. We will focus on wide bandgap insulators ($\sim$ 9 eV) since these were the object of our studies. The reader should bear in mind however, that most of the processes described below are valid for metals and especially semiconductors as well, dielectrics being similar to semiconductors from a solid state point of view and showing metal-like (except for the stronger electron-phonon coupling in dielectrics) properties under strong excitation. At first, we will be interested in the excitation stage of the solid (radiative ionization) where we will consider interaction of laser light in the near-visible part of the spectrum ($\sim$ 1.5-3 eV). This makes necessary the usage of short pulses ($\sim$ fs-ps for the case of our investigation) in order to achieve the high intensity regimes ($\sim 10^{12}$ W/cm^2) without which an efficient radiative excitation of the solid would be most difficult. The next step will be to describe the early relaxation stage ($\sim$ ns) of the irradiated solid at room temperature (following our experimental conditions). The remarkable property of trapping, met in some insulators will be included in our description. In this framework, we will discuss the ablation process and the different theoretical models used to model this interaction.

1.1 Introduction

The solid structure is characterized by the presence of both ions and electrons in different arrangements depending on the solid nature. At this stage, we shall distinguish the core electrons from the valence ones. The core electrons are bound to the ions and are localized, their binding energy being quite high (∼several tens to hundreds of eV) they will not interact with photons used in our experiments. On the other hand, valence electrons are associated with atoms and they are responsible for chemical bonding between atoms. These electrons being "weakly" bound to the ions, they are the only ones being able to interact with optical excitations.

Delocalization of these electrons calls for a non spatial representation of their energy and this is being achieved by placing them in the scheme of band structure, where their energy as a function of the crystal momentum is illustrated. The band structure of a solid characterizes its nature (from a thermal/electrical response point of view) and we can mainly distinguish three types of ideal[1] solids at zero temperature :

1. Metals or conductors: Electrons partially occupy a band called CB where they can circulate "freely"[2] under optical or thermal excitation or even application of a direct current (DC) potential.

2. Semiconductors: Valence electrons are filling a band called VB where electrons are under the effect of a crystalline potential. A forbidden band gap (electrons may not occupy this band) separates the VB from the CB. In the case of semiconductors it is of the order of 1 to 2 eV, making light excitations in the visible or near-IR spectrum of the electrons to the CB possible.

3. Insulators or dielectrics: The VB is completely filled while the CB is empty as in semiconductors but the band gap is much larger in this case (∼ 10 eV). In other words, no thermal band-to-band transitions are possible and linear optical transitions (involving photon absorption) are accessible by photons with large energies (of the order of the corresponding band gap), which is outside the framework of this thesis.

We have seen until now how the different energy levels are occupied at temperature T=0. Now, in the case where the temperature is raised the occupancy of these levels by electrons is governed by the laws of statistical mechanics and more in particular the Fermi function :

[1] Defect-less

[2] Quasi-freely to be exact: interaction with other electrons is not considered when referred to as "free"

$$f(E) = \frac{1}{exp[(E - E_F)/k_bT] + 1} \tag{1.1}$$

with E the given state energy, E_F the Fermi energy, k_b Boltzmann's constant and T the temperature. Figure 1.1 illustrates an electron population following a Fermi-Dirac distribution.

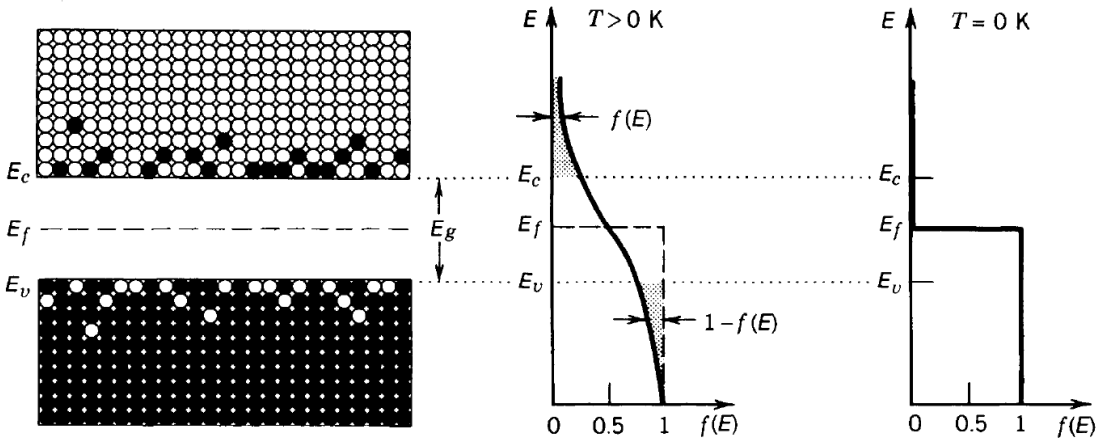

Figure 1.1: The fermi function f(E) is the probability that an energy level E is filled with an electron; 1-f(E) is the probability of occupancy by a hole in the valence band. At $T = 0$ K, f(E)=1 for $E < E_F$; i.e., there are no electrons in the conduction band and no holes in the valence band. Figure from [82].

From now on, we will be focusing on the dielectric case. Let us state that it is possible to breach the band gap by multiple photon absorption at high intensities where nonlinear effects take place. Such transitions, along with a typical crystal band structure are represented in figure 1.2. This will be the object of section 1.2.

The fact of having considered an ideal solid simplifies the representation of its band structure but it fails to account for situations encountered in reality. Perfect or defect-less crystals do not exist, instead multiple defects may be present and hence modify the crystal's band structure. These may be planar, linear or point defects. Point defects are more common and they may include vacancy defects: an ion is missing from its natural position in the lattice, interstitials: an ion is misplaced in the lattice, impurities: ion replacement etc. All these defects have as a result the formation of energy levels in the previously forbidden band gap. This is an important result because both excitation and relaxation processes may be assisted by the presence of such defect states. However, the use of sub-picosecond pulses disfavours assisted-excitation as we will see in the following section (1.2.2).

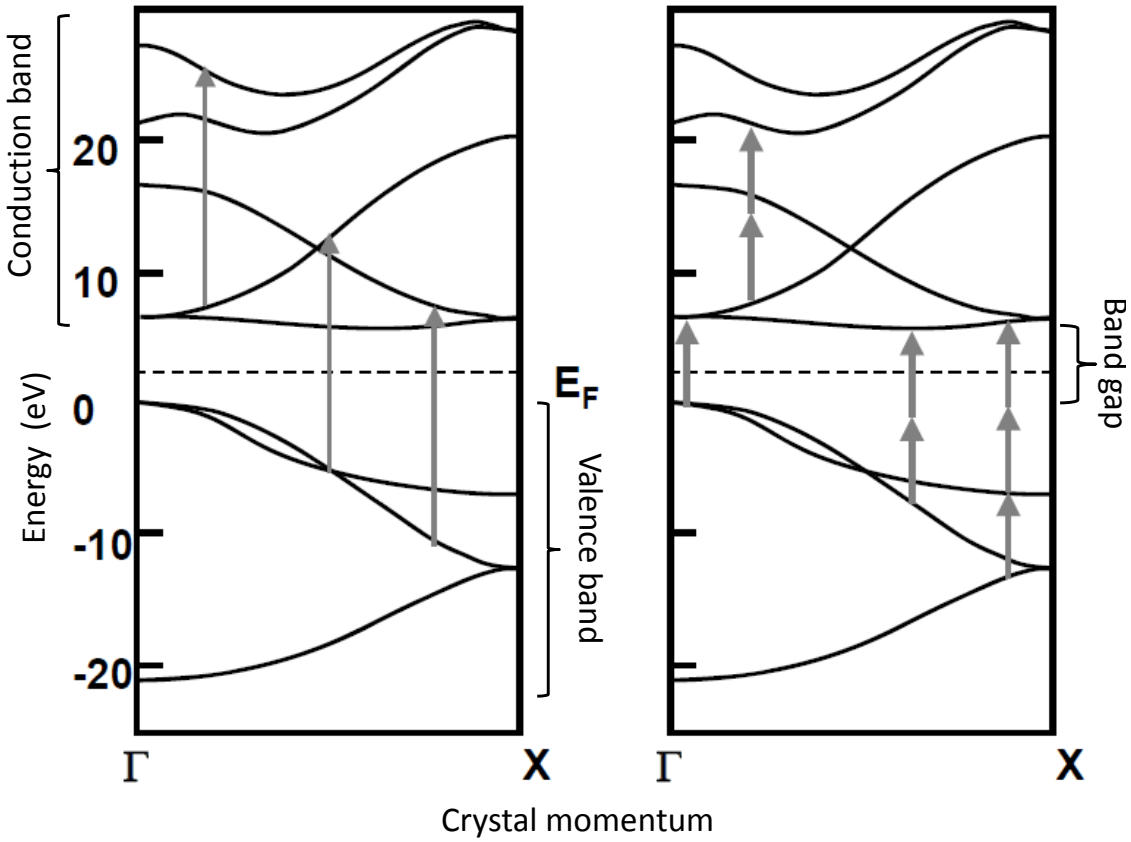

Figure 1.2: Band structure of a perfect solid crystal and possible electronic transitions by absorption of optical radiation. On the left: 1-photon transitions. On the right: multiphoton transitions. E_F is the Fermi level. Figure from [67].

Defect states may be induced by radiation itself, as in SiO_2 and thus potentially be associated with ablation process. This will be discussed more in detail in section 1.4.

1.2 Excitation processes in dielectric solids

The following section describes all those processes that result in the raise of the excitation density (number of electrons per unit volume in the CB). It has been found out that damaging in the ultrashort pulsed-laser regime involves excitation of electrons in the CB. These electrons may be found in defect states , or in the VB and thus it is necessary to supply enough energy for these transitions to take place. This, at low intensities ($\leq 10^{11}$ W/cm^2) can be done by absorption of a photon with energy $E = \hbar\omega \geq E_g$ with E_g being the band-gap energy, $\hbar$ and ω the reduced Planck constant and angular frequency respectively. Such photon energies are available with excimer lasers but such interactions are out of the scope of this thesis (photon energies $\sim$1.5-3 eV). There are however, other possibilities for the electrons to participate in such transitions. A summary of radiative ionization processes is being illustrated in figure 1.3 and these will be discussed in detail here below. Briefly, we may distinguish three types :

1. multiphoton ionization (MPI). Simultaneous absorption of n photons ensures the band-to-band electron transition. It is represented in middle part of the figure.

2. Defect-assisted ionization. The presence of defect states lower the multiphoton absorption order. It is represented on the left part of the figure.

3. tunnelling ionization (TI). The strength of the applied laser field has as a result the decrease of the surrounding coulomb potential. It is represented on the right part of the figure.

Once an initial excitation density has been created, it is possible to further excite the conduction band electrons through photon absorption and thus "heat up" the electrons to superior energetic levels. Eventually another type of ionization may take place, called collisional ionization resulting in an electronic avalanche.

In time, different mechanisms among the above-mentioned, have been held responsible for the ionization and subsequent optical damage of dielectric solids. Already in 1974, Bloembergen [9](operating in 1.06 and 0.69 μm and pulses as short as 10^{-11} s) driven by the nearly identical behaviour of the laser-induced breakdown and DC breakdown threshold in the alkali halides suggested the same physical mechanism being operative. At the time that was generally accepted to be (for DC breakdown) avalanche, or cascade, ionization. He expressed the rate of increase in the electron density N as a rate equation :

$$\frac{\partial N}{\partial t} = \eta(E)N + (\frac{\partial N}{\partial t})_{tunnel} - (\frac{\partial N}{\partial t})_{loss} \tag{1.2}$$

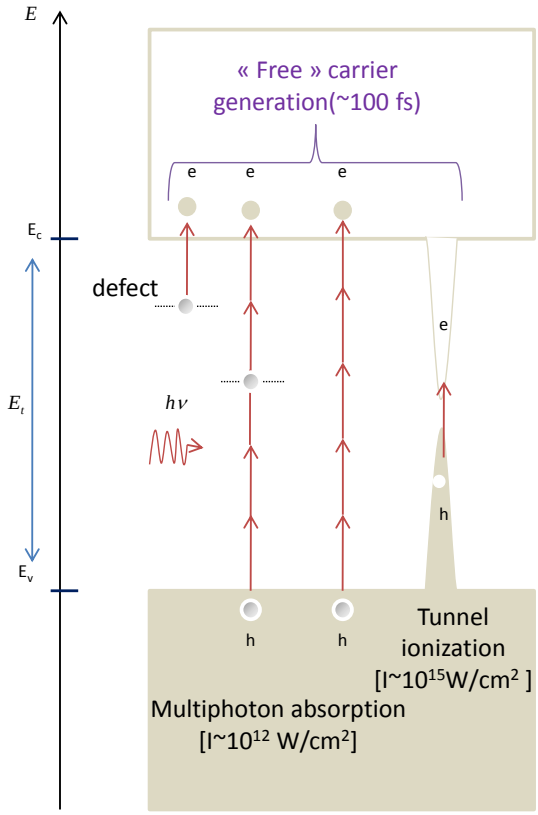

Figure 1.3: Possible excitation mechanisms involved in the interaction of a wide band-gap dielectric with an ultrashort pulse. E_c, E_v and E_g stand for conduction, valence and band gap energy respectively. Electrons (e) and holes (h) are represented. Red straight arrows stand for IR photons.See text for more details.

the first term on the right-hand side standing for cascade multiplication, the second for tunnelling (or multiphoton) ionization (TI or MPI respectively) and the last for losses due to diffusion, recombination, trapping etc.

Quickly the efficiency of an impact ionization mechanism was questioned by Schmid et al. [83]. He performed directional emission measurement of halogen atoms from alkali halides and found a signal depending on the multiphoton ionization order. Later Shen [87] defended the multiphoton absorption mechanism as well by measuring the photoacoustic signal corresponding to the heating of a pre-excited carrier density (by the 4th harmonic of Nd-YAG laser) with 100 ps pulses at 1024 nm and variable energy, he did not see any sign of impact ionization in both SiO_2 and NaCl.

For some time, the threshold measurement technique has been the dominant experimental tool to investigate associated mechanisms, this being an indirect ap-

proach however, as it involves modelling and fitting of the measurements through the excitation density criterion. Du et al. [23] performed threshold measurements in the 150 fs to 7 ns (780 nm wavelength) range, in fused silica to suggest that avalanche ionization still plays an important role for short-pulses, although initial CB electrons are provided by classical photoionization processes (MPI or TI). Stuart [95] performed his measurements in similar conditions defending the impact ionization mechanism but suggesting that multiphoton ionization should dominate for "extremely" short pulses (< 30 fs). Lezner et al. [52] extended the threshold study (at 780 nm) for pulse durations ranging from 5 fs to 5 ps and found MPI or impact ionization to be the dominant channel for free electron generation depending on the band gap (impact ionization for fused silica). Both studies used a critical excitation density (10^{21} cm^{-3}) as threshold criterion.

In the continuous quest of finding the responsible mechanism for optical breakdown Quere [72] using a more direct approach to measure excitation density (time-resolved frequency domain interferometry), found the MPI mechanism to be dominant for pulses as short as 60 fs (790nm) in SiO_2, Al_2O_3 and MgO. This was supported by polarization dependent excitation density measurements (in fused silica using time resolved imaging interferometry with 50 fs pulses, 800 nm) performed by Temnov [98], suggesting MPI to dominate as well.

More recently, absorption measurements attracted interest in the community. Rajeev [73] suggested a strong field assisted avalanche ionization playing an important role for short pulses (down to 43 fs) while traditional avalanche was held responsible for breakdown with longer pulses (up to 1.26 ps). Grojo et al. [35] proposed a model to fit their nonlinear absorption measurements and it was found out that avalanche plays a significant role in the free carrier generation by 45 fs pulses in SiO_2.

Finally, an attempt to explain damage and ablation thresholds by using a thermal criterion this time was made by a group in Marseille [18]. Their results indicate that impact ionization is one of the major absorption channels even for short pulses (< 50 fs) in fused silica.

This small review makes it straightforward to think that the excitation step still remains a rather obscure process. Let us now bring insight to these mechanisms by giving a more detailed description.

1.2.1 Muliphoton ionization

It is possible to overcome the band-gap obstacle by simultaneous absorption of N photons of energy $\hbar\omega$ with the total energy being greater than E_g. With this in mind we can deduce that the simultaneous character of the absorption leads to an N^{th} order dependency on the laser intensity, qualifying such processes as nonlinear. The multiphoton transition probability per time unit W can be written in that

case :

$$W = \sigma_N \Phi^N \tag{1.3}$$

Φ being the photon flux density defined by $\Phi = \frac{I}{\hbar\omega}$ with I the laser intensity in W/cm^2 and σ the generalized cross section for N-photon transitions (in cm$^{2\mathrm{N}}$s$^{1-\mathrm{N}}$). Its order may be estimated by [67] :

$$\sigma_N \approx 10^{-19}(10^{31\pm2})^{1-\mathrm{N}} \tag{1.4}$$

A more precise estimation of generalized cross sections may be realized by using nonlinear photoconductivity, photoacoustic absorption (a summary of the values obtained with these technique in alkali halides may be seen in [48]), phase shift measurements [55] etc.. All these techniques involve measurements of the excitation density as a function of the laser intensity. An indirect method consists in measuring the ablation threshold at different intensities and then model the evolution of this threshold with σ[3] being a free parameter. Such results have given large deviations for a 6-photon process in SiO_2: calculation by Keldysh [50] predicted a value of $\sigma_6 = 2.68\ 10^{-42}$ cm^{9}s^{5}J^{-6} whereas experimentally the values where: $\sigma_6 = 9.9\ 10^{-50}$ cm^{9}s^{5}J^{-6} [58], $\sigma_6 = 6\ 10^{-52}$ cm^{9}s^{5}J^{-6} [52], $\sigma_6 = 3\ 10^{-56}$ cm^{9}s^{5}J^{-6} [54]. We can observe a general tendency to underestimate this cross section experimentally. Such deviations may be explained by the indirect nature of the measurements. More theoretical attempts of an ab-initio calculation have been made [24, 104], but it is not the object of this manuscript to give a detailed list of the different estimations.

Keeping in mind that multiphoton absorption does not require the presence of conduction band electrons, let us express the multiphoton absorption probability per irradiated surface unit P_v :

$$P_v = N_\mathrm{v}\sigma_N(\frac{F}{E_p\tau})^N\tau \tag{1.5}$$

with N_v the valence band electron density (in cm^{-3}), F the laser fluence (in J/cm^2), E_p the photon energy ($= \hbar\omega$) and τ the pulse duration. From a quantitative point of view, we can see that this probability is inversely proportional (for $N = 2$) to the pulse duration and hence that ultrashort pulses favour such intrinsic absorption processes.

Until now, we have considered fixed energy levels. However, in the presence of an external electric field it is necessary to consider the alternating current (AC) Stark shift of the bands which has the result of increasing the band gap of a value

[3] In fact a reduced cross section has been measured: $\tilde{\sigma} = \sigma_N/(\hbar\omega)^N$

called the ponderomotive energy, U_p. This quantity corresponds to the cycle-averaged kinetic energy of an electron, considered to be free, oscillating in the presence of the field and it can be expressed as :

$$U_p = \frac{e^2 E^2}{4 m_0 \omega^2} \tag{1.6}$$

with e and m_0 the electron charge and mass respectively and E the electric field. A more convenient evaluation of this shift (at ionizing intensities $\sim 10^{13}$ W/cm^2) may be given as: $U_p = 0.93\ eV(\lambda/(1\ \mu\text{m}))^2$. This shows that the ponderomotive shift can exceed a photon's energy at this intensity level. The now corrected ionization potential, taking into account the ponderomotive shift is given by [50]:

$$\tilde{E}_g = E_g + U_p \tag{1.7}$$

In which case the multiphoton order is modified following $N = [\tilde{E}_g/\hbar\omega + 1]$.

The limit of the multiphoton regime may be estimated by using the Keldysh parameter. Keldysh [50] in his formulation describing the Strong-Field ionization (SFI) introduced the adiabatic parameter γ, defined as the ratio between the bandgap and the electron oscillation energy (ponderomotive energy). It can be expressed as $\gamma = \omega\sqrt{m_0 E_g}/eE = \omega/\omega_t$. Alternatively this parameter can be seen as a ratio between the optical cycle duration ($2\pi/\omega$) and the tunnelling time ($2\pi/\omega_t$). In the limit of $\gamma \gg 1$, i.e. tunnelling is not possible within an optical cycle and multiphoton regime dominates. For $\gamma \ll 1$ however, the electron is given enough time to tunnel through the potential barrier and this will be the object of section 1.2.3.

1.2.2 Defect-assisted ionization

In a non-ideal insulator, point defects that are present create energy levels in the bandgap. Subsequently, new transitions, of lower energy, are available to the electrons. Populated defects may be ionized by photon absorption and thus promote electrons to the conduction band this way. Another way defect absorption participates in the radiative ionization process is by assisting multiphoton absorption. Defect states close to the bottom of the CB that are populated through multiphoton ionization, may eventually be ionized by the same means and thus promote the electrons in the CB. These processes are illustrated in figure 1.3. Such transitions will lower the number of photons N participating in the process and even linear absorption may become possible. Similarly to multiphoton absorption, the probability for defect absorption rate per irradiated surface unit P_D may be expressed as [67]:

$$P_D = N_D \sigma_1 \frac{F}{E_p} \tag{1.8}$$

with N_D being the defect state population. An important result of this representation is that defect absorption (in the linear case) is independent on pulse duration. Thus at lower intensities defect absorption will dominate upon intrinsic one. This may be the case of photoemission experiments (see 3), where intensities are considerably lower than the damage threshold. In conclusion, by evaluating the ratio between multiphoton and defect absorption probabilities at a given fluence (corresponding to a threshold criterion), one sees that ultrashort pulses allow operating at higher laser intensities without nonetheless reaching the damage threshold.

1.2.3 Tunnelling ionization

Coming back to the Keldysh parameter introduced in 1.2.1 we saw that for $\gamma \ll 1$ the multiphoton absorption loses its efficiency upon tunnelling ionization. To illustrate the tunnelling process, let us consider that the electron is confined in a potential barrier, corresponding to the coulomb potential seen by the electron. For low to moderate optical fields, this potential remains unchanged. However, if the applied field's strength is comparable to the atomic unit of intensity (3.5 10^{16} W/cm^2), the coulomb potential will be perturbed and lowered in the presence of the strong laser field and hence allow tunnelling of the electron through the lowered barrier (see figure 1.4). Schematically, we may represent this by a distortion of the band gap, allowing 1-photon band-to-band transitions. Such intensities are beyond the ones used in the experiments described in this manuscript however, and thus we will consider that this mechanism is not efficient for what will follow. For more details on this mechanism the reader is invited to consult [50].

1.2.4 Forest fire

Recently[30], a complementary mechanism to the ones present in the Keldysh description (multiphoton, tunnelling) called "forest fire" has been suggested to enhance the optical Field ionization (OFI). During the pulse, rapid ionization results in the creation of electron-hole pairs. Once these holes are created, the local electric field is the sum of the laser field and the field created by these holes. Under high (solid state) plasma density conditions the hole electric field is rapidly screened (within 1 Å). However, at the periphery of the ionized region and during its spatial development, the screening is not contributing and as a result local deviations from the self-consistent field can occur. This results in an enhanced ionization along the boundary of the ionized region and the propagation of the

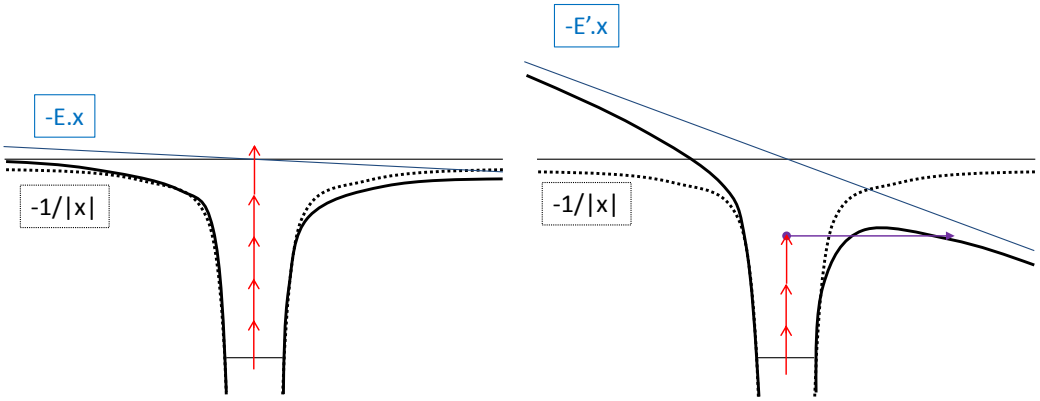

Figure 1.4: The electrostatic potential seen by the electron, in the presence of an external electric field is represented in black solid lines (in form of wells). Dotted lines represent the atomic potential while blue solid lines the external potential related to the applied field. In the case of low-to-moderate electric field strength multiphoton absorption dominates (left part of the figure, red arrows correspond to absorption of laser light photons). When the laser intensity is of the order of the atomic unit, then the overall potential is modified and tunnelling (violet arrow) is possible, assisted by photon absorption. Horizontal lines represent the vacuum level.

ionization front as in a forest fire. Authors of [69] have implemented the forest fire model in a multiple rate equation description and they have found that for short pulses (50 fs) and peak laser intensities below about 10^{13} W/cm^2 the forest fire mechanism dominates the laser-dielectric interaction and may result in an electron density increase of several orders of magnitude.

1.2.5 Electron "heating" and collisional ionization

By the time radiative ionization has promoted electrons in the bottom of the CB, further excitation may take place by absorbing remaining photons present in the laser pulse, or in a separate laser pulse arriving at a delay where "free" electrons are still present in the CB. Such transitions obey energy and momentum conservation. This actually means that if 1-photon direct interbranch transitions are not possible at a given lattice wave vector, then interaction with a third body is needed to provide the necessary momentum shift. In that case and since photons hold small momentum, conservation is respected in a three-body interaction scheme. These indirect transitions are represented in figure 1.5. Such third particles, following laser intensity regimes, have been more often suggested to be phonons (low intensities) and more recently ions [77, 13, 86](moderate intensities). At higher inten-

sities Belsky et al. have proposed a direct, multiphoton, interbranch transitions as a dominant mechanism [5] modelling their photoemission spectra in CsI and other dielectric materials. The result of a sequence of "inverse Bremsstrahlung" (non-resonant photon absorption by electrons) and other direct electron "heating" events is the raise in the kinetic energy of the electrons.

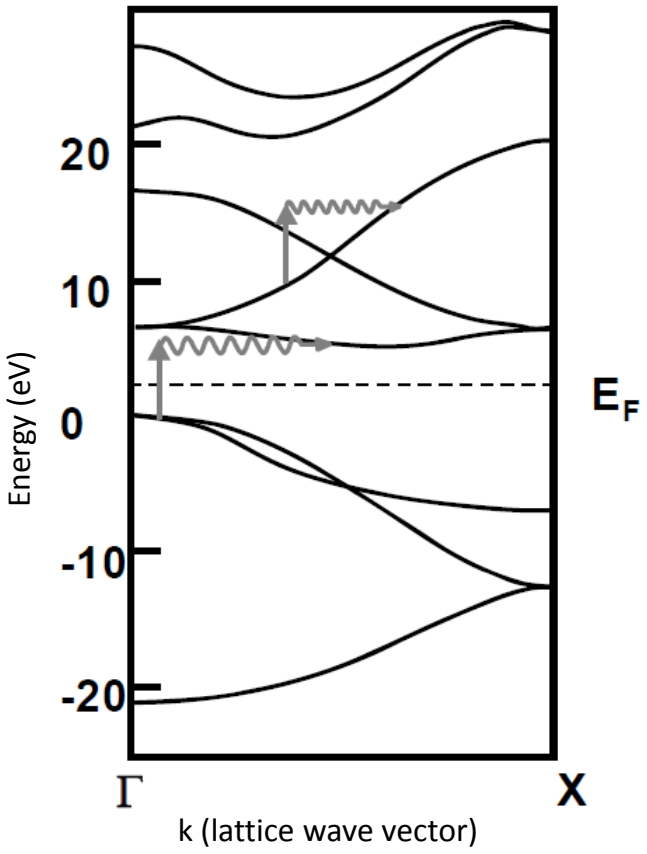

Figure 1.5: Indirect transitions in a phonon-assisted photon absorption scheme in a crystalline solid. Two types are represented (intraband and interband). figure from [67].

Now if the electron energy reaches sufficiently large levels it is commonly proposed that another ionization mechanism may be activated: the impact ionization. This consists of a CB electron with energy above a threshold energy being able to collide with electron from the VB and thus promote the latter in the bottom of the CB. This may be an iterative process and hence raise the total excitation density exponentially ($N_f(t) = N_i * 2^{t/\tau_i}$, with τ_i, time between a collisional event, t time, N_f and N_i, final and initial excitation density respectively). The latter

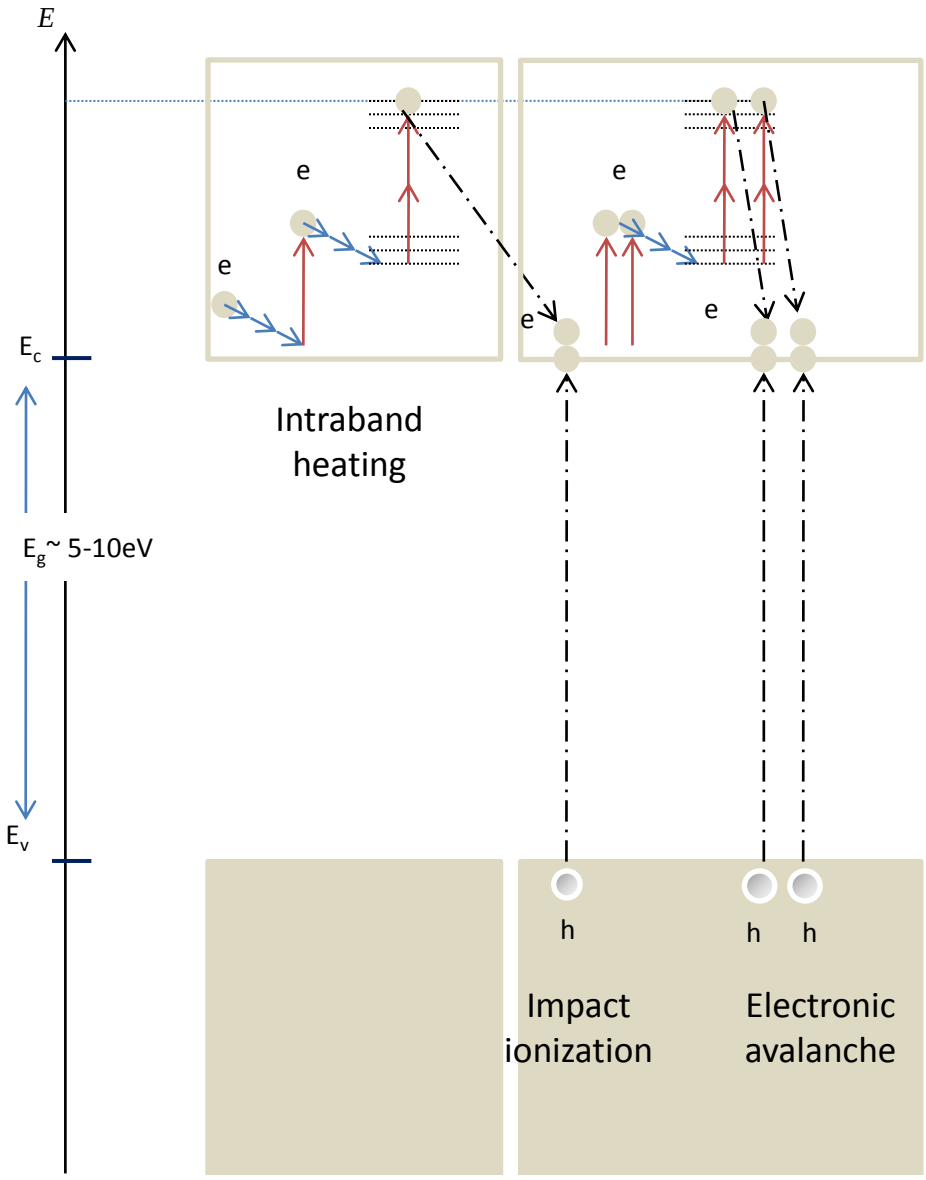

Figure 1.6: Illustration of electron "heating" by inverse bremsstrahlung, eventually followed by impact ionization and resulting in electronic avalanche, in a crystalline solid.

is often qualified as avalanche ionization and it is a very efficient way of electron multiplication and energy relaxation. An illustration of this mechanism (heating plus impact ionization and avalanche) is given in figure 1.6. Coming back to the threshold energy for impact ionization, according to Ridley [80] and for bands with parabolic dispersion:

$$E_{imp} = (\frac{1+2\mu}{1+\mu})\tilde{E}_g \tag{1.9}$$

with $\mu = \frac{m_c}{m_v}$ being the ratio of conduction and relevant valence band effective masses.

Typically this value is greater or equal to 13.5 eV for SiO_2. In order to reach this kinetic energy, an electron irradiated by 800nm(1.55 eV) photons has to undergo 9 inverse Bremsstrahlung absorption events before impact ionization can occur. This for a 60 fs pulse represents a 0.15 fs^{-1} collision rate with phonons or ions. Such transition rates are not accessible at intensity regimes of the order of 10^{12} W/cm^2: a calculation with an indirect transition rate cross section[4] σ at 10^{-19} cm^2 [2] gives rates of only 0.4×10^{-3} fs^{-1}. This result suggests that the intensity has to be raised at surprisingly high values to be able to heat the electrons at such values. Impossibility of reproducing photoemission spectra obtained experimentally in CsI motivated Belsky et al. [5] to replace the indirect transitions by direct ones considering that the conduction band is not a simple parabola but moreover it is a certain amount of branches one above the other allowing direct absorption of photons. In CsI the direct transition cross section was found to be $10^{-16} - 10^{-17}$ cm^2 (the probability for 1, 2 or 3-photon transitions being the same at 10^{13} W/cm^2) thus giving rates at 0.2 $fs^{-1} > 0.15$ fs^{-1}. In fact these rates are also dependent on the electron kinetic energy and the wavelength. Presumably a high excitation density may also affect the electron-phonon scattering and thus the indirect transition rate by electrical screening.

All these calculations suggest that at the time scale of the laser pulse duration, no energy relaxation mechanism is activated although the energy absorption mechanisms will most probably dominate the energy relaxation. However, in wide bandgap insulators where the coupling of electrons with phonons is high it is possible that this scattering time becomes of same order of magnitude as the photon absorption time and thus compete with each other preventing impact ionization. Moreover, contrarily to the energy relaxation without energy deposition on the lattice with impact ionization, phonon scattering is actually part of the thermalization of the lattice and thus a very efficient mechanism of depositing energy to the medium. Such energy relaxation mechanisms will be discussed in the following section.

[4]Calculated from optical interaction rate with acoustic phonons for 0-30 eV electrons

1.3 Energy relaxation mechanisms

In the previous section, we saw how the initial ionization stage takes place and furthermore, the activation of a carrier "heating" mode during the presence of the laser pulse. The counterpart of this "heating" is the carrier "cooling" due to scattering. This involves several components: (1) electron-phonon scattering, (2) electron-ion scattering (after some excitation has already taken place) and (3) electron-electron scattering (at high excitation densities).

Electron interaction with phonons has been well studied in SiO_2 [3] where the different contributions from acoustic and 153-meV and 63-meV LO phonon have been considered (see figure 1.7). The electron-acoustic phonon scattering rate is increasing from 0.1 fs^{-1} at 0 eV to 10 fs^{-1} at 6 eV and then slowly decreases for increasing electron energies. LO-phonon scattering rates remain more or less constant, following the same slowly decreasing rate as acoustic phonons, around 0.1 fs^{-1}. However, since energy (very low for acoustic phonons) and momenta (lower for optical phonons) are not the same the contributions to the energy or to momentum relation rate may not be estimated from the scattering rates alone. A more detailed analysis has shown that acoustic phonons are mainly responsible for the momentum relaxation while optical phonons dominate the energy relaxation at electron energies from 0-5 eV. Experimental results from photoemission spectra for the hot-electron transport in SiO_2 layer are in agreement with these values [2]. Typically an electron going through collisions with the 153 meV-LO phonon loses 0.0153 eV/fs in the best case which is considerably lower than the energy gain rate during a 800 nm laser pulse at 11 TW/cm^2 (0.3 eV/fs).

Thermal equilibrium in the "free" electron gas is mainly achieved by electron-electron scattering. Inelastic electron-electron scattering rate have been included in a Monte Carlo simulation to reproduce photoemission experimental results in [57] and it has been estimated to be 0.3 fs^{-1} for 8 eV electrons in SiO_2. Christensen et al. [19], used a generalized scattering rate expression (electron-phonon and electron-electron) in the Drude model for the refractive index (under assumptions of Drude absorption, Debye screening etc.). The expression for the electron-electron scattering was given by:

$$\Gamma_{e-e} = \frac{4\pi\epsilon_0}{e^2}\sqrt{\frac{6}{m_0}}(k_B T_e)^{3/2} \tag{1.10}$$

with T_e the electron temperature and the other parameters corresponding to the commonly used notations. Surprisingly, this rate doesn't depend on the electron density and other approaches should be able to take this into account.

One shouldn't forget radiative recombination which is taking place much later($\sim$ 1 ns) and when other relaxation processes are deactivated. Notably, this is possible at low temperatures while at ambient temperature non radiative recombination

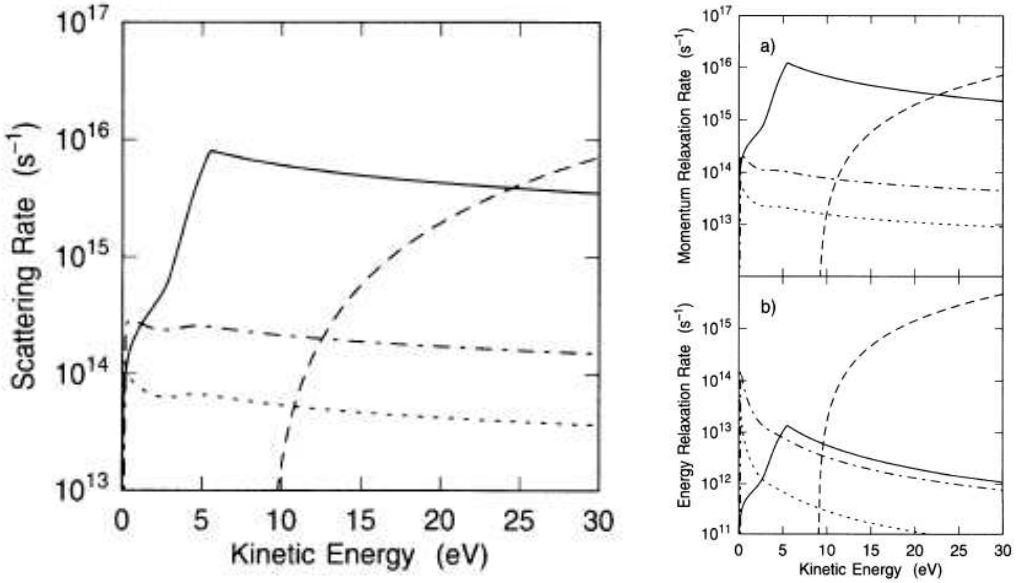

Figure 1.7: On the left part, semi-empirical scattering rates in SiO_2 at 300 K as a function of the electron kinetic energy. On the right, momentum relaxation rates (panel a) and energy relaxation rates (panel b) in SiO_2 versus electron kinetic energy. The solid curve is the acoustic-phonon scattering rate, the dot-dashed curve is the 153-meV LO-phonon scattering rate and the dotted curve is the 63-meV LO-phonon scattering rate. Figure from [3].

takes place.

1.4 Conduction band depopulation

There are mainly two ways for the electrons in the conduction band to recover. As it has been above mentioned this may be done by radiative or non-radiative recombination which is a long time scale process depending on the respective density of "free" electrons and holes[5], thus N^2. This recombination process is characteristic in materials such as Al_2O_3, MgO etc. that are going to be later studied in this manuscript under the long electron-lifetime qualification.

Alternatively, trapping (intrinsic or extrinsic) may be a process responsible for carrier relaxation. Extrinsic trapping takes place when the material possesses imperfections that are being represented by several stable ionization states. Apart from impurities, oxygen vacancies in Al_2O_3, known as F-center and subsequently F^+ center when ionized, can trap an electron and become an F-center. An equivalent of hole trapping may be found in silica with the non bridging oxygen hole center (NBOHC).

Intrinsic trapping, related to the irradiation defect formation is a characteristic of mainly alkali halides and quartz. The STE is among the best studied radiation induced defects. Luminescence experiments in quartz have shown a strong emission peak around 2.8 eV at low temperature accompanied by a lattice volume variation and a transient absorption at 5.2 eV [97]. The STE presence in quartz involves an electron trapping on a silicon atom while a hole is trapped by an oxygen atom. This has as a result the displacement of the oxygen atom at an interstitial position, this displacement being of about 0.4 $\mathring{A}$ [26]. This lattice distortion is responsible for the volume raise and hence it illustrates the strong correlation between acoustic phonon-electron coupling and STE's. The radiative emission has been attributed to the transition versus the fundamental state of the STE (trap lifetime) and it is accompanied by a release of 1.4 eV to the lattice, corresponding to the return the oxygen atom to its equilibrium position. The absorption peak at 5.2 eV corresponds to an excited state of the STE.

Interferometry and absorption measurements in quartz have revealed that the presence of an STE is related to the rapid ($\sim$ 150 fs) trapping of the "free" carriers [37]. The actual rise time of an STE corresponds to this trapping time and it has thus been held responsible for the trapping process.

It is the same with NaCl where the trapping of a hole on a Cl^- atom leads to the formation of a V_k center, i.e. a molecular ion of type Cl_2^-. The subsequent trapping of an electron on the V_k center results in the formation of an STE. However, trapping kinetic in this case is intensity dependent. In other words, the higher the excitation density, the faster the trapping process.

[5] "free" electron density is equal to the hole density following ionization in electron-hole pairs

1.5 Theoretical models

This manuscript being mainly based on experimental investigation of the different processes discussed we will try to avoid detailed discussion of the different theoretical descriptions of the subject. However, the writer considers that it is worth giving a short description of the different models used and some important theoretical papers as references for a more in depth comprehension.

Different theoretical descriptions have been used in time to describe the laser-matter interaction. One way is to consider the lattice and the electrons as two separate thermodynamical systems at equilibrium. In this case, lattice and electrons are characterized by two different temperatures and the electron-lattice coupling is being taken into account as a phenomenological parameter describing the energy exchange between those two systems. The so-called two temperature models have been widely used in metals and in free electron gases in general [46]. However, the use of a kinetic model instead in dielectrics by Kaiser et al. [49] has shown that results obtained with the two temperature model are valid close to damage threshold and beyond it but they fail to account for the electronic distribution below it and hence a finer approach is necessary..

A more detailed description of the electronic excitation is necessary whereas to fluencies below the threshold. This can be achieved with the use of kinetic models such as Boltzman equation [49] where the different contributions to the ionization and the energy relaxation can be considered to obtain a detailed description of the electron distribution. A more simplified description has been achieved with the use of rate equations along with discretization of the different energy levels in the CB [75].

1.6 Damaging criteria

The final state of the matter after interaction with a short laser pulse depends on the fluence used. We are able today to distinguish mainly three regions [62]. At low fluencies the solid doesn't change its properties after passage of the pulse. Then, while raising the laser fluence we come across a permanent structural modification of the matter often accompanied by a refractive index change. At higher fluencies damaging takes place along with a morphology change on the surface. Finally, a fluence threshold exists for the ablation of the material which is synonym of matter ejection. Depending on the diagnostic used one may see all these regions (from permanent modification to material removal) or just some of them. Thus, it is normal to consider that different mechanisms contribute to the different final states.

While trying to model this interaction one has to carefully choose a criterion for a corresponding threshold. In earlier literature an intensity threshold was used above which optical breakdown would occur. However, this has revealed to be rather subjective and later it was often a critical density criterion that was used as a damage threshold, most probably this being related to bond breaking due to the absence of sufficient valence electrons (damage related) and/or electronic ablation. The latter has been discussed(multipulse experiment) in [92] in the form of coulomb explosion(at low number of pulses) as being the responsible damaging mechanism in Al_2O_3 for 100 fs pulses. The coulomb explosion suggests that after removing the electrons responsible for the bonding in the lattice, matter will explode by mutual repulsive interaction of the ions. The electronic damage is supported by the fact of severely probing phenomena related to the electronic temperature with an ultrashort (femtosecond) pulse, the pulse durations being below the typical times for energy transfer from the electrons to the lattice (50 ps in SiO_2 [31]). However, Coulomb explosion could only account for 10% of the ablated volume which makes it an excellent candidate for surface desorption [14] but maybe not for ablation.

Thermal ablation shouldn't be excluded, as often molten matter has been observed on the periphery of the craters or in the center for greater number of pulses [92]. The critical density criterion has thus been severely criticized and more recently other more energy related criteria have been proposed involving deposited energy per volume unit resulting in a lattice temperature above the melting point [86, 18].

The question today still remains open: is damaging in the ultrashort pulse scale thermal or of Coulombian nature?

Chapter 2

Experimental investigation of electron excitation and recombination processes

Intrinsic solid properties, upon ultrashort laser pulse irradiation, have been studied experimentally by means of time-resolved spectral interferometry. This involves the direct electron density measurement of the irradiated material under different excitation conditions, leading to the quantification of the laser-solid interaction process. The measurements, carried out at the optical breakdown threshold utilizing different pulse durations, raise questions regarding the usage of critical excitation density as a universal damage criterion. A new criterion related to the exchanged energy is proposed. Additionally, the use of an experimental setup implementing a double pump pulse allows the identification of different excitation mechanisms taking place at time scales of the order of the pulse duration used. Electron multiplication is observed in some materials ($\alpha - SiO_2$, NaCl) while this is not the case for others (Al_2O_3, MgO). These differences are discussed in detail.

2.1 Introduction

The state of art at the start of this thesis has motivated a new series of experiments in an attempt to clear up the fuzzy field of the interaction between ultrashort laser pulses and dielectric media. Previously, the majority of experiments have been concentrated on damage threshold measurements [94, 52, 18]. However, this process is complex, involving a complicated temporal evolution of the sample and the laser pulse, both being linked by the change of optical constants of the solid during the pulse. The latter is induced by the promotion of a large density of carriers, electrons in the CB and holes in the VB. If one concentrates only on this initial process of electronic excitation, the controversy still exists, and the importance of different possible excitation mechanisms is still under debate: multiphoton and/or avalanche ionization [18, 35, 2, 98, 25, 73, 103] . For transparent dielectrics, the photon energy of fs lasers is usually much below the band gap, and the dominant initial excitation process must be nonlinear: multiphoton or tunnelling ionization.

Furthermore, the later stages of excitation, eventually leading to damage, along with the energy transfer mechanisms remain relatively unknown. Hence, it is necessary to draw up the energy balance of the interaction. In order to achieve this one has to combine excitation density and energy distribution measurements. The first is the object of this chapter. The second will be the object of the next chapter containing the photoemission spectra.

In a previous set of experiments, we have studied the evolution of the carrier density, as a function of laser intensity, below and above breakdown threshold, for different pulse durations and in different materials. This is achieved by measuring the negative phase shift observed in Fig. 3 at a fixed time delay, as a function of the pump laser intensity. For short pulses (60 fs), the phase-shift evolution measured in Al_2O_3 is shown in Fig.2.1, and our conclusions were the following [72] :

- First, at low intensity, i.e. a few TW/cm^2, the density of carriers increases nonlinearly, following a multiphoton excitation rule: the phase shift measured by the interferometry technique is proportional to I^n, where I is the laser intensity and n the minimal number of photons needed to promote an electron from the VB to the CB. This is the signature of a multiphoton excitation.

- Then, when we approach the breakdown threshold, this highly nonlinear evolution saturates. We have shown that this saturation can be explained if one takes into account the evolution of the optical properties of the solid. Since the critical density is reached during the pulse, the surface of the sample becomes highly reflective, and a thin layer of dense plasma behind the surface strongly absorbs the remaining part of the pulse. These two effects combine to prevent further penetration of the pump beam, and thus the saturation

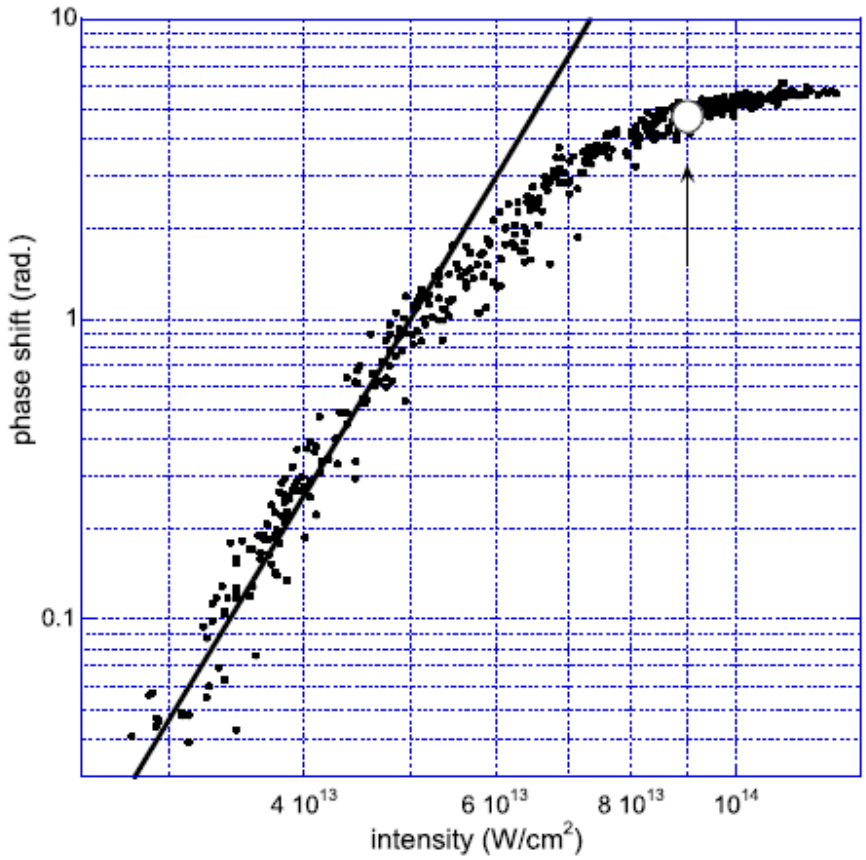

Figure 2.1: Phase shift as a function of laser intensity measured in Al_2O_3. The pump wavelength is 800 nm and the duration is 60 fs. The line is indicating an I^6 dependence law. The arrow and empty circle indicate the breakdown threshold. Figure from [72].

of the signal. It should be noted that this result has been confirmed later by another group which has performed similar measurements on $\alpha - SiO_2$ and Al_2O_3, and has arrived at the same conclusions [98].

At that point we could think that the process of electronic excitation is entirely understood. However, when we reach the breakdown intensity, the excitation process may change and this can be obscured for two reasons. First, this change of excitation mechanism could occur only in a very thin layer at the surface, which contributes to only a part of the signal and cannot be detected. Second, such an effect may also be hidden anyway by the saturation process, which is unavoidable since the critical density is attained at the surface. This being the starting point of these experiments we tried to complete our data and get a more detailed knowledge

of the excitation and energy deposition process and our results will be presented in what follows.

2.2 Interferometry

2.2.1 Goal

This chapter is dedicated to the development of an experimental technique to measure the excitation density in a solid. As it will be described in the model developed, one can access the excitation density in a dielectric sample by measuring the change in the refractive index induced by an intense laser pulse (pump pulse). The interferometric techniques have been, for a long time now, a common tool for determining phase shifts. At this point, it is important to underline the importance of a time resolution in such experiments, so that the different excitation and relaxation processes taking place in time can be recorded. This requirement is met by using a pump and probe scheme. The pump pulse is modifying the optical response of the solid sample and the probe pulse carries the information related to the modification induced. For the shake of simplicity, we are going to assume that this modification is negligible at the time scale of the probe pulse (fs pulse).

We are going to see, in what follows, that the spectral interferometry technique, coupled to the pump and probe experiment, is a convenient tool for direct, time-resolved measurement of the excitation density in a solid, dielectric sample.

2.2.2 Spatial interferometry

Optical interferometry, from a general point of view, refers to the superposition of two (or more) electromagnetic waves. The result of this interaction allows investigation and extraction of many meaningful properties of the waves. Such examples involve, among others, measurement of the wavelength λ, light source bandwidth $\Delta\lambda$, precision spatial measurements and refractive index n. The latter is the application we are being interested in our experiment.

To start with, we need two light sources that are mutually coherent. This can be achieved either by *wavefront splitting* or *amplitude splitting*. The choice of the interferometer ensures that one or the other is achieved. Three different types of interferometry techniques can be distinguished : the *spatial*, *temporal* and *spectral*. Let us have a closer look to the case of spatial interferometry and find out if we can adjust it to serve our needs.

The most common example of a spatial interferometry technique is the Young's double slit configuration. In figure 2.2, the experimental setup is illustrated. Interferences are being observed on a screen placed at distance D from the light source's axis. The fringes spacing is $\frac{\lambda D}{a}$ (λ representing the wavelength,a is the distance between the two slits and D the distance between the slit plane and the observation plane). If a phase object, of refractive index n is placed on the path of one ray, then the whole interference pattern is being shifted by $\frac{(n-1)eD}{a}$ in

a way to compensate the delay added. Here e represents the width of the object. It is straightforward to imagine placing the object of an unknown refractive index n and thus determine the latter by measuring the shift of the fringes.

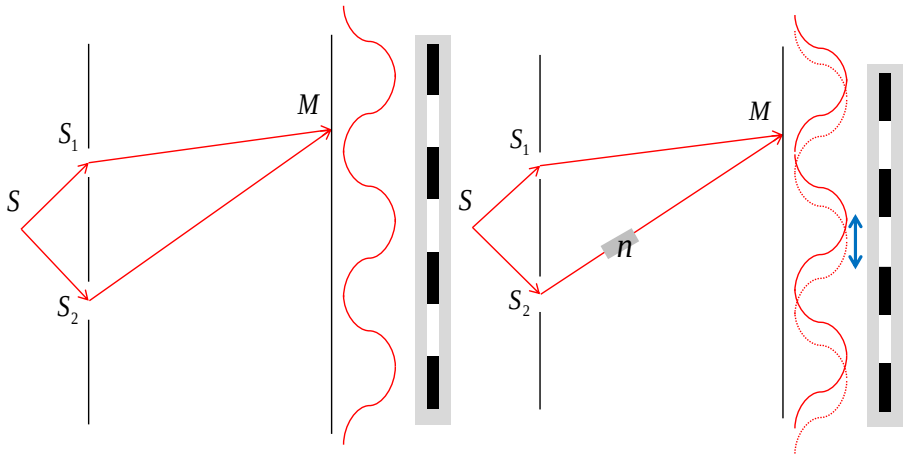

Figure 2.2: Young's double slit experiment, on the right part an object of homogeneous refractive index n has been added in the path of one ray, a is the separation between the slits, D the distance between the slits plane and the observation plane, S is the light source, S_1, S_2 are the two slits, M is a point on the observation plane and x is the shift of the fringe pattern due to the phase object

Unfortunately, a certain number of difficulties arises when trying to measure phase shifts of the order of $\frac{1}{1000}$ of a fringe in this configuration. The two major contributions to the sensitivity of this measurement are : the number of fringes and the precise control of the two optical paths. The number of fringes is delimited by the path difference. The latter should be large enough to produce more fringes but in the mean time it should be maintained smaller than the coherence length. On the other hand, optical distortions and vibrations deteriorate the resolution by producing oscillations of the optical paths. A suggestion, to reduce the impact of these contributions, has been made. What if both beams where to travel the same optical path ?

2.2.3 Temporal interferometry

The condition of both beams going through exactly the same path restrains our choices down to temporal or spectral interferometry. In the case of interferometry in time domain the light source is amplitude split (e.g. Michelson interferometer) in a reference and probe pulse. Subsequently, scans are being performed on one branch of the interferometer, thus providing an interference signal as a function of

the time delay between the reference and the probe pulses. This process is repeated for each pump and probe delay, in order to obtain the temporal evolution of the phase shift.

The corresponding experimental setup is illustrated in figure 2.3. There are two cases to distinguish. In the first case, reference and probe pulse travel through exactly the same medium. In the other case, an intense pump pulse induces a perturbation in the material. The reference pulse interacts with the unperturbed medium while the probe pulse arrives after the pump pulse, thus carrying the information related to the perturbation.

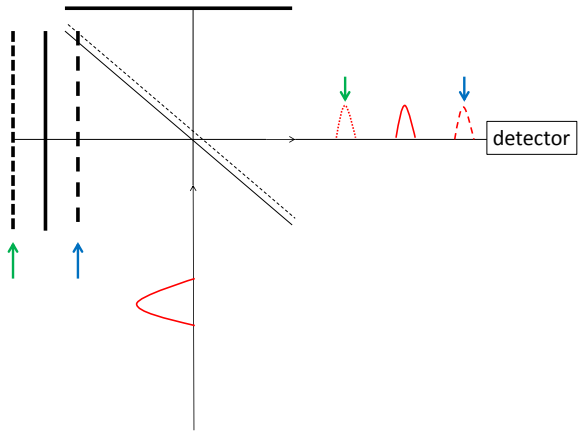

Figure 2.3: A possible experimental setup for temporal interferometry is presented. Moving one mirror of the Michelson interferometer changes the optical path (delay) between the pulses.

Let us express the electric field for the reference pulse :

$$E_1(t) = E_0(t)e^{i\omega_0 t} \tag{2.1}$$

E_0 being the amplitude, ω_0 the angular frequency and t time. Now the probe pulse (without the presence of a pump pulse) will be :

$$E_2(t) = E_0(t - dt)e^{i\omega_0(t-dt)} \tag{2.2}$$

dt representing the delay between the reference and probe pulses.

The signal measured by the detector is the square of the modulus sum of the two electric fields :

$$S(t) = I(t) = |E_1 + E_2|^2 \tag{2.3}$$

which gives

$$S(t) = I_0[1 + cos(\omega dt)] \tag{2.4}$$

with

$$I_0(t) = I'_0 e^{\frac{-t^2}{\tau^2}} \tag{2.5}$$

for a gaussian shaped pulse, τ being the pulse duration. The final expression of the intensity received by the detector is :

$$S(t) = I'_0 e^{\frac{-t^2}{\tau^2}} [1 + cos(\omega dt)] \tag{2.6}$$

If now a pump pulse interacts with the medium before the probe pulse and after the reference pulse, we will have to take into account the change in the transmission of the sample and the phase shift experienced by the probe pulse. Its (the probe's) expression is modified as follows :

$$E'_2(t) = \sqrt{T} E_0(t - dt) e^{i(\omega_0(t-dt)+\Delta\Phi)} \tag{2.7}$$

T represents the transmittance of the medium and $\Delta\Phi$ the phase shift. The new expression for the signal detected is :

$$S'(t) = I'_0 e^{\frac{-t^2}{\tau^2}} [1 + T + \sqrt{T} cos(\Delta\Phi - \omega dt)] \tag{2.8}$$

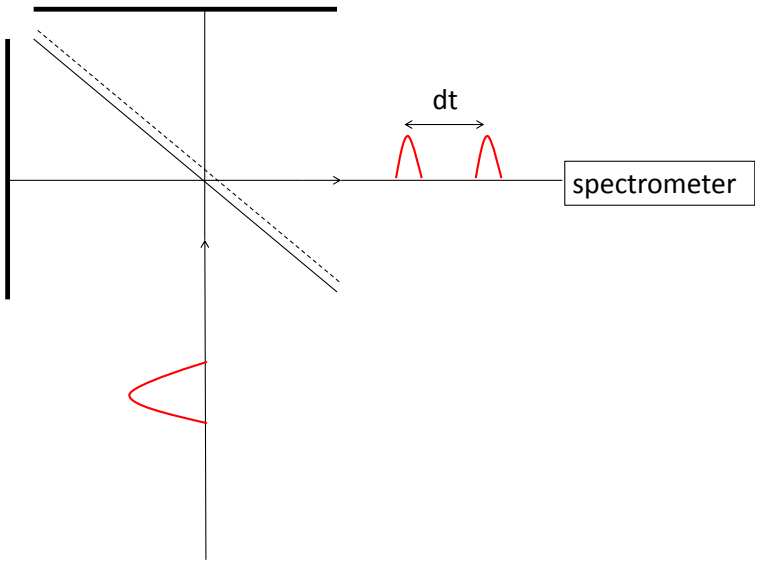

Figure 2.4: The simulated interference is plotted. Blue solid curve correspond to the case where reference and probe pulse go through the same medium. Green, dotted curve correspond to a $\pi/2$ phase shift, induced by a pump pulse preceding the probe pulse.

Both cases (in the presence of a pump pulse and without it) are simulated and the corresponding results are plotted in figure 2.4. For the simulation, a 10 fs

pulse at 800 nm has been used. The transmittance, due to the presence of the pump has been estimated at 0.1 and the phase shift $\Delta\Phi$ is $\pi/2$. An interference pattern in a gaussian envelope is clearly observed. The interference period being proportional to the wavelength and the width of the envelope being related to the pulse duration. The phase shift of the probe pulse, due to the presence of the pump pulse, induces a shift in the interference pattern in time. Lastly, the fringe contrast is reduced as well.

In conclusion, the presented technique is suitable for measuring changes in refractive index but it presents two major drawbacks. Indeed, one difficulty with time-domain interferometry is that the signal oscillates very quickly with the optical path, the oscillation period being the central wavelength. This means that a large number of data points must be acquired and even then the optical path must be known with a very good accuracy [53]. But the biggest disadvantage of this technique is the long scans needed. Since for each pump-probe delay a probe-reference scan must be made, the scanning time is multiplied and the sensitivity of the technique is deteriorated.

2.2.4 Frequency-domain interferometry

The spectral interferometry technique has been worked out by Froehly and coworkers several years ago [29] and its development, in the fs and broadband pulses, followed several years later [99, 33]. The principle lies on the analogue of mixing two waves of different frequency (i.e. two Dirac peaks in frequency domain). It is widely known that two waves, of two different frequencies, that interfere at the same point in space produce beats in the amplitude of the resulting signal, in time domain. The converse situation is to observe these beats in frequency domain, for which one would need to Fourier transform two Dirac peaks in the time domain. In reality, the Dirac peaks will correspond to two fs laser pulses.

Let us consider two laser pulses(see figure 2.5), as in the case of temporal interferometry, only this time with a fixed delay dt between them. The power spectrum is :

$$S(\omega) = |FT^1(E_1(t) + E_2(t))|^2 \tag{2.9}$$

Introducing the Fourier transforms, $\tilde{E}_1(\omega)$ and $\tilde{E}_2(\omega)$ respectively, derived from expressions 2.1 and 2.2 into 2.9 results in :

$$S(\omega) = 2\tilde{I}_0(\omega)[1 + cos(\omega dt)] \tag{2.10}$$

with [2], [3]

$$\tilde{I}_0(\omega) = |E_0(\omega - \omega_0)|^2 = |\tilde{E}_0(\omega) * \delta(\omega - \omega_0)|^2 \tag{2.11}$$

[1] **FT** is the Fourier transform operator.

[2] $*$ is the correlation product.

[3] $\delta(\omega - \omega_0)$ is the Dirac function centred at ω_0.

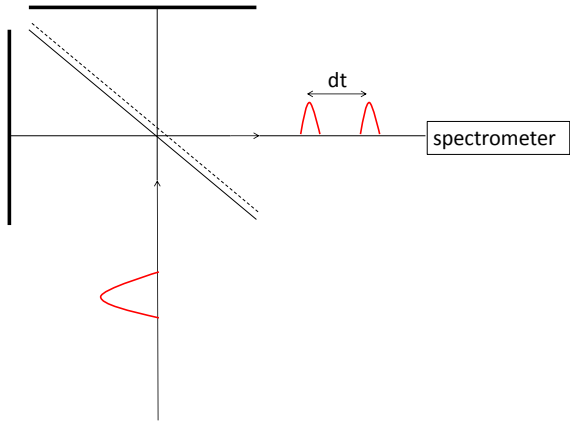

Figure 2.5: A possible experimental setup for spectral interferometry is presented. The positions of the mirrors are fixed, thus defining the time delay between the two pulses.

If we take into account the gaussian nature of the pulse :

$$I_0(t) = I_0 e^{\frac{-t^2}{\tau^2}} \tag{2.12}$$

the expression 2.10 becomes :

$$S(\omega) = \tilde{I}(\omega) = [\sqrt{2} I_0 e^{\frac{-(\omega-\omega_0)^2\tau^2}{4}}](1 + cos(\omega dt)) \tag{2.13}$$

The result is plotted in figure 2.6 for a 10fs pulse at 800nm. The pulse delay has been chosen to be 50fs. Once again (as in temporal interferometry) an interference pattern is observed, this time in spectral domain. The fringe separation (solid blue curve) is $\frac{2\pi}{dt}$.

Let us discuss now the case where the pump pulse is present. The expression of the electric field for the probe pulse is the one of equation 2.7 and by performing a similar calculation to the previous one, we obtain the modified expression of the spectrum (for a gaussian pulse) :

$$S'(\omega) = [\frac{\sqrt{2}}{2} I_0 e^{\frac{-(\omega-\omega_0)^2\tau^2}{4}}](1 + T + 2\sqrt{T} cos(\Delta\Phi - \omega dt)) \tag{2.14}$$

This spectrum is plotted along with the previous one (see green curve in Figure 2.6) and once again we observe the shift in the fringes (related to $\Delta\Phi$) and the reduced contrast (signature of the absorption of the probe pulse).

From an experimental point of view, the spectrum is obtained by stretching the two pulses in the spectrometer. This temporal stretching must be greater then the delay between the pulses in order to observe the interference.

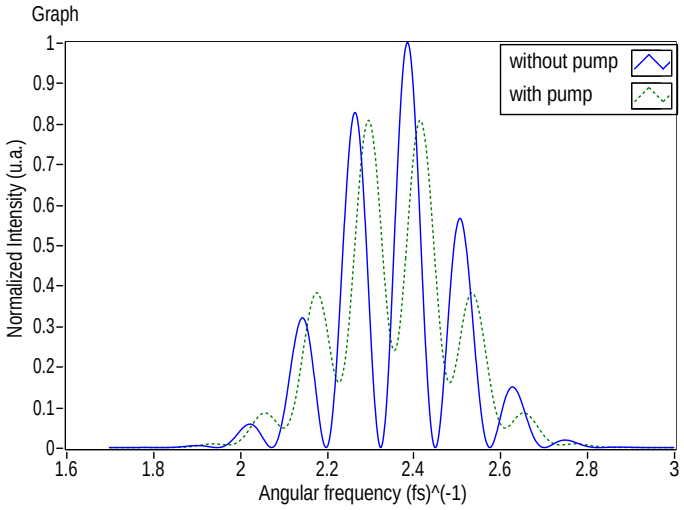

Figure 2.6: The simulated interference is plotted. Blue solid curve correspond to the case where reference and probe pulse go through the same medium. Green, dotted curve correspond to a $\pi/2$ phase shift, induced by a pump pulse preceding the probe pulse.

To conclude, the spectral interferometry technique can be used for the same purposes as in temporal interferometry but with a significant gain in time. Unlike in time-domain interferometry, the whole interferogram can be recorder simultaneously by the use of a CCD[4] detector. Furthermore, small fluctuations of the optical path do not invalidate the interferogram, although they do reduce the fringe contrast if their time scale is shorter than the exposed time [53].

2.2.5 Extraction of the phase shift

In the introductory section, we saw that we were interested in the modification of the optical properties of the solid that is included in the phase shift experienced by a pulse arriving right after a pump pulse. In the mean time, the presented experimental technique of spectral interferometry gives access to the phase shift through the intermediate of the shift of the fringe pattern. Let us see now how this is done.

Starting from the inverse Fourier transform of spectrum power we obtain :

[4]Charged Coupled Device

$$FT^{-1}[\tilde{I}_\omega] = (1+T)FT^{-1}[\tilde{I}_0(\omega)] + 2\sqrt{T}FT^{-1}[\tilde{I}_0(\omega)] * FT^{-1}[cos(\Delta\phi - \omega dt)] \quad (2.15)$$

Let's set :

$$FT^{-1}[\tilde{I}_0(\omega)] = G_0(t), FT^{-1}[\tilde{I}(\omega)] = G(t) \quad (2.16)$$

Finally :

$$G(t) = (1+T)G_0(t) + \sqrt{T}[G_0(t+dt)e^{i\Delta\phi} + G_0(t-dt)e^{-i\Delta\phi}] \quad (2.17)$$

We have, for a gaussian pulse :

$$G_0(t) = I_0 e^{\frac{-t^2}{\tau^2}} e^{i\omega_0 t} \quad (2.18)$$

and thus

$$G(t) = I_0[(1+T)e^{\frac{-t^2}{\tau^2}} e^{i\omega_0 t} + \sqrt{T}(e^{i\Delta\phi} e^{\frac{-(t+dt)^2}{\tau^2}} e^{i\omega_0(t+dt)} + e^{-i\Delta\phi} e^{\frac{-(t-dt)^2}{\tau^2}} e^{-i\omega_0(t-dt)})] \quad (2.19)$$

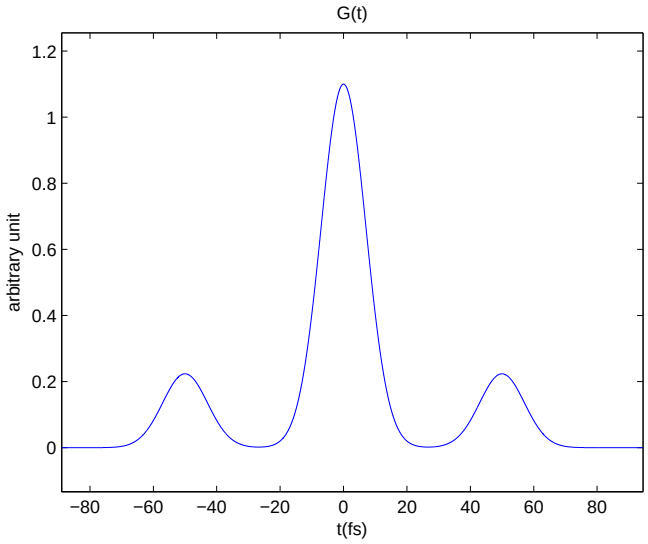

Figure 2.7: The simulated inverse Fourier transform of the spectrum.

The equation above has been simulated for a 10 fs pulse at 800nm, the phase shift is $pi/4$ and the delay between the pulses is 50fs. The transmissivity is 0.1.

This function presents three peaks (see figure 2.7), corresponding to the three different terms of the equations. The satellite peaks contain the information about $\Delta\phi$.

At $t = dt$, $G(t)$ becomes:

$$G(dt) = I_0[(1+T)e^{\frac{-dt^2}{\tau^2}}e^{i\omega_0 t} + \sqrt{T}(e^{-i\Delta\phi} + e^{i\Delta\phi}e^{\frac{-(2dt)^2}{\tau^2}}e^{i\omega_0(2dt)})] \tag{2.20}$$

The transmissivity T is determined by dividing equation 2.14 by 2.13.

Thus it becomes possible to extract $\Delta\phi$ from the value of $G(dt)$. It is straightforward to think that for the latter to be true, it is necessary that the time interval dt between the pulses is large compared to the pulse duration τ. This implies that in order to improve the signal-to-noise ratio one needs to increase the number of the fringes in the spectrum. Finally, the phase shift $\Delta\phi$ is related to the variation of the real part of the refractive index Δn by :

$$\Delta\phi = \Delta kL = \frac{2\pi}{\lambda_{probe}}\int_0^L \Delta n(z)dz \tag{2.21}$$

$$\Delta\phi = \frac{2\pi}{\lambda_{probe}}\int_0^L [Re(n(z)) - n_0]dz \tag{2.22}$$

k is wavenumber, L is the probed length supposed homogeneous and λ_{probe} the probe's wavelength. If we assume a homogeneously excited medium, then 2.22 becomes:

$$\Delta\phi = \frac{2\pi L}{\lambda_{probe}}\Delta n \tag{2.23}$$

2.3 Experimental setup

In the following section we are going to present the experimental setup employed to implement the spectral interferometry technique in a pump and probe scheme. The different elements consisting the experiment will be discussed in

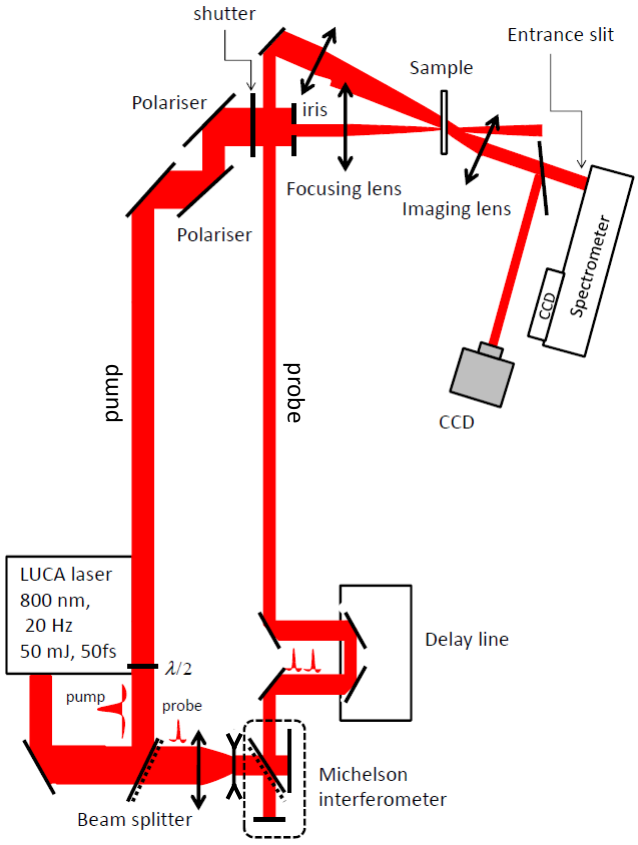

Figure 2.8: The experimental setup in its simplest version.

detail. In order to satisfy the growing demands, several modifications of the configuration have been proposed and performed during this thesis. A description of the latter will be given along with the evolution of the setup. A schematics is being presented in figure 2.8.

2.3.1 Overview

In the previous section, we have discussed the need of a pump and probe configuration in order to excite the medium and follow its time evolution by delaying the probe pulse. In our case, the probe pulse is an actual double pulse (reference

and probe) from which the spectrum is recorded. Furthermore, a certain number of optical elements ensure the tunability of the most important laser parameters, that are crucial for the excitation part of the solid. Let us now have a look at the simplest version of the setup, where we'll only include what is necessary to obtain a first set of results.

At first, the LUCA Ti:Sapphire laser server at CEA Saclay provides 50 fs laser pulses at 800 nm. Each pulse has en energy up to 50 mJ, thus making it possible to attain large intensities (10^{17}W/cm^2) with an average focusing (f=200 mm, beam diameter 6 mm). The repetition rate at 20 Hz is sufficient for the experiment, allowing both single-shot and multi-shot experiments with an acceptably strong signal.

The next step is to separate the laser beam in a pump and probe pulse. This is being done with a beam splitter ($T = 10\%$) sending the two beams in two separate paths. The pump pulse's energy can be adjusted by turning a half-wave plate coupled to a double set of reflective polarizers. Finally, the beam goes through a shutter (ability to do single shot or multi-shot experiment), an iris and it is then focused with a lens on the sample (its surface in most cases).

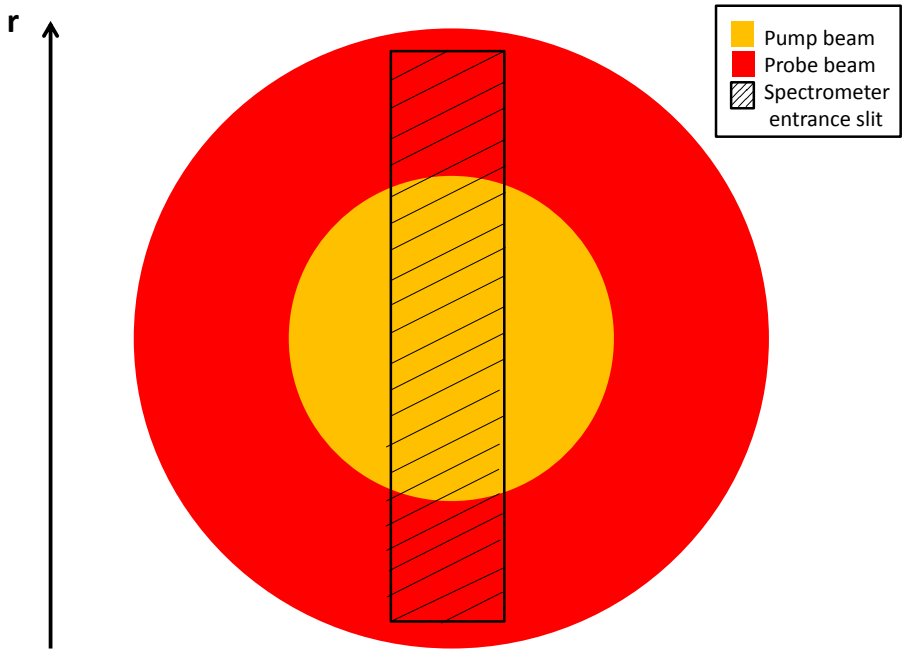

Figure 2.9: Spectrometer front view.

The probe pulse itself is amplitude split in a Michelson interferometer resulting in a sequence of two pulses (reference and probe) with a fixed time delay between them. The next step is to focus both of them on the sample, keeping the pump

spot in the center (see figure 2.9). The sample is vertically translated after each shot and a "fresh" surface is made available for the next shot. The lens behind the sample images the interaction plane both at the entrance of the monochromator and a CCD camera. The CCD camera provides imaging of the surface of the sample thus monitoring any contrast change[5] induced by the pump pulse (damage criterion).

In parallel, inside the spectrometer the two pulses are being stretched, making it possible to overlap in time and interfere (see figure 2.10). This interference pattern is actually the $I(r, \lambda)$ spectrum, r being the transverse coordinate of the beam. As a result, it is possible to extract the phase information by performing an inverse FT for each r position. The latter allows the acquisition of the spatial profile of the beam for each time delay ($\Delta\phi(r, t)$). Finally the presented plots ($\Delta\phi(t)$) are obtained by integrating in space. There are three regions to be integrated : two containing the reference phase information, at each side of the phase shift and one containing the phase shift itself (see figure 2.11 for more details). A simple subtraction afterwards results in a single value of $\Delta\phi$ per time step.

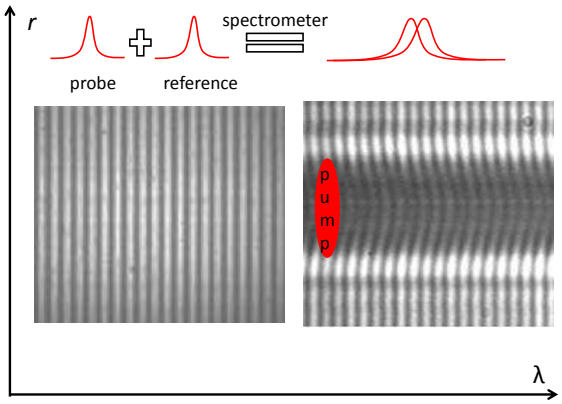

Figure 2.10: CCD camera view inside the spectrometer. On the left is the interference pattern observed without pump pulse and on the right with a pump pulse in the center. The displacement of the fringes in the center is signature of the phase shift change.

2.3.2 Setup discussion and optimization

One of the main issues of this thesis was to modify the initial experimental setup so that it satisfies emerging needs. What follows is a detailed report of the limitations of the experiment and the modifications applied.

[5]Criterion for threshold definition is a 50% chance of contrast modification on the surface.

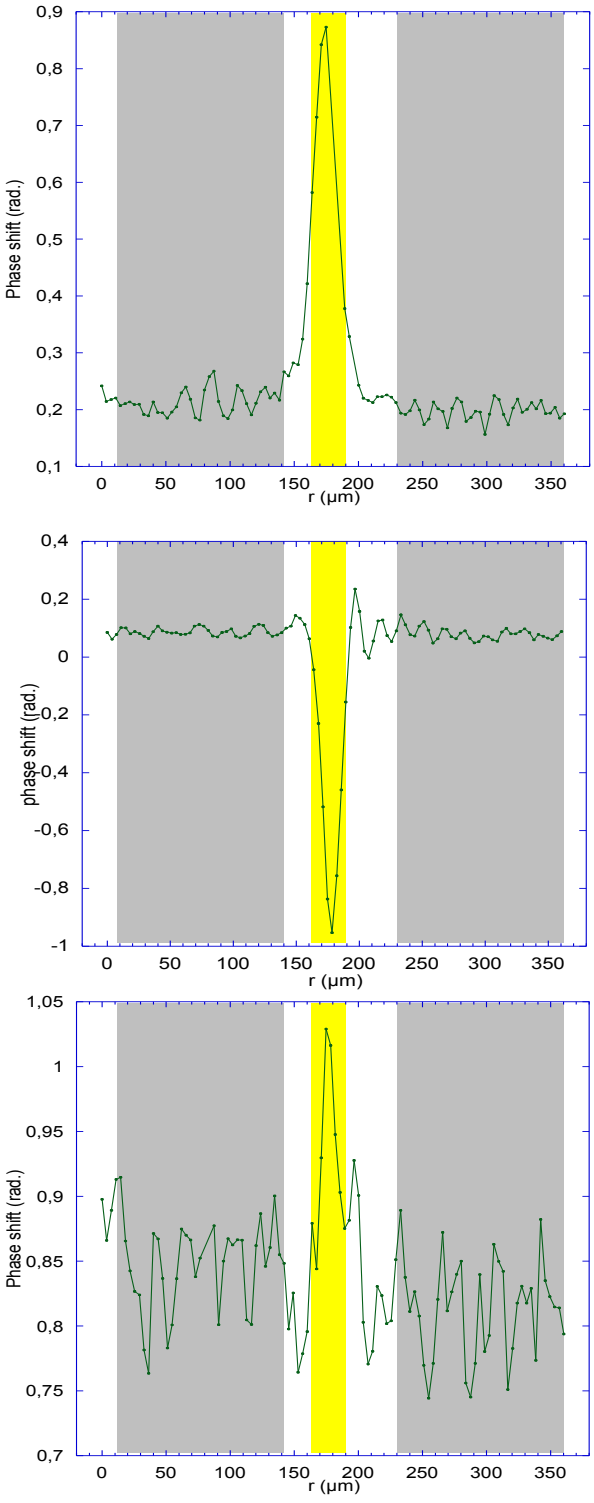

Figure 2.11: Phase shift as a function of the transverse coordinate of the beam r, for three pump-probe delays. From top to bottom different contributions encountered are : Kerr effect, free carrier generation and trapped carrier formation respectively (see section 2.4.1 for more details) The three different regions to be integrated are illustrated, with light grey being the integration over the ground level and yellow the actual measured signal.

Separation of short time scaled phenomena

In the introductory chapter, we have discussed the different excitation mechanisms involved during the excitation of a dielectric with a fs intense pulse. In particular, these mechanisms (MPI,TI and avalanche ionization (AI)) take place at time scales of the order of our laser pulses (some tenths of fs). It is therefore impossible to distinguish them in time, in the current configuration.

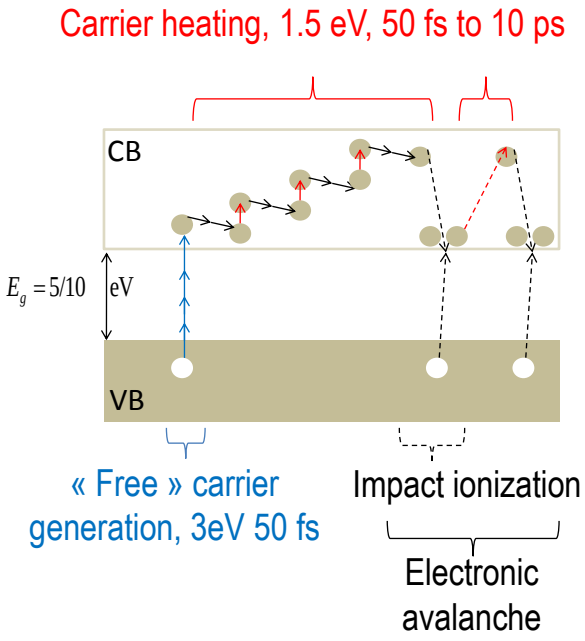

Figure 2.12: Illustration of the approach used to separate the different excitation mechanisms.

To get around this problem, we have suggested using two pump pulses instead of one (see figure 2.12). At first, a UV laser pulse (central wavelength centred at $400nm$) pre-excites the solid (generation of an initial excitation density by multi-photon absorption) and then an IR pulse (central wavelength centred at 800 nm, variable pulse duration) is sent at variable time delay, to "heat" the carriers and thus trigger the eventual impact ionization (seeding the electronic avalanche), if any. At this point, it is crucial to ensure both spatial and temporal overlap between the pulses. Imaging the surface of the sample allows spatial superimposing, by keeping the pulse's energy at a level where the damage takes place only when both pulses overlap. The zero time delay (delay at which IR and UV pulses arrive together on the sample) is determined by frequency tripling, right before the sample's surface. The latter serves as a correlation measurement between the UV pulse of known duration and a stretched IR, thus allowing measurement of the IR

pulse duration.

The choice of wavelengths contributes to the stability of the measurement, keeping in the mean time the two processes (multiphoton absorption and carrier heating) as independent as possible. More precisely, the UV light is preferred to IR for the initial excitation stage and IR light is used for "heating" the CB electrons. One of the reasons for such a choice is to eliminate as much as possible the energy fluctuations. The UV photon energy being higher, less of them are needed to breach the band gap. This has as a result a power lower exponent for the intensity at the multiphoton ionization rate and thus the impact of fluctuations is lowered as well. A second reason is that CB electrons absorb IR photons at a much higher rate than UV, this being related to the lower absorption cross section for UV light. This along with the fact that is easier to change the pulse duration of the IR, results in the "heating" process being governed only by the IR pulse making the two processes independent. Then, cross-excitation effects (excitation involving photons from both pulses when they overlap in time) are disfavoured. The latter is important as we want the two pulses to be spent in different, independent processes without contributing with a combined signal to the phase shift.

Temporal scan limitation.

In the previous subsection, we saw a basic version for the application of the frequency domain interferometry (FDI) in the pump and probe scheme. However, a certain number of difficulties arises when ones studies closer the laser-solid interaction.

First, the time delay between the probe and reference pulse is limited by the spectral resolution of the spectrometer. In our case, it is of the order of some tenths of ps. This value determines the maximum time delay between the pump and the probe at which one can measure the absolute phase shift (phase shift compared to a zero phase signal) due to limitations of the present configuration (see figure 2.13). However, it is possible to overcome this obstacle by calculating the relative phase shift and fitting it to a model [55]. Of course such a process is sensible only to large variations of the phase shift, in the time scale of the probe-reference delay. The different situations are illustrated in figure 2.14.

In order to measure absolute phase shift at all time delays and thus increase the precision of the measurement, we suggested changing the interferometer. Indeed, the limitation is related to the fact of having the probe and the reference pulse propagating in the same optical path, inside the medium. Selecting a Mach-Zender (see figure 2.15) interferometer instead pushes the limitation to the resolving power of the spectrometer. On the other hand, selecting independent paths for the two pulses lowers the sensitivity of the measurement. This is due to the probe pulse's phase being modulated by the sample's surface imperfections along with the phase

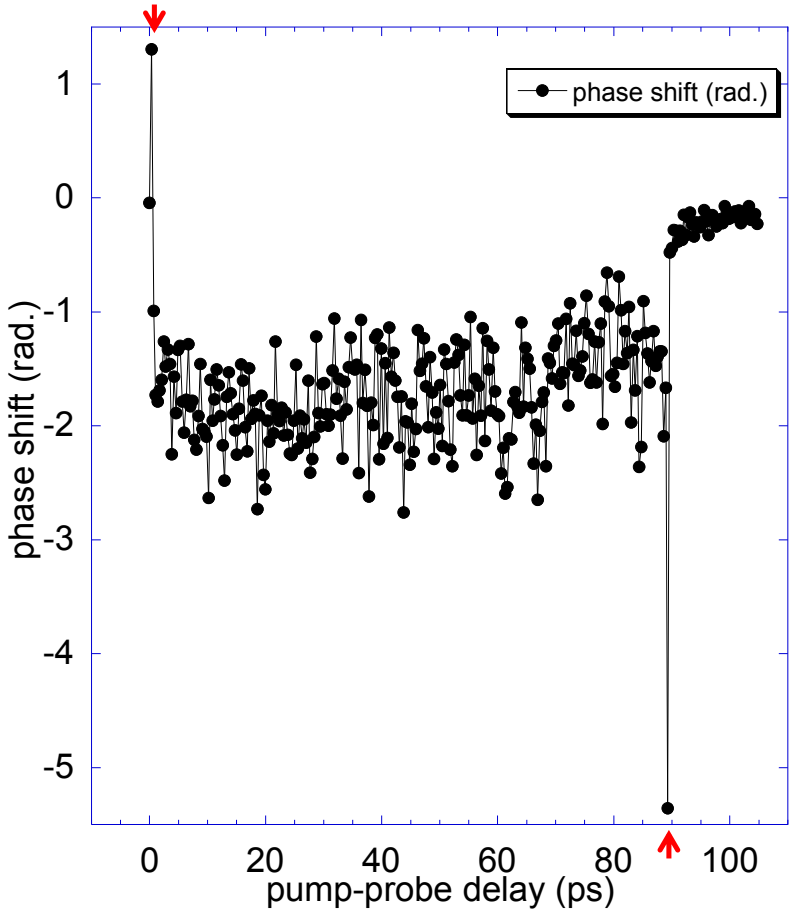

Figure 2.13: Experimental result of the phase shift as a function of an IR pump-probe delay in SrTiO. The positive and negative peaks represent the beginning and the end of the absolute phase shift scan respectively.

fluctuations induced by the different path for the reference and the probe pulse.

The final choice of the interferometer and its placement on the setup involves both an increased sensitivity and the possibility of long temporal scans. This has been achieved by using a Michelson interferometer behind the sample. After passage through the interferometer, two identical spots are created. The key point here, is to tilt one spot with respect to another, in the transverse plane (see figure 2.16). That way, the excited, perturbed part in the center of one beam (probe pulse) interferes with the unexcited, peripheral part of the other beam (reference pulse). A fixed delay is still imposed between the two pulses, only this time the delay with the pump can be extended arbitrarily, and just the number of the fringes observed is affected. Finally the interference pattern is once again recorded in the spectral domain.

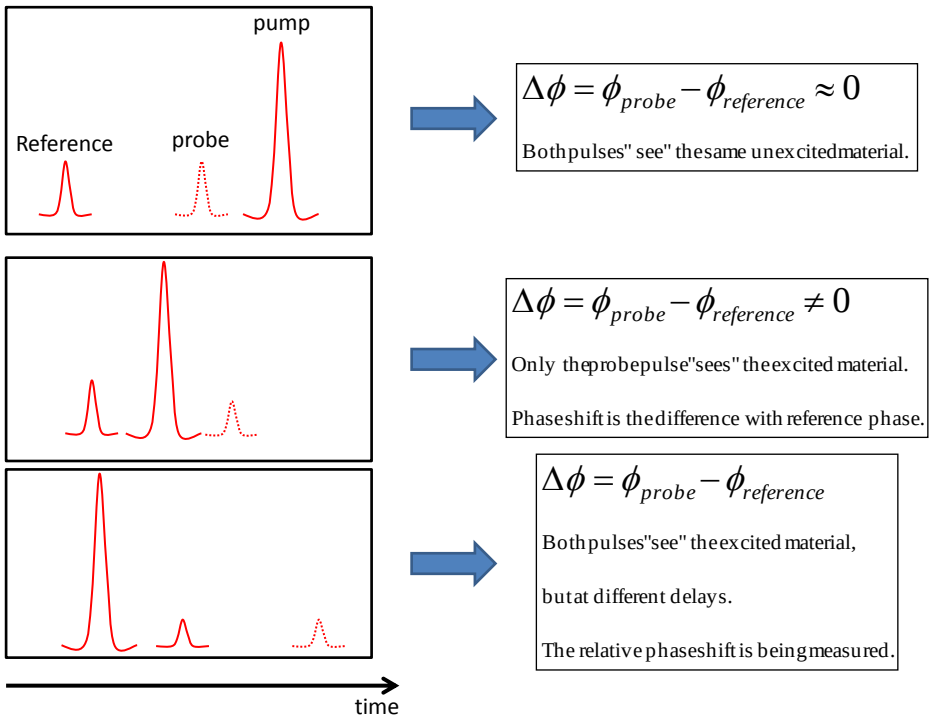

Figure 2.14: Illustration of the different cases distinguished depending on the pump-probe delay. Probe and reference pulse delay is fixed.

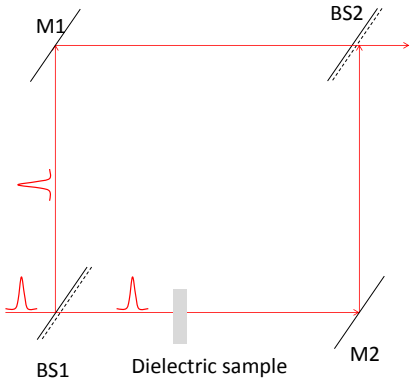

Figure 2.15: Illustration of the Mach-Zender interferometer.

The maximum pump-probe delay is limited only by the length of the delay line and it is of the order of 1 ns in our experiment (15 cm delay line).

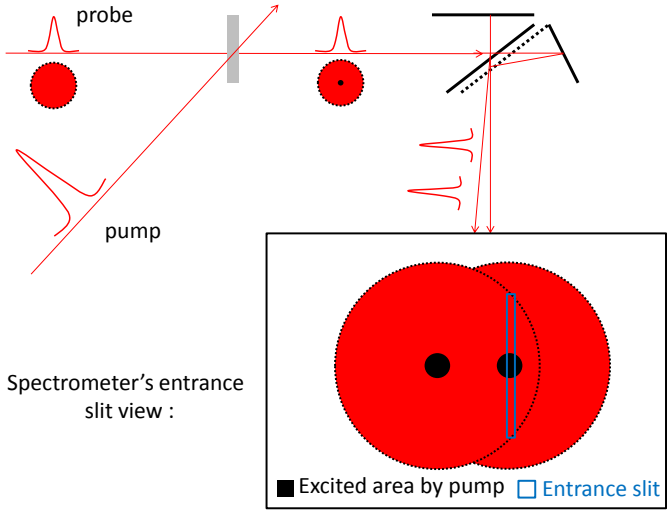

Figure 2.16: Principle of using a Michelson interferometer behind the sample for spectral interferometry.

Probed volume limitation

Another limitation comes from the geometry of the interaction. The pump and the probe pulses propagate almost co-linearly (see figure 2.17a) and as a result the signal acquired is the addition of the different contributions at different depths. The probed length L in this case is $R/sin\phi$ and the depth probed $dz = R/tan(\phi)$. In our focusing conditions for a UV pulse, L was of the order of 200 μm and dz 50 μm. The inhomogeneous excitation of the sample, due to the strong absorption of the beam behind the surface, results in the absence of any spatial resolution in depth of the sample. Of course, the ambiguity can be overcome if one focuses on the evolution of a given parameter, in the same conditions.

A solution to decrease the large probed length is to change the geometry of the probe with respect to the pump. The setup has been modified so that the probe beam arrives perpendicular to the pump and thus the probed length is equal to the diameter of the beam at that given depth. If one is interested at the surface, then the probe has to be internally reflected on the rear side of the surface (see figure 2.17b). In both cases, there is almost no ambiguity due to the inhomogeneous excitation in depth and only the transverse excitation profile has to be taken into account. The probed length L, in the same focusing conditions as before for a UV pulse, is of the order of 50 micrometers (focusing on the surface of the solid sample). Reduction of the probed length by a factor of four has been achieved, not without losing in sensitivity though. The other important feature is the reduction of the probed depth down to almost 2 μm.

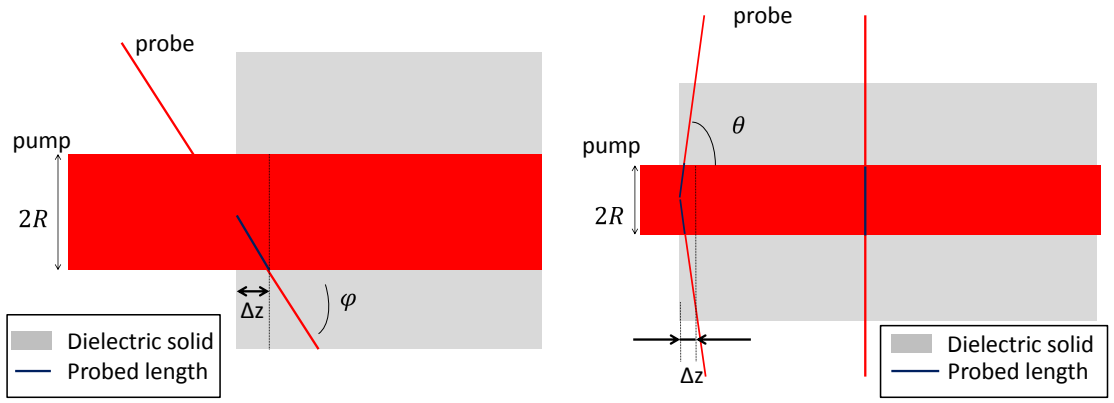

(a) Collinear geometry.

(b) Perpendicular geometry.

Figure 2.17: Illustration of the two possible configurations for the pump and the probe. The probe beam is represented by a single line representing the ray entering the monochromator's entrance slit. Refraction has been neglected and a top hat profile for the pump beam has been employed for the figure.

In this perpendicular geometry proposed, the probe beam's propagation depends on the morphology of the surface of the sample and on the respective angles of the cubic samples used ($5 \times 5 \times 5$ mm^3). Alignment becomes more challenging and so does the acquisition of a strong signal due to the smaller probed length. In the case of collinear geometry, wafers have been used ($10 \times 10 \times 0.5$ mm^3).

Another advantage of the perpendicular geometry is the possibility to measure the phase shift at different depths behind the sample and thus probe propagation effects within the pump beam.

Various modifications

A certain number of complications arises as to an acquisition of noiseless signal. For example, the faults in the flatness of the mirrors in the Michelson interferometer lead to a "noisy" reference phase, along the spectrometer's entrance slit, even in the absence of the pump pulse. This ground noise has been eliminated by acquiring the spectrogram, at each time step, with and without the presence of the pump. Finally, the phase shift is being obtained by subtracting the two phase lines recorded.

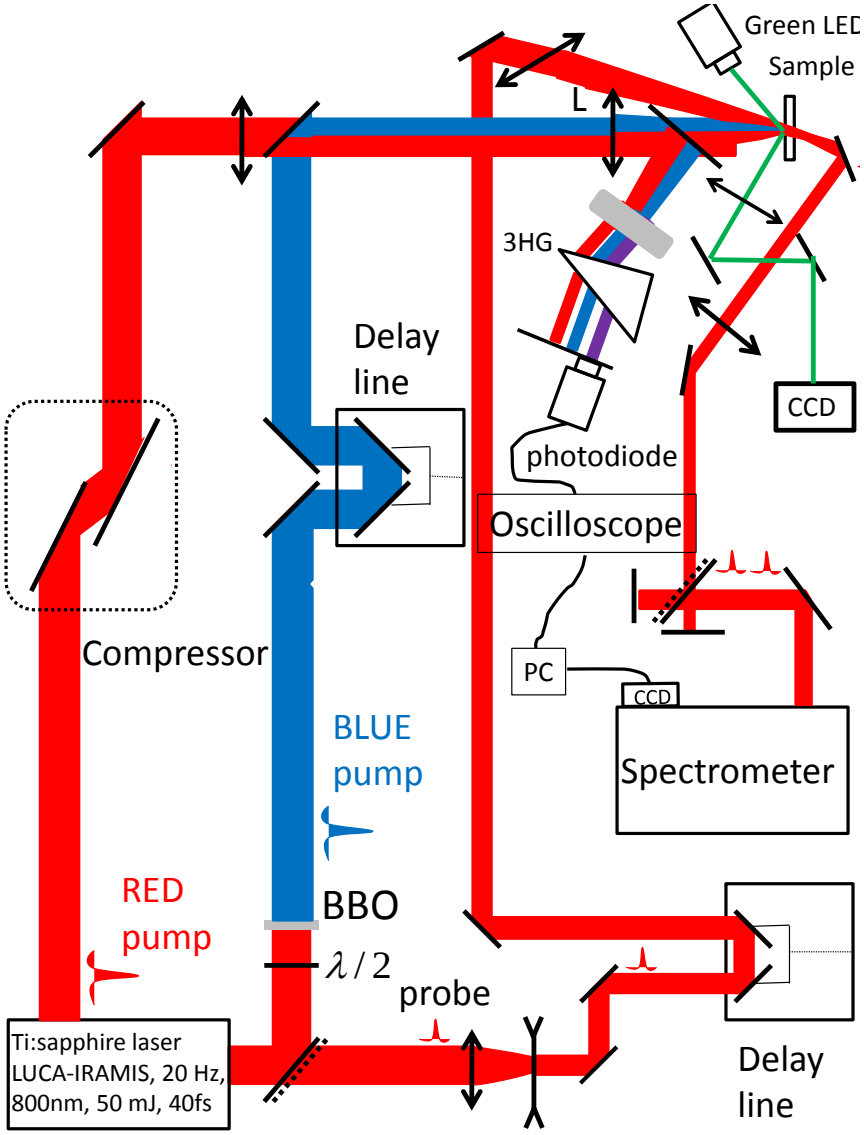

Figure 2.18: Optimized version of the initial experimental setup.The almost collinear configuration is being represented, with the perpendicular one being possible as well. Double pump and probe experiment is possible with variable radiation parameters.There is possibility of translating the sample in all three directions.

2.3.3 Final version of the experimental setup

The imaging system employed (illuminating with infrared light) has been modified as well. An additional imaging system was installed allowing higher brightness,

resolution and magnification. Thus it was easier to distinguish phase modifications of the solid (permanent modification and/or damage thresholds).

Finally, a spatial filtering system has been included on the probe path in order to obtain an approximately flat phase (plane wavefront at the surface) over r. The reason is that having a varying phase degrades the phase resolution and thus the minimum phase shift measured.

The revised version of the experimental configuration is being presented in figure 2.18. It includes parts of the advancements achieved during this thesis and it has been the configuration used for most of the experiments performed as it proved to be the most successful.

Of course, the evolution of the experimental setup doesn't end here, the current version could become even more powerful by including further additions such as implementing a reflectivity measurement along with the rest. Finally, some minor changes could push even further the overall performance : smaller spectrometer for more compact setup, longer delay line for longer scans etc.

2.4 Theoretical considerations

In this section, we will discuss the different contributions to the signal measured in an attempt to identify the excitation and relaxation stages. The interpretation of the experimental results will be based on this detailed description, de-convoluting when possible the different contributions. Finally, the relation of the measured phase shift with the excitation density will be given.

2.4.1 Different contributions to the phase shift

In the beginning, of the chapter, we have underlined the main purpose of these experiments, which was to measure the excitation density as a function of time. It has been suggested to do so, by recording the change in the optical behaviour of the solid (dielectric constant) which is easily accessible by measurement of the phase shift. Before presenting the experimental results, we shall give a detailed description of the different contributions to the refractive index (related the intrinsic properties of the solid) in order to be able to understand the curves that will follow. It is reminded that phase shift and refractive index variation are related through : $\Delta\phi = \frac{2\pi}{\lambda_{probe}} L \times \mathrm{Re}(\Delta n)$

From our point of view, we were able to distinguish two types of dielectric materials depending on their optical behaviour. The plots in figure 2.19 illustrate the latter. There are three regions of interest on these plots. At first, positive phase shift was followed by a negative one is common for both materials and then while for the Al_2O_3 it stays negative for a long time scale, it becomes rapidly positive for $\alpha - SiO_2$. Of course the signal in Al_2O_3 does come back to zero after longer delay (see figure 2.20).

Kerr Effect

The refractive index of many optical materials depends upon the intensity of the light itself. At high intensities, such non-linear processes become significant enough to be detected. In centrosymmetric media, such as the crystals studied, the second order polarization term is absent. The next term is a third order one and it is the one responsible for the optical Kerr effect. This self-induced term is expressed as [12] :

$$\Delta n = n_2 I \tag{2.24}$$

with n_2 being the non-linear refractive index of the medium and I the intensity of the pump.Typical values for glasses are $10^{-16} - 10^{-14}$ cm^2/W and they can be calculated in our case from interferograms. In the case of our experiment, the probe will "see" a positively modified refractive index for as long as it is present

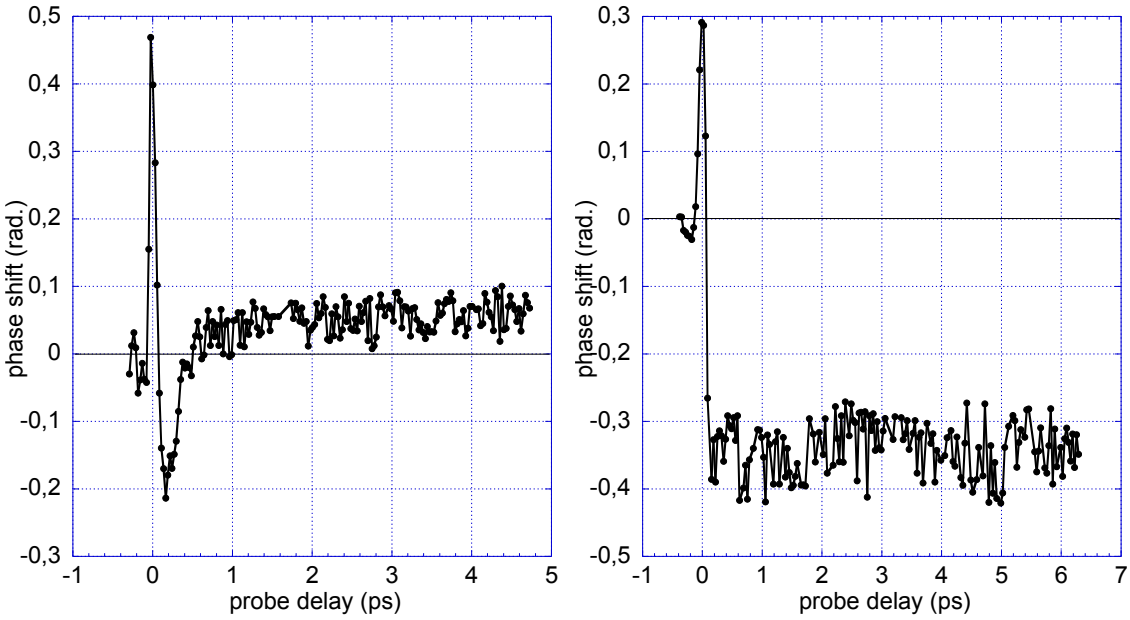

(a) $\alpha - SiO_2$: Fluence $= 0.53 J/cm^2$, pulse duration $= 50 fs$

(b) Al_2O_3 : Fluence $= 0.55 J/cm^2$, pulse duration $= 60 fs$

Figure 2.19: Phase shift measurements as a function of the pump-probe delay, for two different materials with a 400 nm pump.

along with the pump pulse. The latter explains the positive phase shift in the beginning of the curves in figure 2.19. Subsequently, the Kerr effect's duration is of the order of the pump pulse duration and its radial distribution allows to define the focused beam profile. Its shape follows the temporal shape of the pulse (Gaussian pulse). This is indeed the way we have processed to measure the beam's spot size experimentally (see figure 2.21). Finally, the peak of this Kerr effect will correspond to the case of zero delay between the pump and the probe.The temporal coincidence of the two pulses will have as a result a positive contribution to the absorption signal as well, representing the situation of cross-excitation (pump and probe photons mutually absorbed for MPI)

"Free" electron model and contribution

Kerr effect is followed by a negative contribution to the phase shift, as it can be seen for figure 2.19b at long time scale and in figure 2.19a for some tenths of fs, before it comes back to positive. The pump pulse, being intense enough, ionizes the dielectric, thus creating electron-hole pairs. These electrons, being now in the CB, modify the optical response of the medium. To account for this

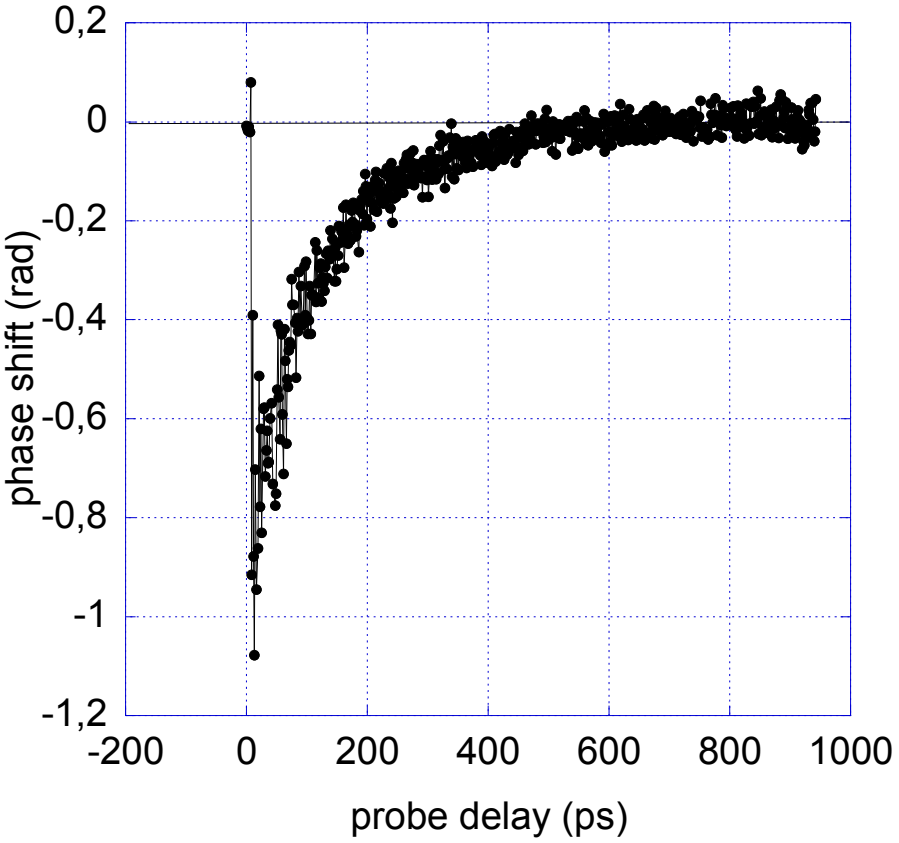

Figure 2.20: Long scan in Al_2O_3 with a 400 nm pump. Fluence is 1.28 J/cm^2 and pulse duration = 60 fs.

contribution, we shall take the Drude model approach for free electrons. We will assume that electrons promoted in the CB, behave as if being free. The possible interactions that can be considered in a fixed collisional rate are the electron-ion, electron-phonon and electron-electron collisions (see 1st chapter, energy relaxation section). In this classical description, the hole contribution to the refractive index is indistinguishable from that of electrons and it may be taken account through the $\frac{f_{\mathrm{CB}}}{m^*}$ parameter with f_{CB} and m^* being the oscillator strength standing for transitions occurring in the CB and the effective mass respectively.

The complex refractive index of a solid n at frequency ω_{probe} in the "free" electron approximation is given by [27] :

$$n^2(\omega_{probe}) = \epsilon_r = n_0^2 - \omega_{plasma}^2 \frac{f_{\mathrm{CB}}}{\omega_{probe}^2 + i\omega_{probe}\omega_c} \tag{2.25}$$

with : ϵ_r the relative permittivity, n_0 unperturbed refractive index and ω_c being

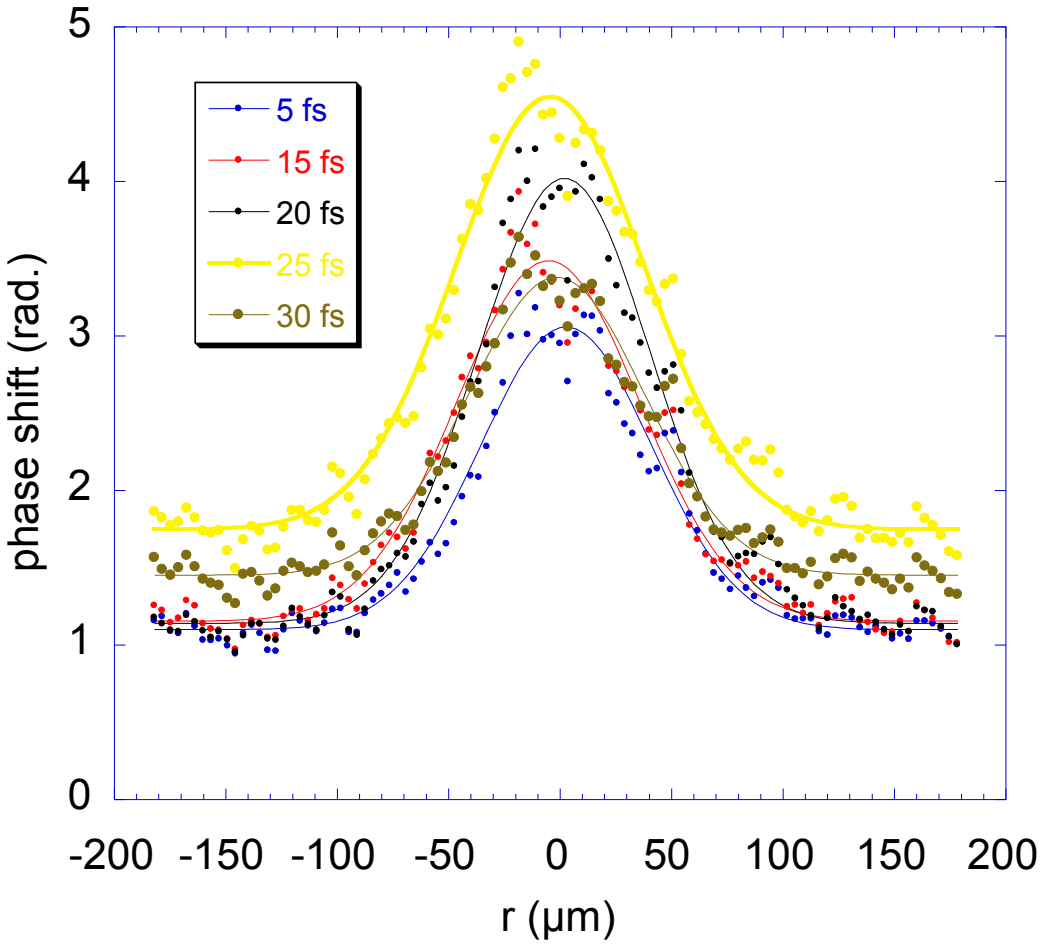

Figure 2.21: Phase shift along the beam's radial coordinate. Different curves stand for different pump-probe delays. Gaussian fit is used to determine the beam's spot size.

related to a damping term and representing the collision probability per time unit. In what follows f_{CB} will be taken equal to 1. The $\frac{f_{\mathrm{CB}}}{m^*}$ quantity can be a free parameter, for the electrons and the holes, and can be estimated while fitting our phase shift and absorption measurements.

ω_{plasma} is the plasma frequency and it is given by :

$$\omega_{plasma} = \sqrt{\frac{Ne^2}{\epsilon_0 m^*}} \tag{2.26}$$

with : N the excitation density, e the elementary charge and ϵ_0 the vacuum

permittivity.

The introduction of an effective mass rather than the free electron mass m_0 allows to account for the movement of the electron inside the CB. Equation 2.25 is plotted in figure 2.22. The probe pulse is at 800 nm and the medium considered is $\alpha - SiO_2$. For blue curves effective mass m^* is equal to m_0 (electron mass) and collisional frequency ω_c is equal to 1 fs^{-1}.

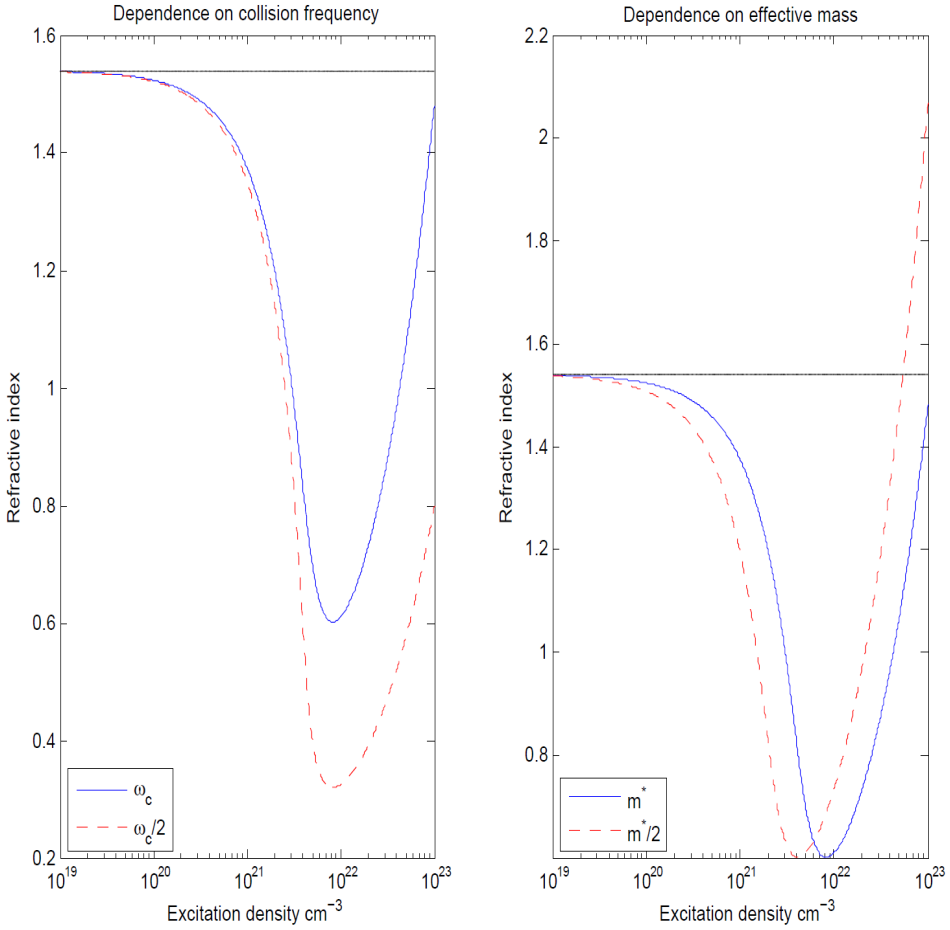

Figure 2.22: Free electron contribution to the real part of the refractive index in $\alpha - SiO_2$. On the left, the two curves are plotted for two different collision frequencies: $\omega_c = 1 fs^{-1}$. On the right, the same is done for two effective masses:$m^* = m_0$. In all cases, the contribution is negative at moderate densities (before reaching N_c). Black curve represents the unperturbed refractive index.

In parallel, let us not forget that ω_c is responsible for the imaginary part of the refractive index, accounting for the fact that electrons may absorb photons while

colliding. In dielectrics, the collisions responsible for the photon absorption are mainly between electrons and phonons.

By looking at figure 2.22 one may define a characteristic density at which the contribution of "free" electrons becomes positive. This is expressed as :

$$N_c = \frac{\epsilon_0 m^* n_0^2(\omega_{probe}^2 + \omega_c^2)}{e^2} \tag{2.27}$$

and it is of the order of $10^{22} cm^{-3}$.

Trapped electron model and contribution

This is the point at which a difference in the behaviour of the two solids is observed. Although phase shift stays negative for a long time (several tenths of ps) in Al_2O_3, accounting for the presence of "free" carriers, it rapidly becomes positive in $\alpha - SiO_2$ (150 fs). This can be explained by supposing, first of all, that the excitation density drops and that some other contribution increases the phase shift above zero. One could suggest the recombination being responsible for the decrease in the excitation density but this is a process occurring at later times and thus no account can be taken at the time scales we are interested in (tens of fs).

Indeed, the trapping time coincides with the rise time of the absorption band of the self-trapped-exciton (see 1st chapter, "free" electron relaxation), leading to the conclusion that the electronic trapping is associated with the formation of STEs [38]. Moreover, it has been shown that more than 90% of the electrons in the CB are being trapped in the band gap, in the case of $\alpha - SiO_2$ [21]. Today, it is generally admitted [55] that STE formation is responsible for trapping of carriers in $\alpha - SiO_2$, NaCl and KBr. The contribution of STEs in the refractive index can be expressed as :

$$n^2(\omega_{probe}) = \epsilon_r = n_0^2 - \omega_{\mathrm{STE}}^2 \frac{f_{tr}}{\omega_{tr}^2 - \omega_{probe}^2 + i\omega_{probe}/\tau_{tr}} \tag{2.28}$$

with

$$\omega_{\mathrm{STE}} = \sqrt{\frac{N_{tr} e^2}{\epsilon_0 m_0}} \tag{2.29}$$

ω_{tr} is the energy difference between the fundamental and the first excited state of the induced defect, $1/\tau_{tr}$ the width of this transition and f_{tr} the corresponding oscillator strength. Different trap levels (ω_{tr}) can be considered as long as the summation over the oscillator strengths is equal to one (Thomas-Reiche-Kuhn law).

Considering a very thin transition line width ($1/\tau_{tr} \simeq 0$) it can be deduced that the STE's contribution to the refractive index, and thus to the phase shift, is

positive in our experimental conditions ($\hbar\omega_{tr} = 2.1\ eV$ for NaCl and 5.2 and 4.2 eV for $\alpha - SiO_2 > \hbar\omega_{probe} = 1.5\ eV$).

Other contributions

Valence band depletion We consider that the fundamental state of a wide-band-gap insulator can be represented by a two level system[55]. In that case the dielectric function reads :

$$n^2(\omega_{probe}) = \epsilon_r = 1 + \omega_{valence}^2 \frac{f_{12}}{\omega_{12}^2 - \omega_{probe}^2 + i\omega_{probe}/\tau_{12}} \tag{2.30}$$

and

$$\omega_{valence} = \sqrt{\frac{N_0 e^2}{\epsilon_0 m_0}} \tag{2.31}$$

f_{12} is the oscillator strength between the valence and the CB, ω_{12} stands for the energy difference between VB and CB (band gap), τ_{12} is the width of the transition and N_0 the VB density. In our case, we are far from resonance ($\hbar\omega_{12} = 9eV \gg \hbar\omega_{12} = 1.5eV$) and the damping term ($\omega_{probe}/\tau_{12}$) responsible for linear absorption can be neglected. Therefore, equation 2.30 is real and it is equal to the square root of the unperturbed refractive index n_0^2. Knowing n_0 and the band gap, we can estimate an effective VB density :

	$\alpha - SiO_2$	Al_2O_3	MgO
N_0	$7.8 * 10^{22} cm^{-3}$	$1.2 * 10^{23} cm^{-3}$	$8.3 * 10^{22} cm^{-3}$
Band gap	9 eV	8.8 eV	7.7 eV
Unperturbed refractive index	$n_0 = 1.54$	$n_0 = 1.77$	$n_0 = 1.736$

Expression 2.31 is valid as long as the solid remains unexcited. When electrons start appearing in the CB, they should be subtracted from the VB, accounting for the depletion of the latter. Thus N_0 becomes $N_0 - N - N_{tr}$ and equation 2.31 is rewritten :

$$\omega_{valence,depl} = \sqrt{\frac{(N_0 - N - N_{tr})e^2}{\epsilon_0 m_0}} \tag{2.32}$$

Introducing 2.32 in 2.30 :

$$n^2(\omega_{probe}) = \epsilon_r = 1 + \omega_{valence,depl}^2 \frac{f_{12}}{\omega_{12}^2 - \omega_{probe}^2 + i\omega_{probe}/\tau_{12}} \tag{2.33}$$

The contribution of depletion has been estimated by replacing n_0^2 in 2.25 by 2.33 and plotting the result, along with the one without depletion, in figure 2.23. N_{tr} has been neglected by placing ourselves at probe delays when trapping has not taken place yet ($< 150fs$). It can be deduced that this contribution is of minor importance.

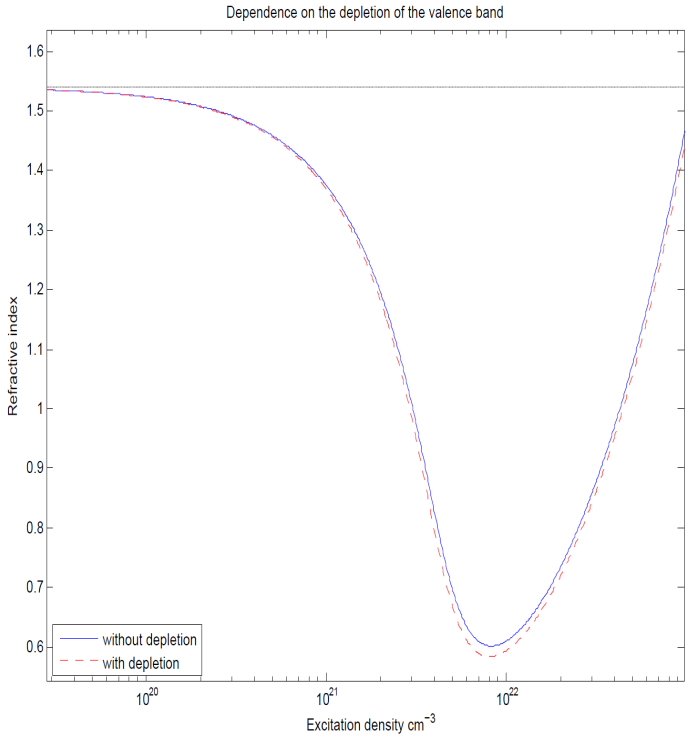

Figure 2.23: Comparison between two models in $\alpha - SiO_2$: one considering VB depletion and the other one not. Black curve is the unperturbed refractive index.

Temperature contribution Another possible modification of the refractive index may result from changing the temperature. Based on the hypothesis that the lattice temperature rises up by depositing energy in the solid with the laser pulse, we can estimate the refractive index dependence on temperature T [105] in Al_2O_3:

$$n_0 = 1.774 + (1.65 \pm 0.25)10^{-5}(T - 300) \tag{2.34}$$

This equation has been plotted in figure 2.24:

Such temperatures of course take time to establish in the lattice (thermalization regime: hundreds of ps). This model shows little impact on the refractive index (less than 1% for a 1000K raise). However, we should take note that the

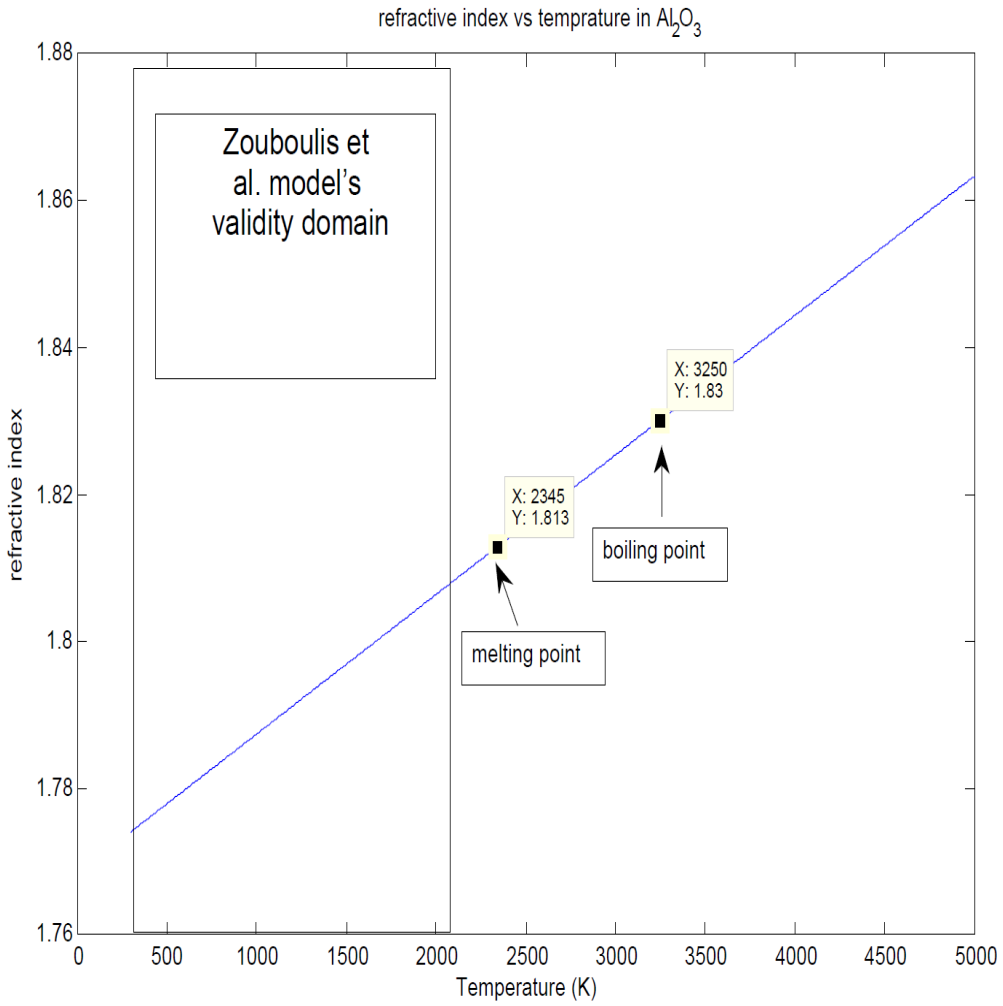

Figure 2.24: Refractive index dependence on temperature in Al_2O_3. Arrows point out melting and boiling points. Black lines delimit the domain at which Zouboulis et al.[105] have developed the model.

conditions of our experiment (near damage threshold intensities) drive us out of the present model's validity domain (see figure 2.24). Therefore, above threshold at long delays, structural modifications of the material may alter the temperature dependence of the refractive index and thus the model may be somewhat questionable. Interpretation of positive phase shift changes as due to temperature may be reasonable upon moderate intensities that is below breakdown threshold.

Phase shift due to transmission Propagation of an electromagnetic (EM) wave front through interfaces of media of different refractive index is characterized by reflection and transmission coefficients, given by Fresnel equations. Let us consider the case of light propagating from vacuum to an excited medium at normal incidence and polarization parallel to the plane of incidence. Its transmission coefficient is given by [40] :

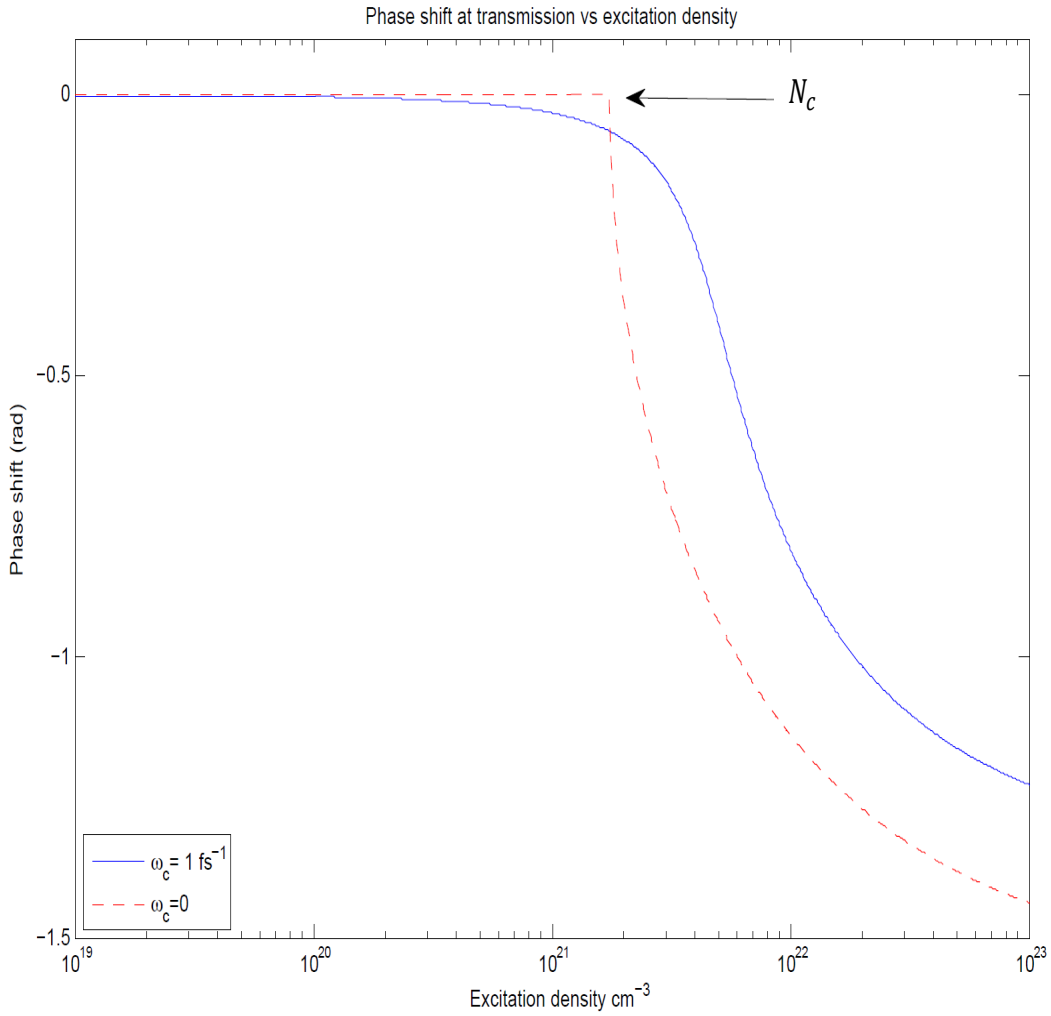

Figure 2.25: Plotted phase shift experienced by a 800 nm pulse through transmission in a medium of excitation density N. Two curves are plotted : one considering a collisional rate and one neglecting collisions.

$$t = 1 - r = 1 - \frac{n-1}{n+1} \tag{2.35}$$

with r reflection coefficient and n the complex refractive index of the excited medium. In the case of a purely real refractive index, t is real as well and no phase shift is induced by this passage. However, if n possesses an imaginary part, this will contribute as additional phase shift to the transmitted wave. Indeed, the only case when n is purely real is (see equation 2.25 and 2.27) for $\omega_c = 0$ and $N \leq N_c(\omega_{probe})$. In which case n becomes :

$$n(\omega_{probe}) = \sqrt{n_0^2 - \frac{\omega_{plasma}^2}{\omega_{probe}^2}} \tag{2.36}$$

In any other case, for $N \geq N_c(\omega_{probe})$ and/or $\omega_c \neq 0$ n is complex and so is t. The phase shift in that case is the argument of t and it is calculated from 2.35 substituting n by 2.22. For the special case when ω_c is equal to zero, then :

$$n(\omega_{probe}) = i\sqrt{\frac{\omega_{plasma}^2}{\omega_{probe}^2} - n_0^2} \tag{2.37}$$

and

$$\Delta\phi = \arg t = \arctan(-x) \tag{2.38}$$

with

$$x = \sqrt{\frac{\omega_{plasma}^2}{\omega_{probe}^2} - n_0^2} \tag{2.39}$$

The phase shift contribution due to transmission has been plotted in figure 2.25. We have considered a 800 nm probe pulse propagating at the interface between vacuum and excited dielectric. Plotting the case where $\omega_c = 0$ allows to see that the contribution becomes significant only above the characteristic density N_c and tends to $\pi/2$ for $N \to \infty$.

2.4.2 Relation between excitation density and phase shift

Until now, we have focused on the different contributions to the phase shift, by the intermediate of contributions to the refractive index. This has been done because the measurable quantity in our experiment is the phase shift. Now let us consider the relation between phase shift and refractive index once again and find the relation with excitation density N:

$$\Delta\phi = \frac{2\pi}{\lambda_{probe}}[\int_0^L Re(n(z) - n_0)dz] \tag{2.40}$$

with $n(z)$ the depth depending (in the direction of the pump pulse) refractive index of the excited medium and L the probed length.

If we consider a homogeneously excited medium expression 2.40 becomes :

$$\Delta\phi = \frac{2\pi}{\lambda_{probe}}\Delta[Re(n)]L \tag{2.41}$$

with

$$\Delta[Re(n)] = Re(n) - n_0 \tag{2.42}$$

Depending on the pump-probe delay, different expressions can be used to estimate n : Kerr effect at time coincidence, "free" carrier generation (up to 150 fs for $\alpha - SiO_2$ and some tenths of ps in Al_2O_3, see figure 2.19) and trapping after 150 fs for $\alpha - SiO_2$ like materials. Since this manuscript focuses on excitation processes, the refractive index n will be estimated from the Drude model (see 2.25), thus involving the excitation density N. Finally, phase shift is calculated from equation 2.41 and the result is plotted in figure 2.26.

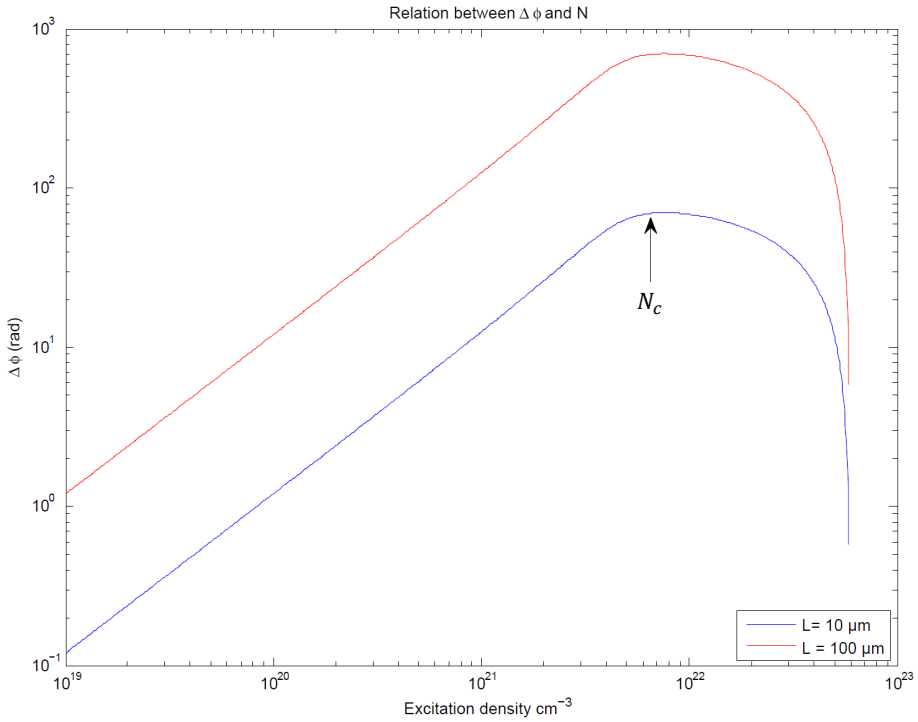

Figure 2.26: Illustration of the phase shift dependence on excitation density. Delay between pump and probe considered is of 50 fs (no trapping occurs). Simulation parameters are : ω_c=1 fs^{-1},λ_{probe} = 800nm, m^* = m_0 and n_0 = 1.54 ($S\alpha - iO_2$).Two probed lengths are plotted : 10 μm and 100 μm. No other contribution to the phase shift has been taken into account (moderate densities assumption).

The two plots represent two different probed lengths. One should bear in mind that knowing L is crucial to be able to estimate excitation density N. Lastly, the

assumption of a homogeneously excited medium gives a good qualitative approach but fails to give a spatial distribution of the excited carriers corresponding to reality. We can see from the plot that the phase shift increases linearly with the excitation density until $N \geq N_c$. Indeed, F.Quéré has shown [71] that for $N \ll N_c$ and $N \ll N_v$ $\Delta\phi$ becomes :

$$\Delta\phi = \frac{2\pi L}{\lambda_{probe}} \frac{k}{2n_0} N \tag{2.43}$$

with

$$k = -\frac{e^2}{m^* \epsilon_0} \frac{1}{\omega_{probe}^2 + \omega_c^2} \tag{2.44}$$

After reaching the characteristic density N_c, we see a change in this linear behaviour with a rapid drop to zero when the VB is completely depleted ($N = N_0$). The validity of the model at these densities is somewhat questionable based on the fact that a complete depletion of the VB may not be possible.

Of course the same type of calculation can be performed to estimate the phase shift relation with the density of trapped carriers N_{trap}.

2.5 Experimental results

In the following section, we will present our experimental results, over the three years, obtained using FDI technique. In the beginning, the long electron lifetime materials will be distinguished from the short lifetime ones. As we are going to see, this separation is the outcome of different processes being possible or not in terms of excitation or relaxation. Our experiments were mainly motivated by the study of the impact ionization mechanism often evoked in the literature but rarely given any direct experimental proof (mostly in experiments with electron beams and harsh radiation). As we have seen in the introduction of this chapter, when we approach the damage threshold, excitation density deviates from the power law corresponding to multiphoton excitation, for a number of reasons developed in 2.1. The main idea is to use a double pump pulse configuration to favour impact ionization (2.3.2). If such a mechanism is involved in the interaction then we should be able to observe the multiplication of the total number of electrons in the CB, thus contributing to higher negative phase shift. Hence the phase shift measured will be, in that case, greater than the sum of the phase shifts measured with a single pump alone.

The results on Al_2O_3 and MgO will be presented first, accounting for the long electron lifetime, and then $\alpha - SiO_2$,NaCl,KBr will follow in the second subsection. In both cases, we have been interested in probing the different excitation and relaxation mechanisms.Precision will be given at each plot on whether perpendicular or collinear geometry has been used, this being a function of the sample geometry (cubic or wafer) and the different experimental drawbacks related. Finally, the double pump scheme, coupled to our imaging system, has been used to determine damage thresholds under particular conditions.

2.5.1 Choice of irradiation parameters

Before presenting our results we would like to discuss the procedure of choosing the irradiation parameters for our experiments and more in particular the energies for the double pulse experiments. First, we have measured the IR energy for a CDTH(UV-IR combination) and this for different UV energies, at fixed delay between them. This actually means that for a given UV energy and delay between UV-IR, the damaging probability was monitored (imaging with a CCD camera) from shot to shot (single shot measurements, spatially translated one from another) for variable IR energy. These results are presented in figure 2.27. The delays chosen for Al_2O_3 (936 fs)and MgO (1.5 ps) correspond to a situation where the IR pulse "sees" an already pre-excited electron density in the CB by the UV pulse. In $\alpha - SiO_2$ the delay of 1.75 ps is synonym of carriers having already been trapped when the IR pulse arrives. On the left and the right part of the curves we can

observe the formation of plateaus that correspond to the SDTH with each pulse alone : left is for IR alone and right stands for UV alone. The results on Al_2O_3 and MgO show clearly that at 70% of the SDTH with UV, a large energy window is available for IR starting from the SDTH with IR alone up to the UV's SDTH. Thus, fixing UV pulse's energy at 70% of the SDTH seems to be ideal in order to probe the pump-probe effect (UV and IR pump pulse) out of the situation where the damage is produced with each pulse alone.

The result with $\alpha - SiO_2$ has been measured with a long delay and this is the reason why at 70% of the UV SDTH we find a shift on the left, versus the plateau values. However, we can expect a translation to the left of our data points for a shorter delay (corresponding to the IR pulse "seeing" the free carriers). This can be explained by the fact of having different power dependencies of the intensity for the different cases, 2 or 3 photon re-excitation of trapped carriers and subsequent photon absorption or direct linear absorption of the already present electrons in the CB.

In what follows, UV energy has been fixed at 70 % of its SDTH and the damage threshold CDTH was identified as the IR fluence in the presence of both pump pulses (UV and IR) at fixed delay between them.

2.5.2 Long electron lifetime materials

Our choice to start our experiments on Al_2O_3-like crystals was made upon electron lifetime criteria. More in particular, the large time interval during which the electrons are present in the CB allowed us to think that it is going to be easier to heat these carriers and thus launch a collisional ionization mechanism. Figure 2.19b shows a typical (in the range of 20%-200% of SDTH) pump and probe scan. The information to extract from this plot is that the phase shift remains negative for a long time (several ps) before it starts decreasing towards zero (2.20). Of course negative phase shift stands for "free" electron density (see section 2.4.1) and it is why the mentioned material is characterized by a long electron lifetime. This particularity in the optical behaviour is common among Al_2O_3 and MgO with lifetimes more or less long (shorter for MgO) depending on the intensity of the pump pulse.

Electronic excitation mechanisms

In this part, our main focus is on the first excitation stage and towards the end in the relaxation processes. We have previously seen that the short time scale (50 fs) of the different excitation processes required the use of a double pump scheme (see 2.3.2). Indeed, the idea is to create all these favourable conditions for the impact ionization to take place, if it is part of the mechanisms involved in the

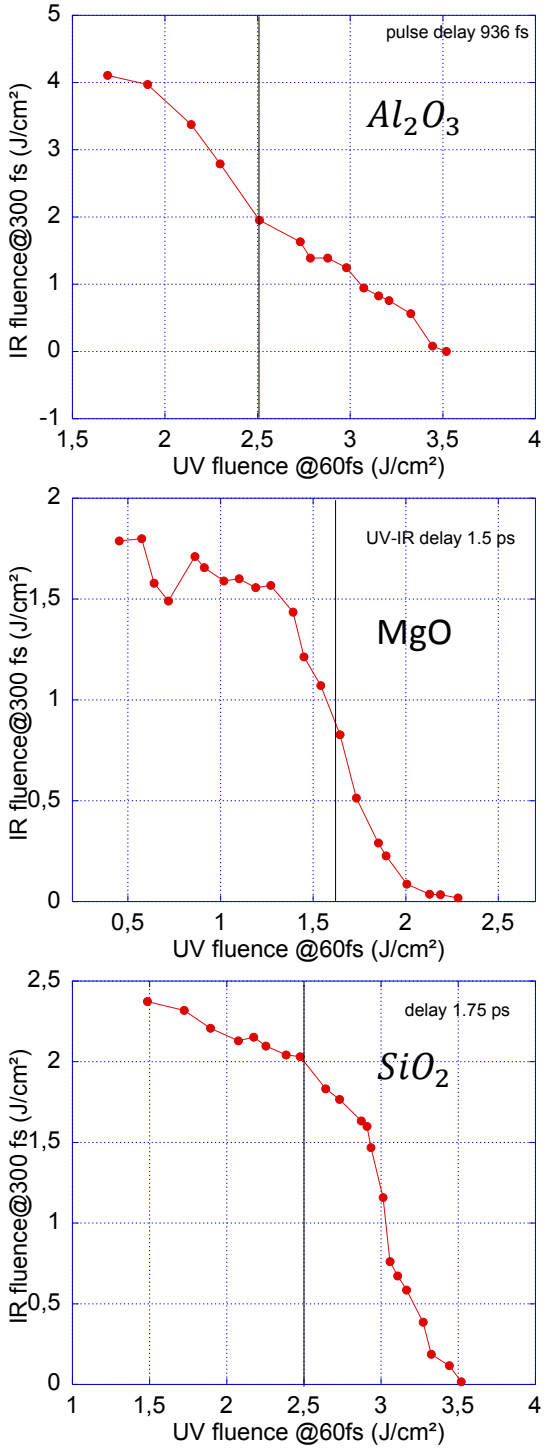

Figure 2.27: Fluence at DTH for a sequence of a IR pulse (300 fs duration) and a UV (60 fs duration) fluence, at fixed delay between them (UV pulse first). Three different materials are represented : Al_2O_3, MgO and $\alpha - SiO_2$. A vertical line is plotted at 70% of the SDTH with the UV pulse alone.

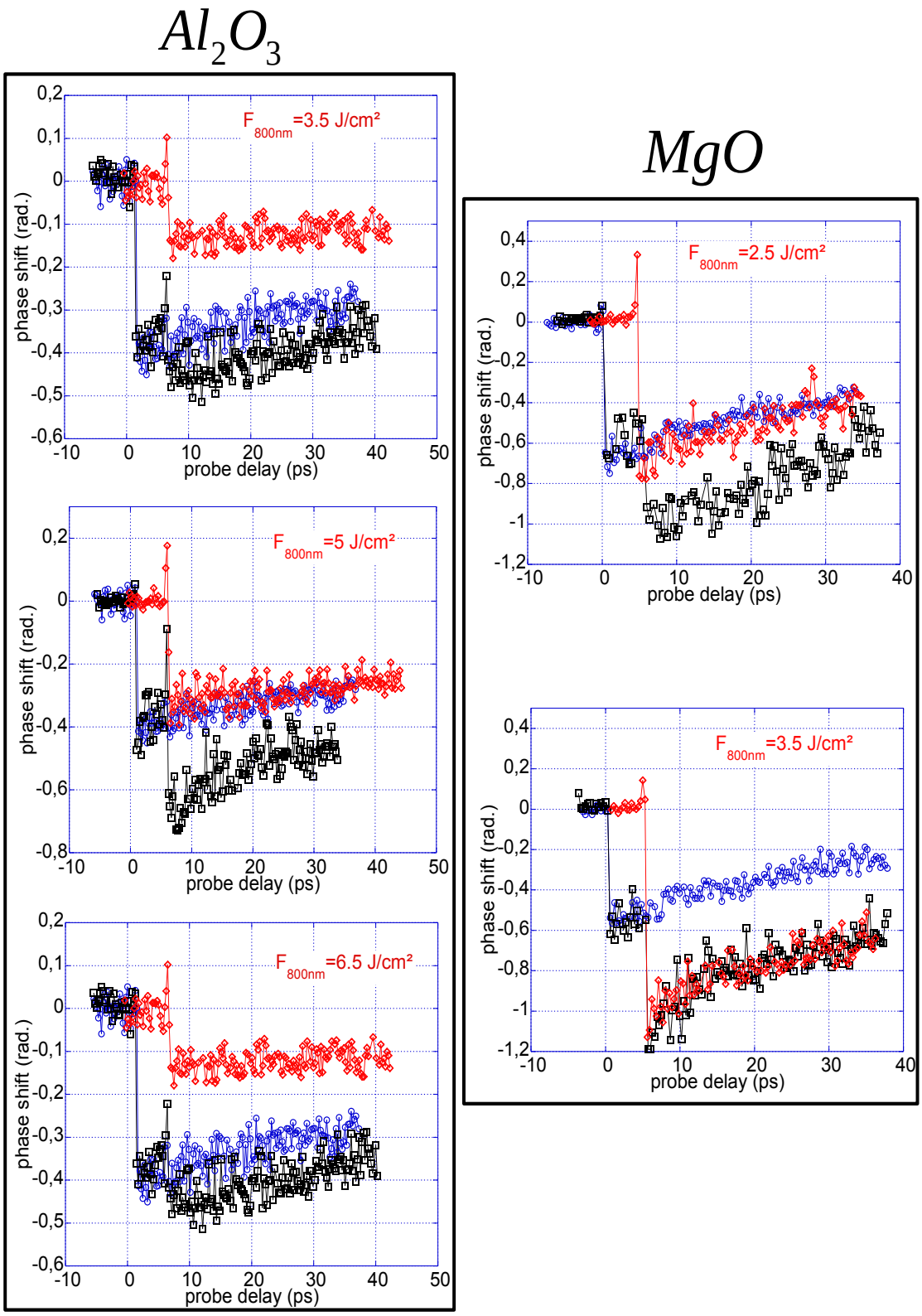

Figure 2.28: Phase shift in a double pump pulse scheme as a function of pump-probe delay measured for different IR fluencies in two different crystals. Phase shift for 400 nm alone is in blue circles, for 800 nm in red squares and for both beams together (7 ps interval, UV first) in black diamonds. On the left, the results for Al_2O_3 and on the right for MgO. UV (50 fs duration) fluence is : 2 J/cm^2 for Al_2O_3 and 1.3 J/cm^2 for MgO. IR (50 fs duration) fluence is increased from top to bottom. CDTH is 5 J/cm^2 for Al_2O_3 and 3.5 J/cm^2 for MgO.

excitation. In solids such as Al_2O_3 this is relatively easy to achieve because of the long electron lifetime. In more detail, a rather large (tens of ps following the carrier generation, see negative phase shift in figure 2.20) time window is made available for the second pump pulse to be sent, before recombination decreases the total number of "free" carriers.

In the first set of measurements, both pump pulses are short (50 fs) and separated by 5 ps. The UV energy is kept at 70% of the SDTH. The IR pulse energy is set after defining the CDTH for the given UV energy at a fixed delay. At first, a scan is performed with the UV and the IR pumps alone and then the signal with the sequence of the two pulses is measured. The results in both Al_2O_3 and MgO are plotted in figure 2.28. Different IR energies have been tested, below and above the CDTH.

No multiplication has been observed either in Al_2O_3 or in MgO. It is clear, by looking at figure 2.28 that the UV-IR combined signal is never greater than the sum of the individual signals alone. In fact, it appears to be less and less than the sum as the IR energy grows bigger. This can be due to the IR pump being partially reflected by the plasma created by the UV pulse and/or the depletion of the IR pump pulse due to nonlinear absorption by electrons present in the CB.

In an effort to further favour impact ionization, the IR pump has been stretched in time. Indeed, our thought was that if we give a longer time interval to the "free" electrons to interact with the laser pulse the probability to heat them will be higher. Rethfeld's simulations using multiple rate equations suggested that longer pulses at higher intensities have a bigger probability to initiate impact ionization [76]. Qualitatively, this means that for shorter pulses linear absorption is less probable because of the relatively high intensity (10 TW/cm^2) favouring higher order phenomena (multiphoton absorption). Thus in our case, we want the IR pulse to be "spent" to the transitions inside the band gap.

The new pulse duration of the IR pump is 10 ps. Once again, UV fluence is kept below SDTH and IR fluence above CDTH and below SDTH. The phase shift is measured once again in an attempt to observe multiplication of the number of electrons in the CB. The result is plotted in figure 2.29. On the left part of the figure, IR energy is 13 μJ and there is no change in the signal when the two pulses are combined. On the right part, IR energy is ten times higher (130 μJ). No increase in the signal is observed, but the recombination kinetics are now modified. Indeed, when we send the IR pulse after the UV pulse, electrons seem to recombine faster. At first glance, a recombination with holes may be considered and thus suggesting second order recombination kinetics.

The rate at which electrons recombine with holes depends on their respective density and it can be written :

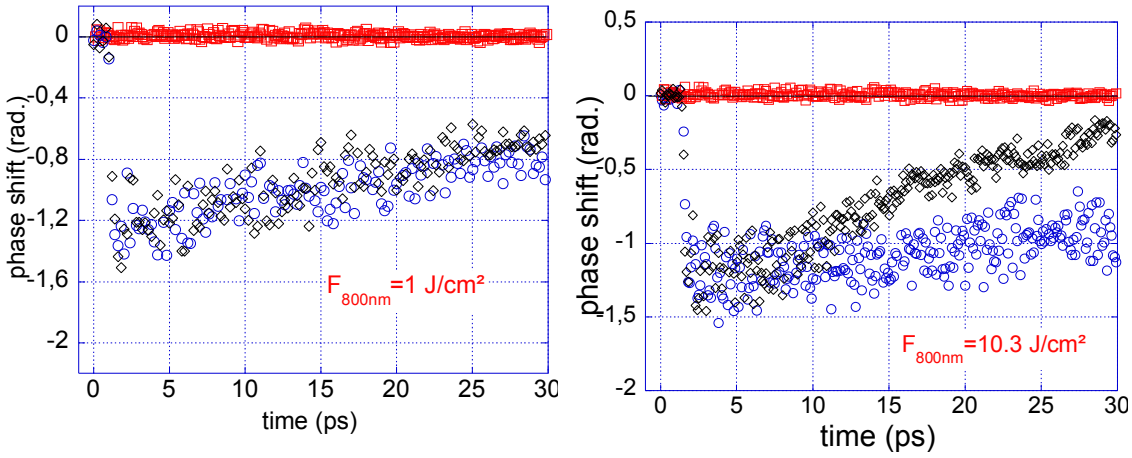

(a) (b)

Figure 2.29: Phase shift in a double pump pulse scheme as a function of pump-probe delay, for two different IR (10 ps duration) fluencies measured in Al_2O_3. Phase shift for 400 nm alone is in blue circles, for 800 nm in red squares and for both beams together (5 ps interval, UV first) in black diamonds. UV (50 fs duration) fluence is 2 J/cm^2.

$$\frac{dN_e}{dt} = -\sigma v N_e N_h \tag{2.45}$$

with N_e the excitation density, v the electron velocity, σ the cross section and N_h the density of holes. It results in :

$$N_e(t) = \frac{N_0}{1 + \sigma v N_0 t} \tag{2.46}$$

Using this equation, a fitting is applied on the experimental results in figure 2.29b and it is presented in figure 2.30 . Accounting for the faster recombination in the case of two pump pulses, one has to multiply the electron velocity by a factor of ten. In conclusion, the IR pulse is absorbed by electrons in the CB, depositing energy (in the form of kinetic energy) in the solid. Although, electrons do acquire more energy in the CB, no impact ionization mechanism is triggered in Al_2O_3.

The phase shift has been measured in similar conditions in MgO (see figure 2.31).

The IR pump pulse is 1 ps long and the delay between the pump pulses is 15 ps. Once again, with the sequence of the two pulses the DTH is reached, while we are under the SDTH for UV and at the SDTH for IR (no damage is observed). The signal with the UV beam alone can be observed in the range 1-15 ps (black

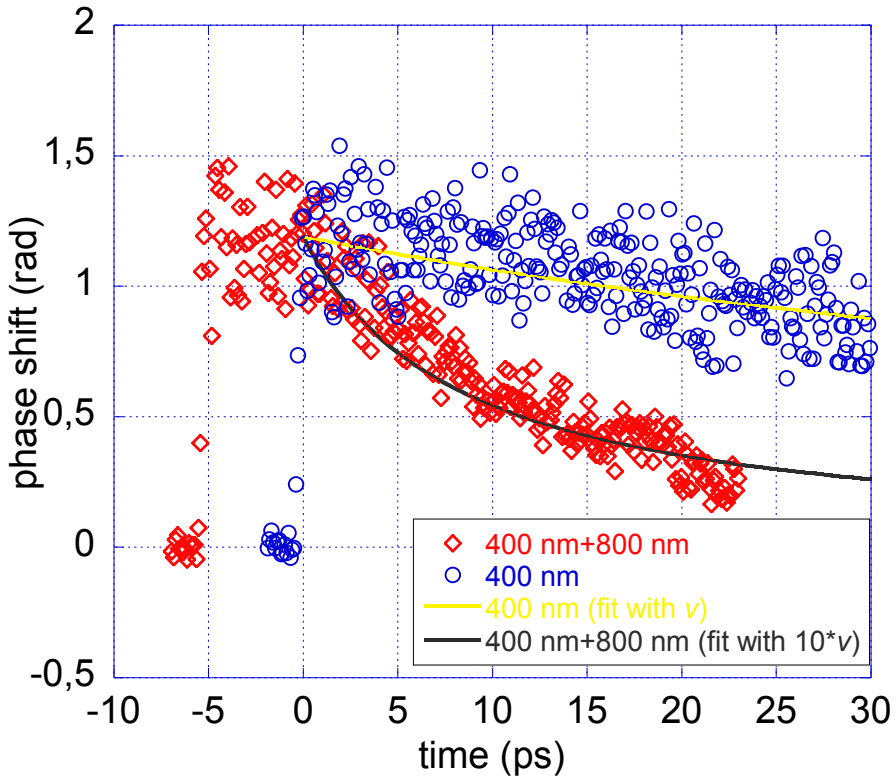

Figure 2.30: Fitting the experimental results from figure 2.29 using a quadratic recombination model (equation 2.46). Fitting the 400 nm + 800 nm signal requires multiplying the electron velocity v by ten.

curve) where no IR is yet present. Then the IR pump hits the sample, raising the total negative signal by an amount equal to the signal produced by the IR pump alone (red curve). Thus, no multiplication is observed where it is supposed to happen. Impact ionization is once again not part of the interaction, suggesting similar processes as in Al_2O_3. Unfortunately, the scan was not long enough to observe the recombination kinetics. Note has been taken and it is part of the experiments to come in the future.

Until now, we have seen how the phase shift is evolving at delays of the order of 30 ps following the pump pulse arrival on the surface. The modifications made during this thesis (see 2.3.2) allowed probing longer delays. For the first time, we could observe the relaxation processes, lasting until almost one nanosecond, in long electron lifetime materials by measurement of the phase shift. Double pump scans have been performed in Al_2O_3 in both co-linear configuration and perpendicular one (see figure 2.32). In the first case (top row), the IR pump is

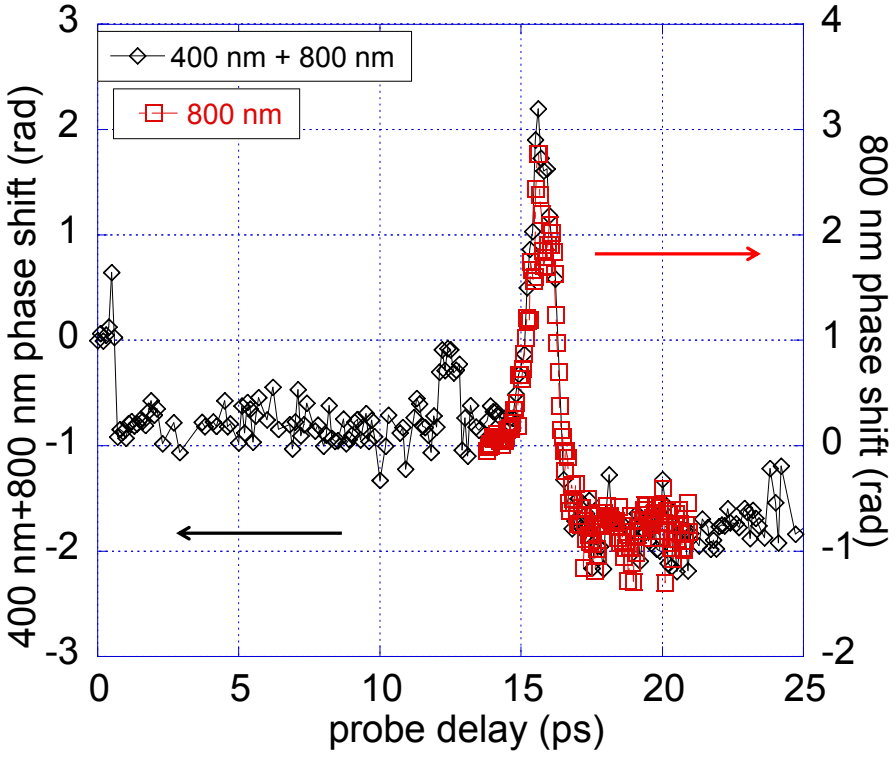

Figure 2.31: Phase shift in a double pump scheme as a function of the pump-probe delay measured in MgO. Fluencies are 0.71 J/cm^2 for UV (50 fs pulse duration) and 5.72 J/cm^2 for IR (1 ps pulse duration). Pulse delay is 15 ps, UV arriving first.

one ps long and it arrives two ps after the UV pump resulting in damage of the target, although fluencies are kept under the SDTH with each individual pump pulse. By comparing the signal with the UV pump alone and the sequence of the two pump pulses, we may deduce two things. First, the recombination is much faster as previously mentioned. The second deduction concerns the positive phase shift signal met at the end (after 100 ps delay). Let us here mention that the modulation of the signal, black curve (top left plot in figure 2.32) is most probably due to an air-conditioning fault. The oscillations of the temperature, related to the air-conditioning functioning, follow the oscillations of the signal.Nevertheless, it is possible to estimate an average positive phase shift that is well above zero.

Theoretically, the carriers in Al_2O_3 are supposed to recombine, after some time, thus bringing the phase shift signal back to zero. Positive phase shift, can be either attributed to temperature (not impossible but of lower impact, see 2.4.1) and/or trapped carriers (see 2.4.1).Radiation induced defects are not known in materials

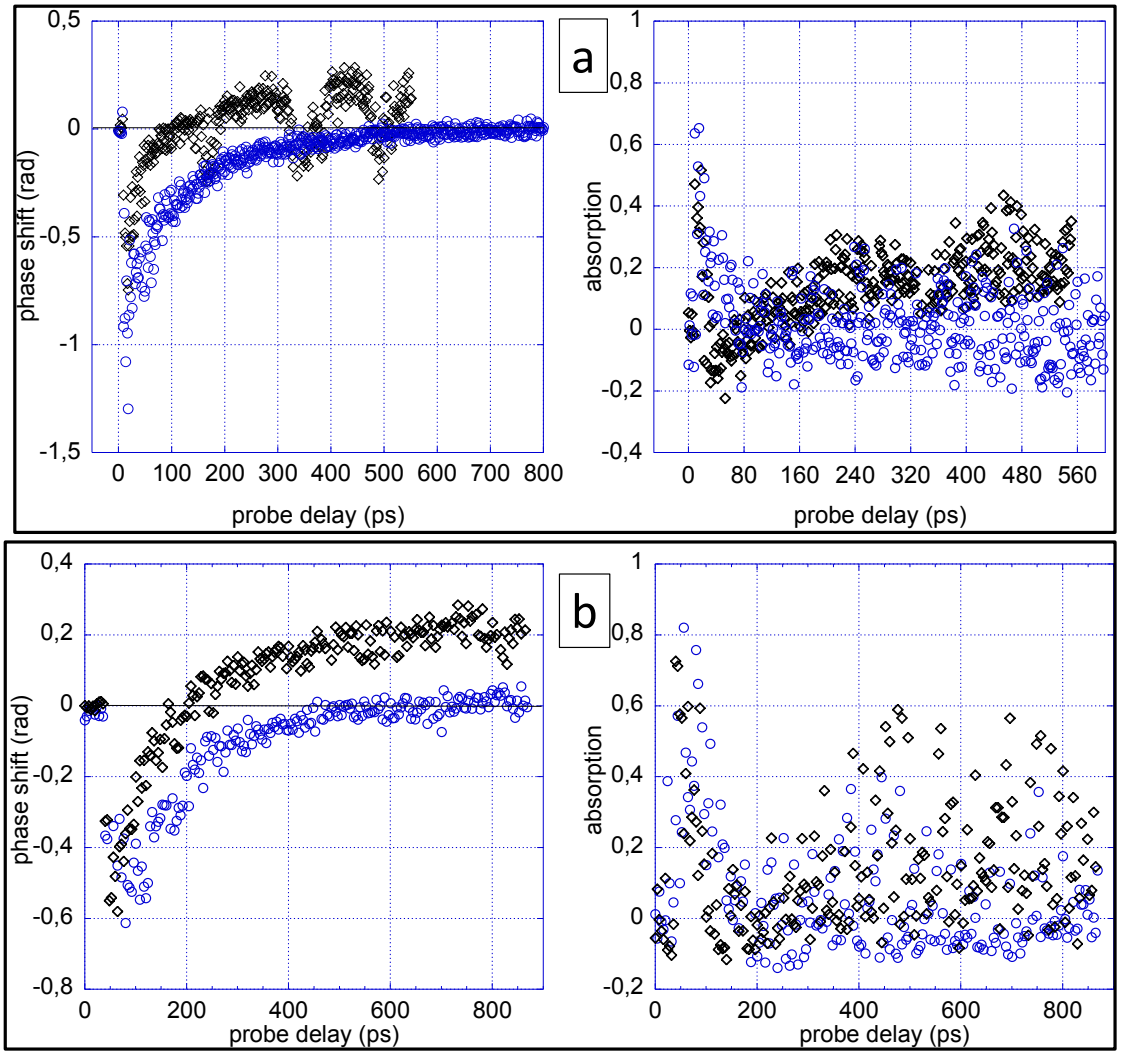

Figure 2.32: Phase shift and probe absorption in a double pulse scheme as a function of the pump-probe delay in Al_2O_3. Signal for 400 nm pulse (50 fs duration) alone is in blue circles, for 800 nm in red squares and for both beams together (UV first) in black diamonds. (a): Fluencies are 1.3 J/cm^2 for UV and 4.14 J/cm^2 for IR (1 ps duration). UV-IR delay is 2 ps. Pump-probe geometry is co-linear.(b): Fluencies are 1.85 J/cm^2 for UV and 7 J/cm^2 for IR (2 ps duration). UV-IR delay is 3 ps. Pump-probe geometry is perpendicular.

such as Al_2O_3 although they are present in other materials ($\alpha - SiO_2$,NaCl etc.). Looking at the probe absorption figure on the right of the first row we can see a rise in the absorption with the two pulses combined (above DTH) while no absorption was observed with the UV pulse alone (delays over 160 ps). The absorption feature

is observed for positive phase shifts. This could be a sign of defect states capable of absorbing probe photons thus contributing to the signal.

The same type of experiment has been carried out in perpendicular configuration (bottom row, figure 2.32). This time, the IR pump is 2 ps long and it follows the UV pump 3 ps later. One again, DTH is reached only with the presence of both pump beams. The results show identical behaviour as for the presence of a positive phase shift and the corresponding lift in absorption.

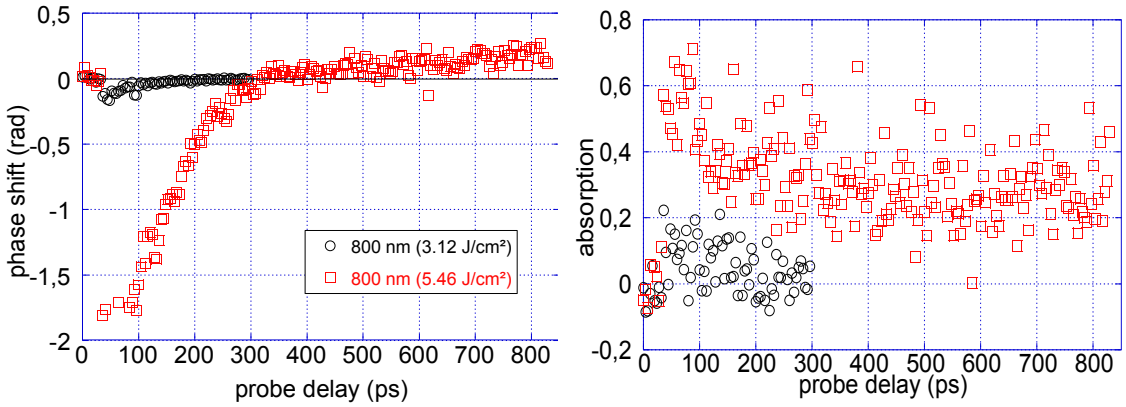

(a) Phase shift measurement.

(b) Absorption measurement.

Figure 2.33: Phase shift and probe absorption measurement, in same experimental conditions, in MgO with a single IR pump pulse (1 ps duration) as a function of the pump-probe delay.

A single pump scan earlier performed in MgO comes in support of the hypothesis of defect existence in these media. Figure 2.33 shows the phase shift and absorption measurements (left and right respectively) with an one ps IR pump at long time delays. Two fluencies have been tested, one at DTH ($F_{800\text{nm}} = 5.46$ J/cm^2) and one at 50% of it ($F_{800\text{nm}} = 3.12$ J/cm^2). Similarly with the results on Al_2O_3, the positive phase shift is present above DTH and it is related to the presence of a relatively long pulse (IR pulse duration is one ps). Also, while absorption comes back to zero when energy is below the DTH, it stays above zero (around 20%) when energy is at DTH and there is a positive phase shift. Thus, we can attribute this positive phase shift to the presence of defects, as in Al_2O_3.

The defect formation may result from either large excitation densities when the threshold is reached. However, such an effect has not been observed (no carrier multiplication) and thus an explanation could be given considering thermally activated defects.

It should be noted that almost no polarization dependence has been observed. When the pump pulses arrive perpendicularly to the sample little or no difference

at all is expected with polarizations in the plane of the surface of the sample. There might be an effect when polarization between UV and IR are perpendicular and this while pulses overlap in time[6], but the temporal resolution of this experiment didn't allow observation of such a phenomenon.

2.5.3 Short electron lifetime materials

In this subsection, we will present the results obtained in materials such as $\alpha - SiO_2$, NaCl and KBr. In these crystals, the lifetime of electrons is shortened due to trapping. More in particular, the electron trapping time corresponds to the rise time of STE's thus relating the latter with the trapping process. Ionizing radiations are responsible for the STE production and are often related to structural modifications. Strong electron-phonon coupling is also associated with formation of such defects. Typically, the lifetime of electrons in the CB for $\alpha - SiO_2$ is equal to 150 fs, while in NaCl this value may vary upon laser intensity. Most of the experiments have focused on $\alpha - SiO_2$ due to extensive studies in literature and thus the solid background acquired. Moreover, this crystal presents great interest, being involved in many applications.

Unlike long electron-lifetime material, we initially expected impact ionization mechanism to be less favourable in these crystals. The reason is that electrons do not remain in the CB for a long time and the choice of pulse duration and pulse delay become critical.

Electronic excitation mechanisms

Pretty much as before, in this first part we have searched to probe the excitation stage in the double pump scheme. Figure 2.34 represents the phase shift and probe absorption measurements in $\alpha - SiO_2$ with a 60 fs UV pump followed -400 fs later-by an IR pump with duration 350 fs. Radiation conditions are kept the same as for Al_2O_3, setting the UV and IR energies below the DTH for each pulse alone. Three different situations are investigated : below, at and above CDTH (from top to bottom respectively in figure 2.34).

In this configuration, a raise in the signal is observed. It is already visible on the first row in figure 2.34, if one focuses on the negative phase shift in the black curve (both pump beams present) and compares it to the blue curve (UV pump alone). This raise, and subsequently electron multiplication sign, is more and more pronounced when the energy of the IR pulse is raised, reaching above CDTH. Even when the IR pump excites some "free" electrons by itself ($F_{800nm} = 5.76$ J/cm^2) the negative phase shift of the black curve is still greater than the sum of the

[6]In principle, polarization dependence could be observed even later due to variation of electron mobility in different directions, but this has not been observed in our case.

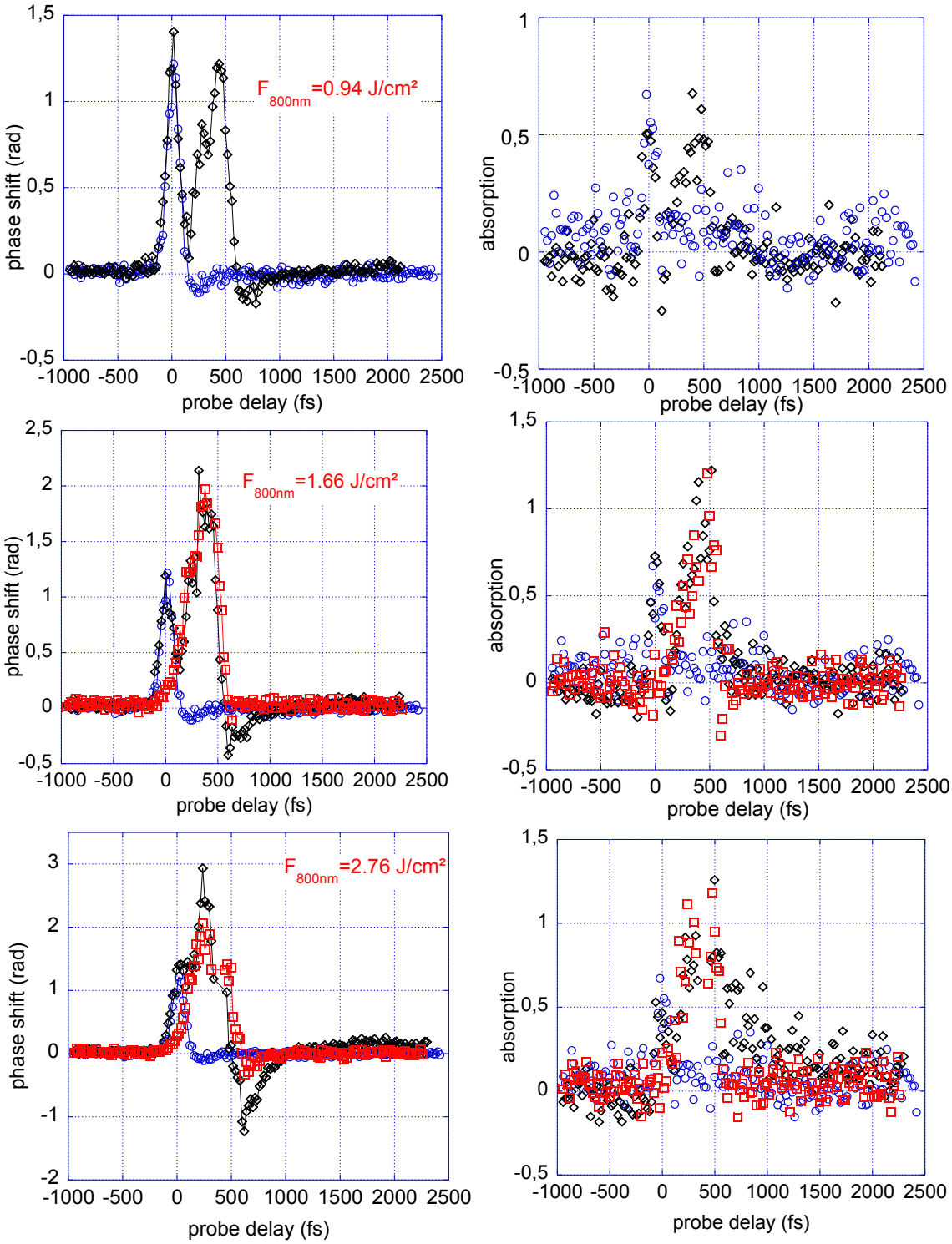

Figure 2.34: Double pump phase shift (and the corresponding probe absorption) measurement in $\alpha - SiO_2$ as a function of the pump-probe delay, for different IR (350 fs duration) fluencies. Signal for 400 nm pulse alone is in blue circles, for 800 nm in red squares and for both beams together (400 fs delay, UV first) in black diamonds. UV (50 fs duration) fluence is 0.7 J/cm^2. CDTH fluence is 1.66 J/cm^2.

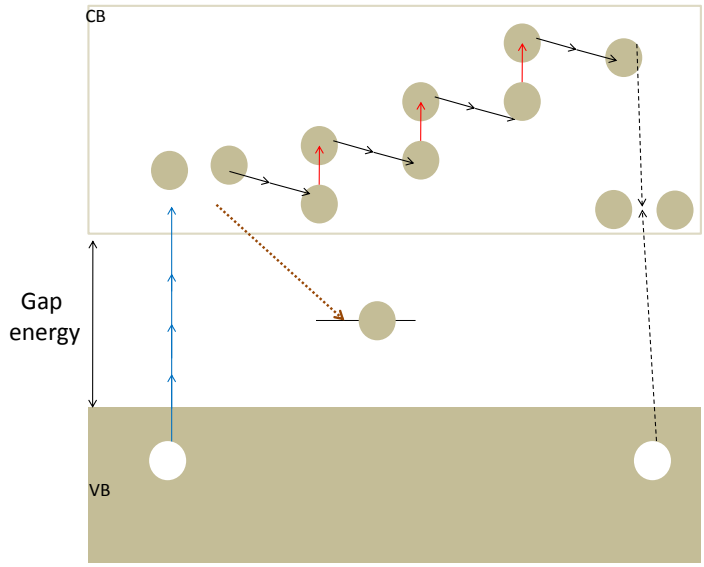

Figure 2.35: Illustration of the competition between trapping and heating processes in $\alpha - SiO_2$. Initially, electrons are promoted in the CB by multiphoton absorption. Then, these carriers are trapped by STE's within 300 fs.

individual negative phase shifts obtained with each pump separately. In parallel, both the phase shift that is following (accounting for trapped carriers that are proportional to the density of "free" carriers) and the absorption are at higher levels than for the UV beam alone. This is indeed the first proof that electron multiplication by impact ionization is possible in $\alpha - SiO_2$ at some extent. At first glance,one can tell that the fraction of impact ionized electrons is rather low when the energy is kept below threshold.

As to the IR pulse duration, this is chosen to be the most adequate to involve all the electrons present in the CB to the heating process. Indeed, 300 fs correspond more or less to the time window when "free" electrons are present in the CB and "ready" to heat up. Other IR pulse durations, along with the UV short pulse, may result in impact ionization taking place but this will be of lower magnitude. The reason is that the carrier heating is in competition with the carrier trapping (see figure 2.35). Longer pulses would be partially spent in interaction with the already trapped carriers, lowering the chances to observe impact ionization.

In an attempt to generalize observations in $\alpha - SiO_2$, we have tested a second crystal with similar behaviour (STE creation) and try to understand whether impact ionization is only efficient in materials with strong electron-phonon coupling where self-trapping occurs. NaCl is a good example, with electrons remaining "free" for almost one ps before relaxing in STE's. Figure 2.36 illustrates the scan

made in NaCl. The phase shift measurement along with the probe absorption, in the same irradiation conditions (below, at and above CDTH) are plotted. The UV-IR pump delay is 500 fs this time.

Once more, the conclusions are the same. The phase shift grows more and more negative (twice as much) with the train of the two pulses, while there is a tremendous raise in the positive phase shift (almost ten times more than for UV alone) and in the absorption, both related to the excitation density. A longer IR pulse may be used for a more important fraction of impact-ionized electrons to be generated, taking into account the longer lifetime of electrons in the crystal.

Lastly, a third available crystal was KBr, belonging to the same group of materials. The lifetime of electrons in this case is of longer than in SiO_2, as in NaCl, and it is of the order of 800 fs. This time, the UV (50 fs) energy is around the SDTH while the IR (500 fs) energy is below SDTH. As before, when the two pump pulses are combined in a "train" separated by 1.3 ps, the CDTH is reached.

The negative phase shift corresponding to the black curve in figure 2.37a is raised by 25% compared to the signal of the UV beam alone (blue line). However, no raise is observable in the positive phase shift or in the absorption.

Co-linear configuration presents a drawback that is due to the large probed length, accumulating the signal over different depths of the sample. It is known that, for a focusing on the surface of the sample, the excitation density drops abruptly within few hundreds of nm. Thus, probing different depths behind the surface results in probing different excitation density profiles where different mechanisms may be responsible for the excitation. In an attempt to clarify this point, we decided to reduced the probed depth. We have measured the phase shift with a double pump in the same irradiation conditions as the ones used to obtain the experimental results in figure 2.34, but this time in the perpendicular geometry. The UV (50 fs) energy is at 70% of the SDTH while the IR (300 fs) is such that CDTH is reached on figure 2.38a and at 130% of this energy for figure 2.38b. This figure illustrates the certain raise in the phase shift (black line) both for the negative part and the residual positive phase shift that follows. Thus, special care has been taken to give concrete information about the existence of the impact ionization mechanism in $\alpha - SiO_2$. In the case of perpendicular configuration, the positive phase shift due to the presence of a second IR pump may be three times bigger than with UV alone (see figure 2.38b), although no contribution from the IR pump alone has been observed.

Double pulse data presented so far are recorded with a fixed delay. It is of course extremely important to make a systematic study of the delay parameter between the two pulses to reveal any time dependence of the observed impact ionization. Previously, the delay has been chosen to be 400 fs so that the second pump pulse would "see" some "free" electrons without overlapping in time with

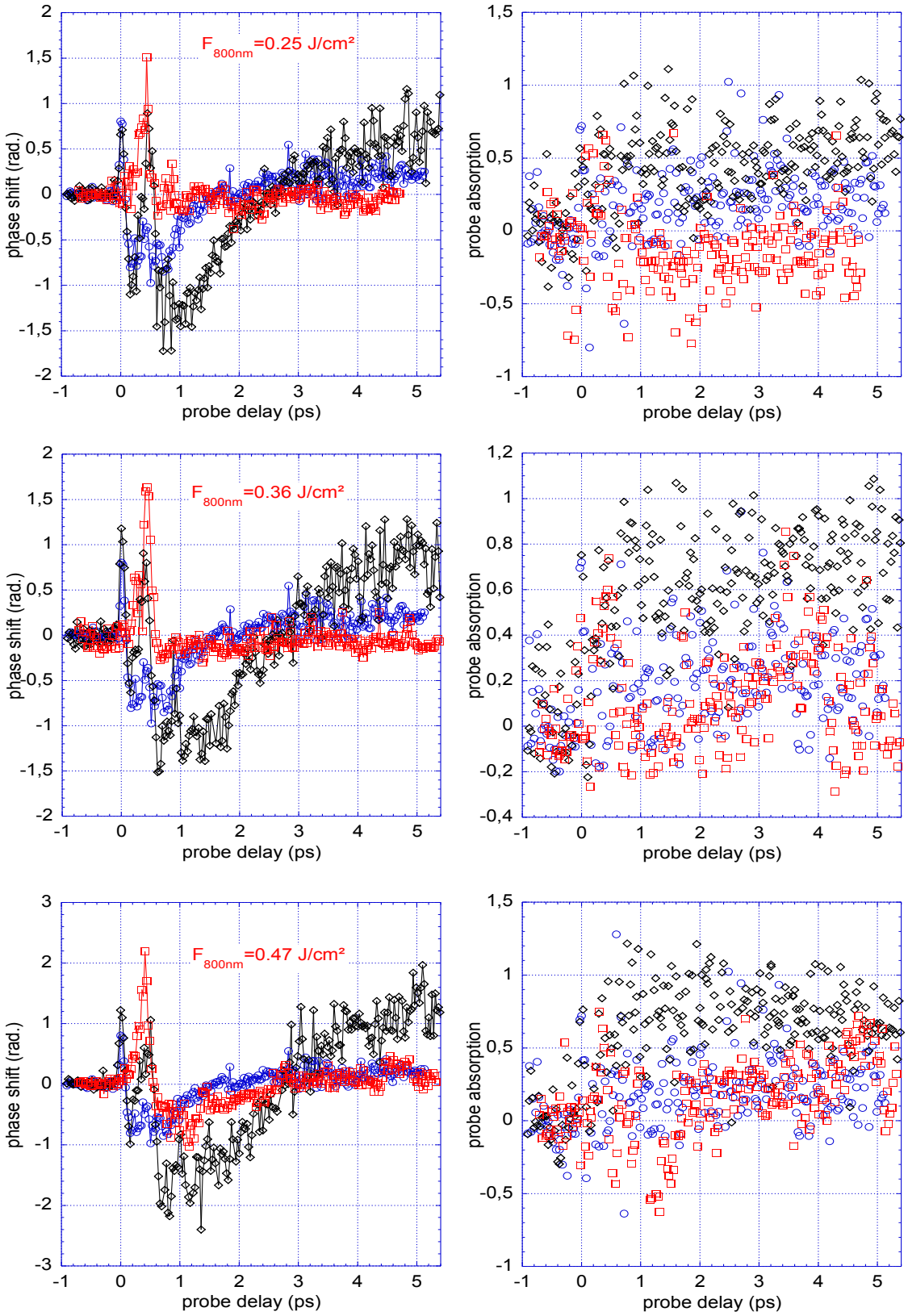

Figure 2.36: Double pump phase shift (and the corresponding probe absorption) measurement in NaCl as a function of the pump-probe delay, for different IR (300 fs duration) fluencies. Signal for 400 nm pulse alone is in blue circles, for 800 nm in red squares and for both beams together (500 fs delay, UV first) in black diamonds. UV (50 fs duration) fluence is 0.4 J/cm^2. CDTH fluence is 0.36 J/cm^2.

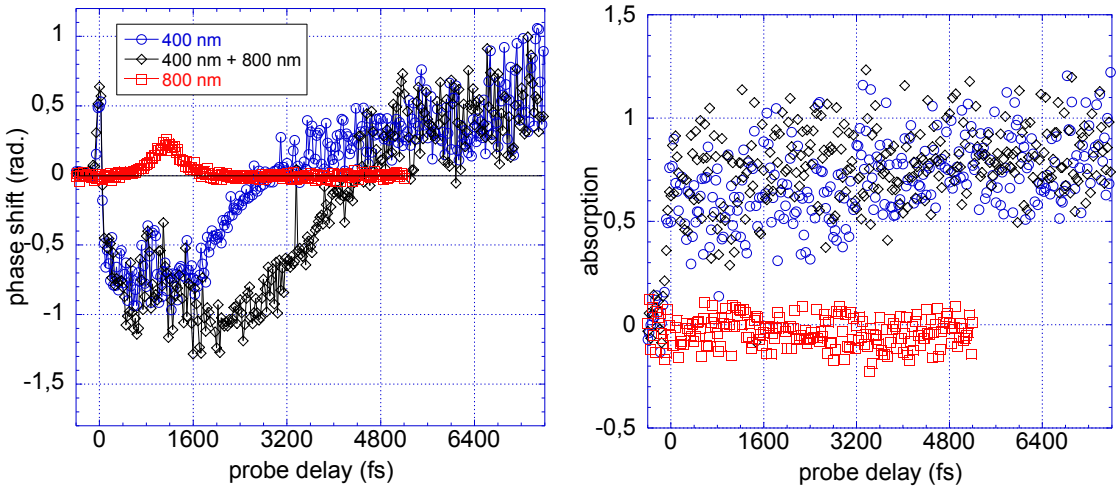

(a) Phase shift measurement.

(b) Absorption measurement.

Figure 2.37: Double pump phase shift (and the corresponding probe absorption) measurement in KBr as a function of the pump-probe delay. UV (50 fs duration) fluence is 0.12 J/cm^2 and IR (500 fs duration) is 0.32 J/cm^2. Delay is 1.3 ps (UV first).

the first UV pump pulse. In the quest of an optimum configuration, double pump-probe scans have been performed for a set of different delays. More in detail, we have started with a 350 fs IR pulse arriving 450 fs before the UV pump pulse (60 fs) and moved it forward until it arrived 600 fs later. Both phase shift and probe absorption were recorded and they are plotted on figures 2.39 and 2.40. UV and IR energies are kept below SDTH and damage happens only when both pulses are present.

We have plotted the phase shift, in the presence of the two pulses (same irradiation conditions as previously), measured for two probe delays: right after the IR pulse (corresponding to the excitation density) and 1 ps after the UV pulse (corresponding to the trapped carrier density). This measurement has been repeated for different UV-IR pump pulse delays. Both phase shifts are plotted because the negative phase shift right after the IR pulse is "partially" hidden by the Kerr effect (positive contribution to the phase shift), thus it is wiser to trust the phase shift measurements at longer delays behind the UV pulse. Figure 2.41 shows that when the IR pump arrives before the UV, no multiplication is observed (in fact the IR energy is not high enough to generate "free" electrons so there can be no effect with the UV pulse coming later when no electrons are present). The appearance of a negative phase shift is closely related to the time overlap between the two pump pulses and/or the IR pulse arriving right after the UV. Therefore, it reaches its

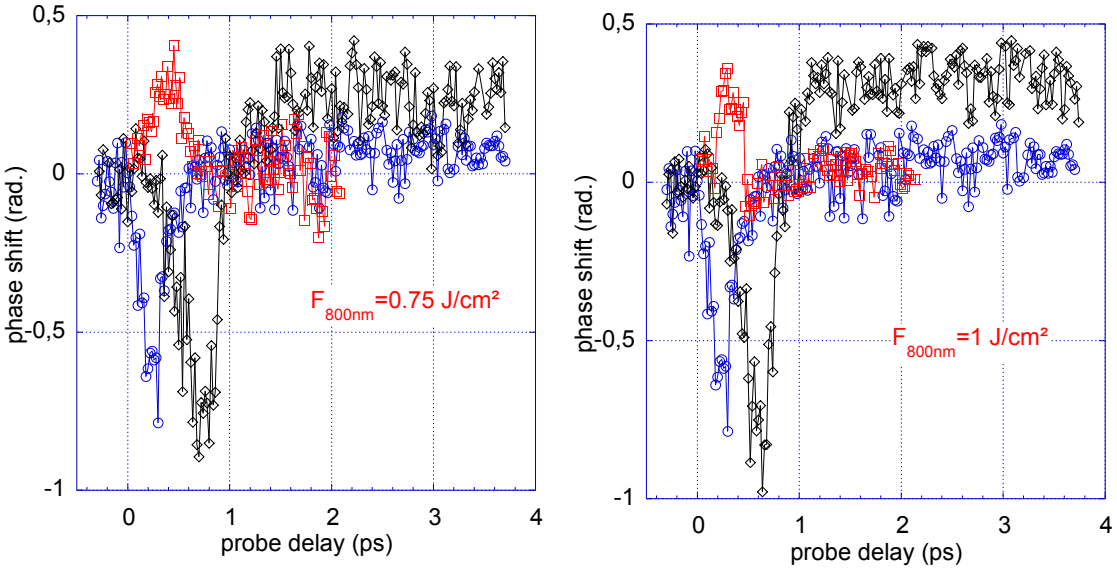

(a) (b)

Figure 2.38: Double pump phase shift measurement in $\alpha - SiO_2$ as a function of the pump-probe delay, for different IR fluencies. Signal for 400 nm pulse alone is in blue circles, for 800 nm in red squares and for both beams together (500 fs delay, UV first) in black diamonds. UV (50 fs duration) fluence is 0.35 J/cm^2 and IR (300 fs duration) is 0.32 J/cm^2.

maximum value when the IR pulse arrives 0-200 fs after the UV pulse (0 corresponding to temporal coincidence). This can be due to two processes : electrons generated by impact ionization and/or cross-excitation with photons from the UV and IR pulse participating in breaching the band gap. Outside this time overlap window, multiplication is still visible (delays greater than 150 fs) . Surprisingly, at 400 fs delay where none would expect an appearance of a negative phase shift (or at least not due to the impact ionization since at such time delay the IR doesn't come across any "free" electrons), there is one. Indeed, when the IR pump pulse arrives at a time delay when all electrons are trapped it is possible to re-excite those in the CB by absorption of two or three IR photons.

Pump scan

The previous series of measurements revealed that two different mechanisms may be responsible for the raise observed in the phase shift. Most importantly, an effort to distinguish cross-excitation from intraband heating followed by impact ionization has been made. We saw before (see figure 2.41) that the resolution of

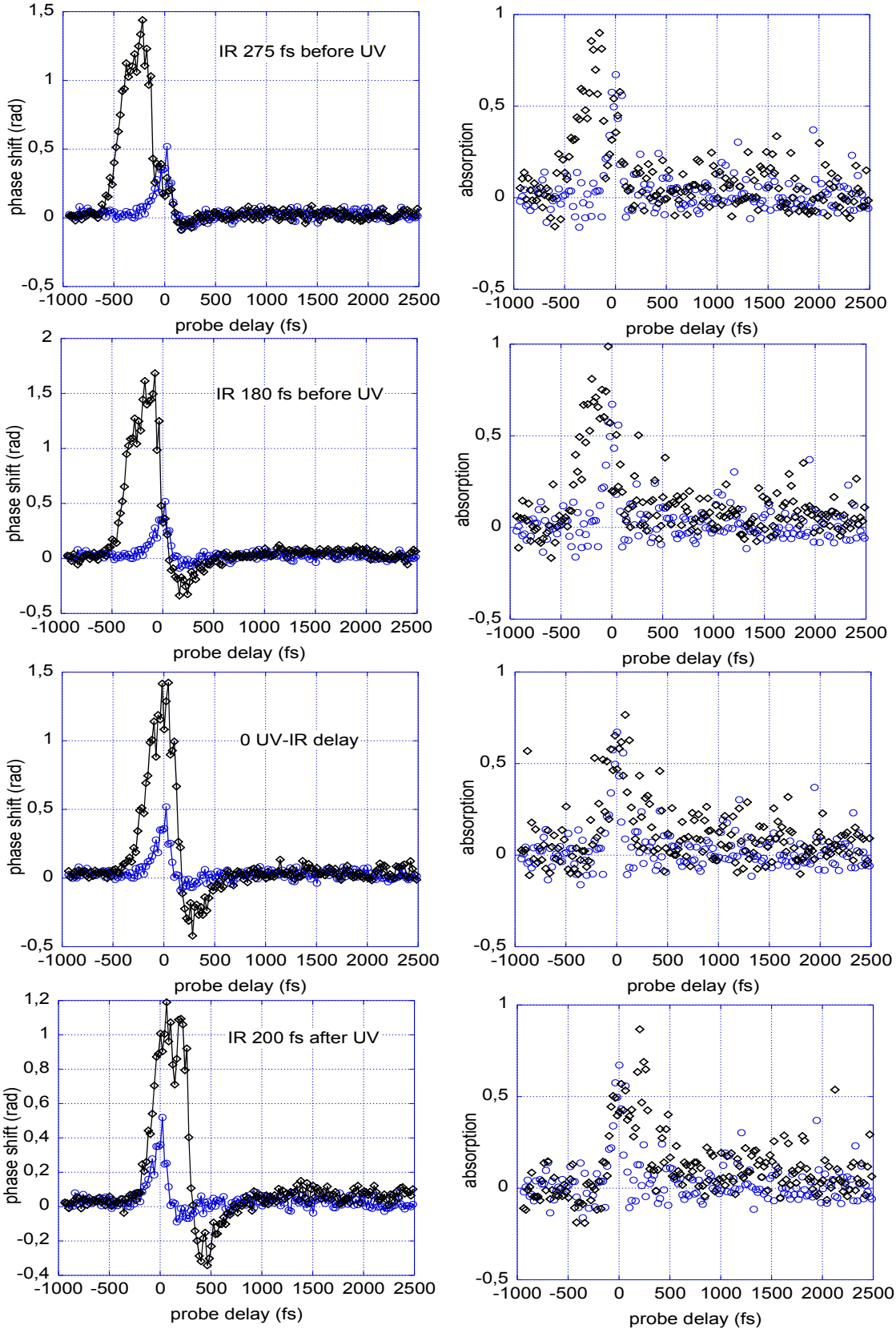

Figure 2.39: Double pump phase shift (and the corresponding probe absorption) measurement in $\alpha - SiO_2$ as a function of the pump-probe delay, for different UV-IR pump delays. Signal for 400 nm pulse alone is in blue circles and for both beams together in black diamonds. UV (50 fs duration) fluence is 0.4 J/cm^2 and IR (350 fs duration) is 1 J/cm^2. IR pulse is being delayed from top to bottom and here the the -275 fs to 200 fs delays are presented.

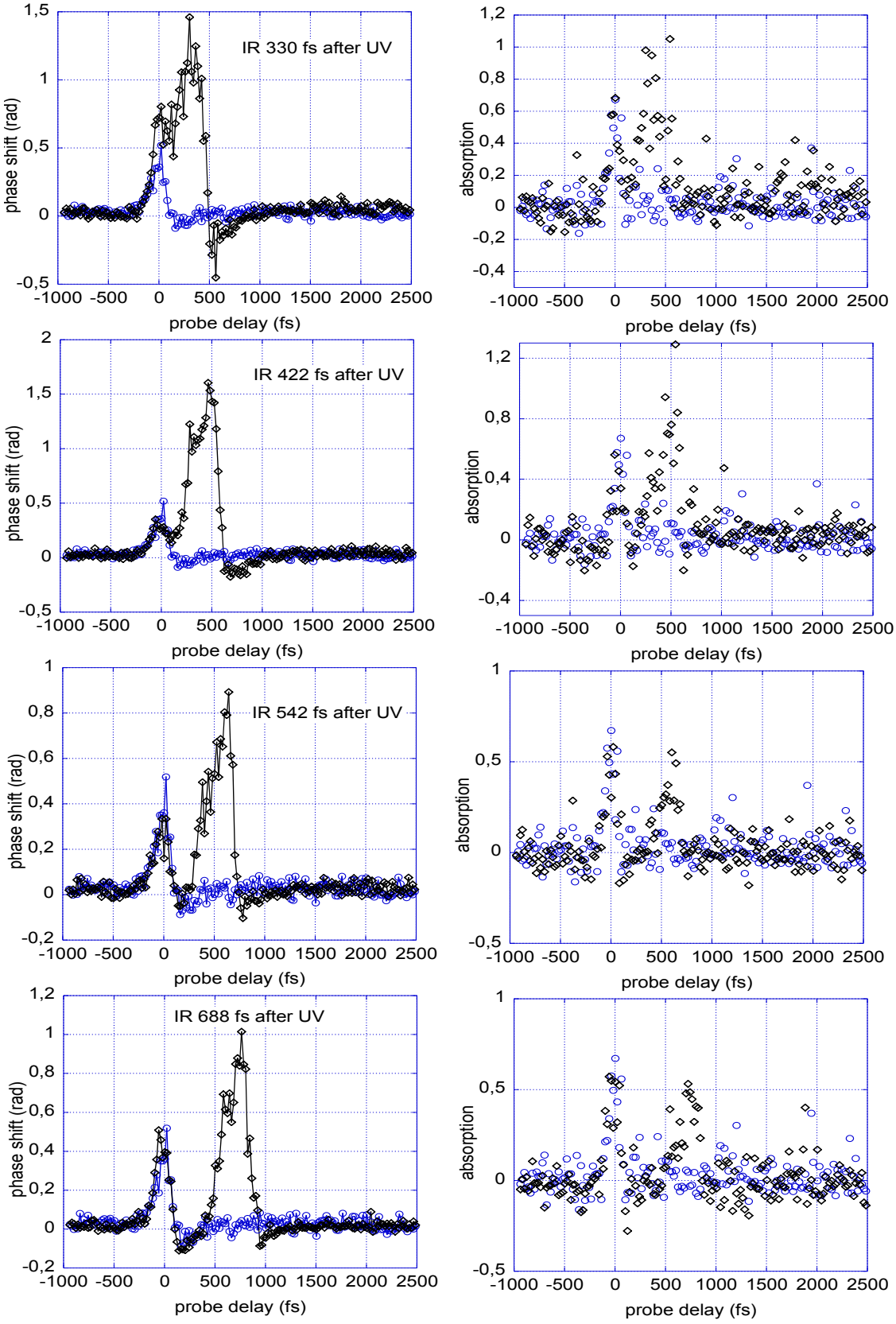

Figure 2.40: Longer UV-IR delays are being explored. Experimental parameters are the same as in 2.39

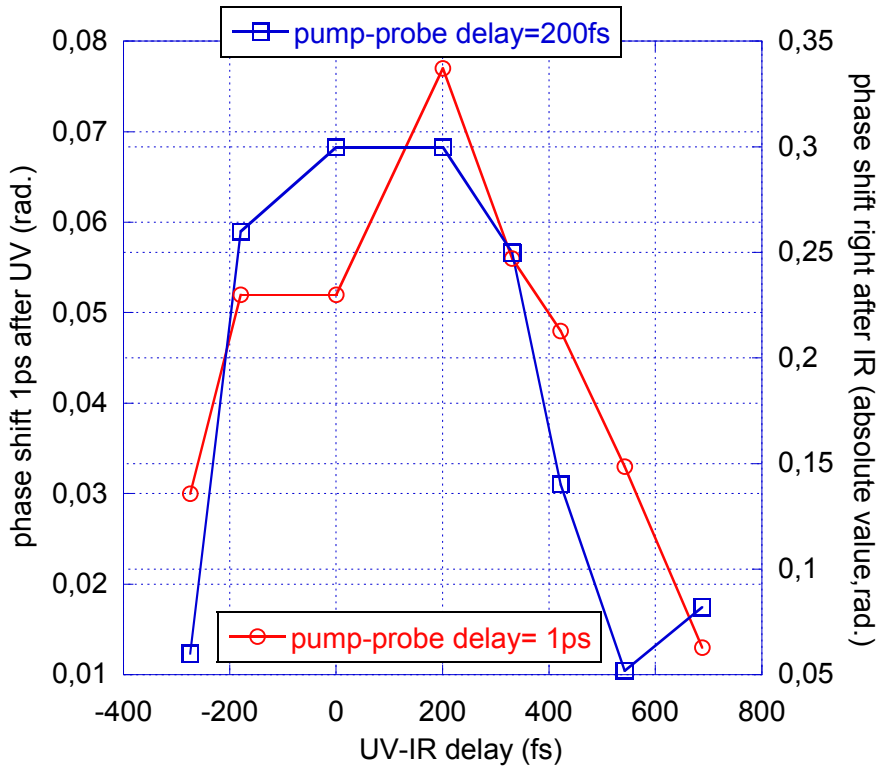

Figure 2.41: Phase shift measured in double pulse scheme for two pump-probe delays: right after IR pulse (200 fs) and 1 ps after UV pulse, as a function of the pump pulses relative delay. Data is taken from figures 2.39 and 2.40.

the measurement was not good enough to clearly separate the different contributions in the time windows from -300 fs to 300 fs. One may think that it would considerably improve our measurements if we acquired a larger number of points (different delays between UV and IR). However, performing a pump-probe scan for each UV-IR delay is time consuming and the risk of drifting is present (laser stability, alignment etc.). Moreover, the additional feature of re-excitation of already trapped carriers has to be studied for longer UV-IR delays.

The above mentioned reasons have motivated a new type of scan : the UV pump- IR pump scan.The procedure starts by first making a UV-probe conventional (single pump) scan (2.42a). Next, let us presume that we are interested in the evolution of positive phase shift at 3.5 ps delay. We fix both UV pump and IR probe in time . Finally, the scan is performed this time by varying the delay between the two pump pulses by using a delay line for the IR pump and this for three different IR energies (2.42b,c,d). The result obtained (black curves on figure 2.42) is nothing less than the evolution of the positive phase shift (measured with

the UV pump alone, at 3.5 ps) as a function of the UV-IR pump delay.

As it has been previously mentioned it is necessary to separate processes that happen at the same time scale. In order to know the exact time window for the cross-excitation mechanism, our idea was to measure the intercorrelation product between the two pump pulses. This is being achieved by generating the third harmonic and measuring its signal with a photomultiplier tube as a function of the pump delay (green curves on figure 2.42). This allows exact knowledge of the time position of the pump pulses and more precisely their temporal coincidence (at peak of third harmonic signal). Finally, the signal with the IR pump beam alone is measured (conventional, but reversed in time, pump-probe scan) and it is plotted along (red curves). Thus, all the information needed as for the individual "free" electron generation, the combined "free" electron generation and the time window during which cross-excitation effects may take place, are present in the same figure.

Note should be taken that positive phase shift in $\alpha - SiO_2$ measurements is a very convenient parameter to measure since it is proportional to the excitation density and it is far away from the hidden from Kerr effect and rapidly evolving phase shift right after arrival of the UV pump. Moreover, positive phase shift is more or less constant for time delays as long as 800 ps.

Irradiation parameters are similar to the previous experiments for figure 2.42. UV energy is at 70% of the SDTH and IR energy is below SDTH as well. A CDTH is rather difficult to define in this case since it is closely related to the UV-IR pump delay which is varying at each time step. The result shows a raise in all black curves (peak centred at zero pump delay) following the convolution of the UV and the IR pump beams (third harmonic signal in green). This is attributed to the "free" electrons generated by cross-excitation that are later trapped thus raising the value of the phase shift. Outside this time overlap of the two pump pulses and for higher IR fluencies (2.13 and 3.13 J/cm^2), the signal remains higher then before following more or less the evolution of the trapping of the carriers (recovery of the negative part of the phase shift). This signal is more important for growing IR energies (2.42d). It is the signature of impact ionization taking place.

Later on, right before the IR pump beam encounters the probe pulse in time, the signal becomes negative (at 3 ps). This has been observed before (bottom phase shift scans on figure 2.40) and it has been attributed to re-excitation of trapped carriers. Finally, the signal comes back to relatively large positive value before it drops back to its ground value. This last contribution comes from the Kerr effect between the IR pump and the probe pulse (it is reminded that the probe has been "stopped" at 3.5 ps). What follows is the signal obtained with the UV pump alone, since the IR pump arrives later than the probe.

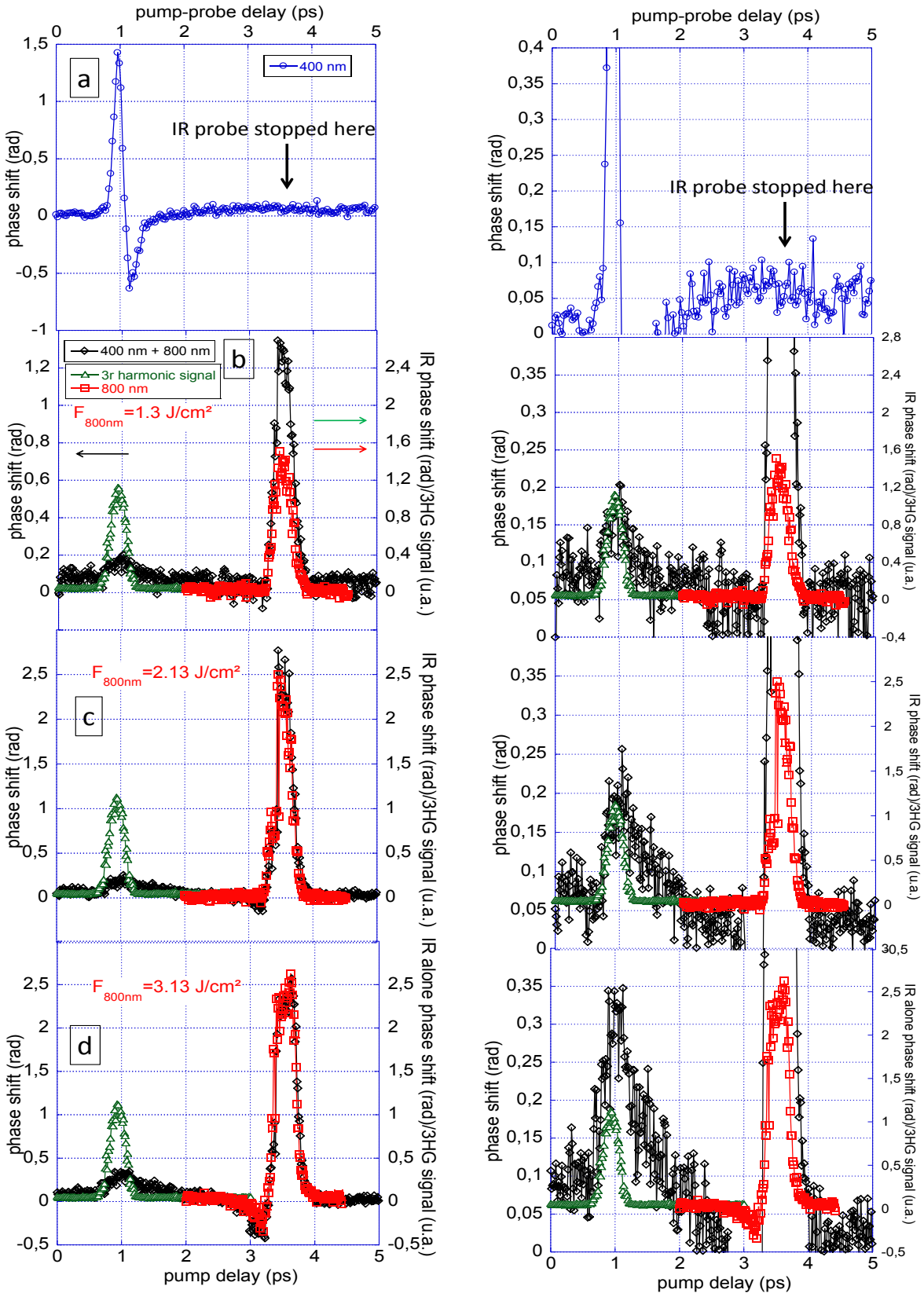

Figure 2.42: SiO_2: Left column: Phase shift in a double pump pulse scheme, at a given UV pump-probe delay, as a function of the UV-IR pump delay, for different IR fluencies. First a conventional UV pump-probe scan is presented (top figure) to illustrate the UV pump-probe delay for which the phase shift variation is measured (black diamonds) as a function of the UV-IR pump delay. The same results at a different scale are presented on the right column. UV (50 fs duration) fluence is 1.12 J/cm^2. Pump-probe geometry is co-linear.

This type of scan has been performed in the perpendicular configuration (see figure 2.43) for two IR energies and once again the same conclusions may be made: a certain carrier multiplication is observed outside the intercorrelation signal of the two pump pulses and re-excitation of the already trapped carriers is possible for longer pump pulse delays.

At this point, let us mention that the IR probe pulse has been stopped at 4.8 ps, approximately where data points are missing (blue curve on top of figure 2.43). However, the level of the signal at that delay is known and this information may be taken from two different sources. First, the positive signal stays constant for long delay thus allowing estimation of an average signal (black, horizontal, solid line on top of the figure). On the other hand, the signal with the UV pump pulse alone is known from the UV-IR scans. Indeed, for IR pulse delays over 5 ps (black curves) the signal corresponds to the phase shift at the delay where the probe pulse was stopped, with the UV pump alone. In conclusion, we do have complete knowledge of the ground level (with UV pump alone) of the signal.

A similar pump-pump scan has been made in NaCl with the same mechanisms contributing to the phase shift evolution (figure 2.44). This time, the impact ionization-related raise in the phase shift: from 0 to 2 ps, lasts longer and the plateau observed coincides with the "free" carriers lifetime in the CB (negative phase shift of blue curve). In fact, in the case of NaCl it is possible to see clearly the contributions of the cross-excitation and of impact ionization. Indeed, the peak on the black curve around zero ps corresponds to the sum of the two contributions while right after this signal drops to the phase shift induced by the impact ionization mechanism itself.

2.5.4 Optical damage and criteria

The process of damage, in the materials studied in the present sections, has been briefly discussed, during experiments with double pump pulses. It is reminded that although no multiplication had been observed in Al_2O_3, damage was still possible and it was accompanied by the change in the recombination dynamics at first stage. Indeed, the criterion of optical breakdown, lying over a critical excitation density is under doubt. The same density of electrons can, in one case, lead to damage while not in another. Another experiment comes in support of the hypothesis of excitation density not being a proper criterion.

Long electron-lifetime materials

Figure 2.45 illustrates the negative phase shift at threshold, just after the pump pulse and absorption, measured in Al_2O_3 and MgO, as a function of the IR pulse duration. Each time, a single pump and probe scan is being made at a given

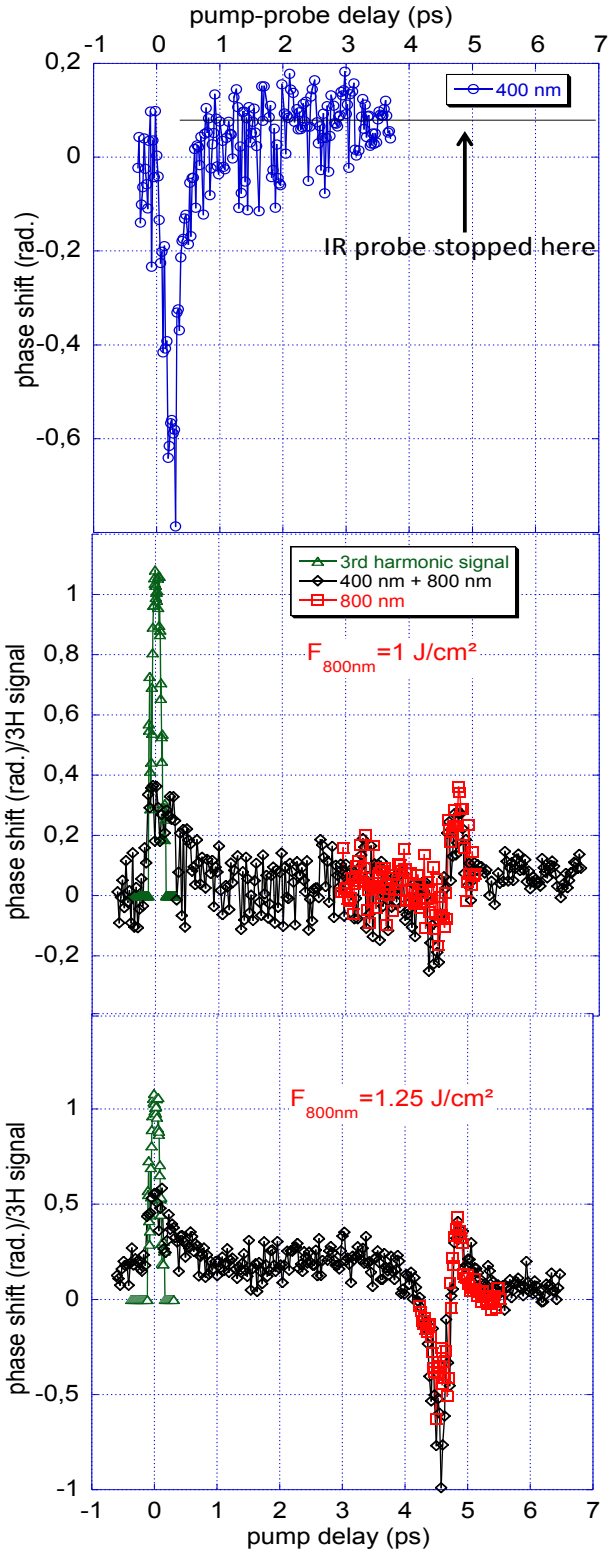

Figure 2.43: SiO_2: Phase shift in a double pump pulse scheme, at a given UV pump-probe delay, as a function of the UV-IR pump delay, for different IR fluencies. First a conventional UV pump-probe scan is presented (top figure) to illustrate the UV pump-probe delay for which the phase shift variation is measured (black diamonds) as a function of the UV-IR pump delay. The same results at a different scale are presented on the right column. UV (50 fs duration) fluence is 1.12 J/cm^2. Pump-probe geometry is perpendicular.

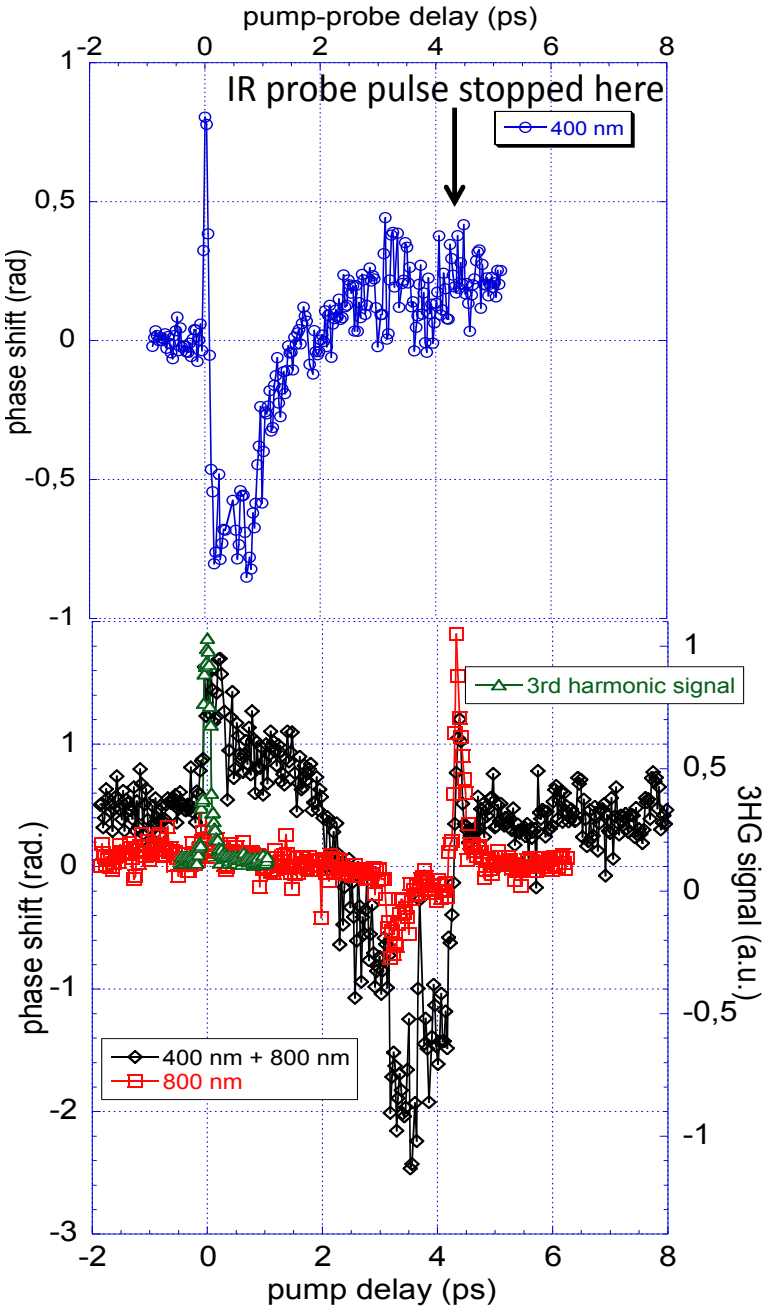

Figure 2.44: NaCl: Phase shift in a double pump pulse scheme, at a given UV pump-probe delay, as a function of the UV-IR pump delay, for different fluencies. First a conventional UV pump-probe scan is presented (top figure) to illustrate the UV pump-probe delay for which the phase shift variation is measured (black diamonds) as a function of the UV-IR pump delay. UV (50 fs duration) fluence is 0.41 J/cm^2. IR (300 fs duration) fluence is 0.47 J/cm^2. Pump-probe geometry is co-linear.

IR pulse duration and the absolute value of the maximum positive phase shift is recorded along with absorption at the given time delay, corresponding to the excitation density in the medium. It is clear that excitation density seems to drop down for longer pulses until it reaches some value near zero (limit of detection of our setup).

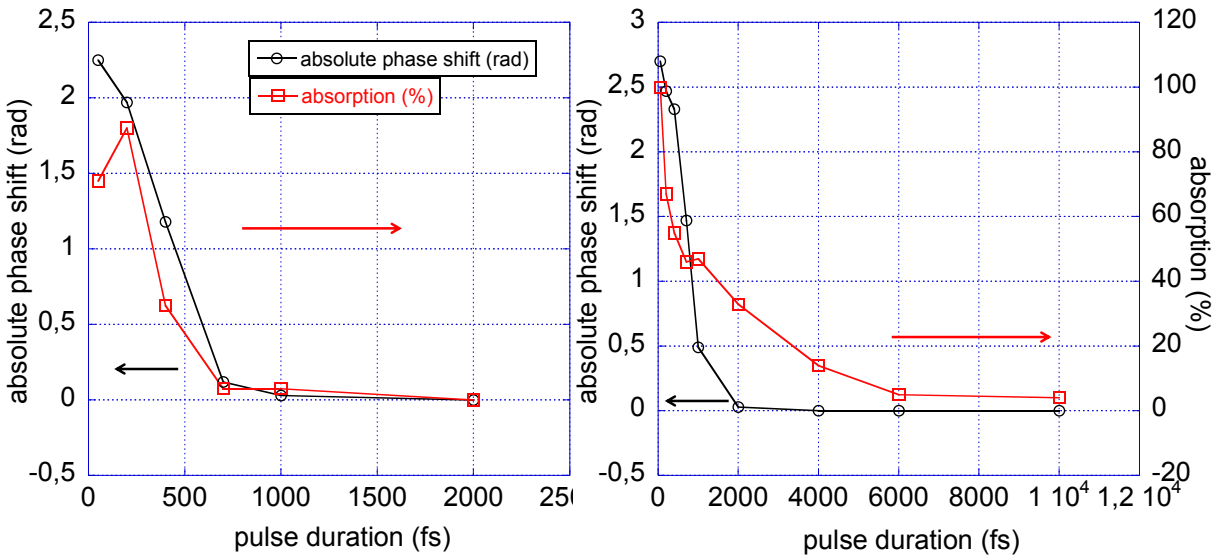

(a) Al_2O_3 (b) MgO

Figure 2.45: Maximum phase shift (single pump pulse) at damage threshold (in absolute value) along with absorption are measured with respect to the IR pump pulse duration.

This is yet another proof that excitation density alone is not responsible for damaging. Moreover, the deposited energy (in terms of electron "heating") on the lattice should be taken into account.

The next experiment was performed in the double pump scheme and aimed at measuring the IR pulse DTH fluencies as a function of the UV-IR pump delay. This data has been recorded for three different IR pulse durations. As in most double pump configurations, the UV pulse energy has been maintained at 70% of the SDTH. These threshold fluencies are plotted on figure 2.46 for both Al_2O_3 and MgO. Two different polarization states have been taken into account : both polarizations along (p) and crossed (s). The criterion for recording the DTH energy is damage happening at 50% of the shots. Once again, the sample is translated vertically after each sequence of shots (one UV and one IR at a given delay).

A general observation is that the IR energy at damage threshold drops down (with respect to the IR pump arriving before UV, negative time scale on x-axis)

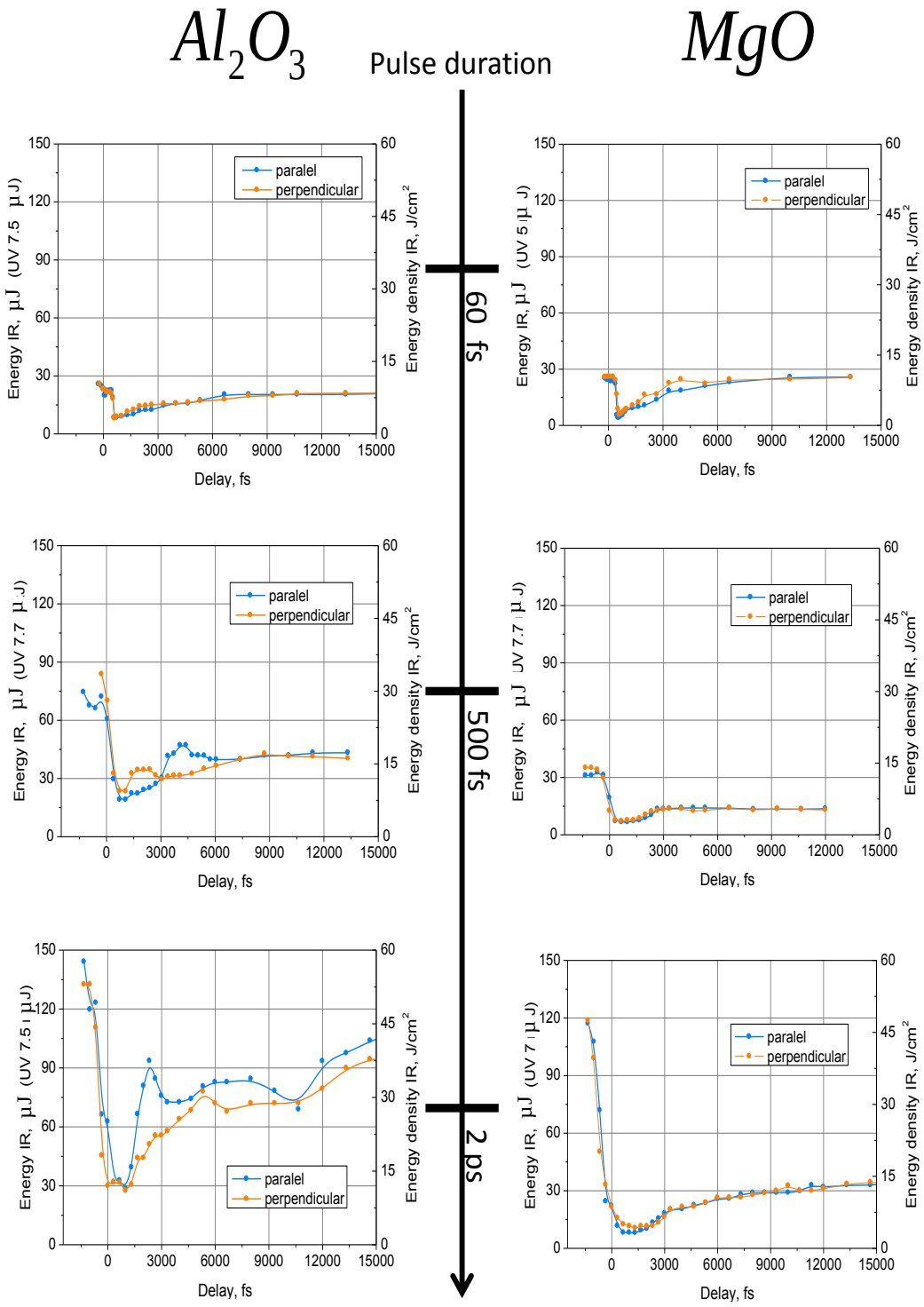

Figure 2.46: Damage thresholds on the surface as a function of UV-IR pump delay, for different IR pulse durations. UV is a short pulse (50 fs) constantly maintained at 70% of SDTH. Two different IR polarizations have been tested : UV and IR polarizations are parallel (blue line) and UV polarization is perpendicular to IR (red line). On the left, we present the results for Al_2O_3 and on the right for MgO.

when the IR pulse arrives right after the UV pulse. This drop is more pronounced for longer pulses (up to ten times in MgO for a two ps pulse). An explanation to this may be given considering the different nature of mechanisms leading to damage, when IR pulse arrives before or after the UV pulse. More in particular, when the IR pulse arrives before, a significant amount of energy is needed to reach the critical intensity for inducing MPI. Naturally, this energy is going to be more important for longer pulses. However, when the IR pulse arrives after the UV pulse, linear absorption in the CB (or two-photon in some cases), is sufficient to induce the damage of the solid. Thus the laser fluence (J/cm^2) is more or less the same for the different pulse durations.

Later, the IR energy recovers more or less fast, depending on the IR pulse duration. Recovery time is generally shorter for short pulses (5 ps). For longer pulses, recovery time follows more or less the free electron relaxation in these materials (50-100 ps). As a general statement and especially in the case of short pulses, we may say that the IR DTH recovers much faster than the electrons recombine with holes, ruling out any correlation between those two. The study should be extended to longer delays (before and after the UV pump) to make safer conclusions.

Short electron-lifetime materials

In a similar way as for Al_2O_3 an attempt has been made to define an damage criterion for $\alpha - SiO_2$. However, measuring the maximum negative phase shift as a function of the IR pump pulse duration (single pump situation) is rather challenging in this material because the phase shift only stays negative for some tenths of fs before becoming positive. Thus, for longer pulses this phase shift will be obscured by the presence of the larger (following pulse duration) Kerr effect. To overcome this difficulty we have chosen to measure the residual phase shift instead, which is still proportional to the excitation density via the density of trapped carriers. This measurement is plotted on figure 2.47.

Pretty much like in the previous section, the excitation density drops rapidly, for longer pulses, to a value non detectable by our setup. The critical density criterion is proven to be invalid following this result.

Finally, the IR damage thresholds have been measured for different UV-IR pump delay and for three different pulse durations. The UV pump (50 fs) is kept at 70% of the SDTH and the damage criterion corresponds to a 50% damage observation (the sample is vertically translated after each shot). Two different polarizations (between pump pulses) are investigated as in the case of Al_2O_3 and MgO (see figure 2.46). The result is presented on figure 2.48.

Surprisingly, the outcome is similar to the case of materials with long electron-lifetime. It is reminded that in $\alpha - SiO_2$ electron relaxation is rapid (150 fs)

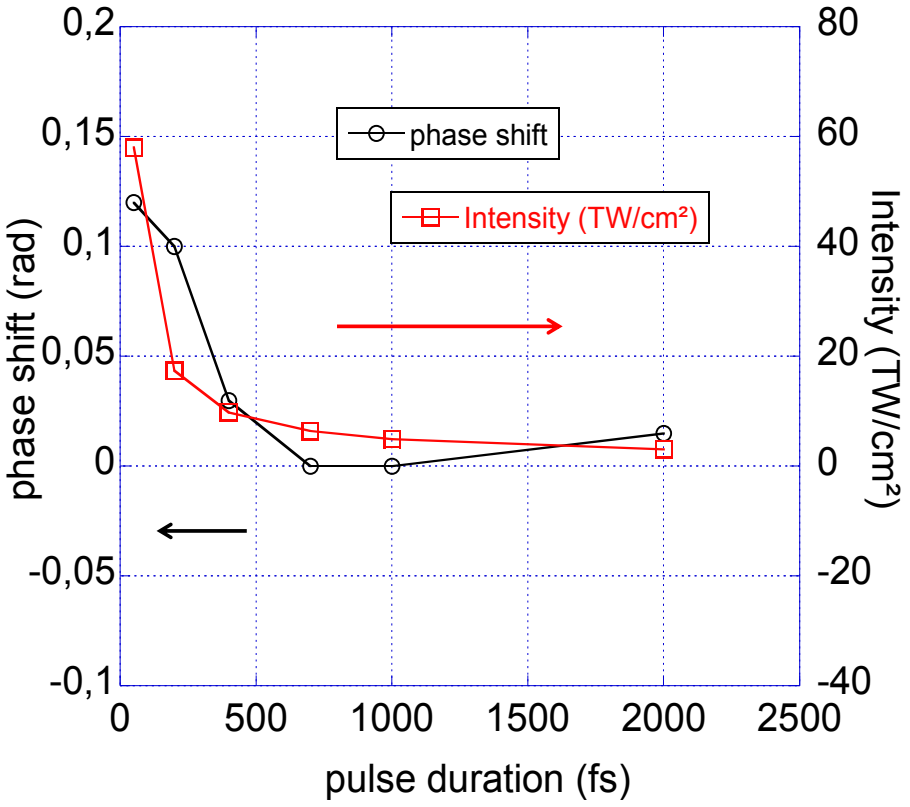

Figure 2.47: SiO_2: Maximum phase shift (single pump pulse) at damage threshold (in absolute value) along with laser intensity are measured with respect to the IR pump pulse duration.

following trapping in STEs. Once trapped these carriers remain at this state for a long time (at least one nanosecond). The IR energy drops at coincidence of the two pump pulses before recovering to its "before UV" value. This recovery time is longer for longer pulses. While recovering, the IR energy forms a plateau at time delays where all electrons are trapped with no evolution. As a result, damaging in this case may be considered in terms of STE formation or re-excitation.

No polarization effect has been observed as in the case of Al_2O_3 and MgO. When the pump pulses arrive perpendicularly to the sample little or no difference at all is expected with polarizations in the plane of the surface of the sample. There might be an effect when polarization vectors of UV and IR are perpendicular and this while pulses overlap in time, but the temporal resolution of this experiment didn't allow observation of such a phenomenon.

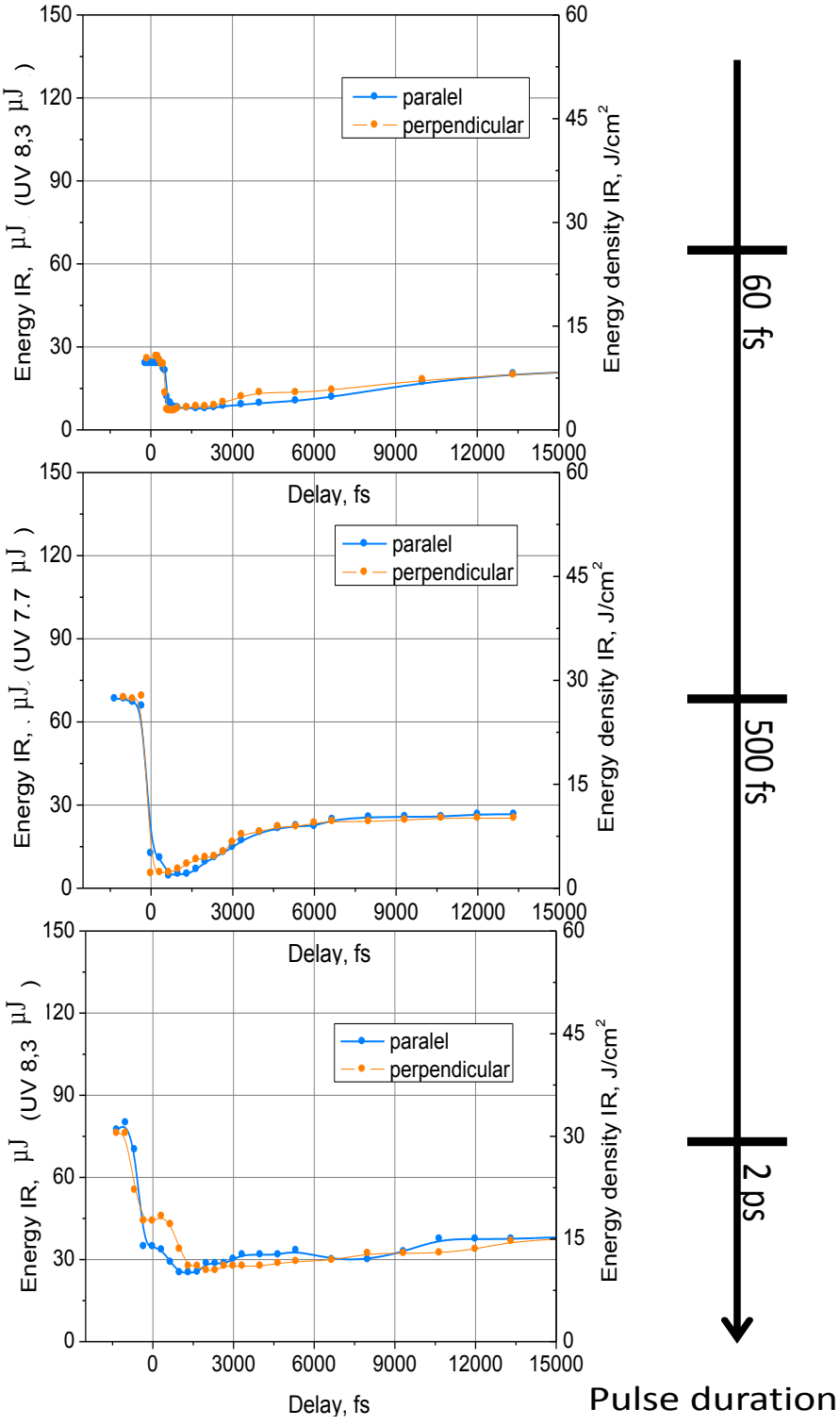

Figure 2.48: Damage thresholds on the surface of $\alpha - SiO_2$ as a function of UV-IR pump delay, for different IR pulse durations. UV is a short pulse (50 fs) constantly maintained at 70% of the SDTH. Two different IR polarizations have been tested : UV and IR parallel plotted on the blue line and UV perpendicular to IR on the red line.

2.6 Conclusion

The frequency domain interferometry experiment has provided new information regarding the excitation and relaxation processes in large band gap dielectric solids. A selected set of crystals with different intrinsic properties has been studied and their response to short laser pulse has been characterized. Over the three years of the thesis duration, the interferometry experiment represents the major part of work time. The setup has been permanently modified and improved, with the aim of the most direct access to the physical processes under investigation. These developments include:

- a new double pump scheme, with the possibility of performing pump-pump scans. This double pump scheme has been decisive for observing the different ionization processes,
- the modification of the interferometer, allowing probing delays up to one nanosecond,
- a new geometry for the probe beam, allowing the investigations of shorter depths and thus making clearer assumptions over the interaction.

The impact ionization mechanism (resulting in avalanche ionization) has been under debate over the years as for its contribution to ionization of dielectric solids and subsequent optical breakdown. During this thesis, we have reported the first direct experimental observation of impact ionization induced by a laser pulse. This process takes place in $\alpha - SiO_2$ and other materials with strong electron-phonon coupling, in which electron-hole pairs form self-trapped excitons. This result could be obtained thanks to the use of a sequence of two pulses in which the two steps of electronic excitation and carrier heating are separated. We found that the optimal conditions for the appearance of impact-ionized electrons are : UV (50 fs) pulse at 70% of the SDTH and IR pulse with durations corresponding to the electron-lifetime in the CB. The combination of those two pulses results in an above breakdown threshold fluence although no damaging is observed for each independent pulse. The delay has been chosen by compromising two conditions : no crossed-excitation and maximum "free" electron density. Furthermore, arrival of the IR pump pulse at later times (over 500 fs) has revealed the possibility to re-excite carriers previously trapped in self-trapped excitons.

In an attempt to generalize the conclusions made in $\alpha - SiO_2$, the study has been extended to other crystals where self-trapping occurs such as NaCl and KBr and similar results were obtained.

Thus our experimental finding indicates a strong link between self-trapping and impact ionization and hence one may think in terms of:

- electron-hole pair localization (as in $\alpha - SiO_2$) or hole localization (as in alkali halides),

- strong electron-phonon coupling

The strong coupling may account for both the effective heating of the carriers in the CB, through inverse Bremsstrahlung, up to a collisional ionization threshold and the higher collision probability through momentum change. The relative importance may be evaluated by looking at electron kinetic energies obtained by photoemission experiments (object of the following chapter). On the other hand, the common feature of hole localization in these crystals may have an effect on the VB branches and hence lower the effective bandgap locally by band distortion. Such situation would certainly favour the impact ionization mechanism. Moreover, the hole localization can be connected with the recently proposed "forest fire" mechanism [30, 69]. The hypothesis of this model is that localized holes enhance the ionization by combination of local field and laser field, without a heating step being involved.

Furthermore, the optimal delay between the two pump pulses (200 fs) in order to observe electron multiplication, corresponds to the case where the second pump pulse interacts with a maximum excitation density. At this stage, two situations may be considered. One, where no hole localization has taken place (a priori connected to the STE establishing time: $\sim$ 500 fs) and hence there can be no connection of the "forest fire" mechanism with the observed multiplication. However, if the hole localization is quasi-immediate ($\sim$ 100 fs), then the second pump pulse could raise the total field (local field plus laser field) and thus induce a multiplication in the signal that would not have been observed if the same pump pulse had been sent alone. In that case, attributing the multiplication to impact ionization could somehow be questioned and the "forest fire" mechanism could be an alternative way of raising the excitation density.

On the contrary, the double pulse experiment has shown no sign of impact ionization[7] in materials with long electron-lifetime, although different irradiation conditions have been tested in favour: pulse durations from 50 fs to 10 ps, above threshold energies and different delays. This could be related to an electron-phonon coupling constant being significantly lower than that of self-trapping materials (10^{13} s^{-1} for Al_2O_3 [85] compared to 10^{15} s^{-1} for $\alpha - SiO_2$). However, it has been revealed that the combination of a short (50 fs) UV pump pulse with a long (10 ps) IR pulse may alter the carrier recombination kinetics, while the DTH is reached. This suggests that the IR pulse deposits energy on the solid by the intermediate of the electron kinetic energy raise. As far as the carrier relaxation is concerned at later times (over 200 ps) in Al_2O_3 and MgO, our results for phase

[7] synonym to electron multiplication

shift (residual phase shift above zero) and absorption (above zero as well for long delays) measurements seem to indicate a defect formation.

Summing up, the impact ionization is certainly present in materials with strong electron-phonon coupling ($\alpha - SiO_2$, NaCl, KBr) while no sign of it has been observed in materials with long electron lifetime (Al_2O_3, MgO), in our experimental conditions. A part of these results has given birth to an article publication [60] and the remaining results are to be published soon.

The strong connection of the electron-phonon coupling with a presumable impact ionization could suggest that the impact ionization cross-section (σ) is material dependent. In that case, the question on why σ would be so different in $\alpha - SiO_2$ and NaCl then in Al_2O_3 and MgO remains open.

The commonly used criterion of critical density at optical breakdown was discussed in this thesis. Taking advantage of the present interferometry setup, we have performed measurements in order to define a proper criterion for optical breakdown. More in detail, the excitation densities have been estimated at threshold for different pulse IR pump pulse durations (50 fs - 2ps) and for three different crystals Al_2O_3, MgO and $\alpha - SiO_2$. All three materials revealed similar behaviour, with excitation density dropping down with longer pulse durations. This suggests that the critical excitation density is not the proper criterion to take into account for optical damage. Instead, a "thermal" criterion should be used, taking into account the deposited energy on the solid. Under the assumption that phase transition (melting) is taking place prior to any damage, this criterion could be:

$$\Delta H_{\mathrm{DTH}} = \Delta H_{T \to T_{\mathrm{fusion}}} + \Delta H_{\mathrm{fusion}} \tag{2.47}$$

with ΔH_{DTH} the threshold enthalpy (per unit volume), $\Delta H_{T \to T_{\mathrm{fusion}}}$ the heat (per unit volume) for a temperature rise of ΔT up to the fusion temperature T_{fusion} and $\Delta H_{\mathrm{fusion}}$ the latent heat of fusion.

The imaging technique, used in the interferometry experiment, allowed measurement of combined-pulse DTH energies as well. More precisely, these have been measured in the case of double pump irradiation as a function of the UV and IR pump delay. The results indicate no correlation of the damage with the "free" electron recombination in Al_2O_3 and MgO. In the $\alpha - SiO_2$ case, damage can be considered in terms of self-trapped exciton or re-excitation for long pulses (2 ps).

Knowing the excitation density in the studied solids and the mechanisms to reach it, the next step should be to obtain the energy spectrum of these electrons. This may be accomplished by the use of photoelectron emission spectroscopy and it is what follows in the next section of the manuscript.

Chapter 3

Experimental study of electron kinetic energy distribution in the CB

In this chapter we will focus on the electron processes that take place inside the CB. These may be divided in excitation processes, in the presence of a femtosecond laser pulse and the electron relaxation processes that start as soon as the excited carriers are above the ground CB level. This investigation will be held with the help of the photoemission spectroscopy (PES) tool, thus measuring the kinetic energy distribution of the electrons either accumulated in time (single-pulse experiments) or time-resolved (double-pulse experiments). The outcome of this study brings insight to the possibility of observing the impact ionization mechanism and helps converging in our interpretation.

3.1 Introduction

It has been previously seen (see 2.5.4) that defining the proper criterion is the key in understanding the excitation (and by extension the optical breakdown) process in wide band gap insulators. Our interferometry experiments, have shown that taking into account the excitation amount in the solid does not account for the damage. Most probably, one has to correlate the number of these electrons to their respective energy (during excitation), thus leading to the deposited energy criterion. Given the fact that interferometry technique only measures the number of electrons per unit volume, there is need for an additional experiment providing information about the energy spectra of the excited electrons.

Moreover, the impact ionization mechanism is dependent upon electron energy. There is a threshold above which collisional ionization may take place. Therefore, the question is whether the kinetic energy acquired by the electrons during the excitation stage is sufficient to launch impact ionization.

Knowledge of these spectra may be given by the powerful, photoemission spectroscopy technique, based on the photoelectric effect [1]. More precisely, the energy of the emitted electrons is measured, previously excited by an ionizing laser light pulse. Thus, the electronic structure of the solid is being revealed and valuable information regarding the different excitation and relaxation processes in solids (liquids and gases as well) can be extracted.

The present chapter is dedicated to these experiments. In the first place, the principle of the technique will be presented along with the drawbacks and their respective solutions. The next stage will be to briefly remind the photoemission experimental results previously obtained on solid targets of our interest ($\alpha - SiO_2$, Al_2O_3 etc.). Finally, we will present the experimental setup used and the results acquired.

3.2 Principle of the photoemission spectroscopy

PES has long been one of the most important tools to study the electronic structures of molecules, surfaces and solids [74]. Its continuous development since the earlier days has had practical implications in various fields like surface chemistry or material science and has significantly contributed in understanding fundamental properties in solid state physics. In what follows, we will present the theoretical background of the photoemission experiments performed.

3.2.1 Single pulse

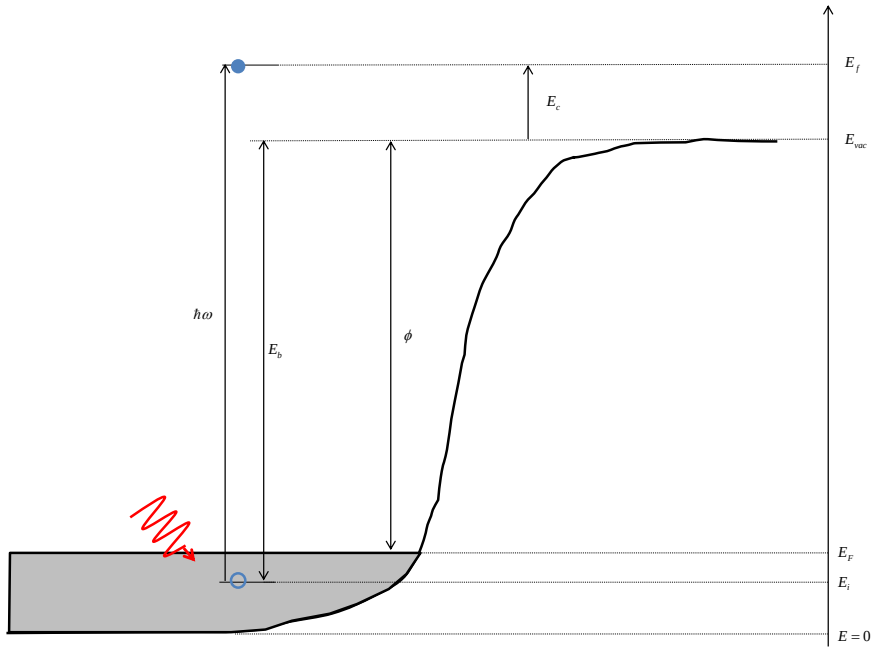

Figure 3.1: Schematic description of photoelectric effect in a solid, near the surface. Red arrow represents incoming photon with energy $\hbar\omega$. Different energy levels are represented : energies of initial and final electron state E_i and E_f respectively, binding energy E_b, work function ϕ, Fermi level E_F, vacuum level E_{vac} and electron kinetic energy E_c. Only electrons with an energy greater than E_{vac} can escape the medium.

There are three basic requirements for performing PES. In the first place, one needs a source of fixed-energy radiation. A large range of incoming radiation may be used depending on the nature of electrons to be studied. IR to vacuum ultraviolet vacuum ultraviolet (VUV) light corresponding to energies from 1.5 to

45 eV is applied when one is interested in valence electrons, while soft x-rays, 200-2000 eV, are proper for the study of core electrons.

The electrons that quit the solid sample are detected by an electron energy analyzer (which can disperse the emitted electrons according to their kinetic energy, and thereby measure the flux of emitted electrons of a particular energy). Finally, a high vacuum environment is necessary (to enable the emitted photoelectrons to be analyzed without interference from gas phase collisions).

PES utilizes photo-ionization and analysis of the kinetic energy distribution of the emitted photoelectrons. Figure 3.1 illustrates the photon absorption process from an electron and its subsequent ionization to a state above the vacuum level. The condition for an electron to be detected is that its energy is greater than the vacuum energy of the solid E_{vac}. In that case, the kinetic energy of the electron E_c, after absorption of a photon with energy $\hbar\omega$, is given by :

$$E_c = \hbar\omega - E_b \tag{3.1}$$

with $E_b = E_{\text{vac}} - E_i$ being the binding energy of the electron.

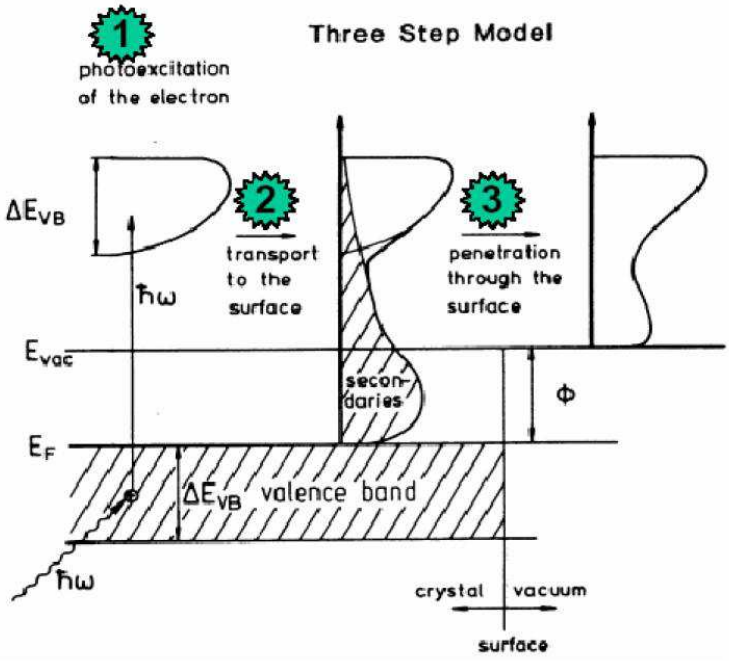

Figure 3.2: Three step model after Spicer. Detection of a photoelectron involves excitation, transport to the surface and emission.

In this basic scheme, the electron managed to escape from the surface without losing any of its energy before. Of course, such a case is unrealistic and electrons

that are detected have previously interacted with the medium before exiting the surface and as a result their energy spectrum is shifted towards lower energies. This is summarized in a three-step model proposed by Spicer [91]. The different steps are illustrated in figure 3.2.

At first, the electron acquires a certain amount of energy equal to the energy of the absorbed photon (step 1 of figure 3.2). Then the electron travels through the medium losing energy through inelastic collisions (step 2), these electrons are called secondary. Finally, electrons arriving at the interface can be emitted (step 3). Thus, it is possible to measure a spectrum that is a complex convolution of: the band structure, the emission probability and the energy loss during transport to the surface . This gives a picture of the energy distribution in the CB.

3.2.2 Double pulse

In an attempt to join the radiation conditions used for the interferometry experiment, two pulses have been used (see double pump interferometry experiment). In the case of PES, the second pulse not only plays the role of a further excitation source, but it serves as a probe pulse as well. Thus it is possible to follow the relaxation process of the electrons, by elastic and inelastic collisions, in the conduction band by looking at the pump and probe signal at a given electron energy.

A summary of the different possible excitation mechanisms is presented in figure 3.3. At first, electrons are promoted from the valence (or defect states) to the conduction pulse by multiphoton absorption. This may be induced by each pulse separately, IR (number 1 in figure 3.3) or UV (number 2). When pulses coincide in time, crossed photon excitation has a certain probability of generating free carriers as well (middle part of figure). If no other mechanism is involved, the resulting PES spectrum is the addition of the respective spectra obtained with each pulse alone.

The previously mentioned "free" carriers can absorb the remaining laser pulse, or a second pulse, and thus raise their energy in the conduction band by electron-photon-phonon interaction or direct interbranch transition (DIT). This gives rise to a "tail" in the PES spectrum extending to higher energies (number 3 in figure 3.3). Such a scenario is possible in the case of a single pulse or a double pulse, the advantage with a second pulse being the adjustable delay thus keeping track of the relaxation stage.

In the particular case of $\alpha - SiO_2$ like materials, free carriers are trapped within 150 fs in STE's (see interferometry chapter). It is then possible to re-excite those trapped carriers at a lower multiphoton order, favouring this process rather than the VB-CB transition. Thus, once all carriers are trapped the PES shouldn't vary a lot with pulse delay. In crystals such as Al_2O_3 the lifetime of electrons is much longer ($\approx$ 150 ps) and it is straightforward to expect a longer pump and probe

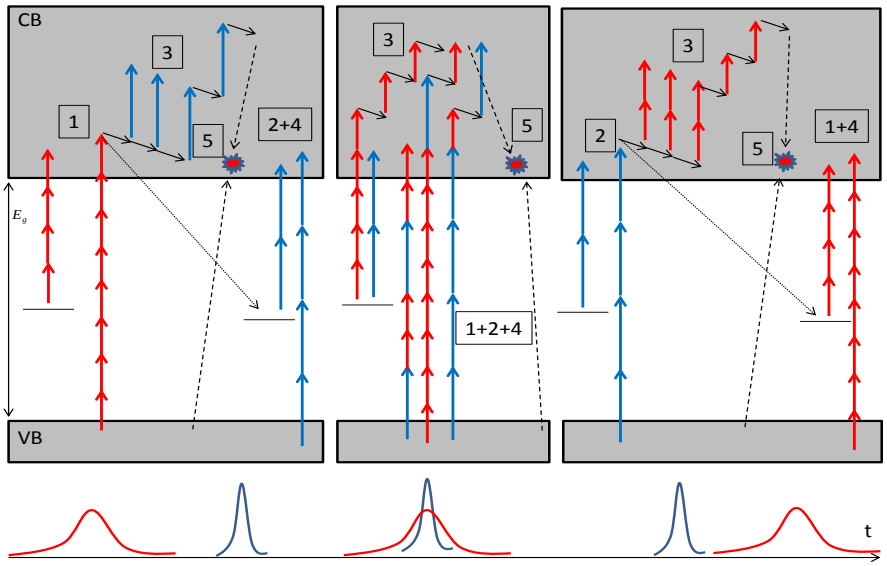

Figure 3.3: Summary of the different processes taking place in a double pulse scheme. An IR (often stretched) pulse and a UV short pulse are used. Three situations are illustrated : IR pulse arrive before, at coincidence and after UV pulse. The mechanisms are numbered from 1 to 5 as follows : 1 and 2 for IR and UV multiphoton ionization respectively, 3 for electron "heating", 4 is the sum of two independent multiphoton ionizations (UV and IR) and 5 is impact ionization. A crossed photon excitation (UV+IR) is represented at coincidence as well. List is not exhaustive.

signal following the slow recombination rate.

Subsequently to the electron "heating" stage and for energies above a certain threshold of the order of the band gap (≈10 eV), impact ionization may arise, seeding an electronic avalanche and thus exponentially increasing the low energy electrons in PES spectra (number 5 in figures 3.3).

It is necessary to underline at this stage that not all processes happen at the same rate. For example, electrons in the conduction band have higher absorption cross sections for IR light than for UV. One should expect the "heating" process to be more efficient in that sense. Same goes for pulse duration, disposing more time for inverse Bremsstrahlung processes will result in higher energies for the electrons.

3.3 Drawbacks and consequences

Unfortunately, measuring photoemission spectra can be revealed to be rather challenging, especially in the case of dielectrics. A certain number of difficulties arises when performing these experiments that alter the signal of the measured spectra. As a consequence, the interpretation of the obtained results becomes a rather complicated affair. Furthermore, using a double pulse scheme amplifies the experimental issues encountered.

Nevertheless, it is possible to overcome these obstacles or in the worst case, to define a "working region". We will now discuss these complications and the respective solutions that can help in making safer conclusions.

3.3.1 Electron mean free path

Until present, no particular discussion has been made as to the origin (in space) of the photoelectrons. Considering that laser light is focused on the surface of the sample, electrons excited within the excitation volume do not contribute equally to the photoemission (PE) spectrum signal. A compilation of several measurements of the electron mean free path λ are presented in figure 3.4. The horizontal axis represents the energy of these electrons. On this figure, a universal law can be observed for all solids. For instance, electrons with energies from 10 eV to 10 keV have a mean free path of the order of a nm, while for lower energies this value becomes more important.

The consequence of this result is important for the lower part of the energy spectrum. If an electron at a distance from the surface $l > \lambda$ manages to escape the solid and reach the detector, it will have suffered several inelastic collisions, losing its energy and contributing as a secondary electron thus raising the the low energy signal. As a result, the lower part of the spectrum is going to be overestimated, with respect to the higher energies. As a remark, it should be mentioned that in the case of a double pulse, most seed electrons will be available at the surface of the sample and thus higher energy counts will be possible since the second pulse will be mainly absorbed at the surface of the sample.

3.3.2 Space charge

Electrons escaping the medium and heading to the detector form a cloud with an intrinsic charge proportional to the number of electrons. Hence, coulomb repulsion within this cloud may become important enough to modify the velocity distribution of these electrons. Furthermore, if the experimental setup involves an extraction potential (applied voltage on the sample), the external field can be coupled to the internal one and accelerate electrons to energies up to 100 eV [68].

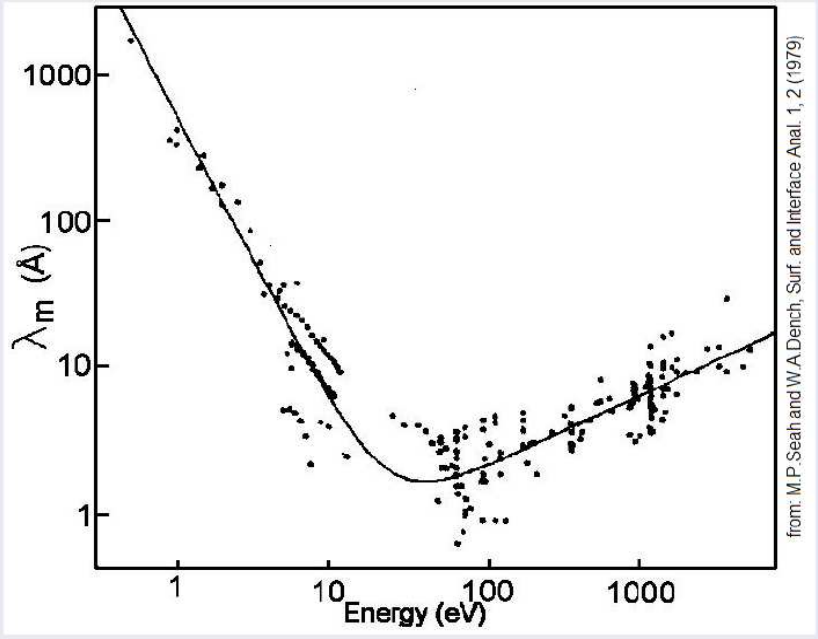

Figure 3.4: Mean free electron path as a function of its kinetic energy in bulk material. Metal case is represented but trend is similar in inorganic solids (such as $\alpha - SiO_2$). A universal law is observed for all solids.

The solution to this problem is to minimize as much as possible either the number of electrons emitted, or the value of the applied extraction potential, or both.

It is possible to evaluate the impact of this effect by applying a variable, negative, external potential on the sample. If no space charge effect is present then the different spectra (at the same radiation conditions) obtained should be similar when translated of an amount of energy equal to the potential applied. This is the case of the measurement presented in figure 3.5a. Indeed, in this case being far from the damage threshold intensity (40% of the SDTH), the amount of electrons emitted is limited and so is the space charge effect. On the other hand, figure 3.5b presents a case where the number of electrons is quite important to induce a deceleration of the electrons when a 60 V potential is applied. This result, coincides with the laser intensity being not far from the threshold (83% SDTH) and thus it is coherent to expect the number of electrons to grow. In this case, the appearance of "negative" kinetic energy electrons proves a measurable space charge effect. Its influence on the PES is however limited, and the spectra measured with 0 V and 60 V overlap quite well.

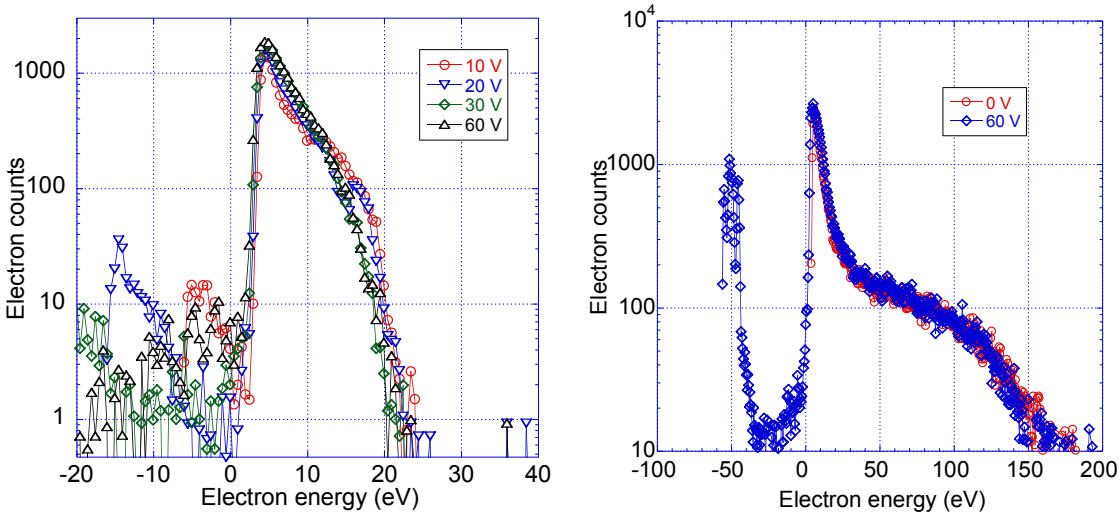

(a) Intensity is 19.8 TW/cm^2.

(b) Intensity is 41.2 TW/cm^2.

Figure 3.5: Different tensions are applied on a $\alpha - SiO_2$ sample to observe if a space charge effect exists. Spectra are translated for comparison. A 800 nm pulse, 28 fs pulse duration has been used as excitation source.

3.3.3 Surface charge formation

Another complication comes with the use of a dielectric solid sample (such problems being absent in PES in metals). Due to the nature of the solid, electrons that are being emitted are not replaced instantaneously and as a results a positive charge is left behind. Therefore, the resulting electric field has an effect on the binding energy of the electrons, raising it at higher levels. Practically, the spectrum varies randomly from shot-to-shot and electrons are being slowed down due to coulomb attraction. This effect is emphasized for smaller excited volumes. Notably, for short wavelengths, the penetration depth is small thus accumulating important positive charges on the surface after emission.

Experimentally, it has been possible to reduce the impact of surface charge formation by replacing the emitted electrons. This can by done by two ways. One way is to heat the sample at temperatures of the order of 400 °C. The result is that electrons that have been trapped at the upper level of the band gap can be re-excited to the conduction band. Also the hole conduction and in some cases (NaCl) the ionic conduction through defects may come into play, compensating the positive space charge. A preliminary measurement should be made (see figure 3.6) in order to subtract the thermal emission contribution from the measured

signal. The measure signal is due to the electron emission from the electrodes used to heat the sample. The inconvenience is that the emission peak seems to fluctuate from one shot to another and thus if one subtracts a constant spectrum from the measured signal, there is a risk of having a negative number of counts in the spectra. In some materials heating the sample might prove insufficient because of the low trapped carrier density (e.g. Al_2O_3) or absent ionic conductivity (e.g. $\alpha - SiO_2$).

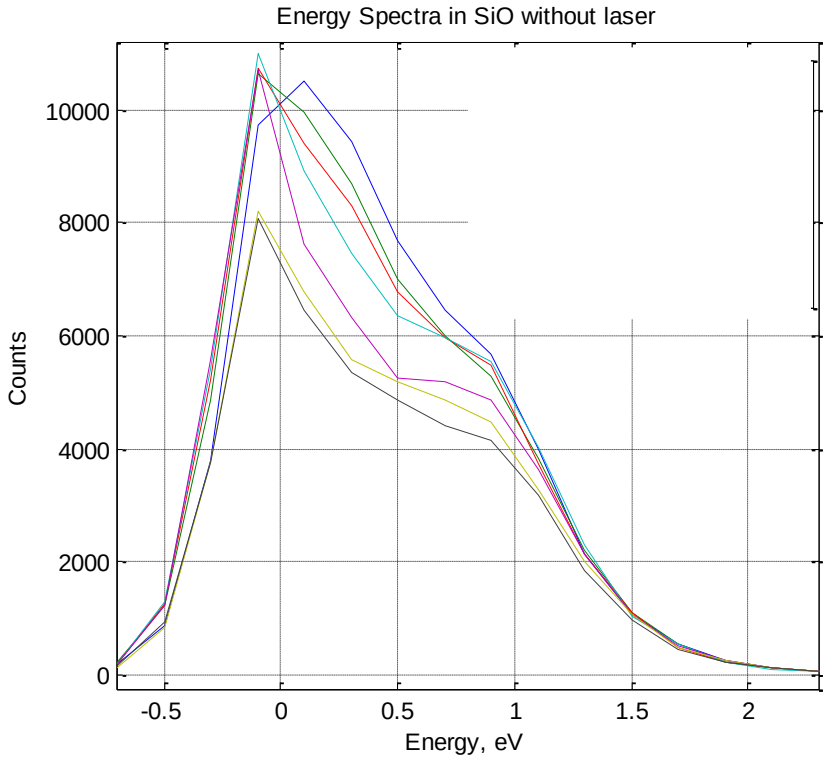

Figure 3.6: Thermal emission spectrum of an $\alpha - SiO_2$ sample heated up at 400 °C. No laser is present and therefore signal is due to electrons being emitted by the electrode used to heat the sample. Fluctuations at the peak are present while the electron maximum energy is constant from one shot to another.

Another way is to use a beam of low energy electrons on the surface of the sample. This can be achieved with the use of an electron gun, with adjustable parameters being the electron energy and the electric current determining the flux. Special care should be taken in that case not to over-compensate the negative charge absence.

Finally, it is important to underline the wavelength dependence of the surface charge formation. It is predicted to be of minor importance in the case of exper-

iments with IR pulses because of their greater penetration depth in the sample and the low excitation densities, incapable of modifying the laser pulse propagation. On the contrary, VUV pulses may amplify the effect because of the lower penetration depth and thus an accumulation of the absorption at the surface.

3.3.4 Surface contamination

A last contribution to the modification of an energy spectrum may be the presence of irrelevant substances or residual gases in the photoemission chamber. In that case, heating the sample during a certain number of hours at 400 °C has a double, positive effect, compensating the space charge one one hand and ensuring the sample's surface purity on the other.

Summing up, a certain number of problems may be encountered in photoemission spectroscopy of dielectric solids. Most of them can be compensated by experimental techniques that have been tested before ([32]). However, the external electron contribution used in some cases may modify the potential at the surface and thus translate the measured spectra of some eV.

3.4 Preliminary discussion

Before presenting the experimental setup used, it is necessary to make a review of the previous results obtained from photoemission experiments, in our group. This will allow a better understanding of the experimental scheme as well as a more solid-based interpretation of the spectra obtained during this thesis.

3.4.1 Photionization

Our experiments in interferometry have revealed the non-linear character of the initial generation of an excitation density. A power law of the intensity I with an exponent n corresponding to the multiphoton order appeared to command the band-to-band transition. However, it is reminded that in PES intensities are often several orders of magnitude lower than in interferometry experiments and as a result the initial stage of excitation is not assured by the same mechanisms.

Remarkable observations from Daguzan [21] have set the basis for the upcoming experiments. In a single pulse frame, several radiation parameters have been tested on Al_2O_3 and $\alpha - SiO_2$. These include two different wavelengths (620 nm and 310 nm) and different pulse durations varying, 80 fs and 30 ps. Intensities were as low as some hundreds of GW/cm^2, being well below damage thresholds in these materials. The evolution of the total number of electrons (in a PE spectrum) has been studied as a function of the pulse energy. Unexpectedly, the power law (I^N, n number of photons) commanding this evolution corresponded to an exponent N lower than the one necessary for multiphoton absorption. This has been attributed to the ionization from defect states, in the band gap. As a result, the sensitivity of PES measurements on defects has been pointed out.

3.4.2 Electron heating

Next the electron heating stage has attracted attention. The appearance of "hot" electrons has been investigated as a function of certain laser irradiation parameters [22]. Although only low energy (1.5 eV) electrons were observed for 310 nm pulses (for intensities up to 500 GW/cm^2 and pulse durations equal to 80 fs), it has been possible to obtain a larger spectrum (up to 8 eV) for the same intensities and pulse duration, but for a different wavelength. Indeed, it has been found that longer wavelengths (620 nm) have a better chance of heating the electrons in the conduction band by electron-photon-phonon absorption processes. However, it is possible to extend this framework for shorter wavelengths provided that a longer interaction interval is made available. Concretely, this corresponds to a longer pulse duration. The effect of intensity has been tested as well and it has been proved that electron "heating" is favoured by higher intensities.

Clearly these results give information about photon absorption cross sections for electrons in the conduction band, these being higher for longer wavelengths.

Quere [71] has been interested in the heating process as well. His experimental work, among others, focused on the electron population measurement (at a fixed energy of 34 eV) as a function of the IR pulse intensity. This result suggested a linear dependence, thus coming to the conclusion that linear photon absorption in the conduction band is dominant at intensities up to 2 TW/cm^2.

Gaudin [32] took these experiments one step forward by investigating intrinsic properties at even larger intensities (up to 10 TW/cm^2) and for several pulse durations (around 100 fs) in both single and double pulse scheme. First, using a single pulse excitation (800 nm, 40 fs), several spectra have been obtained for several intensities, varying from 0.3 to 3.5 TW/cm^2 (see figure 3.7). These measurements show the appearance of electrons having acquired energies several times the photon energy used.

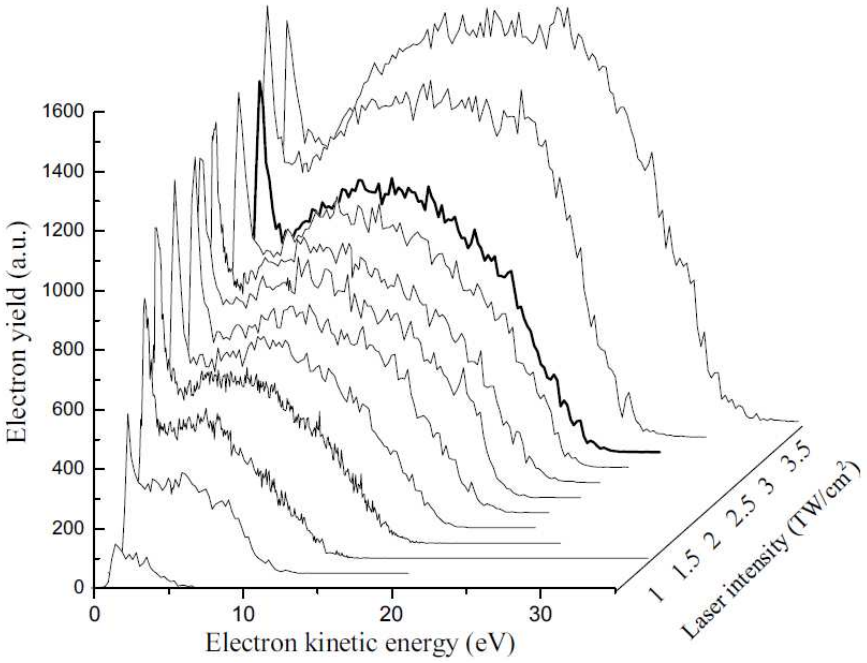

Figure 3.7: Photoelectron spectra on $\alpha - SiO_2$ excited by 40 fs pulses at 800 nm for different intensities. Figure from [102].

Pretty much as in interferometry experiments, G.Geoffroy and her group from centre lasers intenses et applications (CELIA), Bordeaux have tried to favour the impact ionization mechanism, motivated by Rethfeld's [76] predictions. Her theoretical model suggested that collisional mechanisms were encouraged for longer pulse durations and higher intensities. Thus, it would be interesting to investigate

the photoemission spectra for different pulse durations at near thresholds intensities for $\alpha - SiO_2$ and Al_2O_3 (those two are the best studied crystals in literature).

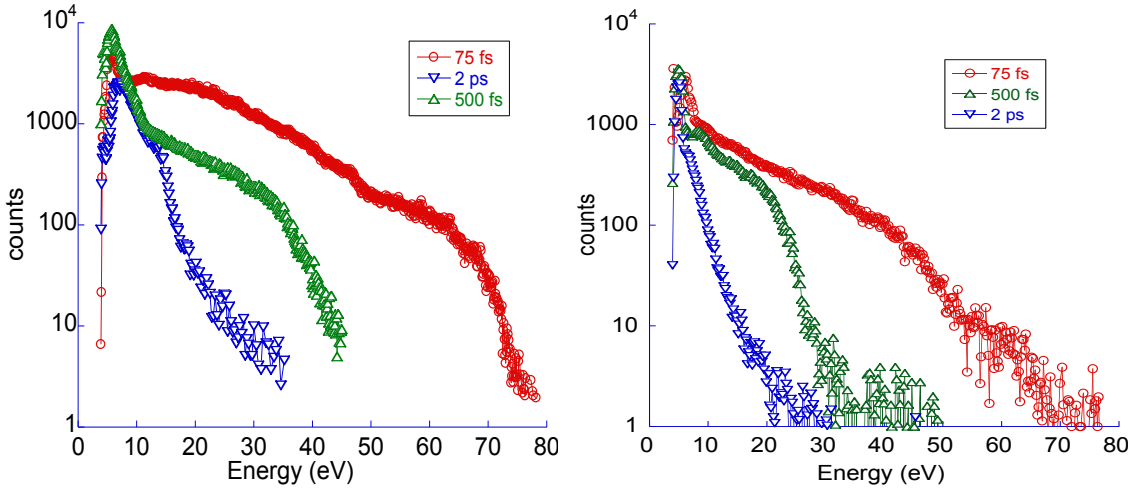

(a) $\alpha - SiO_2$: Intensities are : 49.4 TW/cm^2 (75 fs), 8.7 TW/cm^2 (500 fs) and 3 TW/cm^2 (2 ps).

(b) Al_2O_3: Intensities are : 31 TW/cm^2 (75 fs), 5.2 TW/cm^2 (500 fs) and 2.4 TW/cm^2 (2 ps)

Figure 3.8: Photoemission spectra for different pulse (800 nm) durations at damage threshold. *Measurements made by G. Geoffroy's group.*

The spectra in figure 3.8 were obtained for 75 fs, 500 fs and 2 ps at different intensities corresponding to the damage threshold (see respective captions). These results show the appearance of a long energy "tail" for shorter pulses, the fraction of the higher energy electrons being smaller for long pulses. As for the total number of electrons emitted (see figure 3.9), this appears to be dropping exponentially with the pulse duration, pretty much like the maximum kinetic energy extent of the measured spectra.

Both materials show similar behaviour concerning the maximum kinetic energy dependence on pulse duration. However, a difference is observed when one focuses on the energetic tail extent and the total number of electrons which appear to be slightly lower for Al_2O_3 than for $\alpha - SiO_2$. Baring in mind the possibility for an impact ionization mechanism, energies as high as almost 8 times the gap energy have been observed for a 75 fs, which is well above the impact ionization threshold.

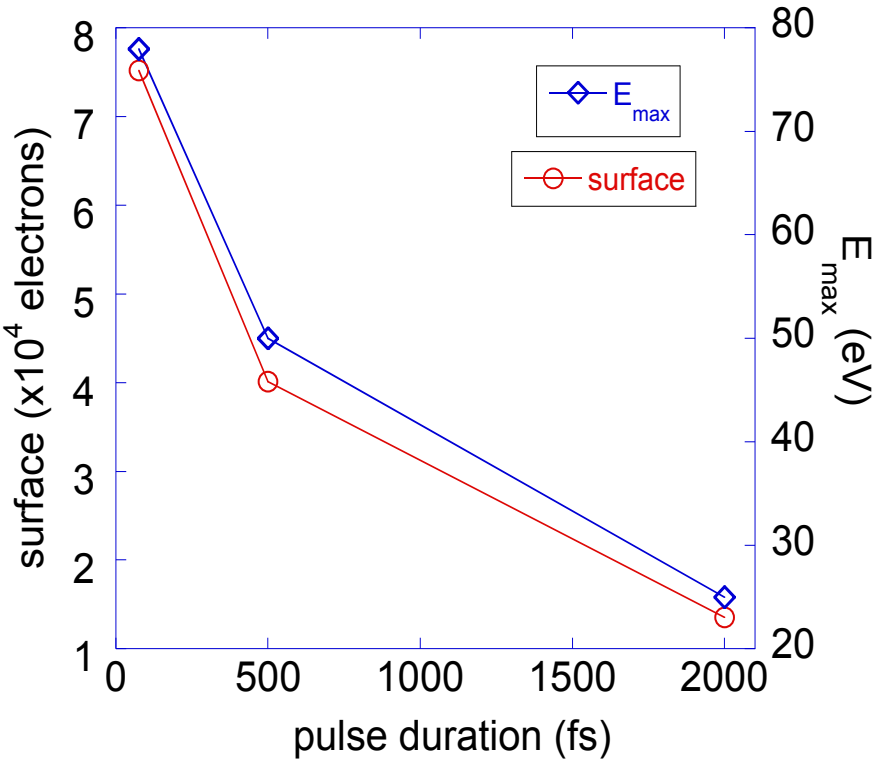

Figure 3.9: Surface, corresponding to the total number of emitted electrons, and maximum kinetic energy measured for different pulse durations in $\alpha - SiO_2$. Processing of data from figure 3.8.

3.4.3 Relaxation dynamics

Based on theoretical results obtained by Daguzan concerning the electron relaxation dynamics in the conduction band, Quere [71] pushed forward the investigation of relaxation times in $\alpha - SiO_2$ by realizing a pump and probe experimental setup to acquire his PE spectra. This double pump scheme involved a VUV pump pulse (38.7 eV, 60 fs) and an IR (1.5 eV, 60 fs) probe pulse with variable delay between them. The idea was to initially excite a certain amount of "free" electrons in the conduction band (with a pump pulse) and then, thanks to the probe pulse and by phonon assisted photon absorption, further excite the electrons. By looking at the spectra for different delays, the relaxation dynamics are probed.

In an attempt to study the electrons responsible for impact ionization, the study has focused on energies above the impact ionization threshold (i.e. above 10 eV). The characteristic times for the pump-probe effect to disappear (IR arriving after VUV) has been measured to be around 10 ps for electrons with energies

around 36 eV. For electrons with lower energies (30.8 eV), this time is even longer, reaching 60 ps [71]. On the contrary, for VUV arriving after IR the characteristic time was of the order of the pulse overlap (85 fs), indicating that no pump and probe effect (IR pulse "probing" the VUV excited material) was present.

During Gaudin's thesis, time resolved experiments have been performed as well using a 40.25 eV pump pulse (600 fs) and an IR probe at 35 fs. Several pump and probe characteristic times have been measured for different electron energies in the conduction band. The remarkable features of this study are : the order of the relaxation time is of some tens of ps and this time is longer for lower energy electrons. The long lifetime observed motivated an explanation involving DIT's taking place at a time scale lower than the time resolution of the experiment thus these experiments might probe already relaxed electrons [36].

3.5 Experimental setup

The experimental setup used is the one illustrated in figure 3.10. It has been conceived in a way that spectra may be acquired under single or double pulse irradiation, with variable pulse delay and pulse duration.

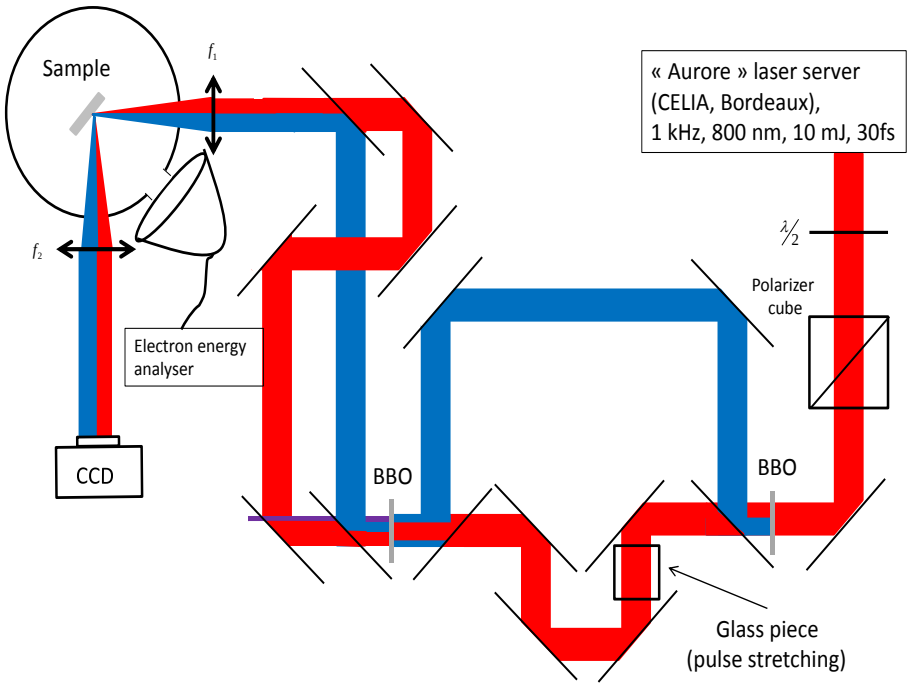

Figure 3.10: Experimental setup used to perform single or double pulse photoemission spectroscopy, see text for details.

A Ti:Sa laser system ("Aurore" server at CELIA, Bordeaux, France) provides 30 fs pulses at 800 nm, at a 1 kHz repetition rate. The pulse energy may rise up to 10 mJ.The combination of a half-wave plate with a polarizer cube allows variation of the pulse energy. The next step is to separate the beam in two parts, one used for the second harmonic generation and one for the IR excitation pulse. The UV pulse is generated in a barium borate (BBO) crystal by frequency doubling and a delay line allows scanning in time with respect to the IR pulse.

The IR pulse may be stretched in time by frequency dispersion from propagation in a fused silica cylinder (glass piece on the figure). The length of the cylinder defines the new pulse duration and in our case 30 and 180 fs IR pulse durations have been used. Finally, the UV and IR pulses enter the vacuum chamber (10^{-9} mbar pressure) and are focused with a 50 cm lens on the sample at a 45° incidence

angle.

In order to vary the delay between the two pulses one needs to know the time zero of temporal coincidence. This is being achieved in two steps. First, the third harmonic is being generated in a BBO crystal to give the pulses coincidence outside the experimental chamber. This is only a large estimate of the real coincidence on the sample since pulses propagation through the entrance window of the vacuum chamber alters the previously found "zero" delay. Then the one pulse is delayed with respect to another while looking at the photoemission signal of the detector. The peak in this signal corresponds to the temporal coincidence of the two pulses.

Another important aspect is the spatial coincidence of the two pulses. For this, an imaging system has been mounted at the exit window of the vacuum chamber allowing detection of the two laser spots with the help of a CCD camera, on the surface of the sample. Meanwhile, another CCD camera gives a global view of the sample within the sample holder, this being the technique used to monitor the damage threshold on the sample.

The photoemission spectrometer is a CLAM 4 ("Combined Lens and Analyser Module") whose entrance axis is normal to the surface of the sample. An electrostatic lens images the electron emission zone on the entrance slit of the analyzer. The collection angle is $\pm 12^{\circ}$. Thus the detection is more efficient for high energy electrons and much weaker for the lower energy ones [32]. The collected electrons are subsequently injected in a hemispherical capacitor with a 15 cm radius. A centrifugal electric field is created by applying a potential difference V across the conductors. As a result, only electrons with an energy HV, H being characteristic of the spectrometer, shall exit the capacitor and be detected. The energy resolution is typically 0.1 eV. The detection system consists of nine channeltrons detecting incident electrons with an energy shift of $\Delta E = 0.02135 \times H \times V$ between two consecutive detectors.

3.6 Experimental results and discussion

Our study has focused on $\alpha - SiO_2$, material widely studied in the literature, although experiments have been performed on Al_2O_3 as well but their understanding is not yet mature enough to be exposed.

In the first place, we measured the photoemission signal for a short (30 fs) UV pulse, a short IR (30 fs) pulse and then the sequence of both pulses coinciding in time on the sample's surface. The data acquired are plotted in figure 3.11. Clearly a combined (pump and probe) effect can be observed when both pulses are present. A rise of the order of 11 eV in the maximum electron kinetic energy is possible, extending the spectrum up to 18 eV (almost twice as much as the band gap).

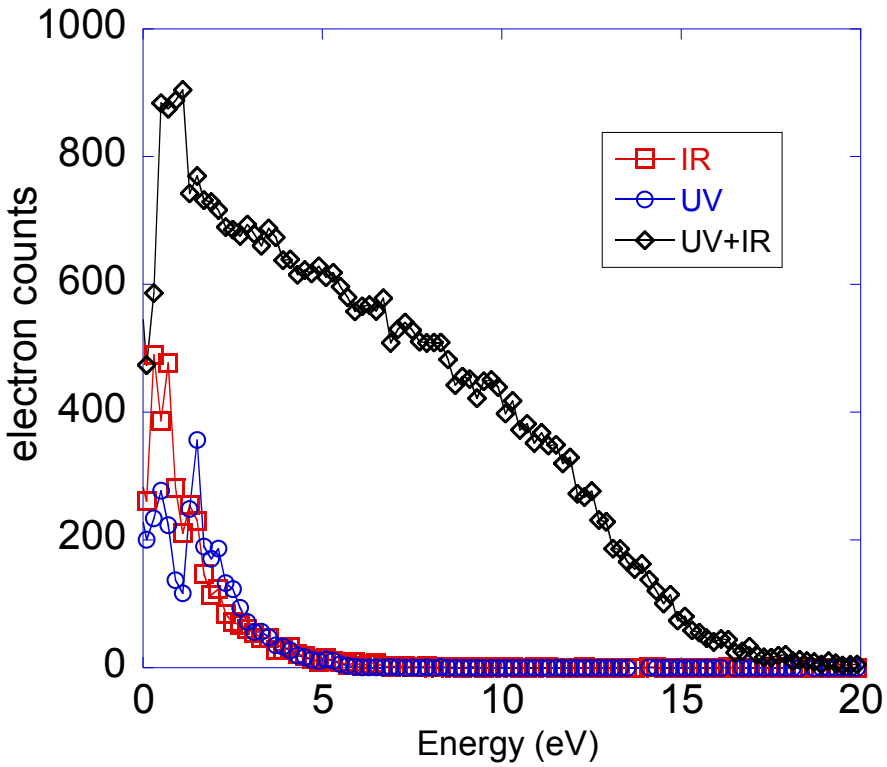

Figure 3.11: Photoemission signal as a function of the electron kinetic energy in $\alpha - SiO_2$. UV: 30 fs pulse duration, 0.01 J/cm^2 fluence); IR: 30 fs, 0.29 J/cm^2) and UV along with IR at temporal coincidence, below DTH.

The same experimental data set has been used to extract information about the relaxation time of electrons in the conduction band for each individual kinetic energy. This time is characteristic of the extinction of the pump and probe effect of the photoemission signal. The results are presented in figure 3.12. Typically,

relaxation times vary from 30 to 180 fs and it appears to be faster as the electron energy grows higher.

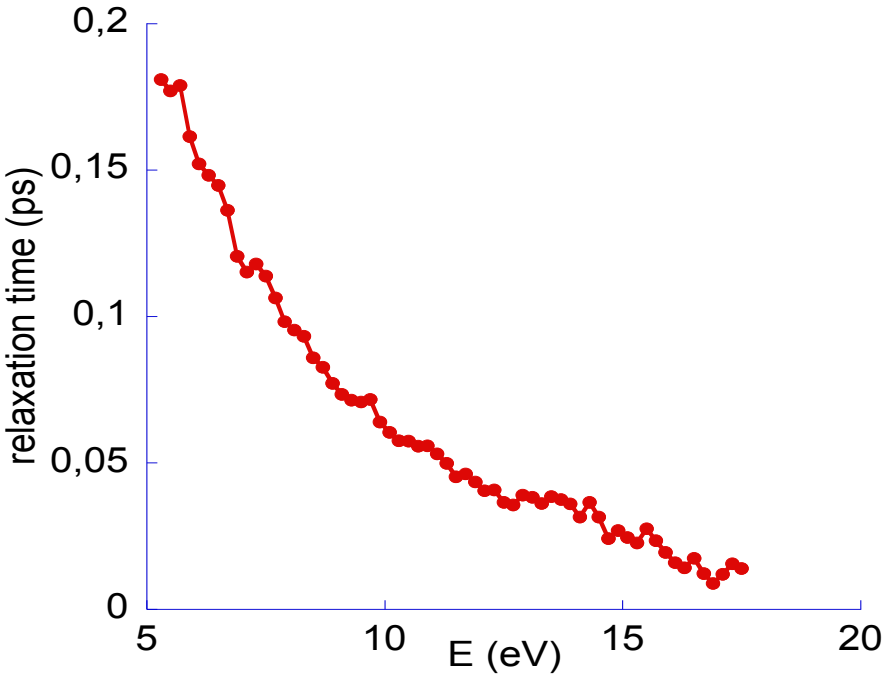

Figure 3.12: Relaxation time of electrons depending on their kinetic energy in $\alpha - SiO_2$. Irradiation parameters are the same as in 3.11.

Figure 3.13 illustrates the interaction process in our experimental conditions. Initially, the band-to-band transition of electrons is assured presumably by the UV pulse through multiphoton absorption. Then, and for a limited time, the IR (and/or the UV itself) pulse excites these carriers by inverse Bremsstrahlung. Relaxation takes place at characteristic times mentioned above, depending on the electron's kinetic energy. Our results, in terms of relaxation times, are in accordance with the simulations by Daguzan using a quantum model for electrons with energies up to 5 eV.

The existing models allowing calculation of relaxation times for higher energy electrons (Quere) give higher values, in the picosecond range. Potentially, reviewing the population loss parameter A, previously independent on kinetic energy, used in this model may be the response. In that case, impact ionization would partially contribute in a faster relaxation.

As far as the relaxation dependence on electron kinetic energy is concerned, our results suggest a slower relaxation for lower energy electrons. This observation has been universally true for photoemission experiments made previously (see 3.4.3) in the 30 eV kinetic energy range. A possible explanation is the one already given

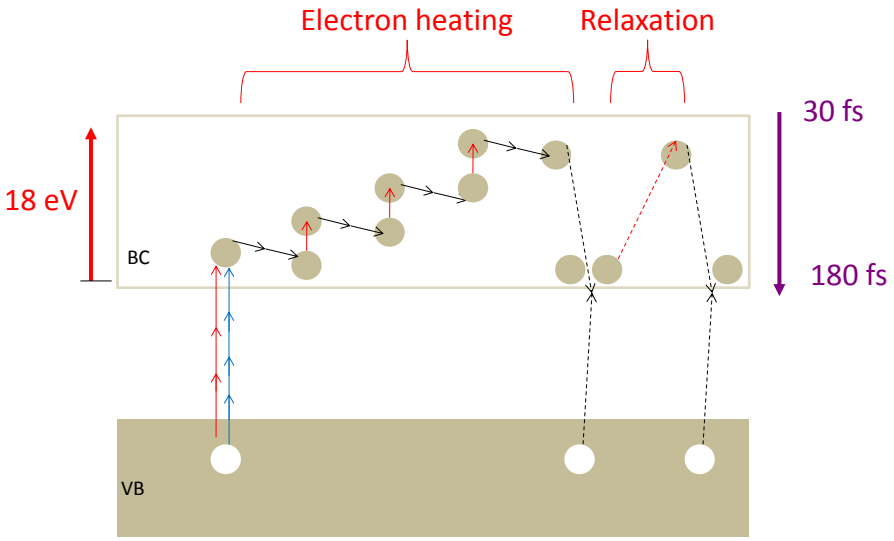

Figure 3.13: Schematic description of the interaction process of a train of pulses with a dielectric. Electrons are promoted in the conduction band by multiphoton absorption and they are acquiring further energy by inverse Bremsstrahlung. Relaxation processes may include impact ionization or other inelastic collision mechanisms (electron-phonon).

by J.Gaudin [32], suggesting that the number of electrons having lower energies decreases slowly. This is because the higher energy electrons, that contribute to the lower energy signal by relaxation, need more time to lose their kinetic energy.

A dramatic increase in the total number of electrons (integrals of the curves), for the sequence of the two pulses, is observed as well.

The next step, was to stretch the IR pulse to 180 fs and repeat the measurement at higher intensities, still under the damage threshold though, (see figure 3.14). Once again, a crossed effect is visible at zero delay between the two pulses, this time obtaining electrons with kinetic energies up to 50 eV, although with each respective pulse alone maximum kinetic energy didn't rise over 38 eV (for UV). Once again this result suggests that the previously proposed heating mechanism is possible.

In figure 3.15, we have plotted the photoemission signal as a function of the UV-IR pulses delay at two given kinetic energies : 35 and 42 eV. The widths of the observed peaks are of the order of the pulse intercorrelation.

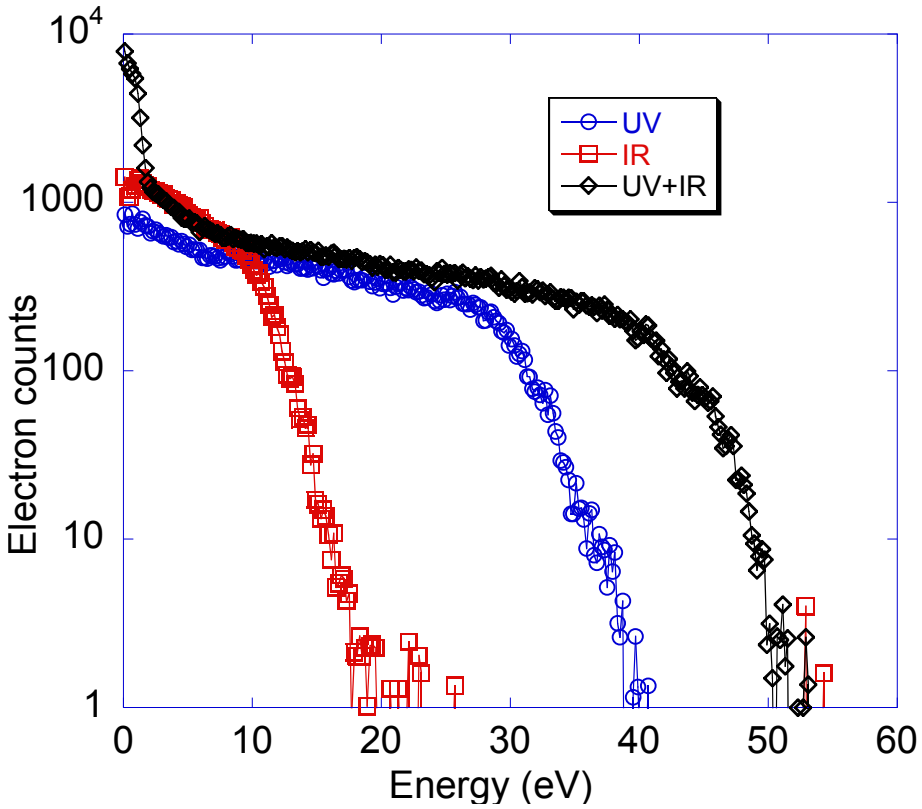

Figure 3.14: Electron counts versus electron kinetic energy in $\alpha - SiO_2$. IR: 200 fs duration, 2.2 J/cm^2; UV: 30 fs duration, 0.03 J/cm^2 and UV along with IR at zero time delay, below DTH.

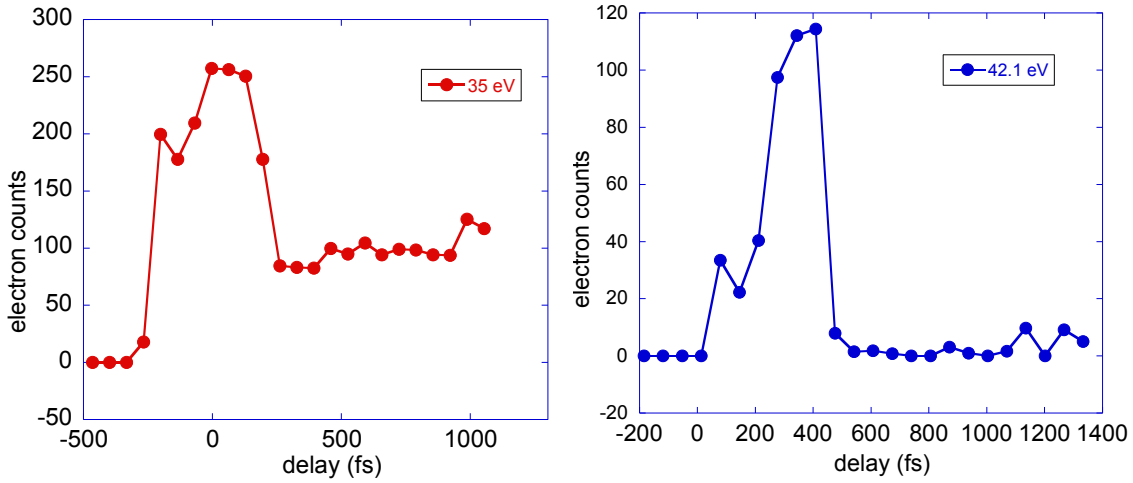

(a) Electrons with an energy of 35 eV.

(b) Electrons with an energy of 42 eV.

Figure 3.15: Photoemission signal as a function of the pulse UV-IR pulse delay at a given electron kinetic energy, in $\alpha - SiO_2$. Negative delay values correspond to IR arriving first. Irradiation parameters are the same as in 3.14.

3.7 Conclusion

The experiments with a single pulse, for several pulse durations at threshold, have indicated that the electron kinetic energy drops for longer pulse durations. This suggests that energy deposition is achieved in two ways, depending on the pulse duration:

- For short pulses ($\sim$ 75 fs), the electron heating mechanism (multiphoton) is more efficient than the relaxation rate, resulting in electrons occupying high energy levels in the CB.
- On the other hand, for long pulses ($\sim$ 2 ps) most probably the sequence of 1-photon absorption and subsequent cooling prevents transitions to higher levels and thus the electrons stay on the bottom of the CB.

The effect is the same (damage) but it may happen in two different ways.

The same experiments have allowed the observation of "hot" electrons, with energies several times the band gap energy, in both $\alpha - SiO_2$ and Al_2O_3.

Focusing on $\alpha - SiO_2$ we have measured the electron kinetic energy spectra with double-pulse (UV+IR) sequences, in an attempt to verify the idea of electron heating in the CB, used in our interpretation of the interferometry experiments (see 2.3.2). This study has been made with pulse sequences at intensities below the damage threshold suggesting that at higher intensities (joining the irradiation regime for interferometry experiments) the heating mechanism, presumably by inverse bremsstrahlung or DIT, may be more effective. A coherent effect has been observed: the "heating" is more efficient for temporally overlapping pulses. The final energies reached are well above the impact ionization thresholds commonly considered ($2 \times E_g$). Thus, the hypothesis developed in 2.3.2 is validated.

Characteristic relaxation times for 5-15 eV electrons may be interpreted in terms of electron-electron scattering. However, the estimated value for 8 eV electrons: 0.3 fs^{-1}[57] seems to overestimate the relaxation stage resulting in a time of 26 fs, although we observe a characteristic time of $\sim$ 100 fs. This is because electron energy relaxation is a step process with higher energy electrons conceding their energy and thus they accumulate at lower energy levels.

Chapter 4

Damage morphology studies in SiO_2

The aim of this chapter is to present the results of the surface morphology experimental studies in $\alpha - SiO_2$, upon ultrashort laser pulse irradiation. The conditions under which these results were obtained may be globally divided in two categories: single and double pulse irradiation for two different wavelengths centered at 400 nm (UV in text) and 800 nm (IR in text). In this framework, different parameters related to the irradiation characteristics have been probed and these involve: pulse duration (50 fs -10 ps), number of shots (1-20 shots per spot) and pulse delay (0-1 ps). Finally, the damaged surface area is characterized by means of SEM.

4.1 Introduction

Previously, we have discussed the different mechanisms involved in the laser-matter interaction, by the intermediate of electron excitation, subsequent heating and eventually recombination or trapping. The irradiated material finds its intrinsic properties modified as a result of this interaction and a permanent modification of the solid may take place. Furthermore, with stronger laser intensity regimes on the surface of the material, accumulation of energy may induce the damage of the irradiated area and even the ejection of matter leading to ablation. Thus, studying the morphology of the laser-induced modifications of the surface may allow going back to the mechanism initially responsible for damaging, often disputed in literature in either being a solid phase transition and/or coulomb explosion.

Damage has been reported to be of different nature depending on the laser pulse duration regime [66], often calling for an athermal ablation in the femtosecond time scale, while the more common melting feature has been used for longer pulses (nanosecond sale). The transition region between these two regimes has attracted our interest and thus the surface morphology has been investigated as a function of the pulse duration using a single, intense and linearly-polarized IR pulse.

Additionally, energy accumulation has a significant effect on the damage morphology and therefore a second part of our investigation involves the study of the number of shots per irradiated spot area parameter to account for these effects.

Finally, the double-pulse scheme used in both interferometry and photoemission experiments has motivated one last series of experiments consisting in looking at the surface morphology as a function of the two pulses relative delay. As we will prove, probing the fast-varying (tens to hundreds of fs) excitation density and electron energy, in some materials, at different delays leads to a difference in the observed damage pattern and/or size, through the intermediate of different mechanisms being involved.

Although many materials have been studied, a more thorough investigation has been performed on the surface of $\alpha - SiO_2$ for several reasons. First, this material has been already well studied in literature and by our group. Thus the solid background acquired is expected to allow safer interpretation of the obtained results. More importantly, extended studies on fused silica have revealed remarkable features. Self-organized structures have been observed on the surface [44, 84, 34] as well as in the bulk material [88, 101, 34]. The formation of laser induced periodic surface structures (LIPSS) of two types have been reported in literature: so-called low spatial frequency LIPSS (LSFL) with a periodicity (Λ) close to the irradiation wavelength λ and high spatial frequency LIPSS (HSFL) with periods significantly smaller than λ [11]. For the above-mentioned reasons, our studies have focused on $\alpha - SiO_2$ and these results will be presented in 4.3. Recently, the surface morphology has been studied under double-pulse irradiation [15, 81, 41] and these results

suggest a connection between induced modifications and the electron dynamics. This type of study has been included in our research as well.

4.2 Experiment

The experimental setup employed for the morphological study is the same as the one already used for time-resolved interferometry experiments (see chapter 2) in its simplified version. We remind that a Ti:Sapphire laser system provides linearly polarized pulses at λ=800 nm with a pulse duration τ=60 fs. The repetition frequency is 20 Hz. Later, the beam is divided in two parts using a beam splitter (variable reflection/transmission ratios): one is used to generate the second harmonic in a BBO crystal at a central wavelength of λ=400 nm, called UV in what follows. The rest of the IR beam goes through a compressor and hence the pulse duration may be varied over a 50 fs-10 ps interval. Both beams are focused on the surface of a wafer sample (10 mm $\times$ 10 mm $\times$ 0.5 mm), at normal incidence, using an achromatic setup consisting in the association of two converging lenses. An electromechanical shutter is used to select the number of the desired shots (N). Finally, there is possibility to translate the sample in all x,y, and z directions using motorized translation stages. The imaging system allows inspection of the surface and definition of the DTH energy.

Once again the zero delay is defined by generating the third harmonic with both beams, in a BBO crystal. The delay between the two pulses may be varied by translating a delay line on the IR path: negative delays correspond to the IR beam arriving before the UV beam on the sample (i.e. -1 ps), while for positive delays the IR beam arrives afterwards, this delay being limited by the length of the delay line. For the experiments described, the maximum delay between the pulses did not exceed 2 ps. The experiments involving a double-pulse sequence always satisfy a condition: UV and IR energies are kept below their SDTH and only the combination of the two pulses results in modification/damaging of the surface. This is actually emanating from the interferometry experiments, performed in the same conditions.

Each spot on the sample surface is irradiated with a given number of single-pulse or double-pulse shots N and it is then vertically translated for the next spot to be irradiated. Thus, in the end different columns, in an xy plane perpendicular to the beam propagation, on the sample allow study of different parameters. Finally, we perform SEM[1] to characterize the sample [65]. The secondary electrons are detected thus revealing the topography of the sample. However, in the case of dielectrics the use of an electron beam on the surface results in accumulation of negative charges (space charge effect) that interact with the incoming electrons and this considerably deteriorates the quality of the image. Other than the metallization of the sample (not our case), a careful choice of the electron emission related parameters: electron flux related to electric current of the electron gun and

[1]MEB-FEG Ultra 55 CARL ZEISS, financed by "Ile de France" region

the aperture size along with the electron energy associated with the high-voltage applied to accelerate them. Additionally, filters may be used to detect electrons in different energy intervals. In all cases, spending a long time on a given surface contributes to the charging and darkens the obtained image.

These results are now going to be presented in the following section.

4.3 Results

In this section we will expose our experimental findings while studying the $\alpha - SiO_2$ surface morphology. The SEM images included hereby contain a white box in the bottom containing all the microscopy related parameters. In particular, the spatial scale is visible on the left, followed by the image magnification (Mag), the high-voltage applied (EHT), the distance of the emission tip from the surface of the sample (WD), the detection mode (Signal A) and the aperture size. Images with higher magnification used for closer examination of interesting features will be often included in the same image as an inset with red or yellow borders.

The section is divided in three parts corresponding to three different parameters being investigated. Starting from the pulse duration, next is the number of pulses and finally the double-pulse delay (Δt). Unless if it is clearly stated otherwise, polarization for both pulses has been kept horizontal.

4.3.1 Pulse duration study

At first, we have used a single IR pulse (N=1) per spot to irradiate the surface. Figure 4.1 presents the induced modification with a 60 fs IR pulse at 150% of the SDTH. At this pulse duration, the interaction is supposed to be this of a laser with a solid. The start of a ripple formation is observed on the periphery of the irradiated spot, along with the presence of nano-filaments pointing outwards. Next, we have chosen to investigate the 1-10 ps pulse duration interval, where the laser pulse is supposed to interact with the excited electron-hole plasma (density is less important than in the fs regime). The pulse energy is maintained at ∼SDTH for all pulse durations.

The induced modification is illustrated in figure 4.2 for the first two pulse durations τ=1 ps at fluence of $F = 6.5$ J/cm^2 (4.2a) and τ=2 ps at fluence of $F = 6.4$ J/cm^2 (4.2b) where bubble-like patterns are being observed. Their diameter is in the 10-300 nm range and their density seems to be higher in the center of the laser spot (~ 60 μm). Also the bubbles in 4.2b are darker inside suggesting a deeper modification.

The second figure 4.3 shows the result with a τ=5 ps pulse at $F = 9$ J/cm^2 (4.3a) and a τ=10 ps pulse at $F = 10$ J/cm^2 (4.3b). Once again we observe this "bubble" formation(visible outside the center) but this time they have grown larger in size (~ 500 nm), while a new structure may be seen in the very center: the "bubble" density being higher, their peripheries seem to have combined with each other to form the observed pattern (inset of 4.3a). Strangely, there is a visible line where "bubbles" have formed in a raw (region delimited by two yellow segments). However, this formation may be attributed to pre-existing defects such as scratches from polishing or other. In the very center, there is relief absence.

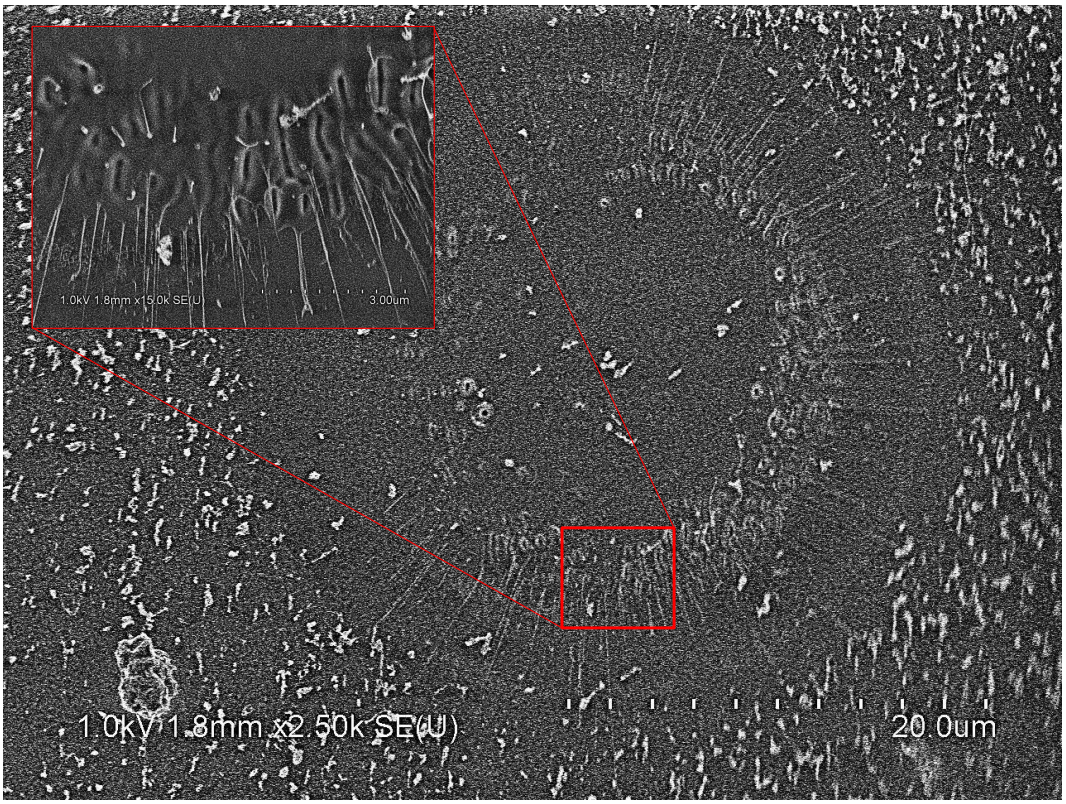

Figure 4.1: SEM image of SiO_2 irradiated with a single IR pulse. Pulse duration is τ=60 fs and fluence at $F = 1.2$ J/cm^2 (corresponding to 150% of the SDTH).

The 10 ps pulse gives more "bubbles-formed-in-a-line" structures and these have been highlighted by yellow segments as well (inset of 4.3b). However, in this case the bubble density is considerably lower while some layer removal has taken place (absence of relief in the center).

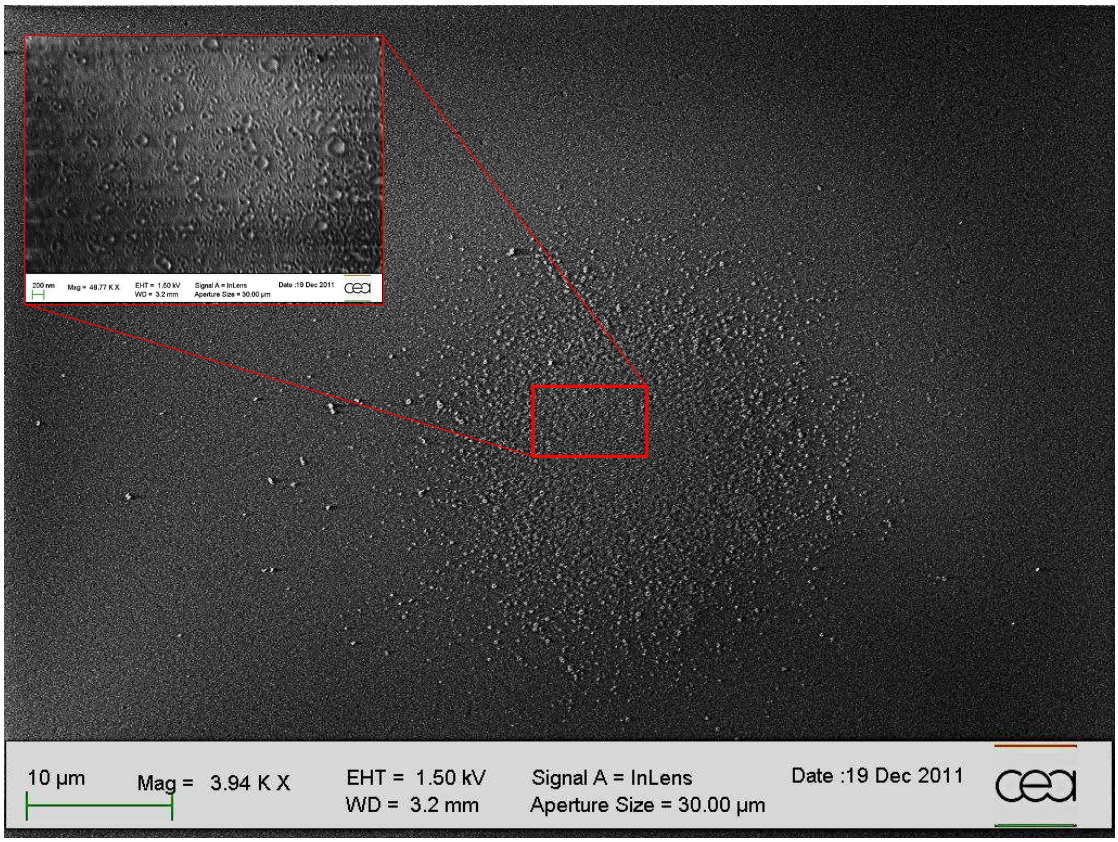

(a) τ=1 ps and $F = 6.5$ J/cm^2

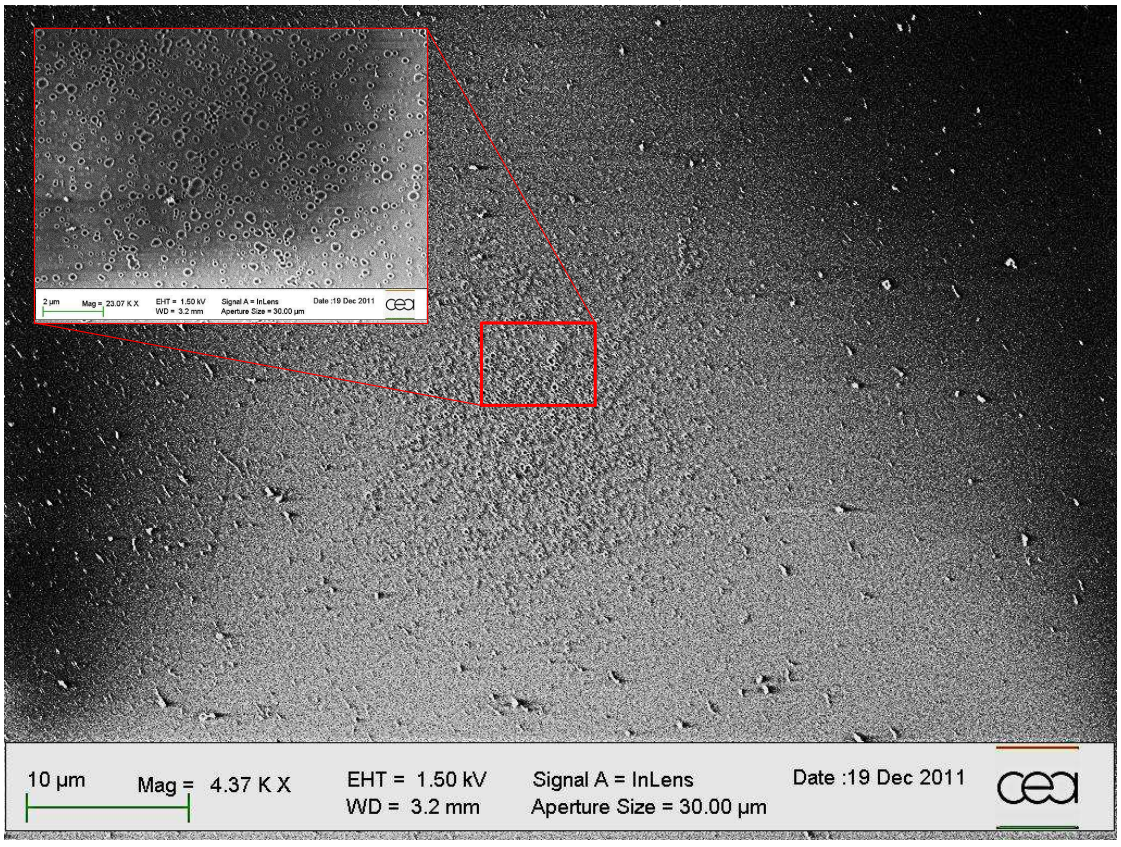

(b) τ=2 ps and $F = 6.4$ J/cm^2

Figure 4.2: SEM image of SiO_2 irradiated with a single IR pulse. Two different pulse durations: 1 and 2 ps with different fluencies are exposed.

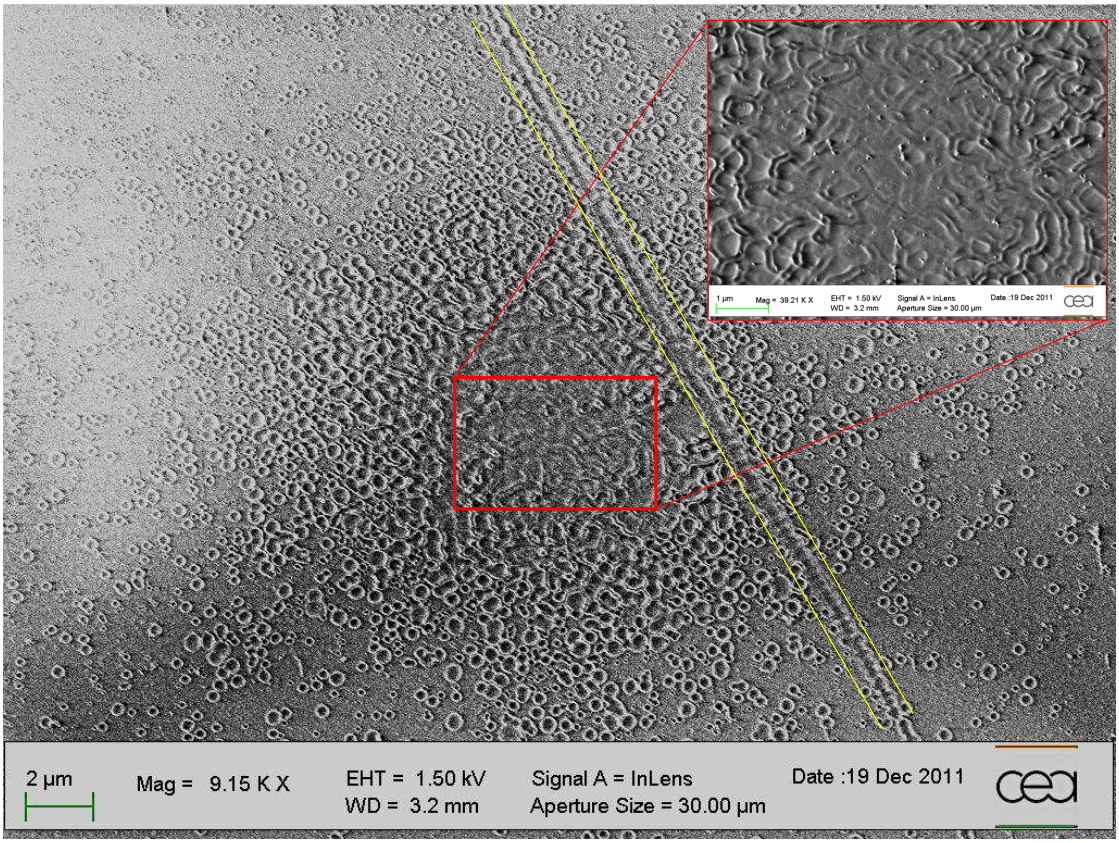

(a) $\tau = 5$ ps and $F = 9$ J/cm^2

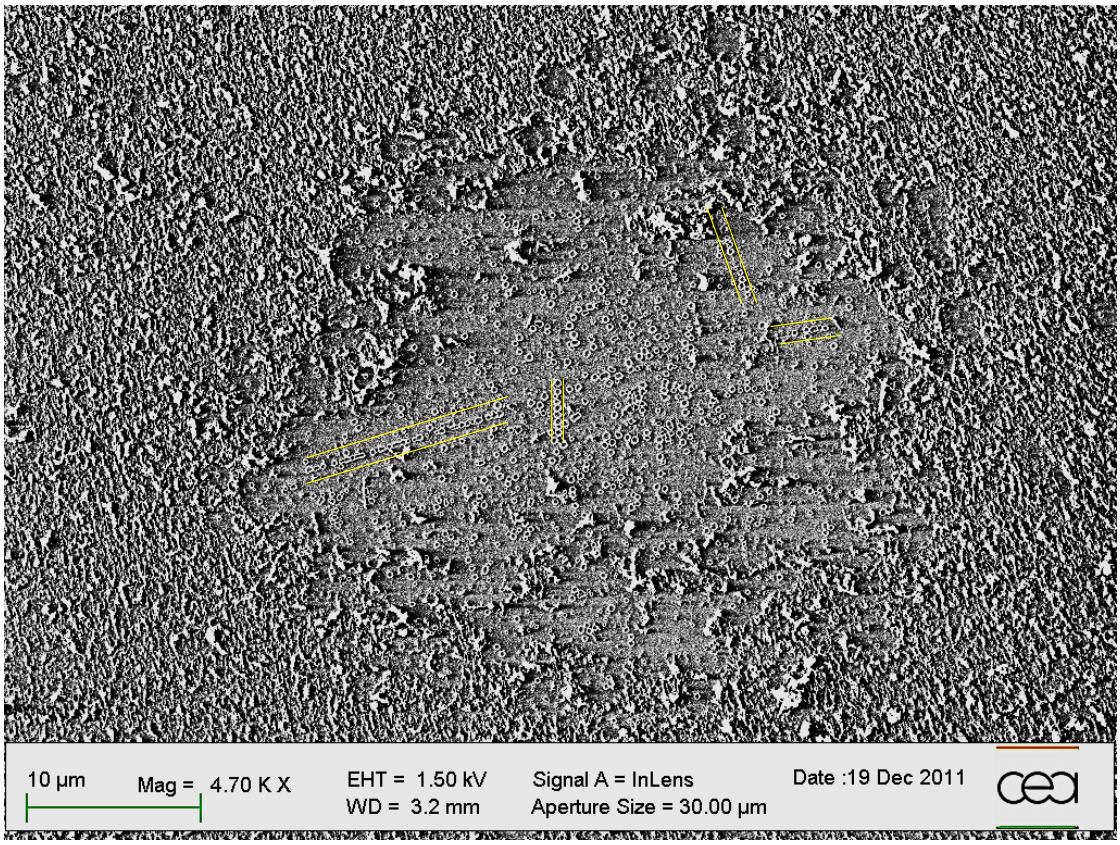

(b) $\tau = 10$ ps and $F = 10$ J/cm^2

Figure 4.3: SEM image of SiO_2 irradiated with a single IR pulse. Two different pulse durations: 5 and 10 ps with different fluencies are exposed.

4.3.2 Number of shots

Our next focus has been the number of shots (single-pulse or double-pulse sequence).

Single pulse study

This time the pulse durations are fixed: $\tau = 300$ fs for IR and $\tau = 60$ fs for UV and so is the fluence: $F = 5.6$ J/cm^2 (for IR) and $F = 3.1$ J/cm^2 (for UV). These fluencies correspond to 130% of the SDTH. The IR polarization is vertical and the UV horizontal. The laser spot sizes are: $90\mu m$ for IR and $27\mu m$ for UV.

The morphology changes with IR pulses is illustrated in figures 4.4 and 4.5 for N$= 2 - 20$ shots. For N$= 2$ (see figure 4.4a), a "pimple" pattern is observed[2] on the periphery of the spot, with filament formation, as if they had been dragged out of the "pimples" and pointing outside the irradiated area. Raising N, results in a LIPSS formation parallel to the beam polarization in the center of the spot, with periodicity of the order of λ suggesting LSFL. Outside that area, HSFL is observed, perpendicular to LSFL and to the beam's polarization. Taking N$= 10$ (see figure 4.5a) enhances the ripple formation, keeping the same characteristics as before. Finally, for N$= 20$ (see figure 4.5b) the LSFL give their place to disordered molten-like matter while the outer HSFL is kept constant with 250-400 nm periodicity.

The same kind of study has been performed with another wavelength (UV), in horizontal polarization and the results can be found in figures 4.6, 4.7 and 4.8. The same "pimple" pattern with filaments pointing outwards is observed for N$= 2$ (see figure 4.6a) on the periphery of the irradiated spot, while LSFL start to form in the same part for N$= 3$ (see figure 4.6b) along with the previously mentioned modifications. At this stage, the pulse's impact is similar to sending to paint ball impact on a wall: filaments being analogous to paint lines. When N is raised to 5 (see figure 4.7b) the ripple formation spreads to the center of the spot although at least one pulse has hit an adjacent area (two "paint ball-like" spots may be observed). At N$= 10$ (see figure 4.7b), LSFL are formed everywhere, quasi-parallel to the beam's polarization and with periodicity around 400 nm ($\sim \lambda$). Let us mention however the absence of HSFL on the periphery. For N$= 20$ (see figure 4.8), the ripples arrange themselves in the same angle, slightly different to the previous case. Once again, no sign of HSFL has been observed.

Concluding the UV case, we have plotted the damaged surface as a function of the number of shots in figure 4.9 and one can see a high rate increase around 1-10 shots while the slope is getting smoother above. The damaged area increase is synonym of the rippled area increase as well.

[2]Actually our previous work has reported sizes in the 10-30 nm scale

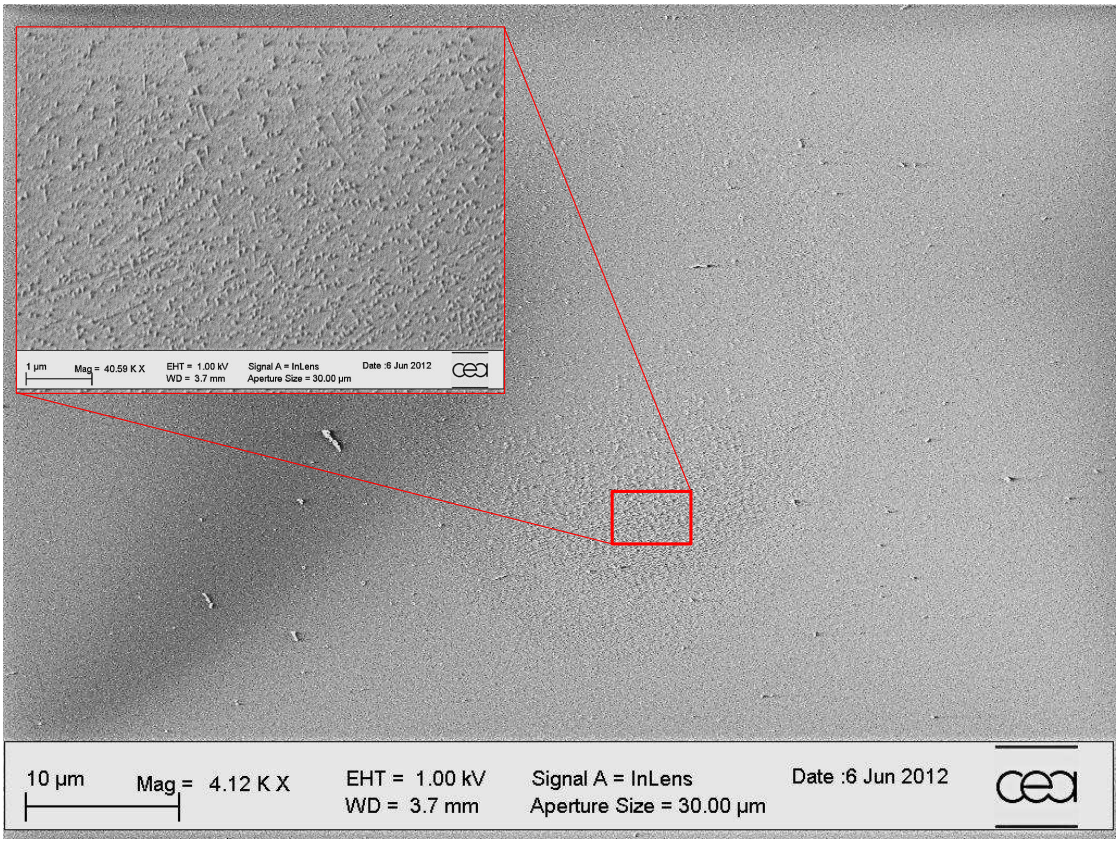

(a) N= 2

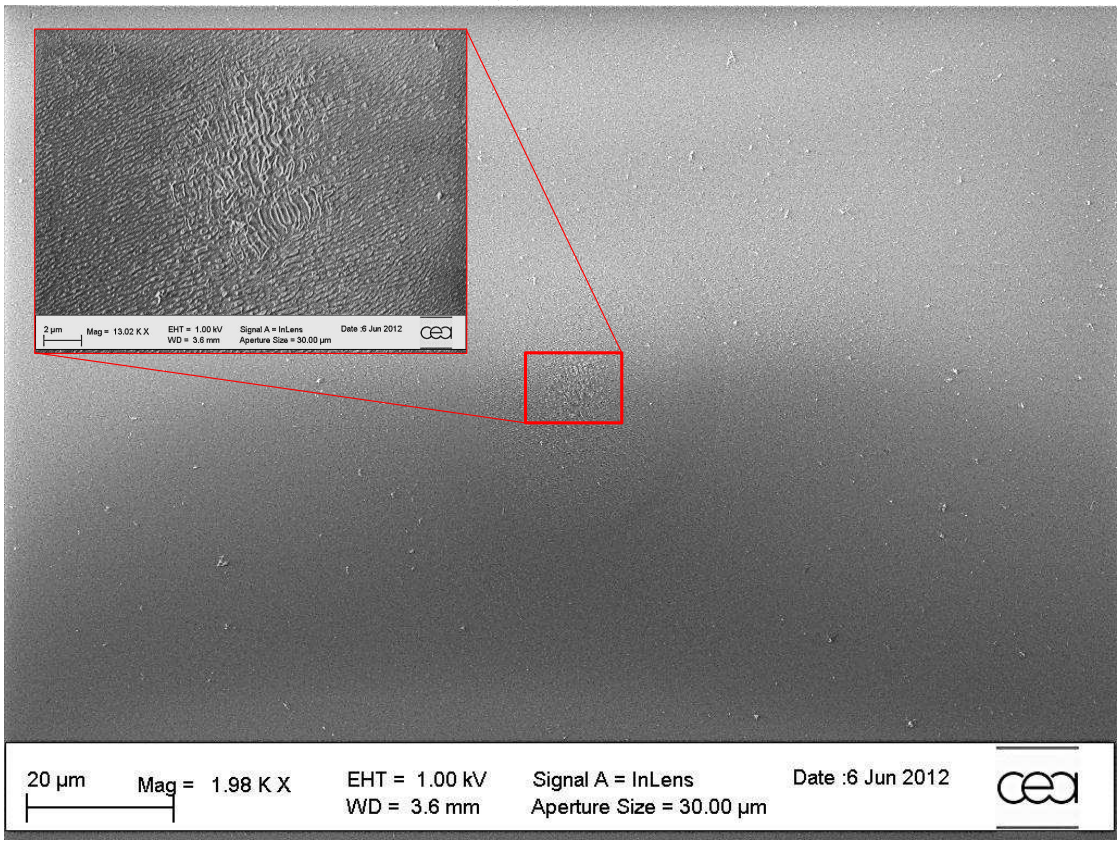

(b) N= 5

Figure 4.4: SEM image of SiO_2 irradiated with N= 2 and N= 5 shots of IR pulses ($\tau = 300$ fs), at a fluence of 5.6 J/cm^2.

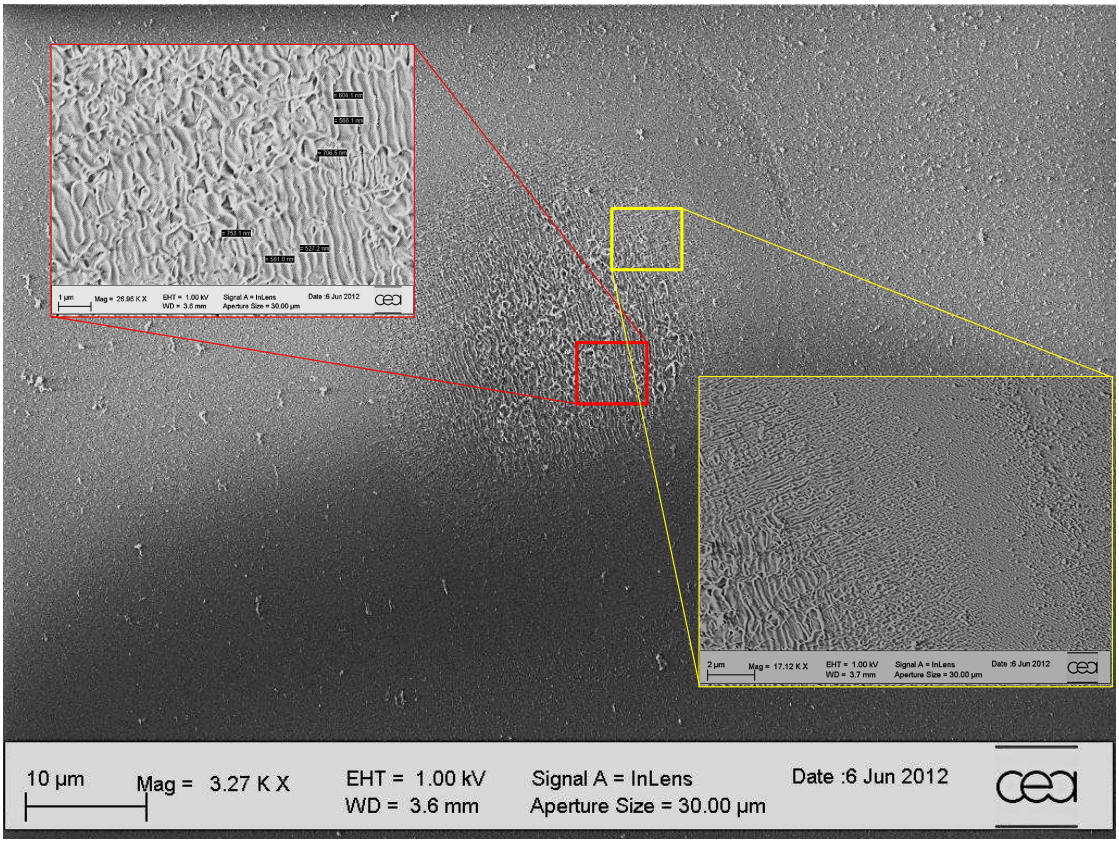

(a) $N = 10$

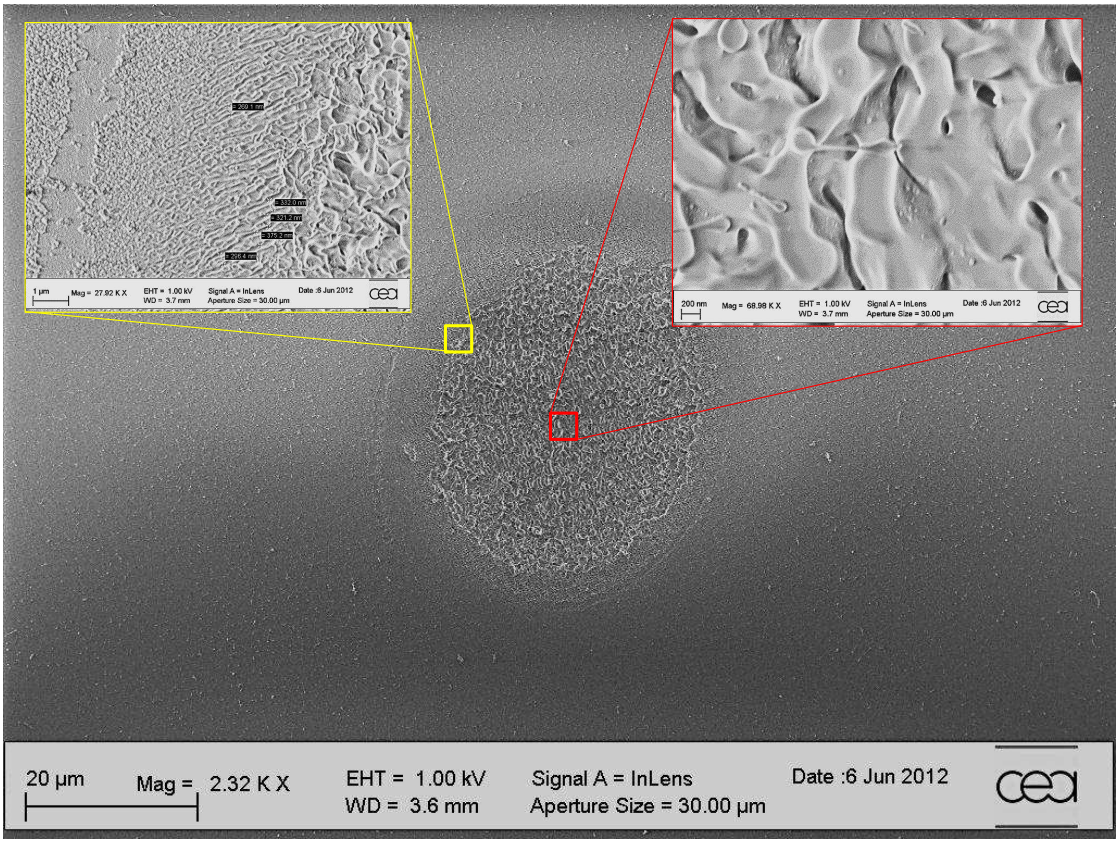

(b) $N = 20$

Figure 4.5: SEM image of SiO_2 irradiated with $N = 10$ and $N = 20$ shots of IR pulses ($\tau = 300$ fs), at a fluence of 5.6 J/cm^2.

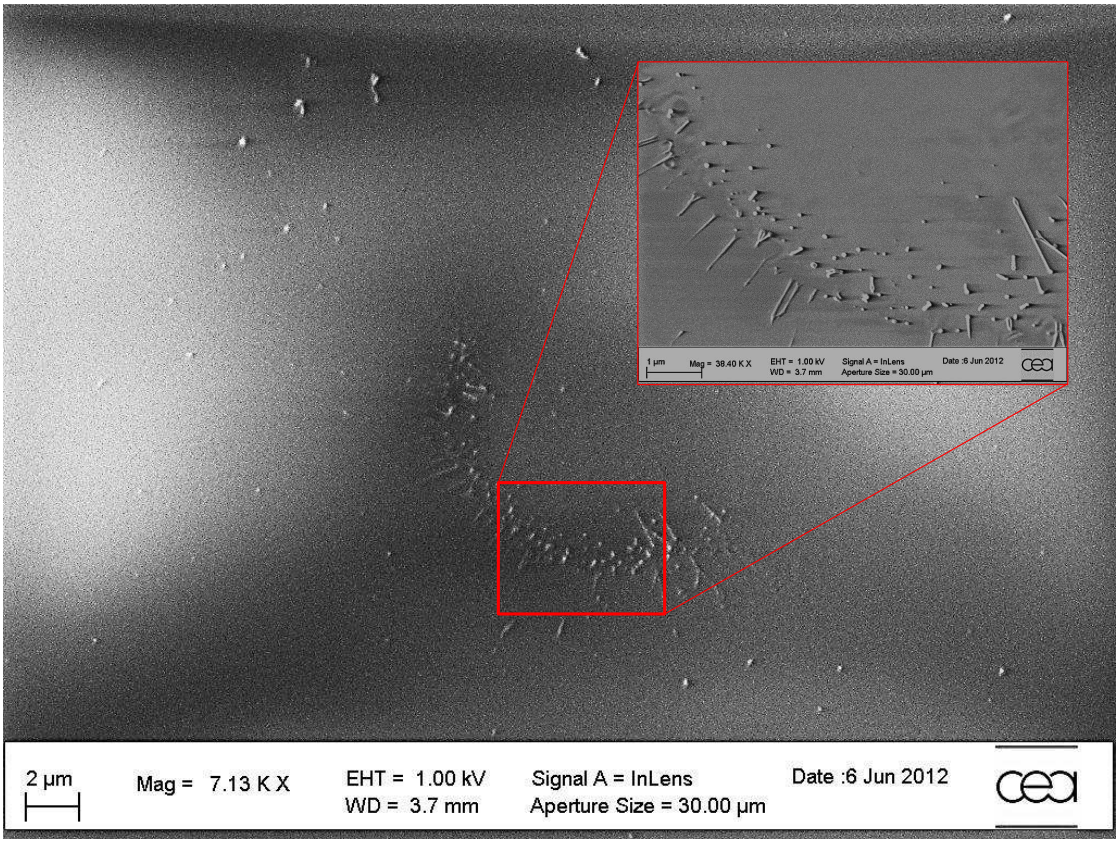

(a) $N = 2$

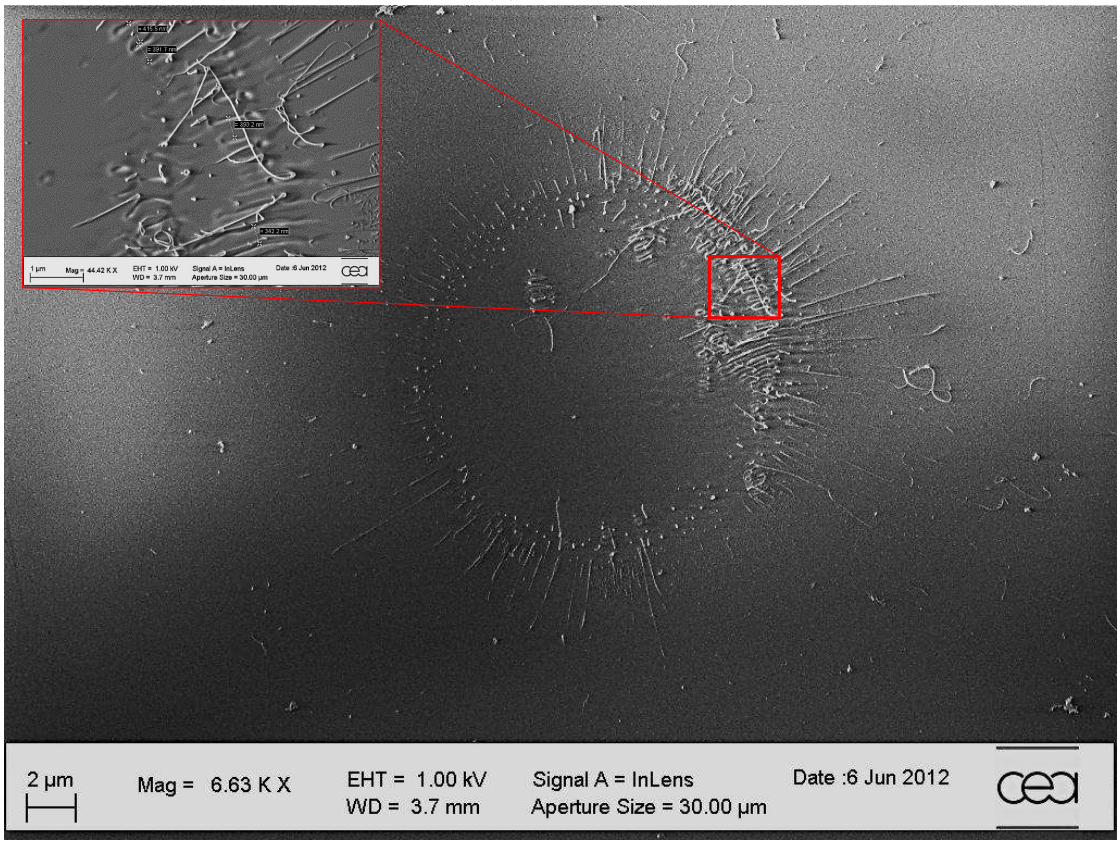

(b) $N = 3$

Figure 4.6: SEM image of SiO_2 irradiated with N= 2 and N= 3 shots of UV pulses ($\tau = 60$ fs), at a fluence of 3.1 J/cm^2.

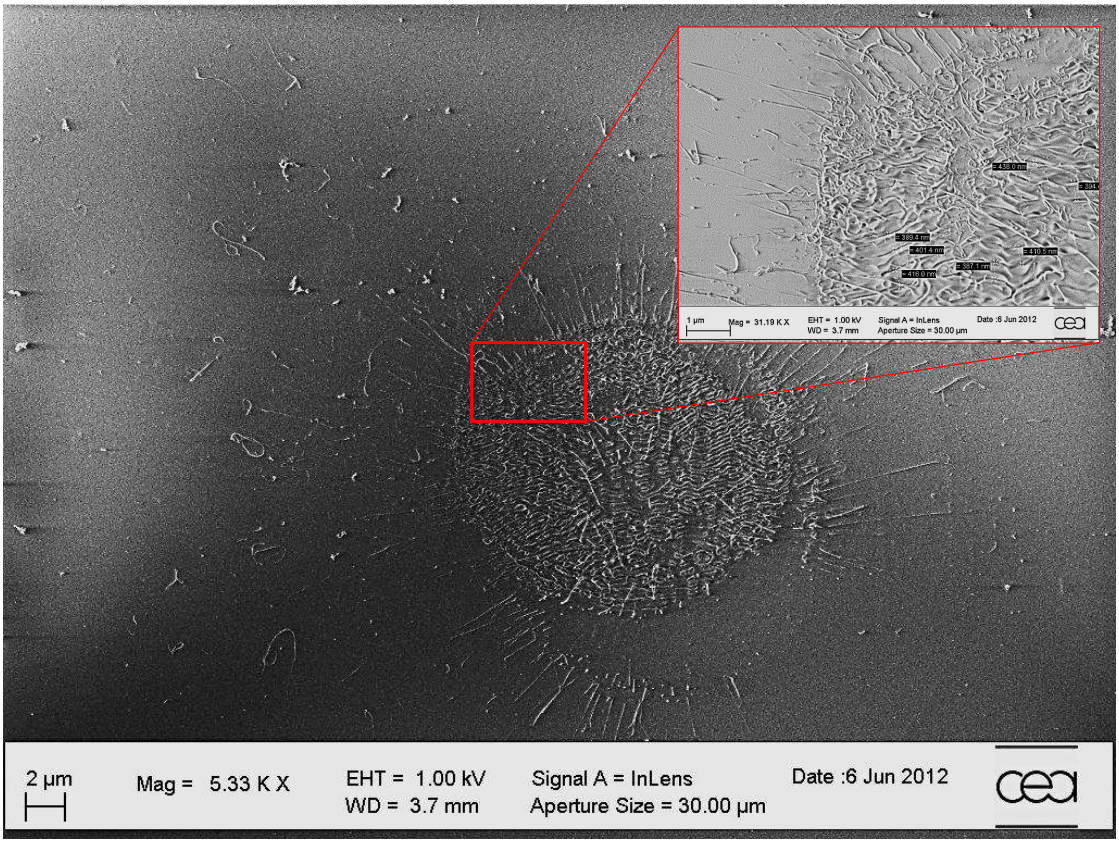

(a) $N = 5$

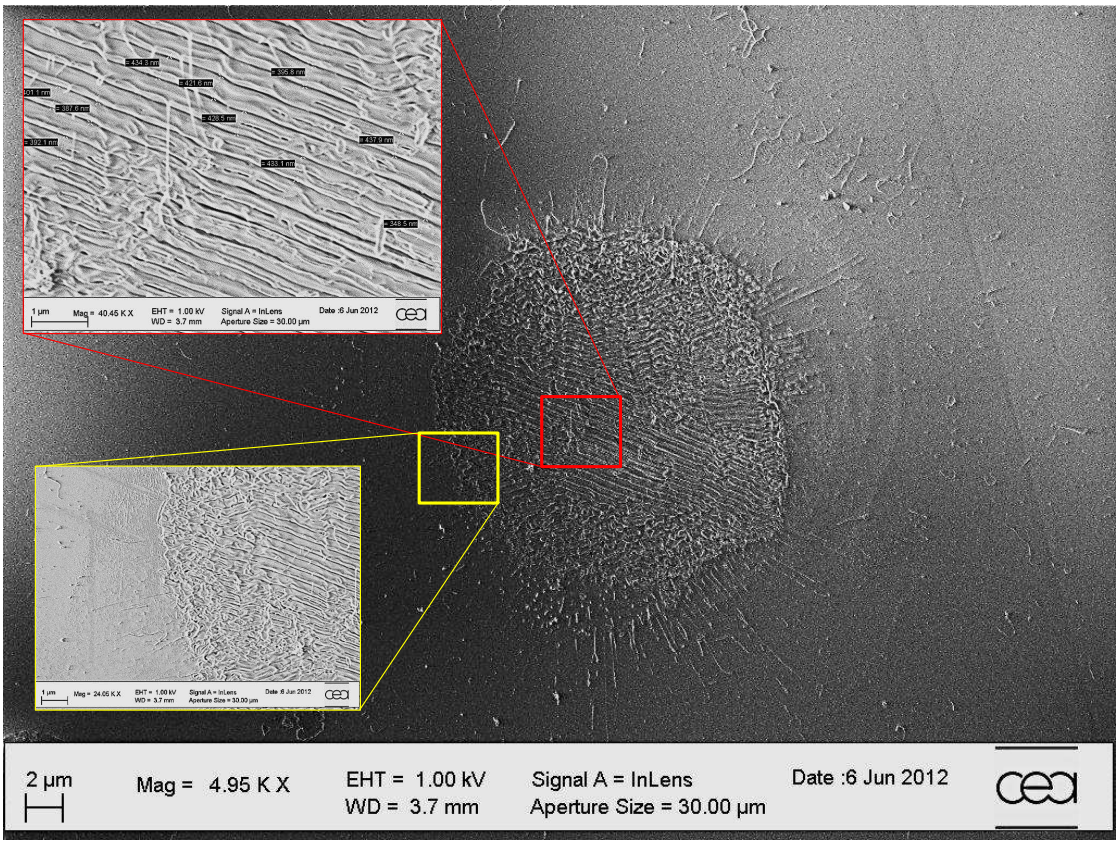

(b) $N = 10$

Figure 4.7: SEM image of SiO_2 irradiated with $N = 5$ and $N = 10$ shots of UV pulses ($\tau = 60$ fs), at a fluence of 3.1 J/cm^2.

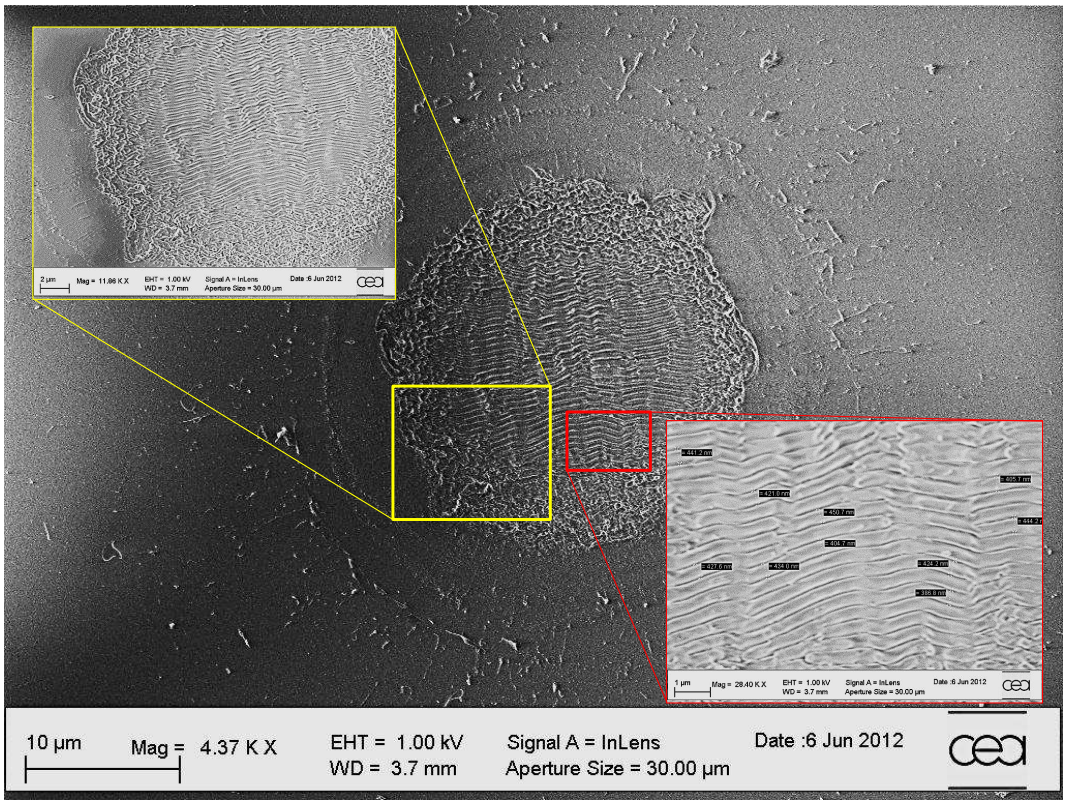

Figure 4.8: SEM image of SiO_2 irradiated with N=20 shots of UV pulses (τ = 60 fs), at a fluence of 3.1 J/cm^2.

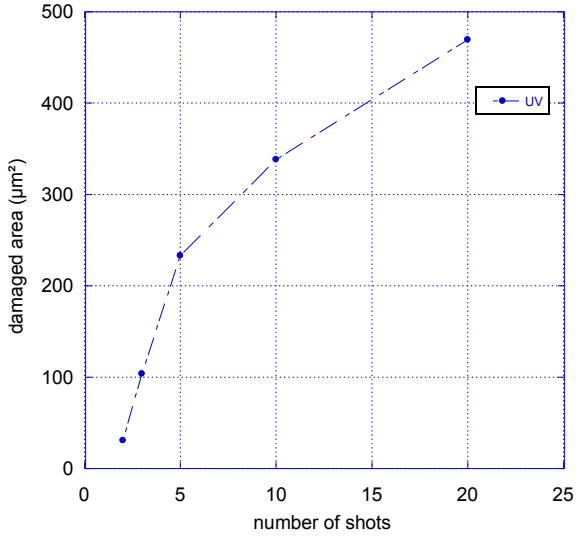

Figure 4.9: Damaged area as a function of the number of shots for a UV pulse, of duration τ= 60 fs, at a fluence of 3.1 J/cm^2

Double-pulse study

For the last case of this study, we combine the two pulses (UV and IR) separated by Δt = 200 fs. Concretely, this corresponds to the same conditions as the ones used in interferometry experiments to observe the impact ionization. As for the respective fluencies, these are lowered compared to the previous experiments so that the total fluence is kept at 130% of the CDTH, while no modification takes place with each pulse alone. In figure 4.10, we are presenting the results obtained for three different N: 5, 10 and 20. For N= 5 (see figure 4.10a), we observe the point pattern spread all over the irradiated area as well as some filaments pointing outwards. More surprisingly, we observe HSFL without LSFL which was not the case for single pulses. Its orientation is perpendicular to the UV polarization as before. Raising N= 10 (see figure 4.10b), enhances the HSFL formation on the periphery, while in the center of the irradiated spot we observe some random pattern of disordered matter. Finally, when N= 20 (see figure 4.10c) the LSFL pattern appears, with orientation parallel to the polarization of the UV beam and periodicity corresponding to the UV wavelength (400 nm). In conclusion, it is the first pulse that defines the final result and the subsequent pattern (periodicity and orientation).

The damaged area as a function of the number of double-pulse sequences has been plotted in figure 4.11 along with the previously obtained result for UV alone. This result shows a linear increase of the area, but the data points are far too

few to make safe conclusions. However, we may retain that the same pattern is observed in both cases, at given N, but in different sizes (smaller damaged area for UV+IR).

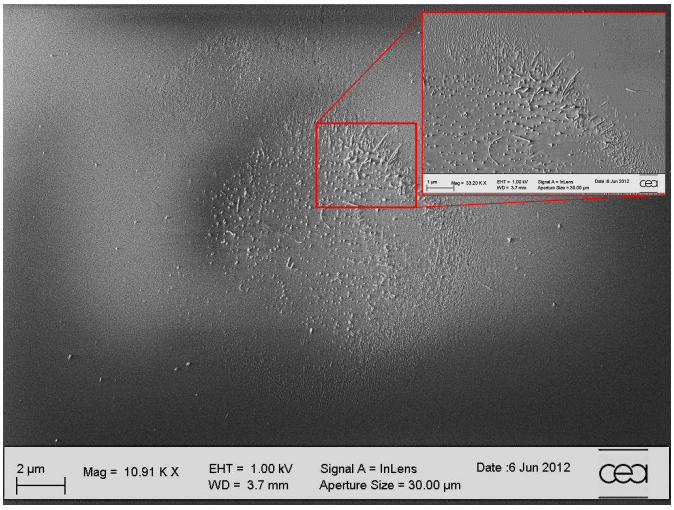

(a) $N = 5$

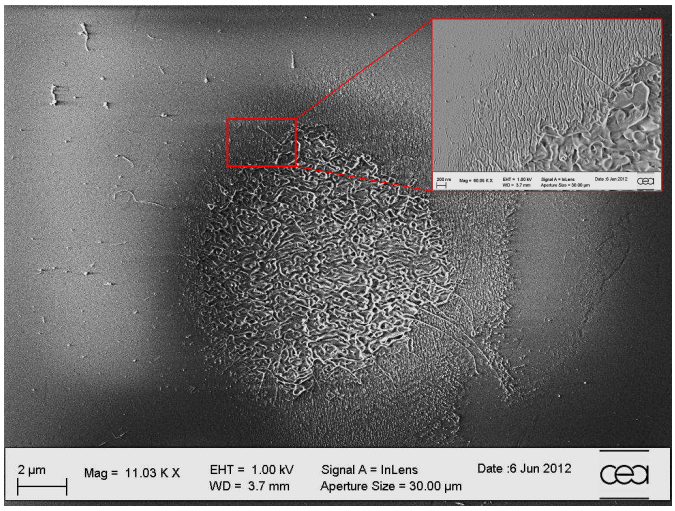

(b) $N = 10$

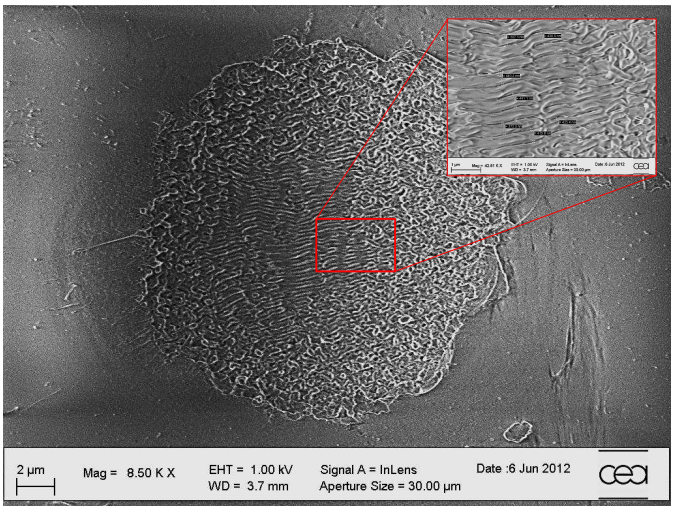

(c) $N = 20$

Figure 4.10: SEM image of SiO_2 irradiated with N= 5, 10, 20 double-pulse (UV and IR) sequences of fixed delay [$\Delta t = 200$ fs] at corresponding fluencies of 1.8 J/cm^2 for UV($\tau = 60$ fs) and 0.8 J/cm^2 for IR($\tau = 300$ fs).

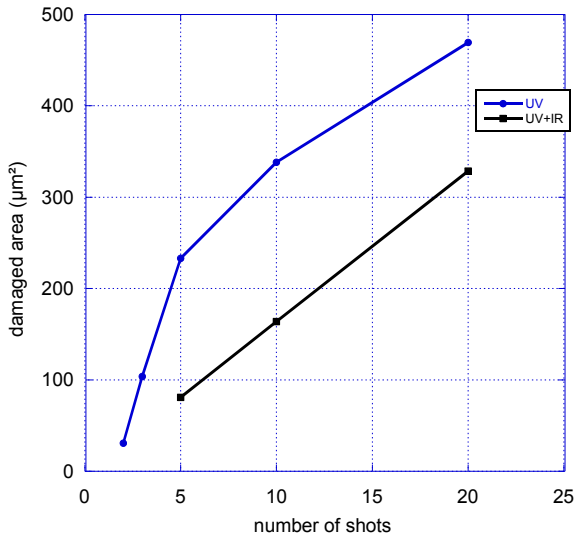

Figure 4.11: Damaged area as a function of the number of shots for a double-pulse sequence of a UV pulse of duration τ=60fs, at a fluence of 1.8 J/cm^2 and an IR pulse, of duration τ=300fs, at a fluence of 0.8 J/cm^2. The same result with UV pulse alone ($F = 3.1$ J/cm^2) is plotted along.

4.3.3 Pulse delay study

The previous result (double-pulse morphology study based on number of shots) along with the interferometry experiment results stating that different mechanisms are being involved for different pump pulse delays, has motivated this last part, focusing on the delay between UV and IR. These experiments have been performed scanning in time the IR pulse, for different number of shot sequences and a IR energy corresponding to 130% of the CDTH[3], defined for a $\Delta t = 200$ fs delay between the pulses. Both polarizations are kept horizontal and no modification is observed when each pulse hit the surface alone at the fluencies used in the double-pulse sequence. Vertical translation of $100\mu m$ follows each step in time (26 fs) to avoid spatial overlapping between different irradiated spots. The scans are performed from $\Delta\tau = -667$ fs (IR arriving before UV) until $\Delta\tau = 1.3$ ps.

To start with, we present the impact from each pulse alone at 130% of the SDTH[4] so that we may have a hint of the individual morphology responses and the size of the modified area. In figure 4.12 we present the result with IR beam alone (see figure 4.12a: laser spot diameter= 90 μm, $N = 10$, $\tau = 300$ fs and $F = 4$ J/cm^2) and UV beam alone (see figure 4.12b: laser spot diameter= 26.3 μm, N = 10, $\tau = 60$ fs and $F = 4.1$ J/cm^2).

The morphology of the impact with the UV pulse alone presents LSFL of periodicity $\Lambda \sim$ 400 nm $= \lambda$, parallel to the laser polarization. On the contrary, HSFL are present when the damage is due to IR pulse alone quasi-perpendicular to the beam's polarization, while in the center we observe signs of molten matter in disorder.

We now combine the two pulses at: $F = 1.9$ J/cm^2 of pulse duration $\tau = 60$ fs for UV and $F = 2$ J/cm^2 of pulse duration $\tau = 300$ fs for IR in figure 4.13. Three shots of double-pulse sequences at same delay are sent per target. Images for 4 different delays have been acquired and no modification has been observed below or above the presented delays. For $\Delta t = 53$ fs (see figure 4.13a) we observe LSFL parallel to the UV polarization, along with long nano-filaments positioned randomly. Some point pattern may be seen on the lower part of the periphery, while outside signs of HSFL formation exist (far right and far left parts of the picture). When $\Delta t = 187$ fs (see figure 4.13b), there is tendency for a more structured morphology with only LSFL present due to UV. With $\Delta t = 500$ fs (see figure 4.13c)the LSFL structure gives its place to smaller size ripples with same periodicity as before, but mainly scattered outside the center of the irradiated spot. Filaments are seen as well pointing outwards. For $\Delta t = 667$ fs (see figure

[3]UV energy is fixed at 70% of the SDTH and the IR comes 200 fs later with an energy chosen in a way that damage takes place on the surface.

[4]In order to ensure that damaging takes place, the energies are raised with respect to the ones used in the double-pulse experiment that will follow.

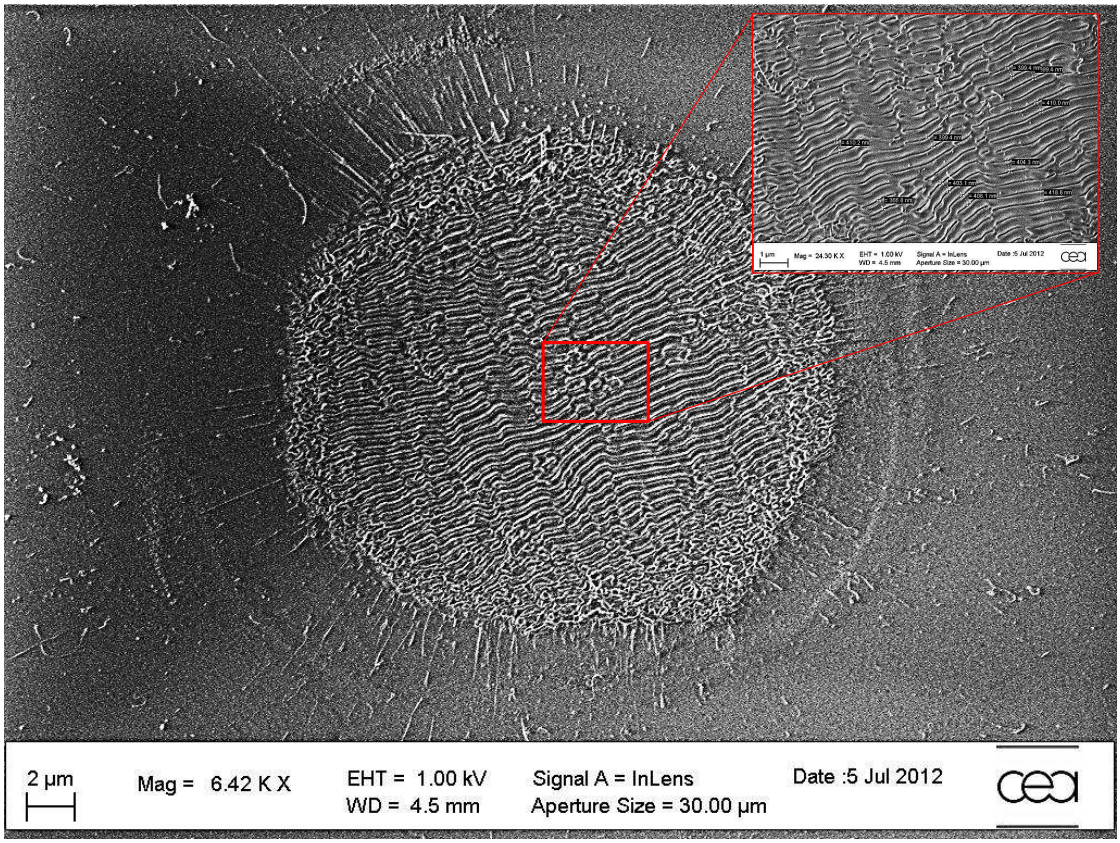

(a) N = 10 shots with a UV pulse (60 fs), at a fluence of 4.1 J/cm^2

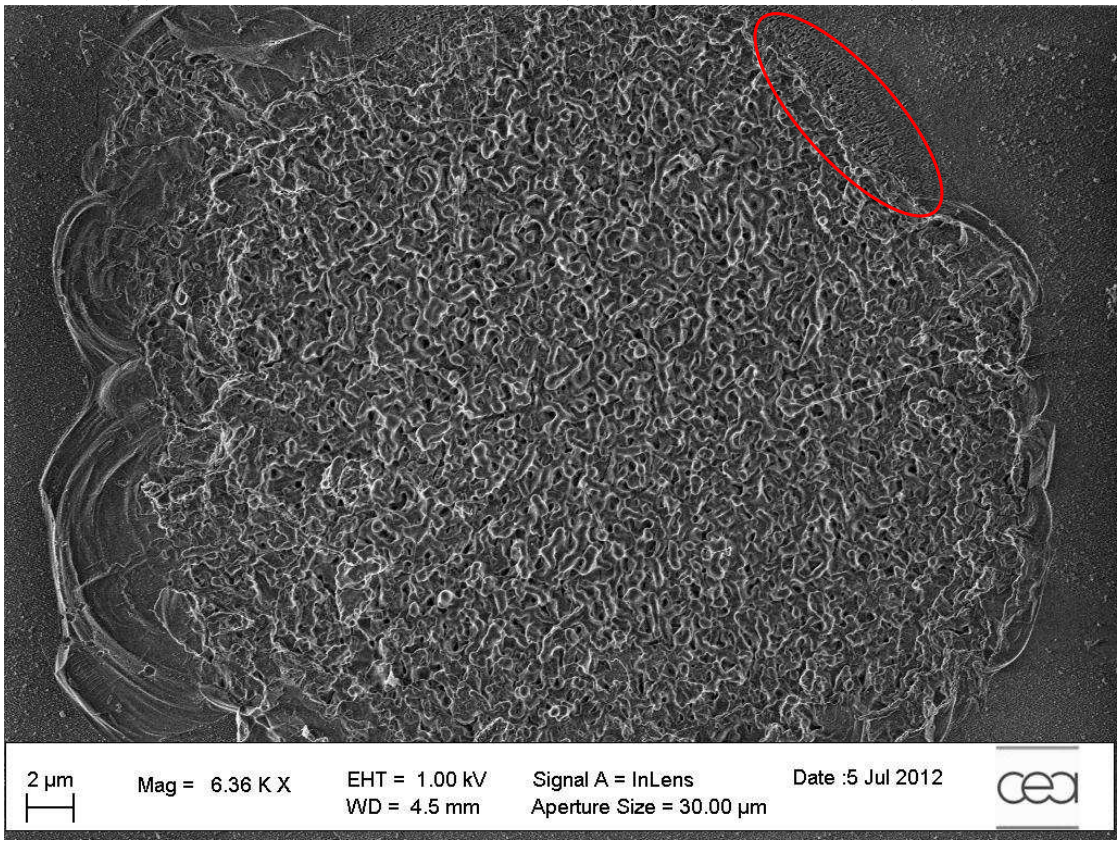

(b) N = 10 shots with a IR pulse (300 fs), at a fluence of 4 J/cm^2. HSFL is highlighted in red.

Figure 4.12: SEM images of SiO_2 irradiated with N = 10 UV and IR shots (upper and lower part of the figure respectively).

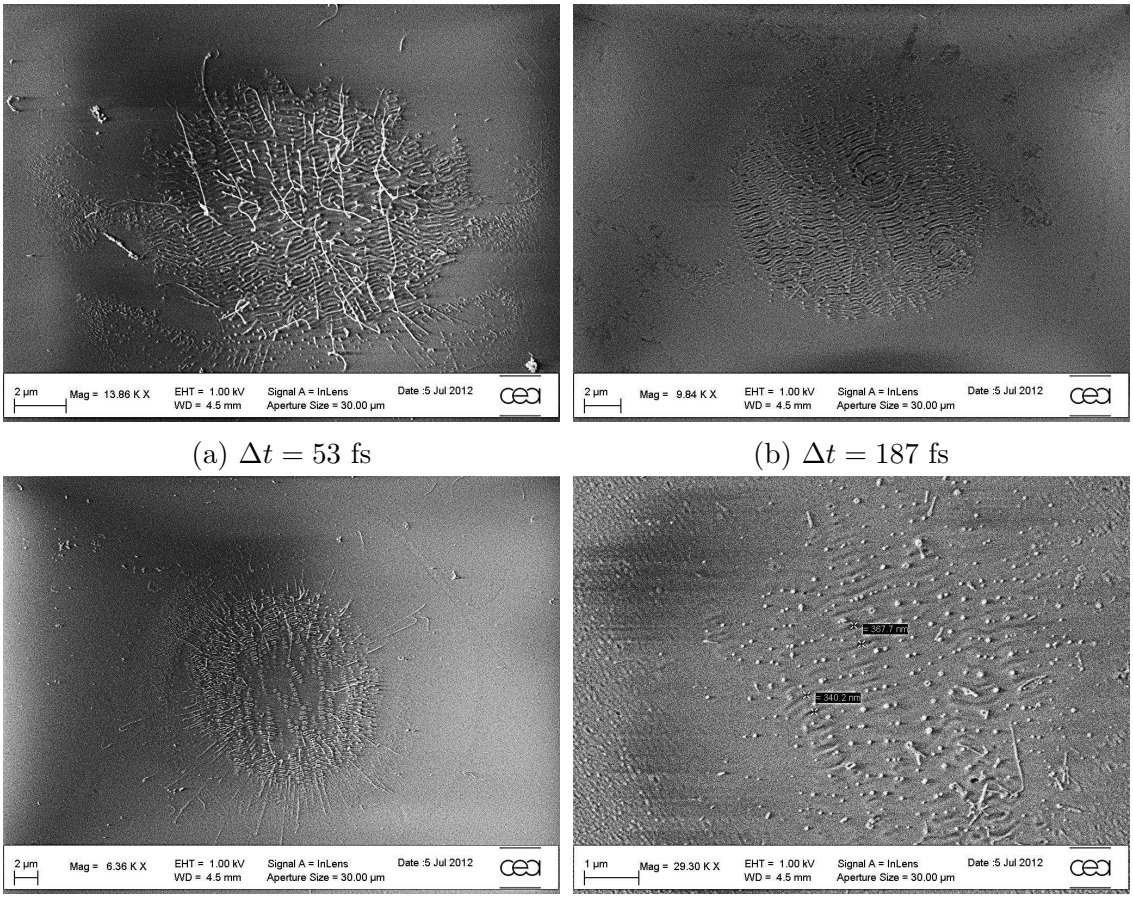

(a) $\Delta t = 53$ fs (b) $\Delta t = 187$ fs

(c) $\Delta t = 500$ fs (d) $\Delta t = 667$ fs

Figure 4.13: SEM images of SiO_2 irradiated with 3 double-pulse (UV and IR) sequences of varying delays [Δt = -667 fs to 1.3 ps] at corresponding fluencies of 1.9 J/cm^2 for UV($\tau = 60$ fs) and 2 J/cm^2 for IR($\tau = 300$ fs). Lower and higher delay for which damaging was observed is represented. Notice the change in scale between the images.

4.13d) we observe a point pattern in the center, with separation between the points being of the order of $\sim$ 400 nm= λ(UV). No damage has been observed below these delays ($\Delta t < 0$) or above ($\Delta t > 667$).

In figure 4.14 we have plotted the damaged area as a function of the pulse delay, along with the damaged area for UV and IR alone (see figure 4.12). The region in which free electron are expected to be present is illustrated in the hatched area (Δt value from interferometry experiments). While a raise is observed for increasing delays in the $0 - 500$ fs range, suddenly this value drops down for 670 fs.

Next, the number of shots per irradiated site was raised to N=5 and another

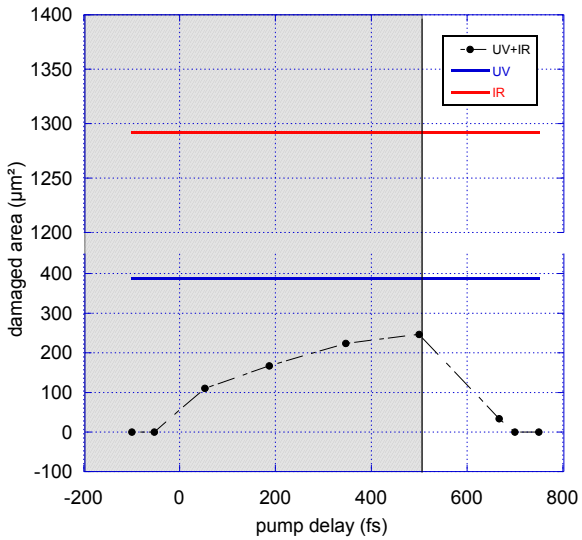

Figure 4.14: Damaged area as a function of the pulse delay (black full circles) for N=3. Single pulse cases are plotted along (blue line for UV and red line for IR). The electron lifetime "window" in CB is represented in the hatched area.

series has been obtained in the exact same conditions as before. This result is presented in figure 4.15 for 4 different delays (same delays as before). Once again, for a short delay (Δt = 53 fs, see figure 4.15a) different elements are mixed up on the surface, including a point pattern and randomly oriented filaments in the center, with a start of LSFL formation all around. This structure is once again parallel to the UV polarization and its periodicity Λ corresponds to λ(UV). At Δt = 187 fs (see figure 4.15b), these ripples are more visible and better structured than before. Nano-filaments pointing outwards can be spotted on the periphery as well. For Δt = 480 fs (see figure 4.15c), the structure remains the same. Finally, when Δt = 667 fs (see figure 4.15d), the surface presents more disorder then before. No damage has been observed below these delays ($\Delta t < 0$ fs) or above ($\Delta t > 667$ fs).

We have plotted the damaged surface as a function of delay (as we did before for N=3) in figure 4.16. This surface, rises almost linearly until Δt = 350 fs, until it reaches a plateau around that value.

A third series has been obtained in the same conditions, but raising further the number of shots at N=10 and it is presented in figure 4.17. The same 4 delays as before have been recorded. This time LSFL formation is observed in the center, for a short delay Δt = 53 fs (see figure 4.17a), while on the periphery the structure seems to be more disordered. For a longer delay (Δt = 187 fs, see figure 4.17b), the same pattern is observed, but this time the LSFL structure is

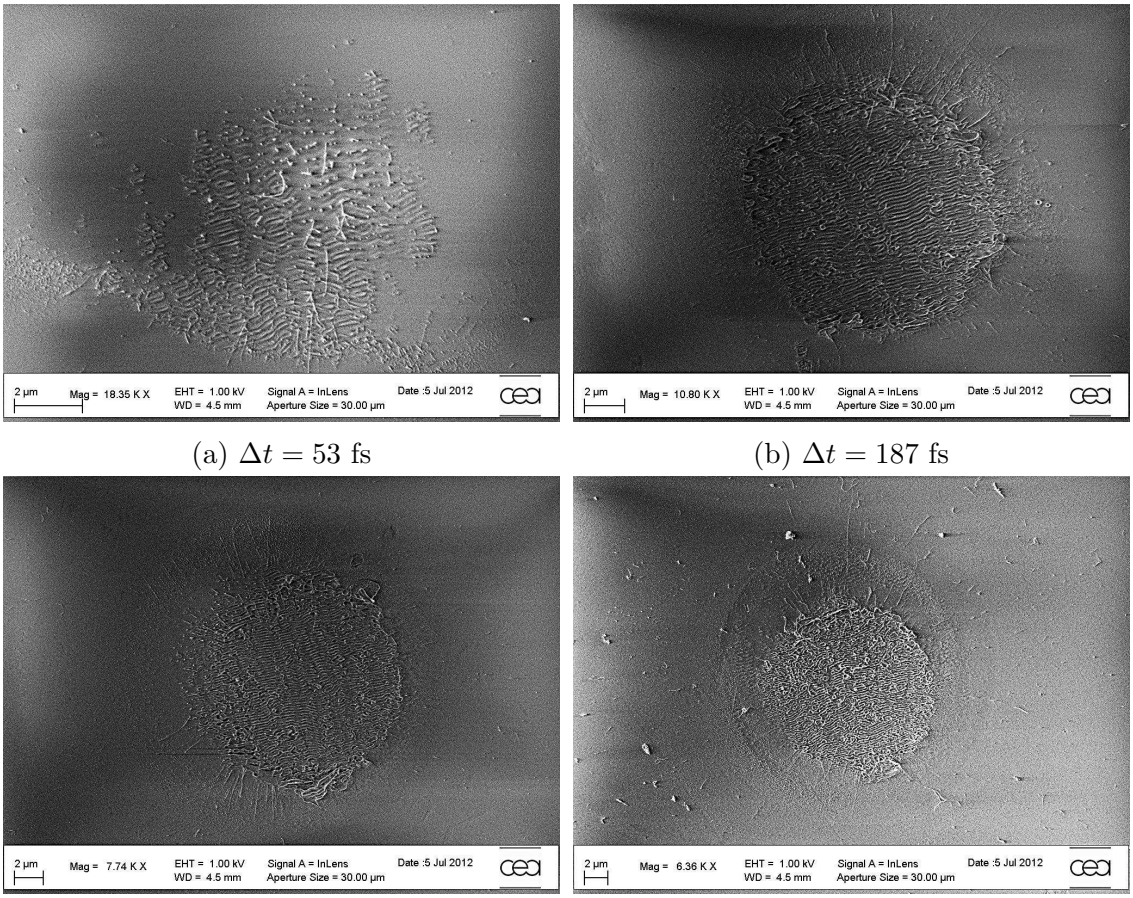

(a) $\Delta t = 53$ fs (b) $\Delta t = 187$ fs

(c) $\Delta t = 480$ fs (d) $\Delta t = 667$ fs

Figure 4.15: SEM images of SiO_2 irradiated with 5 double-pulse (UV and IR) sequences of varying delays [Δt = $-$667fs to 1.3 ps] at corresponding fluencies of 1.9 J/cm^2 for UV($\tau = 60$ fs) and 2 J/cm^2 for IR($\tau = 300$ fs). Lower and higher delay for which damaging was observed is represented. Notice the change in scale between the images.

more visible in the center, the periodicity has been measured and it was found to be ~ 395 nm $\sim \lambda$(UV) (see figure 4.18). When $\Delta t = 480$ fs (see figure 4.17c), a new pattern is observed that looks like a common LSFL structure, at the same angle as before and with periodicity $\Lambda \sim 410$ nm $\sim \lambda$(UV). At $\Delta t = 667$ fs (see figure 4.17d), the rippled structure gives its place to disordered molten matter. No damage has been observed below these delays ($\Delta t < 0$ fs) or above ($\Delta t > 667$ fs).

Finally, we plot the damaged surface as a function of the delay for N=10 in figure 4.19. Yet this time, the damages surface size rises until $\sim \Delta t = 350$ fs and then slowly drops down.

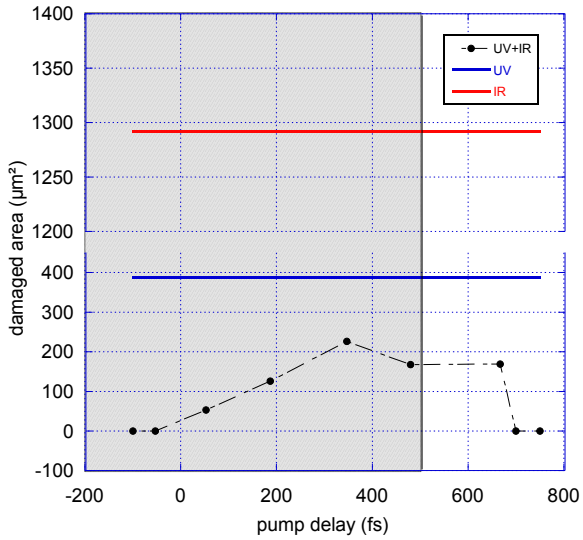

Figure 4.16: Damaged area as a function of the pulse delay (black full circles) for N=5. Single pulse cases are plotted along (blue line for UV and red line for IR). The electron lifetime "window" in CB is represented in the hatched area.

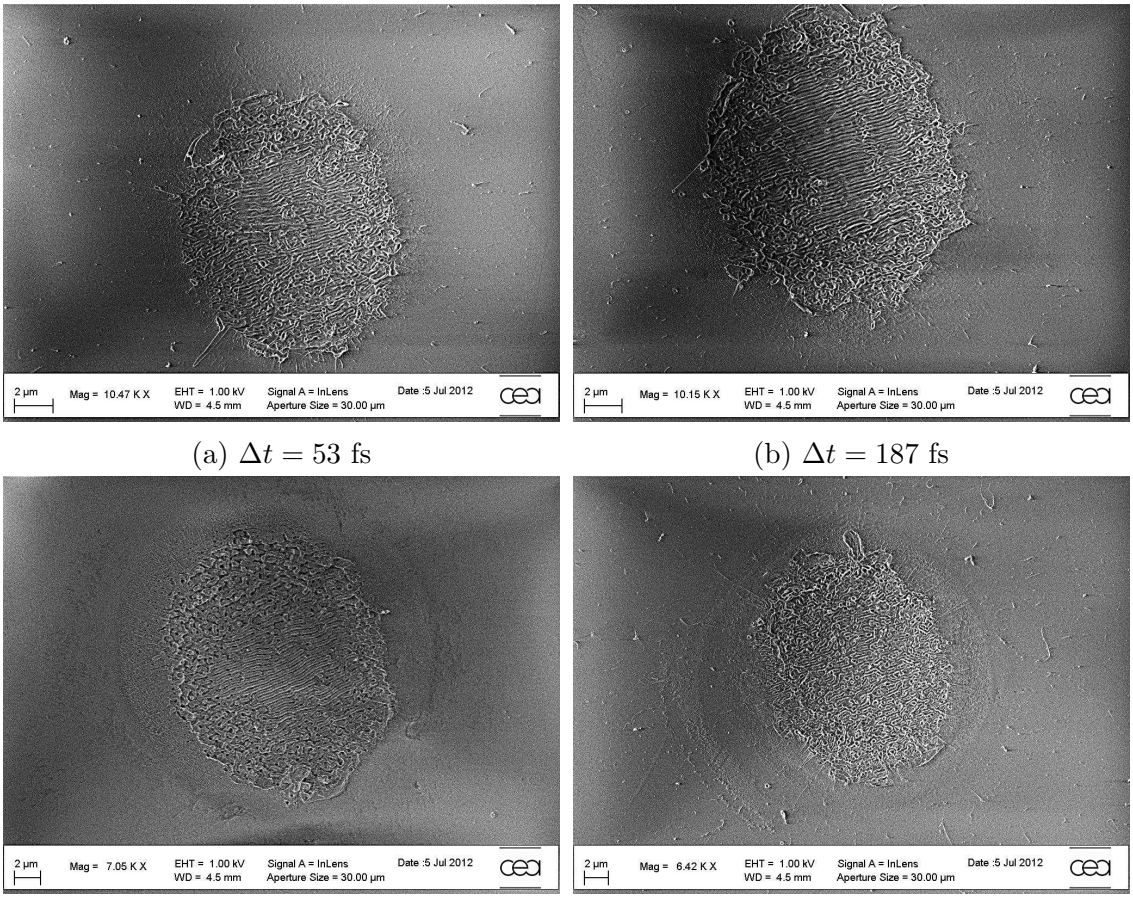

(a) $\Delta t = 53$ fs (b) $\Delta t = 187$ fs

(c) $\Delta t = 480$ fs (d) $\Delta t = 667$ fs

Figure 4.17: SEM images of SiO_2 irradiated with 10 double-pulse (UV and IR) sequences of varying delays [$\Delta t = t = -667$ fs *to* 1.3 ps] at corresponding fluencies of 1.9 J/cm^2 for UV($\tau = 60$ fs) and 2 J/cm^2 for IR($\tau = 300$ fs). Lower and higher delay for which damaging was observed is represented. Notice the change in scale between the images.

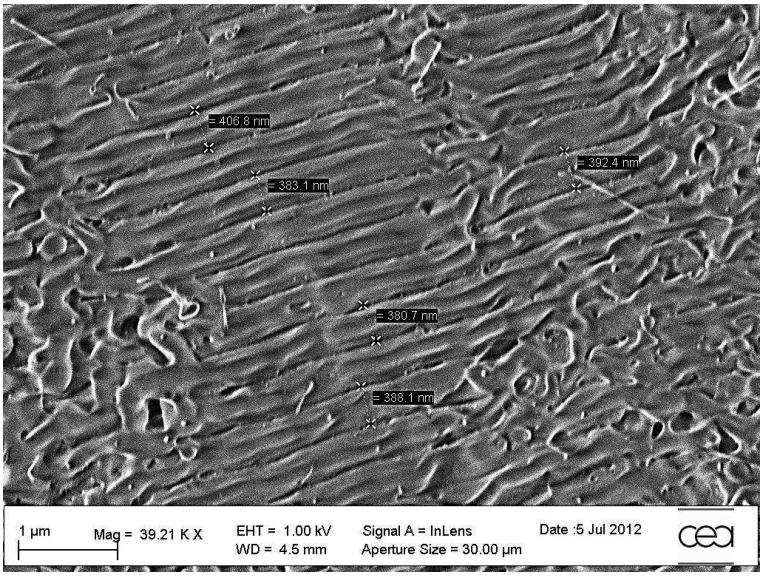

Figure 4.18: Magnified view of 4.17b.

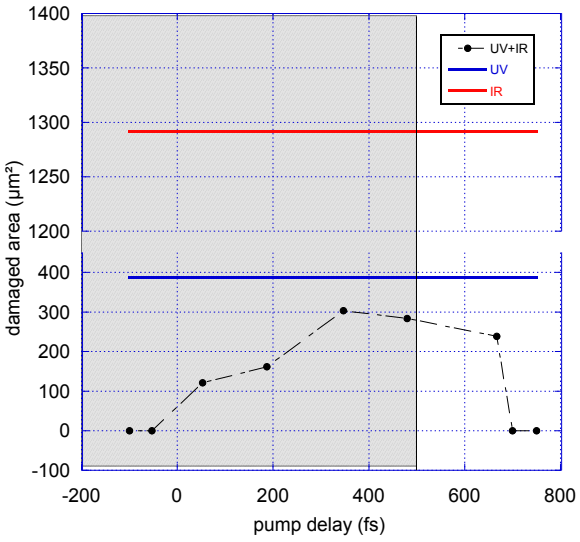

Figure 4.19: Damaged area as a function of the pulse delay (black full circles) for N=10. Single pulse cases are plotted along (blue line for UV and red line for IR). The electron lifetime "window" in CB is represented in the hatched area.

4.4 Conclusion

Study of the damage with variable pulse duration ($1-10$ ps) revealed an extrinsic character. It has been observed, that damage develops around visible defects on the surface (4.3a). This extrinsic process in these pulse durations has already been predicted theoretically (1.2.2). The low excitation densities measured for the same pulse durations (2.47) at SDTH indicate that the damage is most probably thermally activated.

The double-pulse experiments come with the conclusion that the first pulse defined the final pattern, contributing with its wavelength and polarization. This result is in agreement with another double-pulse experiment performed in fused silica [81]. In our configuration, none of the pulses alone (UV and IR) induce damage or ripples. Moreover, the fact of using a second pulse (IR) that produces no ripples and no damage itself, suggests that the first UV pulse inscribes the necessary information in the material and that the IR pulse contributes with its energy, "printing out" the structure on the surface. The memory effect may use information based on a periodically organized excitation density, spatial profile.

To summarize our measurements concerning the damaged surface size as a function of pulse delay Δt, for N= $3, 5$ and 10, we have plotted all of them together in figure 4.20. The same trend is being observed for all three curves in the $0-350$ fs interval which is a raise in the size with increasing delay. Later, the monotonous behaviour of the variation changes and the results indicate a slow drop (N= $5, 10$) or stabilization (for N= 3). Overall, and for most delays, the damaged surface size is higher for $N = 10$.

Moreover, the ripple formation is mainly observed for delay in the $\sim 0-500$ fs time window. These two results combined suggest that damage (and self-organized structure) is related to the electron lifetime in $\alpha - SiO_2$. This is supported by similar conclusions made in ZnO [61] and more recently in fused silica ([81], double-pulse) where two types of behaviour have been observed depending on the nano-structured pattern periodicity [41] : metal like behaviour, where characteristic LSFL area decays with excitation density ($\sim$ 150 fs, revealed by double-pulse experiment) and dielectric behaviour with longer characteristic times ($\geq$ 20 ps). Only the metal-like behaviour has been observed in our experimental conditions. However, it should not be excluded that the dielectric behaviour may be observed as well at different fluencies (pattern formation strongly dependent on the first pulse characteristics).

However, more recent studies in bulk fused silica have shown a relation of the nano-gratings with STE. More in particular, both spatial distribution map of the 488 nm excited photoluminescence ([59], 800 nm, 130 fs) and polarization contrast intensity (PCI) measurement along with absorption measurements ([79, 78], double-pulse, 800 nm, 150 fs) from photo-inscribed LSFL, revealed that the pres-

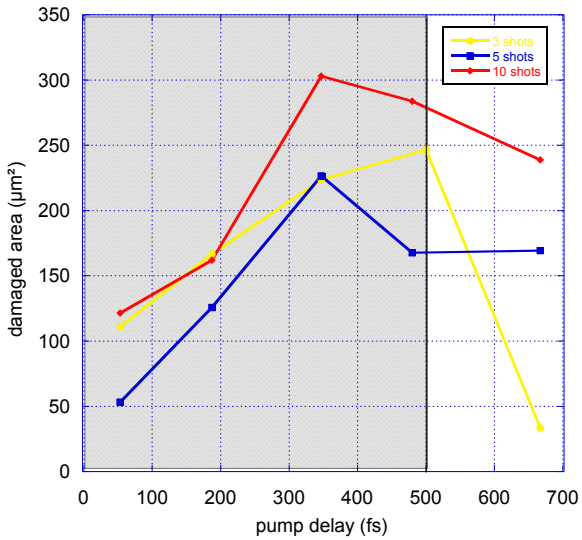

Figure 4.20: Damaged area as a function of the pulse delay (black full circles) for N=3, 5 and 10.

ence of NBOHC was closely connected to the nano-sized structural modification, enhancing the residual absorption of the material. Moreover, the absorption spectra measurements indicate the presence of E' centers that remain active even 2 weeks after the nano-grating inscription. Thus, the "memory" effect has been attributed to these point defects, previously formed from relaxation of the STE.

In conclusion, we may distinguish two regimes for surface nano-structuring of periodic patterns: metal ($\sim \lambda$ LSFL period, "short-time memory" dependent on electron-hole plasma lifetime) and dielectric ($\sim 0.7 \times \lambda$ LSFL period, "long-time memory"). The dielectric type may be attributed to defect formation and the question remains open as to the relative importance of each one of them (NBOHC, E' centers)[5] in the rippled pattern formation. The metal regime could be connected to the interference of the incident light with waves in the induced plasma [88].

[5]Details on defects in oxide glasses can be found in [89]

General conclusion & Perspectives

An experimental study of the fundamental physical mechanisms of the ultrashort laser pulse interaction with dielectric solids, involving different complementary techniques, has been performed. This interaction has been investigated at different intensity regimes, covering the case from below the permanent modification threshold up to ablation of the irradiated target.

The FDI technique has brought interesting results as to the existence of a carrier multiplication mechanism, presumably the one of impact ionization or more recently proposed "forest fire" mechanism. The study of crystals with different intrinsic properties has allowed a distinction between two groups of materials, depending on the possibility to observe this multiplication in our experimental conditions: double-pulse experiment with a first 60 fs, UV pulse pre-exciting electrons in the CB and a variable pulse duration (60 fs-10 ps), IR arriving later to probe this excitation. More precisely, crystals with strong electron-phonon coupling such as $\alpha - SiO_2$, NaCl and KBr have been revealed to be excellent candidates for observing this carrier amplification. The experimental conditions to observe this multiplication have been chosen so that the IR pulse duration corresponds to the carrier lifetime in the CB and that the accumulating fluence exceed the CDTH. On the contrary, no sign of multiplication has been detected in Al_2O_3 or MgO, for a large range of fluence (exceeding the CDTH) and pulse duration (60 fs-10 ps).

An increased recombination rate has been observed in Al_2O_3 for the sequence of a short (60 fs) UV pulse with a long (10 ps) IR pulse, suggesting modified second order recombination kinetics via an increased electron velocity. At later delays (> 500ps) residual absorption could be attributed to the presence of defects. These defects are yet to be identified by the use of common spectroscopic techniques (raman spectroscopy or absorption spectra).

The common feature of hole localization in materials with strong electron-phonon coupling makes us think that a connection with the forest fire mechanism might exist, without ruling out the possibility of simultaneous contribution from impact-ionized electrons. In that case, there is need of a way to de-convolute the

respective multiplication sources. This can be achieved by modelling the interaction by including both mechanisms and try to reproduce the raise observed in our data for the combination of the two pulses. This model can be based on rate equations to account for excitation, heating and relaxation. An experimental approach could be based on the multiplication efficiency with pulse duration: forest fire is theoretically more efficient for short pulses (increased intensity), while we may expect a peak in the impact ionization efficiency at pulse duration corresponding to the lifetime of the carriers in the CB. If one is able to de-convolute those two in the measured signal (by the presence or not of a peak) then we could have a hint on the existence of those two mechanisms.

Furthermore, we have shown that the excited density criterion, commonly used to estimate the threshold for laser-induced damage in solids, is not valid. By measuring the excitation density, at breakdown threshold, in Al_2O_3, MgO and SiO_2 we have observed a decrease of this quantity for increasing pulse duration. Thus a thermal related criterion has been proposed instead, based on the energy that is being deposited on the solid.

PES spectroscopy results in both $\alpha - SiO_2$ and Al_2O_3 indicate that electron kinetic energy distributions at damage threshold are dependent on the pulse duration as well. Short pulses ($\sim$ 60 fs) are more efficient for heating the carriers in the CB while long pulses ($\sim$ 2 ps) contribution to heating is limited and thus outbalanced by the cooling of the carriers. An extended energy tail has been observed in $\alpha - SiO_2$ for the combination of two pulses and this comes to validate our initial hypothesis over heating with a double-pulse in the interferometry experiments.

Our morphological studies on laser-induced damage on the surface of SiO_2 bring important insight as to the influence of different laser parameters. Damage in the 1-10 ps pulse duration range is extrinsic and its development depends on the defect concentration. Double-pulse experiments have been held to investigate LIPSS. These reveal the dominant role of the first pulse in the pattern formation, contributing with its polarization and wavelength to determine the ripples direction and spatial period respectively. Moreover, these nano-structures seem to be closely related to the excitation density of the material, since no pattern was observed for longer pulse delays, corresponding to fully trapped carriers.

Summing up our results, we may conclude that laser-induced damage is of intrinsic character for short pulses (60 fs -$\sim$800 fs) while it is extrinsic for longer ones ($\sim$ 1-10 ps). The intrinsic character is synonym to initial multiphoton absorption and subsequent carrier heating and simultaneous energy deposition on the lattice. No impact ionization or forest fire mechanism seems to participate in the damage of the solid, since their contributions are only measurable above DTH. For longer pulses, damaging involves small excitation densities and the presence of defects starts to play an important role for pulses longer than 1 ps.

Bibliography

[1] A.Einstein. *Ann. Physik*, 17(132):54, 1905.

[2] D. Arnold and E. Cartier. Theory of laser-induced free-electron heating and impact ionization in wide-band-gap solids. *Physical review B*, 46(23):15102, 1992.

[3] D. Arnold, E. Cartier, and DJ DiMaria. Theory of high-field electron transport and impact ionization in silicon dioxide. *Physical Review B*, 49(15):10278, 1994.

[4] M. Barberoglou, V. Zorba, E. Stratakis, E. Spanakis, P. Tzanetakis, SH Anastasiadis, and C. Fotakis. Bio-inspired water repellent surfaces produced by ultrafast laser structuring of silicon. *Applied Surface Science*, 255(10):5425–5429, 2009.

[5] A. Belsky, P. Martin, H. Bachau, AN Vasil'ev, BN Yatsenko, S. Guizard, G. Geoffroy, and G. Petite. Heating of conduction band electrons by intense femtosecond laser pulses. *EPL (Europhysics Letters)*, 67(2):301, 2007.

[6] A. Ben-Yakar, A. Harkin, J. Ashmore, R.L. Byer, and H.A. Stone. Thermal and fluid processes of a thin melt zone during femtosecond laser ablation of glass: the formation of rims by single laser pulses. *Journal of Physics D: Applied Physics*, 40(5):1447, 2007.

[7] L. Bergé, S. Mauger, and S. Skupin. Multifilamentation of powerful optical pulses in silica. *Physical Review A*, 81(1):013817, 2010.

[8] MK Bhuyan, F. Courvoisier, PA Lacourt, M. Jacquot, R. Salut, L. Furfaro, and JM Dudley. High aspect ratio nanochannel machining using single shot femtosecond bessel beams. *Applied Physics Letters*, 97(8):081102–081102, 2010.

[9] N. Bloembergen. Laser-induced electric breakdown in solids. *Quantum Electronics, IEEE Journal of*, 10(3):375–386, 1974.

[10] F. Bonneau, P. Combis, J.L. Rullier, J. Vierne, B. Bertussi, M. Commandre, L. Gallais, J.Y. Natoli, I. Bertron, F. Malaise, et al. Numerical simulations for description of uv laser interaction with gold nanoparticles embedded in silica. *Applied Physics B: Lasers and Optics*, 78(3):447–452, 2004.

[11] J. Bonse, J. Krüger, S. Höhm, and A. Rosenfeld. Femtosecond laser-induced periodic surface structures. *Journal of Laser Applications*, 24(4):042006–042006, 2012.

[12] R.W. Boyd. *Nonlinear optics*. Academic Pr, 2003.

[13] Oliver Brenk and Bärbel Rethfeld. Electron dynamics in transparent materials under high-intensity laser irradiation. *Optical Engineering*, 51(12):121810–1, 2012.

[14] NM Bulgakova, R. Stoian, A. Rosenfeld, IV Hertel, and EEB Campbell. Electronic transport and consequences for material removal in ultrafast pulsed laser ablation of materials. *Physical Review B*, 69(5):054102, 2004.

[15] I.M. Burakov, N.M. Bulgakova, R. Stoian, A. Rosenfeld, and I.V. Hertel. Theoretical investigations of material modification using temporally shaped femtosecond laser pulses. *Applied Physics A: Materials Science & Processing*, 81(8):1639–1645, 2005.

[16] G. Cheng, K. Mishchik, C. Mauclair, E. Audouard, and R. Stoian. Ultrafast laser photoinscription of polarization sensitive devices in bulk silica glass. *Optics express*, 17(12):9515–9525, 2009.

[17] BN Chichkov, C. Momma, S. Nolte, F. Von Alvensleben, and A. Tünnermann. Femtosecond, picosecond and nanosecond laser ablation of solids. *Applied Physics A: Materials Science & Processing*, 63(2):109–115, 1996.

[18] B. Chimier, O. Utéza, N. Sanner, M. Sentis, T. Itina, P. Lassonde, F. Légaré, F. Vidal, and JC Kieffer. Damage and ablation thresholds of fused-silica in femtosecond regime. *Physical Review B*, 84(9):094104, 2011.

[19] Bjarke Holl Christensen and Peter Balling. Modeling ultrashort-pulse laser ablation of dielectric materials. *Physical Review B*, 79(15):155424, 2009.

[20] A. Couairon, L. Sudrie, M. Franco, B. Prade, and A. Mysyrowicz. Filamentation and damage in fused silica induced by tightly focused femtosecond laser pulses. *Physical Review B*, 71(12):125435, 2005.

[21] P. Daguzan. *Dynamique ultra-rapide des porteurs photoexcités dans les solides à grande bande interdite*. PhD thesis.

[22] P. Daguzan, S. Guizard, K. Krastev, P. Martin, G. Petite, A.D. Santos, and A. Antonetti. Direct observation of multiple photon absorption by free electrons in a wide band-gap insulator under strong laser irradiation. *Physical review letters*, 73(17):2352–2355, 1994.

[23] D. Du, X. Liu, G. Korn, J. Squier, and G. Mourou. Laser-induced breakdown by impact ionization in sio_2 with pulse widths from 7 ns to 150 fs. *Applied Physics Letters*, 64(23):3071–3073, 1994.

[24] C. Duan, Z. Gu, J. Li, D. Wang, and S.F. Ren. Application of green's-function technique to the calculation of multiphoton absorption coefficients of crystalline solids. *Physical Review B*, 57(1):10–13, 1998.

[25] L. Englert, B. Rethfeld, L. Haag, M. Wollenhaupt, C. Sarpe-Tudoran, and T. Baumert. Control of ionization processes in high band gap materials via tailored femtosecond pulses. *Opt. Express*, 15(26):17855–17862, 2007.

[26] AJ Fisher, W. Hayes, and AM Stoneham. Theory of the structure of the self-trapped exciton in quartz. *Journal of Physics: Condensed Matter*, 2(32):6707, 1999.

[27] M. Fox. Optical properties of solids. *Recherche*, 67:02, 2001.

[28] PA Franken, AE Hill, C.W. Peters, and G. Weinreich. Generation of optical harmonics. *Physical Review Letters*, 7(4):118–119, 1961.

[29] C. Froehly, A. Lacourt, and J.C. Vienot. Time impulse response and time frequency response of optical pupils.: Experimental confirmations and applications. *Nouvelle Revue D'Optique*, 4:183, 1973.

[30] LN Gaier, M. Lein, MI Stockman, PL Knight, PB Corkum, M.Y. Ivanov, and GL Yudin. Ultrafast multiphoton forest fires and fractals in clusters and dielectrics. *Journal of Physics B: Atomic, Molecular and Optical Physics*, 37(3):L57, 2004.

[31] E.G. Gamaly, S. Juodkazis, K. Nishimura, H. Misawa, B. Luther-Davies, L. Hallo, P. Nicolai, and V.T. Tikhonchuk. Laser-matter interaction in the bulk of a transparent solid: Confined microexplosion and void formation. *Physical Review B*, 73(21):214101, 2006.

[32] J. Gaudin. *Processus électroniques d'excitation et de relaxation dans les solides diélectriques excités par des impulsions IR et XUV ultracourtes*. PhD thesis, Université Sciences et Technologies-Bordeaux I, 2005.

[33] JP Geindre, P. Audebert, A. Rousse, F. Fallies, JC Gauthier, A. Mysyrowicz, A.D. Santos, G. Hamoniaux, and A. Antonetti. Frequency-domain interferometer for measuring the phase and amplitude of a femtosecond pulse probing a laser-produced plasma. *Optics letters*, 19(23):1997–1999, 1994.

[34] J. Gottmann, D. Wortmann, and M. Hörstmann-Jungemann. Fabrication of sub-wavelength surface ripples and in-volume nanostructures by fs-laser induced selective etching. *Applied surface science*, 255(10):5641–5646, 2009.

[35] D. Grojo, M. Gertsvolf, S. Lei, T. Barillot, DM Rayner, and PB Corkum. Exciton-seeded multiphoton ionization in bulk sio_2. *Physical Review B*, 81(21):212301, 2010.

[36] S. Guizard, AN Belsky, J. Gaudin, G. Geoffroy, P. Martin, G. Petite, A. Philippov, and BN Yatsenko. Time resolved two-colour vuv-ir photoemission in wide band gap dielectrics. *physica status solidi (c)*, 2(1):223–227, 2005.

[37] S. Guizard, P. Martin, P. Daguzan, G. Petite, P. Audebert, JP Geindre, A. Dos Santos, and A. Antonnetti. Contrasted behaviour of an electron gas in mgo, al_2o_3 and sio_2. *EPL (Europhysics Letters)*, 29(5):401, 1995.

[38] S. Guizard, P. Martin, G. Petite, P. D'Oliveira, and P. Meynadier. Time-resolved study of laser-induced colour centres in. *Journal of Physics: Condensed Matter*, 8(9):1281, 1999.

[39] S. Guizard, A. Semerok, J. Gaudin, M. Hashida, P. Martin, and F. Quéré. Femtosecond laser ablation of transparent dielectrics: measurement and modelisation of crater profiles. *Applied surface science*, 186(1):364–368, 2002.

[40] E. Hecht. Hecht optics. *Addison Wesley*, 997:213–214, 1998.

[41] S. Höhm, A. Rosenfeld, J. Krüger, and J. Bonse. Area dependence of femtosecond laser-induced periodic surface structures for varying band gap materials after double pulse excitation. *Applied Surface Science*, 2012.

[42] M. Huang, F. Zhao, Y. Cheng, N. Xu, and Z. Xu. Large area uniform nanostructures fabricated by direct femtosecond laser ablation. *Optics express*, 16(23):19354–19365, 2008.

[43] H.P. Huber, F. Herrnberger, S. Kery, and S. Zoppel. Selective structuring of thin-film solar cells by ultrafast laser ablation. *Proceedings of SPIE Commercial and Biomedical Applications of Ultrafast Lasers*, 8(688):688117, 2008.

[44] J. Ihlemann, B. Wolff, and P. Simon. Nanosecond and femtosecond excimer laser ablation of fused silica. *Applied Physics A: Materials Science & Processing*, 54(4):363–368, 1992.

[45] Y. Ishida, N. Sarukura, and H Nakano. *Conference: Ultrafast Phenomena VII,*, 1990.

[46] T.E. Itina, J. Hermann, P. Delaporte, and M. Sentis. Laser-generated plasma plume expansion: Combined continuous-microscopic modeling. *Physical Review E*, 66(6):066406, 2002.

[47] A.P. Joglekar, H. Liu, GJ Spooner, E. Meyhöfer, G. Mourou, and AJ Hunt. A study of the deterministic character of optical damage by femtosecond laser pulses and applications to nanomachining. *Applied Physics B: Lasers and Optics*, 77(1):25–30, 2003.

[48] S.C. Jones, P. Braunlich, R.T. Casper, X.A. Shen, and P. Kelly. Recent progress on laser-induced modifications and intrinsic bulk damage of wide-gap optical materials. *Optical Engineering*, 28(10):281039–281039, 1989.

[49] A. Kaiser, B. Rethfeld, M. Vicanek, and G. Simon. Microscopic processes in dielectrics under irradiation by subpicosecond laser pulses. *Physical Review B*, 61(17):11437, 2000.

[50] L.V. Keldysh. Ionization in field of a strong electromagnetic wave. *Soviet Physics Jetp-Ussr*, 20(5):1307, 1965.

[51] AI Kuznetsov, J. Koch, and BN Chichkov. Nanostructuring of thin gold films by femtosecond lasers. *Applied Physics A: Materials Science & Processing*, 94(2):221–230, 2009.

[52] M. Lenzner, J. Krüger, S. Sartania, Z. Cheng, C. Spielmann, G. Mourou, W. Kautek, and F. Krausz. Femtosecond optical breakdown in dielectrics. *Physical Review Letters*, 80(18):4076–4079, 1998.

[53] L. Lepetit, G. Cheriaux, and M. Joffre. Linear techniques of phase measurement by femtosecond spectral interferometry for applications in spectroscopy. *JOSA B*, 12(12):2467–2474, 1995.

[54] M. Li, S. Menon, J.P. Nibarger, and G.N. Gibson. Ultrafast electron dynamics in femtosecond optical breakdown of dielectrics. *Physical review letters*, 82(11):2394–2397, 1999.

[55] P. Martin, S. Guizard, P. Daguzan, G. Petite, P. d'Oliveira, P. Meynadier, and M. Perdrix. Subpicosecond study of carrier trapping dynamics in wide-band-gap crystals. *Physical Review B*, 55(9):5799, 1997.

[56] C. Mauclair, G. Cheng, N. Huot, E. Audouard, A. Rosenfeld, I.V. Hertel, and R. Stoian. Dynamic ultrafast laser spatial tailoring for parallel micromachining of photonic devices in transparent materials. *Optics express*, 17(5):3531–3542, 2009.

[57] FR McFeely, E. Cartier, LJ Terminello, A. Santoni, and MV Fischetti. Soft-x-ray–induced core-level photoemission as a probe of hot-electron dynamics in sio_ {2}. *Physical review letters*, 65(15):1937–1940, 1990.

[58] M. Mero, J. Liu, W. Rudolph, D. Ristau, and K. Starke. Scaling laws of femtosecond laser pulse induced breakdown in oxide films. *Physical Review B*, 71(11):115109, 2005.

[59] K. Mishchik, G. Cheng, G. Huo, I.M. Burakov, C. Mauclair, A. Mermillod-Blondin, A. Rosenfeld, Y. Ouerdane, A. Boukenter, O. Parriaux, et al. Nanosize structural modifications with polarization functions in ultrafast laser irradiated bulk fused silica. *Optics express*, 18(24):24809–24824, 2010.

[60] A. Mouskeftaras, S. Guizard, N. Fedorov, and S. Klimentov. Mechanisms of femtosecond laser ablation of dielectrics revealed by double pump–probe experiment. *Applied Physics A: Materials Science & Processing*, pages 1–7, 2012.

[61] L. Museur, A. Manousaki, D. Anglos, and A.V. Kanaev. Surface modification of monocrystalline zinc oxide induced by high-density electronic excitation. *Journal of Applied Physics*, 110(12):124310–124310, 2011.

[62] Varkentina N. *Interaction laser femtoseconde-diélectrique à intensitée moderée: analyse du dépot d'énergie et application à l'ablation de la silice fondue et de la cornée.* PhD thesis, Université d'Aix-Marseille, 2012.

[63] J. Neauport, L. Lamaignere, H. Bercegol, F. Pilon, and J.C. Birolleau. Polishing-induced contamination of fused silica optics and laser induced damage density at 351 nm. *Optics Express*, 13(25):10163–10171, 2005.

[64] S. Nolte, G. Kamlage, F. Korte, T. Bauer, T. Wagner, A. Ostendorf, C. Fallnich, and H. Welling. Microstructuring with femtosecond lasers. *Advanced Engineering Materials*, 2(1-2):23–27, 2000.

[65] M. Perrin. Microscopie electronique a balayage et microanalyse (in french). `http://www.cmeba.univ-rennes1.fr/Principe_MEB.html`.

[66] MD Perry, BC Stuart, PS Banks, MD Feit, V. Yanovsky, and AM Rubenchik. Ultrashort-pulse laser machining of dielectric materials. *Journal of applied physics*, 85(9):6803–6810, 1999.

[67] G. Petite. Mécanismes fondamentaux de l'ablation laser femtoseconde en flux "intermédiaire". *arXiv preprint cond-mat/0502132*, 2005.

[68] G. Petite, P. Agostini, R. Trainham, E. Mevel, and P. Martin. Origin of the high-energy electron emission from metals under laser irradiation. *Physical Review B*, 45(21):12210, 1992.

[69] GM Petrov and J. Davis. Interaction of intense ultra-short laser pulses with dielectrics. *Journal of Physics B: Atomic, Molecular and Optical Physics*, 41(2):025601, 2008.

[70] PP Pronko, SK Dutta, J. Squier, JV Rudd, D. Du, and G. Mourou. Machining of sub-micron holes using a femtosecond laser at 800 nm. *Optics communications*, 114(1):106–110, 1995.

[71] F. Quéré. *Etude des mécanismes d'excitation électronique associés au claquage des diélectriques induit par un champ laser intense*. PhD thesis, Université Paris-Sorbonne-Paris IV, 2000.

[72] F. Quéré, S. Guizard, and P. Martin. Time-resolved study of laser-induced breakdown in dielectrics. *EPL (Europhysics Letters)*, 56(1):138, 2007.

[73] PP Rajeev, M. Gertsvolf, PB Corkum, and DM Rayner. Field dependent avalanche ionization rates in dielectrics. *Physical review letters*, 102(8):83001, 2009.

[74] F. Reinert and S. Hüfner. Photoemission spectroscopyfrom early days to recent applications. *New Journal of Physics*, 7(1):97, 2005.

[75] B. Rethfeld. Unified model for the free-electron avalanche in laser-irradiated dielectrics. *Physical review letters*, 92(18):187401, 2004.

[76] B. Rethfeld. Free-electron generation in laser-irradiated dielectrics. *Physical Review B*, 73(3):035101, 2006.

[77] B Rethfeld, K Sokolowski-Tinten, D Von der Linde, and SI Anisimov. Ultrafast thermal melting of laser-excited solids by homogeneous nucleation. *Physical review B*, 65(9):092103, 2002.

[78] S. Richter, M. Heinrich, S. Döring, A. Tünnermann, S. Nolte, and U. Peschel. Nanogratings in fused silica: Formation, control, and applications. *Journal of Laser Applications*, 24(4):042008–042008, 2012.

[79] S. Richter, F. Jia, M. Heinrich, S. Döring, U. Peschel, A. Tünnermann, and S. Nolte. The role of self-trapped excitons and defects in the formation of nanogratings in fused silica. *Optics letters*, 37(4):482–484, 2012.

[80] B.K. Ridley and BK Ridley. *Quantum processes in semiconductors*. Clarendon Press Oxford, 1988.

[81] M. Rohloff, SK Das, S. Hohm, R. Grunwald, A. Rosenfeld, J. Kruger, and J. Bonse. Formation of laser-induced periodic surface structures on fused silica upon multiple cross-polarized double-femtosecond-laser-pulse irradiation sequences. *Journal of Applied Physics*, 110(1):014910–014910, 2011.

[82] B.E.A. Saleh, M.C. Teich, and B.E. Saleh. *Fundamentals of photonics*, volume 22. Wiley New York, 1991.

[83] A. Schmid, P. Bräunlich, and P.K. Rol. Multiphoton-induced directional emission of halogen atoms from alkali halides. *Physical Review Letters*, 35(20):1382–1385, 1975.

[84] G. Seifert, M. Kaempfe, F. Syrowatka, C. Harnagea, D. Hesse, and H. Graener. Self-organized structure formation on the bottom of femtosecond laser ablation craters in glass. *Applied Physics A: Materials Science & Processing*, 81(4):799–803, 2005.

[85] J. Shan, F. Wang, E. Knoesel, M. Bonn, and T.F. Heinz. Measurement of the frequency-dependent conductivity in sapphire. *Physical review letters*, 90(24):247401, 2003.

[86] N.S. Shcheblanov and T.E. Itina. Femtosecond laser interactions with dielectric materials: insights of a detailed modeling of electronic excitation and relaxation processes. *Applied Physics A: Materials Science & Processing*, pages 1–5, 2012.

[87] XA Shen, S.C. Jones, and P. Braunlich. Laser heating of free electrons in wide-gap optical materials at 1064 nm. *Physical review letters*, 62(23):2711–2713, 1989.

[88] Y. Shimotsuma, P.G. Kazansky, J. Qiu, and K. Hirao. Self-organized nanogratings in glass irradiated by ultrashort light pulses. *Physical review letters*, 91(24):247405, 2003.

[89] L. Skuja, M. Hirano, H. Hosono, and K. Kajihara. Defects in oxide glasses. *physica status solidi (c)*, 2(1):15–24, 2005.

[90] DE Spence, P.N. Kean, and W. Sibbett. 60-fsec pulse generation from a self-mode-locked ti: sapphire laser. *Optics letters*, 16(1):42–44, 1991.

[91] W.E. Spicer. The electronic structure of crystalline solids and photoemission spectroscopy: From einstein to high temperature superconductors. *Journal of Physics and Chemistry of Solids*, 59(4):527–552, 1998.

[92] R. Stoian, D. Ashkenasi, A. Rosenfeld, and EEB Campbell. Coulomb explosion in ultrashort pulsed laser ablation of al_2o_3. *Physical Review B*, 62(19):13167, 2000.

[93] D. Strickland and G. Mourou. Compression of amplified chirped optical pulses. *Optics Communications*, 55(6):447–449, 1985.

[94] BC Stuart, MD Feit, S. Herman, AM Rubenchik, BW Shore, and MD Perry. Nanosecond-to-femtosecond laser-induced breakdown in dielectrics. *Physical Review B*, 53(4):1749, 1996.

[95] BC Stuart, MD Feit, AM Rubenchik, BW Shore, and MD Perry. Laser-induced damage in dielectrics with nanosecond to subpicosecond pulses. *Physical Review Letters*, 74(12):2248–2251, 1995.

[96] T. Tamaki, W. Watanabe, and K. Itoh. Laser micro-welding of transparent materials by a localized heat accumulation effect using a femtosecond fiber laser at 1558 nm. *Optics Express*, 14(22):10460–10468, 2006.

[97] K. Tanimura, T. Tanaka, and N. Itoh. Creation of quasistable lattice defects by electronic excitation in sio_ {2}. *Physical review letters*, 51(5):423–426, 1983.

[98] V.V. Temnov, K. Sokolowski-Tinten, P. Zhou, A. El-Khamhawy, and D. Von Der Linde. Multiphoton ionization in dielectrics: comparison of circular and linear polarization. *Physical review letters*, 97(23):237403, 2006.

[99] E. Tokunaga, A. Terasaki, and T. Kobayashi. Frequency-domain interferometer for femtosecond time-resolved phase spectroscopy. *Optics letters*, 17(16):1131–1133, 1992.

[100] AY Vorobyev, AN Topkov, OV Gurin, VA Svich, and C. Guo. Enhanced absorption of metals over ultrabroad electromagnetic spectrum. *Applied Physics Letters*, 95(12):121106–121106, 2009.

[101] R. Wagner, J. Gottmann, A. Horn, and E.W. Kreutz. Subwavelength ripple formation induced by tightly focused femtosecond laser radiation. *Applied surface science*, 252(24):8576–8579, 2006.

[102] BN Yatsenko, H. Bachau, AN Belsky, J. Gaudin, G. Geoffroy, S. Guizard, P. Martin, G. Petite, A. Philippov, and AN Vasil'Ev. Creation of high energy electronic excitations in inorganicinsulators by intense femtosecond laser pulses. *physica status solidi (c)*, 2(1):240–243, 2005.

[103] I.N. Zavestovskaya, P.G. Eliseev, O.N. Krokhin, and N.A. Menkova. Analysis of the nonlinear absorption mechanisms in ablation of transparent materials by high-intensity and ultrashort laser pulses. *Applied Physics A: Materials Science & Processing*, 92(4):903–906, 2008.

[104] W. Zhang, Y. Zhou, L. Zhong, X. Nie, and D. Wang. Self-consistent calculation of the multiphoton absorption coefficients of crystalline solids. *Optics communications*, 126(1):61–65, 1996.

[105] ES Zouboulis and M. Grimsditch. Refractive index and elastic properties of single-crystal corundum ($\alpha - al_2o_3$) up to 2100 k. *Journal of applied physics*, 70(2):772–776, 1991.